



HAL
open science

Development of electroactive polymer actuators for next generation mirror : Live-Mirror

Kritsadi Thetpraphi

► **To cite this version:**

| Kritsadi Thetpraphi. Development of electroactive polymer actuators for next generation mirror :
| Live-Mirror. Electronics. Université de Lyon, 2020. English. NNT : 2020LYSEI058 . tel-03186873

HAL Id: tel-03186873

<https://theses.hal.science/tel-03186873>

Submitted on 31 Mar 2021

HAL is a multi-disciplinary open access archive for the deposit and dissemination of scientific research documents, whether they are published or not. The documents may come from teaching and research institutions in France or abroad, or from public or private research centers.

L'archive ouverte pluridisciplinaire **HAL**, est destinée au dépôt et à la diffusion de documents scientifiques de niveau recherche, publiés ou non, émanant des établissements d'enseignement et de recherche français ou étrangers, des laboratoires publics ou privés.



N° d'ordre NNT : 2020LYSEI058

THESE de DOCTORAT DE L'UNIVERSITE DE LYON
opérée au sein de
L'Institut National des Sciences Appliquées de Lyon

Ecole Doctorale N° ED160 EEA
ÉLECTRONIQUE, ÉLECTROTECHNIQUE, AUTOMATIQUE

Spécialité/ discipline de doctorat : Génie électrique

Soutenue publiquement/à huis clos le **15/07/2020**, par :
Kritsadi THETPRAPHI

**Development of Electroactive Polymer
Actuators for Next Generation Mirror:
Live-Mirror**

Devant le jury composé de :

CAVILLE, Jean-Yves	Professeur Emerite/INSA-Lyon & Head of ELyTMaX Lyon site	Président
DANTRAS, Eric PUTSON, Chatchai	Maître de Conférence HDR/ CIRIMAT Associate Professor/PSU	Rapporteur Rapporteur
COLIN, Annie LANGLOIS, Maud USON, Juan	Professeure/ESPCI Paris Directrice de Recherche/CRAL Professeur/IAC	Examinatrice Examinatrice Examineur
PETIT, Lionel CAPSAL, Jean-Fabien	Professeur/INSA-Lyon Maître de conférences/INSA-Lyon	Directeur de thèse Co-directeur de thèse
AUDIGIER, David KUHN, Jeff MORETTO, Gil	Maître de conférences/INSA-Lyon Professeur/Univ. Hawaii Docteur/CRAL	Invité/Co-directeur Invité/Co-directeur Invité/Co-directeur

Département FEDORA – INSA Lyon - Ecoles Doctorales – Quinquennal 2016-2020

SIGLE	ECOLE DOCTORALE	NOM ET COORDONNEES DU RESPONSABLE
CHIMIE	CHIMIE DE LYON http://www.edchimie-lyon.fr Sec. : Renée EL MELHEM Bât. Blaise PASCAL, 3e étage secretariat@edchimie-lyon.fr INSA : R. GOURDON	M. Stéphane DANIELE Institut de recherches sur la catalyse et l'environnement de Lyon IRCELYON-UMR 5256 Équipe CDFA 2 Avenue Albert EINSTEIN 69 626 Villeurbanne CEDEX directeur@edchimie-lyon.fr
E.E.A.	ÉLECTRONIQUE, ÉLECTROTECHNIQUE, AUTOMATIQUE http://edeea.ec-lyon.fr Sec. : M.C. HAVGOUDOUKIAN ecole-doctorale.eea@ec-lyon.fr	M. Gérard SCORLETTI École Centrale de Lyon 36 Avenue Guy DE COLLONGUE 69 134 Écully Tél : 04.72.18.60.97 Fax 04.78.43.37.17 gerard.scorletti@ec-lyon.fr
E2M2	ÉVOLUTION, ÉCOSYSTÈME, MICROBIOLOGIE, MODÉLISATION http://e2m2.universite-lyon.fr Sec. : Sylvie ROBERJOT Bât. Atrium, UCB Lyon 1 Tél : 04.72.44.83.62 INSA : H. CHARLES secretariat.e2m2@univ-lyon1.fr	M. Philippe NORMAND UMR 5557 Lab. d'Ecologie Microbienne Université Claude Bernard Lyon 1 Bâtiment Mendel 43, boulevard du 11 Novembre 1918 69 622 Villeurbanne CEDEX philippe.normand@univ-lyon1.fr
EDISS	INTERDISCIPLINAIRE SCIENCES-SANTÉ http://www.ediss-lyon.fr Sec. : Sylvie ROBERJOT Bât. Atrium, UCB Lyon 1 Tél : 04.72.44.83.62 INSA : M. LAGARDE secretariat.ediss@univ-lyon1.fr	Mme Sylvie RICARD-BLUM Institut de Chimie et Biochimie Moléculaires et Supramoléculaires (ICBMS) - UMR 5246 CNRS - Université Lyon 1 Bâtiment Curien - 3ème étage Nord 43 Boulevard du 11 novembre 1918 69622 Villeurbanne Cedex Tel : +33(0)4 72 44 82 32 sylvie.ricard-blum@univ-lyon1.fr
INFOMATHS	INFORMATIQUE ET MATHÉMATIQUES http://edinfomaths.universite-lyon.fr Sec. : Renée EL MELHEM Bât. Blaise PASCAL, 3e étage Tél : 04.72.43.80.46 infomaths@univ-lyon1.fr	M. Hamamache KHEDDOUCI Bât. Nautibus 43, Boulevard du 11 novembre 1918 69 622 Villeurbanne Cedex France Tel : 04.72.44.83.69 hamamache.kheddouci@univ-lyon1.fr
Matériaux	MATÉRIAUX DE LYON http://ed34.universite-lyon.fr Sec. : Stéphanie CAUVIN Tél : 04.72.43.71.70 Bât. Direction ed.materiaux@insa-lyon.fr	M. Jean-Yves BUFFIÈRE INSA de Lyon MATEIS - Bât. Saint-Exupéry 7 Avenue Jean CAPELLE 69 621 Villeurbanne CEDEX Tél : 04.72.43.71.70 Fax : 04.72.43.85.28 jean-yves.buffiere@insa-lyon.fr
MEGA	MÉCANIQUE, ÉNERGÉTIQUE, GÉNIE CIVIL, ACOUSTIQUE http://edmega.universite-lyon.fr Sec. : Stéphanie CAUVIN Tél : 04.72.43.71.70 Bât. Direction mega@insa-lyon.fr	M. Jocelyn BONJOUR INSA de Lyon Laboratoire CETHIL Bâtiment Sadi-Carnot 9, rue de la Physique 69 621 Villeurbanne CEDEX jocelyn.bonjour@insa-lyon.fr
ScSo	ScSo* http://ed483.univ-lyon2.fr Sec. : Véronique GUICHARD INSA : J.Y. TOUSSAINT Tél : 04.78.69.72.76 veronique.cervantes@univ-lyon2.fr	M. Christian MONTES Université Lyon 2 86 Rue Pasteur 69 365 Lyon CEDEX 07 christian.montes@univ-lyon2.fr

ABSTRACT

We have developed new and interdisciplinary technology for creating extremely lightweight, diffraction-limited, meta-material-based optical systems with exceptional optical quality and spectacularly lower cost and production time: Live-Mirror. The novelty is to replace classical rigid and heavy optical mirrors with “live” and light dynamic optoelectronic systems consisting of a thin optical glass sheet actively supported by multiple force-actuators/sensors integrated and miniaturized via additive manufacturing and 3D printing. Our breakthrough Live-Mirror features and active shape control with many-degrees-of-freedom force actuators achieved by developing an additive 3D-printing-based technology to apply an optimized electroactive polymer (EAP) system to a sandwich of thin glass surfaces, thus creating a novel hybrid meta-material with superior stiffness-to-density ratio properties.

This thesis describes the development of soft actuators based on modified/doped EAPs, here dubbed terpolymer P(VDF-TrFE-CFE). We will show that this new and Live-Mirror customized terpolymer matrix features an outstanding electromechanical coupling property, particularly when doped with a plasticizer, e.g. diisononyl phthalate (DINP). Here we demonstrate that by optimizing the structured multilayer design, the electromechanical coupling of the modified terpolymer can be enhanced, yielding high dielectric permittivity, low Young modulus, and exceptional dielectric strength. This leads to a large strain response as well as high mechanical energy density under relatively low electric fields according to the electrostriction phenomenon - the main goal of the high-level specifications of Live-Mirror.

In addition to a customized terpolymer matrix, the concept of stacked multilayers is demonstrated as a simple and effective technique to boost actuation abilities. Several 3D-printed, proof-of-concept (in the lab) experimental results, which are in good agreement with numerical models, validate the actuator performance with a large electromechanical response. This technology shows feasibility for active optical surface shape control and demonstrates the Live-Mirror optical shape control and correction with only a few degrees-of-freedom. Such a novel and advanced actuator application via additive manufacturing technology are compliant for ground- and space-based astronomy and communications telescopes as well as many modern electronic devices.

ACKNOWLEDGMENTS

First of all, I wish to acknowledge the help provided by Prof. Lionel Petit for being my thesis director as also give me the continuous support of my Ph.D. study and research.

I would like to express my very great appreciation to my thesis co-director Dr. Jean-Fabien Capsal for his valuable and constructive suggestions during the planning and development of my Ph.D. research work. His patience, motivation, enthusiasm, immense knowledge, and willingness to give his time so generously have been very much appreciated.

I also would like to thank all co-advisors in the Live-Mirror team, Dr. Gil Moretto, Prof. Jeff Kuhn, and Dr. David Audigier. Their guidance helped me in all the time of experimental manipulation, data analysis, and writing of this thesis.

I wish to acknowledge my Ph.D. scholarship provided by the Development and Promotion of Science and Technology Talents Project (DPST), Thailand, and Franco - Thai Scholarship from Campus France.

My sincere thanks also go to Prof. Laurent Lebrun and Dr. Mickaël Lallart for offering me the Ph.D. position during my first year being in France.

Besides my advisors, I would like to thank the rest of my thesis committee: Prof. Jean-Yves Cavaille, Dr. Eric Dantras, Dr. Chatchai Putson, Prof. Annie Colin, Dr. Maud Langlois, and Prof. Juan Uson for their encouragement, insightful comments, and hard questions.

I am particularly grateful for the assistance given by Dr. Pierre-Jean Cottinet and Dr. Minh-Quyen Le for their dynamism, vision, sincerity, and motivation which deeply inspired me to carry out the research.

I would also like to thank staffs and colleagues in LGEF laboratory, Mr. Frederic Deformerie: my good friend & skillful technician, Mrs. Veronique Perrin: a fabulous electronic technician, and Dr. Laurence Seveyrat: a brilliant technician team manager, for helping me to fix problems on my experimental setup as well as providing me the lab facilities. A big thanks to and Ms. Evelyne Dorieux: my good friend & wonderful secretary for helping me with every administrative work. Thanks to mama Zina Sassi for being supportive and make me feel like home.

My special thanks are extended to my colleagues and friends, Dr. Francesco Pedroli: my French brother—even he is Italian, Ms. Yan Zhang: my French sister—even she is Chinese, Dr. Bhaawan Gupta: my high-class Ph.D. friend, Dr. Thomas Huguet: my ecology idol, Ms. Giulia Lombardi: my funny & beautiful Italian girl...say rice~!, Dr. Gildas Coativy: the young face assistant professor, Dr. Amine Boussadi: the Algerian papa, Ms. Ziyin Xiang: my computer software storage, Ms. Xiaoting Zhang: my office mate who always see my computer screen, Ms. Annalisa Flochini: the gentle Italian girl, Ms. Hiba Haisoune: my canteen gang, Ms. Giulia D' Ambrogio: the carbon black girl, Mr. Omar Zahaf: the trilingual boy, and Mr. Amaury Fimbel: the heir of plasticized terpolymer.

Assistance provided by Ms. Suphita Chaipo (Beam), Mr. Waroot Kanlayakarn (Boom), and Mr. Jakkapat Khao-iam (Jame) being as motivated and enthusiastic interns was greatly appreciated. I am pleased how we could work synchronously and efficiently.

I would like also to thanks Dr. Naruemon Rueangkham (Mon): my best friend ever since, Dr. Natsuda Klongvessa (Ong): my awesome roommate & my travel buddy, Mr. Kanthanet Tharot (Naam): my French brother & YouTube channel association, Ms. Arissara Konghuairob (Praew): my little girl roommate & private pâtissier, Mrs. Netchanok Battaglini (Mo): the magnificent chef of Thai food and Mr. Johan Romieu: my lovely boyfriend for being supportive in every situation.

Last but not the least, I would like to thank my family: my parents Mr. Tassanai Thesprapee & Mrs. Kancharat Thesprapee, my brother Mr. Nontakron Thesprapee for their love, caring and supporting me spiritually throughout my life.

Family and friends are two of the greatest facilitators of happiness.

–John C. Maxwell

Kritsadi THETPRAPHI

Foamie

TABLE OF CONTENTS

ABSTRACT	V
ACKNOWLEDGMENTS.....	VII
TABLE OF CONTENTS	IX
Lists of Figures	XIII
Lists of Tables	XXI
Nomenclatures.....	XXIII
THESIS OUTLINES	XXVII
LE RESUME DE THESE EN FRANCAIS	29
CHAPTER 1.....	43
I. Introduction.....	43
Introduction.....	43
Electroactive Polymers (EAPs)	44
Smart EAP Materials Use for Actuators & Sensors	47
1. EAPs as Emerging Actuators	47
2. EAP Sensor Applications	49
EAPs Actuator Improvement & Development Technologies	51
1. EAPs Force-Actuator Selections.....	52
2. EAPs Composite Modification Approaches.....	55
2.1 Carbon Nanomaterial-Polymer Composites.....	56
2.2 Plasticizer for EAPs Electromechanical Reinforcement.....	57
2.3 Terpolymer Composites for Electronic Applications Perspectives.....	58
3. Multilayer Actuator Approach.....	59
EAPs Actuators and Sensors to Control Precise Optical Surfaces - Live-Mirror Project.....	62
Summary	64
CHAPTER 2.....	67
II. Material Elaborations and Characterizations	67
Material Elaborations.....	67
1. Materials and Tools	67
2. Thin Film Preparation.....	68
2.1 Pure Terpolymer Preparation	70
2.2 Terpolymer Composite Preparation	70
3. Material Characterization Techniques	71
Material Characterization: Results & Discussions.....	73
1. Electrostrictive Material Models.....	73
2. Terpolymer Filled Carbon Black Composite	75
2.1 High Permittivity Terpolymer/Carbon Black Composite.....	75
a. Dielectric Permittivity.....	75
b. Electrothermal Coupling Concept (Pseudo-pyroelectric)	76
c. Terpolymer CB Composites Polarization and Temperature Effects	78
2.2 Conductive Terpolymer/Carbon Black Composite	80
a. Young Modulus	82
b. Electrical conductivity	82
3. Plasticized Terpolymer for Soft Actuators Optimization.....	87
3.1 DINP and DOA Improving Terpolymer Electrical Properties.....	88
3.2 DINP and DOA Improving Terpolymer Mechanical Properties.....	90
3.3 Dielectric Strength (Breakdown Electric Field)	91
3.4 Electrical Conductivity	93
Summary	95
CHAPTER 3.....	99

III. Electromechanical Performance and Multilayer Design.....	99
Electromechanical Characterization Technique	99
Electromechanical Performance	101
1. Electrostrictive Phenomena	101
2. Strain Measurement under Applied Electric Fields.....	102
3. Current Behavior of Plasticized Terpolymer under High Applied Voltage.....	107
4. Empirical Modeling with Debye–Langevin Formula for HV Operation.....	110
Multilayered Actuator	116
1. EAPs Multilayer Initiative	116
2. Multilayer Strain Boosting	117
2.1 Multilayer Stack Fabrication.....	117
2.2 Electromechanical Performance of Multilayer Stack.....	118
a. Total Strain VS Number of Layers	118
b. Total Strain VS Applied Forces.....	119
Summary	120
CHAPTER 4	123
IV. Live–Mirror Application.....	123
Live–Mirror Project.....	123
Live–Mirror EAPs Conceptual Design.....	125
1. EAP Actuator–Sensor Hybrid System.....	126
Live–Mirror Prototypes Proof–of–Concept.....	128
1. Displacement Measurement Techniques.....	128
1.1 Interferometric Dynamic Calibrator.....	128
1.2 Zygo Interferometer Wavefront Analysis.....	129
2. Experimental Results.....	130
2.1 Single Stack Sandwich Prototype	130
a. Prototype Schematic	130
b. Dynamic Deformation Preliminary Test	131
c. The Control Surface Profile of Sandwich Prototype– Single Stack	132
2.2 Four–Actuator Stacks Sandwich Prototype	133
a. Prototype schematic.....	133
c. The Control Surface Profile of the Sandwich Prototype– Four Stacks	136
2.3 Shear Actuator Proof of Concept.....	138
a. Shear Prototype Design	139
b. Shear Actuator for Glass Deformation.....	139
c. Multilayer Shear Actuator Prototype.....	141
d. Adhesive Interlayer Shear Effect of Multilayer Shear Actuator.....	143
Summary	146
CHAPTER 5	149
V. 3D–Printed EAP actuator	149
Dielectric Elastomer Printing.....	150
3D–Printing Technique Interfaces.....	151
Printable Electrode Investigation	154
1. General Electrically Conductive Ink Composite.....	154
2. Conductive Terpolymer Carbon Black Composite.....	156
Full–Printed EAP Actuator Performance	157
1. Actuator Design.....	157
2. Full–Printed Prototype	159
2.1 Practical Difficulties of The Full–Printed Actuator.....	159
a. EAP and Electrode Printed Layer	159
b. Plasticizer Migration & Leaching.....	160
2.2 Full–Printed Single Actuator Prototype	163
a. Single Layer Actuator	163
b. Multilayer Actuator.....	165
2.3 Multi Single Layer Actuator	167
COMSOL Glass Deformation Modeling.....	170
1. Material and Simulation Parameters	170

2. Control Surface (S_c) Simulation	171
3. Maximum Displacement (D_{pp}) In Lab VS Model	173
Summary	177
CONCLUSION	181
VI. Overall Research	181
VII. Future Work.....	183
Material Perspectives	183
Live-Mirror Prototype Development	184
Numerical Model Development-Local Curvature Analysis.....	184
BIBLIOGRAPHY.....	187
APPENDIX	193
PUBLICATIONS	201
CONFERENCES	203

Lists of Figures

Figure 1 EAP actuator applications (a) Artificial muscles: (a-1) an android head making facial expressions and (a-2) robotic hand made from EAP actuators ^[50] ; (b) Micro-pump system: (b-1) before and (b-2) after pumping ^[48] ; (c) Smart guide-wire: (c-1) the structure design purposely providing (c-2) two degree of freedom of deformation ^[44] ; and (d) Tunable lens: (d-1) images at different focal distances and (d-2) the schematic of measurement setup verifying the tunable lens capability ^[49]	48
Figure 2 Review of EAPs diagram ^[25,27,65 - 70] represented blocking stress (kPa) versus maximum strain generated annotating to working limitation range of actuation capability.....	52
Figure 3 Longitudinal strain (S_{33}) of four different EAPs without external load under different applied electric fields.....	53
Figure 4 Blocking force (Block F) of different EAPs at a different level of electric fields.....	54
Figure 5 Carbon nanomaterials structures differentiated dimensionally: 3D of graphite nanoparticles and nanodiamonds used as a potential material in medical and biological electronic applications; 2D of graphene nanosheets (GNs); 1D of carbon nanotubes (CNTs); and 0D of fullerenes or carbon black nanoparticles (CBNPs or CB).....	56
Figure 6 The tradeoff between high permittivity and conductivity of a terpolymer composite permits its development and optimization into various electronic applications (sensors & actuators) ^[2,5,33,97,98] . This thesis will concentrate on the terpolymer composite actuators and conductivity issues.....	59
Figure 7 Multilayer actuator applications and designs; (a) bi-stable design using silicone membrane with aluminum nitride (AlN) piezoelectric layer, (b) multilayer stack-actuator schematic made from dielectric electroactive polymers (DEAP), and (c) Piezoelectric microelectromechanical systems (MEMS): (c-1) free-standing (PEI/PAA)/(PU/PAA) multilayer actuator membranes, (c-2) actuation cycles with regular pulses 40Vpp and (c-3) bending curvature versus PU/PAA: PEI/PAA thickness ratio in water and methanol.....	61
Figure 8 (Left-Bottom): A simulated warpable glass surface and the surface force correction mechanism: the surface roughness is controlled by the electromechanical activity generated in each "EAP-spring" actuator. (Right): A design for the hybrid structure Live-Mirror a sandwich of warpable surfaces separated by a lattice of variable force EAP actuators in series with force EAP sensors. The upper surface (fired polished glass) is called the control surface and the lower surface (glass) is the reaction surface. The static force of each force EAP sensor is controllable and determined by independent metrology of the top surface shape. This particular sensor-actuator geometry assumes preliminarily only vertical (gravity) external force components with assumed lateral material stiffness of the actuators. Section AA' - The 1/2 meter Live-Mirror prototype using the additive manufacturing via 3D Printing technology is in development to fulfill the miniaturized requirements: each individual sensor-actuator system must fit into a circle of less than 5 cm diameter (pitch).....	63
Figure 9 The flowchart for the thin film preparation methods, required conditions, and techniques to fabricate an optimized EAP Terpolymer and its composites.....	69
Figure 10 Samples preparation with gold electrode sputtering both sides (top&bottom) (a) for the electrical characterizations with gold electrodes with a diameter of 8mm and (b) for the electromechanical characterization with gold electrodes with a diameter of 20mm.....	73
Figure 11 Experimental measurements of the dielectric permittivity (a) and the dielectric loss (b) of a terpolymer and its composites under applied bias voltage 1 Vpp. Measurement was handled	

throughout sweep frequencies Solartron 1260 impedance-analyzer from 0.1 Hz to 1 MHz under a low applied electric field of 1VAC at ambient temperature.....	76
Figure 12 The pseudo-pyroelectric working principles: (a) dielectric material with randomly dipoles arrangement (zero mean polarization) when no applying electric field; (b) a polarization appears as an electric field is applied; (c) when the temperature increases, the thermal agitation of dipoles leads to a decrease of the mean polarization, as the required energy to overcome the thermal agitation increases ^[33]	77
Figure 13 Polarization measurements polarization of terpolymer thin films in various percentages of CB filler under $E_{max} = 2$ kV/mm at room temperature.....	78
Figure 14 Polarization of terpolymer doped 2wt% carbon black as a function of an applied electric field for five different temperatures: (a) the hysteresis loop under bias voltage is applied and (b) the zoom into the part of maximum polarization represented the diminution of polarization while temperature increase. The polarization versus with temperature was measured by the following set up: (i) the sample was soaked in a silicone oil bath and high voltage was applied by an amplifier driven by waveform generator; (ii) the temperature of the sample was controlled via test chamber device; (iii) following voltage application and warming up, the generated current was measured by a low noise current preamplifier connected to an oscilloscope.....	79
Figure 15 The comparison of conductivity range between conductive polymers composites with insulators, semiconductors, and metals (reproduced from ^[30]). Note that its conductivity is in the range of semiconductor materials.....	80
Figure 16 The Carbon Filler percentages on the mechanical property of the material (Young modulus) for the terpolymer (TP3) composite. The terpolymer/CB composited thin films (1 cm × 4 cm) were prepared by solution casting method (Figure 7). The measurements were handled by fixing the tensile specimen between a metal holder and a force sensor LC102-TC-10N. The samples are stretched transversely with 0.5% of strain under frequency 0.1 Hz at room temperature.....	82
Figure 17 The electrical conductivity versus frequency for the terpolymer (TP3) filled with different carbon black contents. The terpolymer/MEK/CB solution was prepared by the solution blending method and CB particles got well-dispersed with an ultrasonic probe.....	84
Figure 18 The electrical conductivity as a function of carbon black particle loading presented a site of percolation threshold for terpolymer (TP3) filled with carbon black particles.....	84
Figure 19 The electrical conductivity in the percolation region as a function of the electric field of terpolymer (TP3) filled with different carbon black loading from 4 to 9% by mass.....	85
Figure 20 (a) The calculated admittance based on the RC parallel circuit as a function of frequency by the use of real capacitance and the real resistance value of terpolymer/CB composite and (b) parallel RC circuit reflected on terpolymer/CB composite.....	86
Figure 21 Cutting frequency under bias applied voltage of Terpolymer/CB above percolation region (over 4% by mass) carried out by experimental measurement; $f_{cut-exp}$, and evaluation model; $f_{cut-model}$. The small right-top graph presenting evaluated cutting frequency affected by an increase in material resistance.	87
Figure 22 The dielectric broadband spectroscopy as a function of the frequency of terpolymer filled with plasticizer agents DOA and DINP. The measurement was handled throughout sweep frequencies Solartron 1260 impedance-analyzer from 50 mHz to 1 MHz under a low applied electric field of 1VAC at ambient temperature.....	90
Figure 23 Young modulus of terpolymer doped plasticizer agents in a mass fraction which shows (a) the comparison of Young modulus of terpolymer filled DINP and DOA and (b) Young modulus versus added DINP contents.	91
Figure 24 The breakdown probability versus electric field of (a) terpolymer/DINP and (b) terpolymer/DOA measured with an applied DC ramp.....	92

Figure 25 The electrical conductivity (DC and AC) frequency dependence for modified terpolymers (a) doped DINP and (b) doped DOA.	94
Figure 26 The setup of the displacement measurement using a capacitive displacement sensor to measure the electromechanical activity of the electrostrictive polymer. The sample holder consisting of the moving structure including the rod and the two discs having the initial weigh of 5 grams was created to measure the longitudinal strain of EAP actuators. An external load can be inserted into this sample holder structure to simulate the weight of a piece of glass in live-mirror applications. All the data were monitored and recorded via DEWE Soft (SIRUS STG), followed by a post-treatment with OriginLab®.	100
Figure 27 The longitudinal strain (S_{33}) and generated current of terpolymer doped with 10% DINP under sinusoidal excitation field of 10 V/ μm	102
Figure 28 The longitudinal displacement of (a) pure terpolymer film of a thickness 222 μm and (b) terpolymer doped 8wt%DINP film of a thickness 176 μm operated under preload 76g as a function of applied electric fields sinusoidal 50 mHz unipolar.	103
Figure 29 The longitudinal strain response in according with various percentages of DINP added to pure terpolymer operated under $E= 10 \text{ V}/\mu\text{m}$. The experimental error is very smaller to be observed in the graph scale.	104
Figure 30 The achievable strain versus maximum electric field squares (electric breakdown field) represents the electromechanical performance depending on plasticizer loads (Pure = DINP0-6%, Plasticized+ = DINP8-10%, and Plasticized++ = DINP >12%).	105
Figure 31 The longitudinal strain response (S_{33}) of the modified terpolymers operated under sinusoidal 50 mHz applied electric fields: (a) the temporal evolution of S_{33} of terpolymer+8wt%DINP activated at $E=15 \text{ V}/\mu\text{m}$ & preload 1.42 N; S_{33} of terpolymer+8wt%DINP versus (b) input electric fields and (c) externally applied forces; and (d) S_{33} of terpolymer doped 2 to 12wt% DINP under two different preloads activated at $E=10 \text{ V}/\mu\text{m}$	106
Figure 32 The current behavior under high electric field applying (15 V/ μm sinusoidal unipolar 50 mHz) constituted of different plasticizer DINP loads from 0 to 10 % by mass.	108
Figure 33 The generated current of terpolymer filled with 10%DINP as a function of applied electric fields (sinusoidal unipolar 100 mHz) with its loss' s estimated guideline. The spikes came from an electric arc in the experimental measurement.	109
Figure 34 The evaluated electrical conductivity (estimated losses) of terpolymer doped 10wt% DINP as a function of applied electric fields.	110
Figure 35 The evaluated electrical behavior represented with the capacitive currents of a plasticized 10%DINP terpolymer under applied electric field $E=20\text{V}/\mu\text{m}$ between estimated model and experimental measurement.	111
Figure 36 The relative dielectric permittivity of terpolymer filled DINP from 2-12 % by mass measured and calculated from the Debye/Langevin evaluation model.	112
Figure 37 The estimated strain of (a) plasticized terpolymers under applied electric field up to 20 V/ μm and (b) the comparison of strain response of terpolymer filled 8wt% DINP between experimental measurement and strain model estimation as a function of an applied electric field.	113
Figure 38 The figure of merit strain generated consideration (FOM_{strain}) of terpolymer filled with various DINP contents (by mass) under activated fields of 10, 20, 30 V/ μm , and nearly breakdown field ($E_{\text{breakdown}}$).	114
Figure 39 The strain generated under activated field 10V/ μm of terpolymer added DINP 0 to 12wt% by reference to their breakdown field (E_{BD}).	115
Figure 40 The multilayer actuator design: (a) the stack of 10 layers-terpolymer+10%DINP 209 μm of each layer thick; and (b) the multilayer topology consists of the EAP layers coated gold electrode, electrically conductive adhesive interlayers, and aluminum foil sheets for HV connection. The multilayer structure was designed imitating several capacitors connected in parallel.	117

Figure 41 The total longitudinal strain (S_{total}) of the pure and the modified 10% DINP terpolymers for single layer and 6-layer stack as a function of electric fields.	118
Figure 42 The total longitudinal strain (S_{Total}) versus the number of layers ($n=1$ to 8) for plasticized (10%DINP) terpolymers operated at $10 \text{ V}/\mu\text{m}$ under applied external loads of 1.42N and 4.58 N.	119
Figure 43 The total strain (S_{total}) generated by multilayer plasticized terpolymer under different external applied forces (F) operated at electric field $10 \text{ V}/\mu\text{m}$	120
Figure 44 The ELF design configuration consists of 16 parabolic apertures (M_{1i}) with diameter 5m—each, a secondary mirror (M_{2i}) with a diameter of 115 mm, and sub-apertures mechanically arranged on a 28m in diameter rim ^[8]	124
Figure 45 The Live-Mirror conceptual design for a hybrid dynamic structure: (a) the hybrid telescope optic (HTO) diameter 5m represented hybrid mirrors, top view & side view, separated by a lattice of variable force EAP actuators; and (b) the hybrid dynamic structure represented a sandwich of warpable glasses (in a blue sky) with the advanced EAP actuators and the operating system support for each component.	127
Figure 46 The interferometer dynamic calibrator setup with the Live-mirror prototype for measuring the deformation of the dynamic control surface (S_c) deformation under subject to an alternating sinusoidal input voltage. A high-resolution interferometer laser (AGILENT 5519A HeNe Laser System) is used to measure the displacement generated by an actuator which was driven by an alternating voltage input.	129
Figure 47 The Zygo interferometer experimental bench used for measuring the surface profile of the optical element. The prototype sample was held with the optic element holder that can be aligned in two axes of tilt. The sample was aligned to the front of the interferometer mainframe and connected to an external voltage amplifier.	130
Figure 48 The sandwich prototype schematic of the EAP multilayer actuator: a single stack of 8-layer-terpolymer doped 10wt%DINP with electrodes with a diameter of 20 mm, as discussed at Chapter 3, section Multilayer Stack Fabrication.	131
Figure 49 The proof of concept of the sandwich prototype— single multilayer 8-layer stack of plasticized terpolymer 10wt%DINP provides different deformation levels of two warpable glasses being pulled by the driven actuator at $E=10$ and $20 \text{ V}/\mu\text{m}$	131
Figure 50 (a) An 8-layer stack of plasticized terpolymer 10wt%DINP sandwiched between two flat circular glass plates: reaction surface (S_r) and control surface (S_c). (b) The interferometric intensity fringes ($E= 0 \text{ V}/\mu\text{m}$) from the front glass control surface (S_c). (c) The 3D-surface for the S_c at $E = 0$ and $20 \text{ V}/\mu\text{m}$ is derived from interferometric fringes (b). (d) The change of the S_c along with a horizontal cut through the glass bump under different applied electric fields. All measurements were done with a Fizeau laser (633 nm) interferometer (Zygo® verifire™).	133
Figure 51 Four-actuator stacks sandwich prototype with four 10-layer stacks of terpolymer doped 10wt% DINP with their electrode diameter size of 2cm implemented between two square (14x16cm) window glasses 3 mm thick.	134
Figure 52 (a) A glass sandwich with a four-stack of actuators in a square distribution and (b) as modeled via COMSOL™. The strain mapping results for the control surface (S_c) laser-interferometrically measured are: (c) four actuators “on” under $E_{12}=10\text{V}/\mu\text{m}$ for actuators #1 and #2 and $E_{34}=13\text{V}/\mu\text{m}$ for actuators #3 and #4; (e) $E_1=10\text{V}/\mu\text{m}$ for actuator #1 “on” and $E_{234}= 0\text{V}/\mu\text{m}$ actuators #2, 3 and 4 “off” . (d) and (f) show the modelization and simulation results respectively for the (c) and (e) configurations.	135
Figure 53 The four actuators sandwich prototype: 10-layer of terpolymer+8%DINP with their electrodes (10 mm in diameter) and individually connected to their electronic paths.	137
Figure 54 The S_c deformation of four-actuator stacks sandwich prototype: (a) the top view prototype presents the actuator positions and the examined cross-section line passing through S_c optical aperture; (b) the S_c deformation, dz of cross-section line when the actuator no.1 was	

actuated; (c) two voltage inputs of 2kV (red line) and 3kV (pink line) were applied to a variety of actuator positions presenting dz of the cross-section line.....	138
Figure 55 The EAP shear prototype design: a terpolymer filled with 8wt% DINP thin film and coated with gold (40mm in diameter) on both sides (top-bottom) of the electrode was silicone adhesive glued on a single circular glass sheet (110mm in diameter and 3mm thick) control surface (S _c).....	139
Figure 56 The 2D illustration of shear actuator prototype: (a) without applying an electric field, (b) under an applied electric field, the glass surface is bent down by the expansion stress from the EAP layer, and (c) the divided segments of the EAP layer showing the ability to transfer their transversal strain.....	140
Figure 57 The maximum displacement at the center of S _c of the shear prototype versus the number of EAP layers in the multilayer structure operated under three different levels of applied electric fields. Each layer of the EAP is made from terpolymer+10wt%DINP 225μm-thick. The invariable deformation region presents the mirror deformation being settled after reaching a certain total thickness of the actuator.	140
Figure 58 (a) A multilayer EAP shear actuator proof-of-concept: a single 2mm thick glass optical surface S _c with an integrated 8%DINP terpolymer 4cm-diameter circular actuator. (b) and (c) show 3D intensity plots on the (0,X) and (0,Y) orthogonal sections for the control optical surface deformation D _z respectively produced by the one-layer and the 5-layer under an electric field E from 0 to 18V/μm applied in a thickness direction.	142
Figure 59 The simplified shear prototype 2D model analysis: (a) shear actuator multilayer geometry: a six-layers 200 μm thick each, a 5mm in diameter of the gold electrode, five adhesive interlayers 50μm thick, applied on a glass substrate 2mm thick and 10mm diameter in diameter; (b) total displacement generated by 6-EAP-layer under for an applied electric field excitation 10 V/μm.....	143
Figure 60 Stress distribution (von Mises stress) analysis of multilayer shear prototype assembled with different Young modulus adhesive interlayer for studying shear stress transferring effect. The sample was analyzed under E=10V/μm with six EAP layers.....	144
Figure 61 The normalized S _c center displacement of shear actuator multilayer topology of 1 to 6 EAP layers under E=10V/μm as a function of the different Young modulus of the adhesive interlayer.....	145
Figure 62 The normalized S _c center displacement from the experimental test in lab and S _c data simulation as a function of EAP total thickness driven by E=10V/μm.....	145
Figure 63 The evolution of Live-Mirror proof of concept presents: (left) the film casting handcrafted four actuators configuration, and (right) the same setup configuration 3D-printed.	150
Figure 64 The OpenSCAD software interface used for creating 3D objects and rendering into the STL file.....	152
Figure 65 The Gcode example used for consistent material deposition additionally with the code to avoid the residual drop from the printing process.	153
Figure 66 The software interfaces used to assemble the full-printed EAP; (a) OpenSCAD freeware for creating 3D object-based script modeler, (b) Repetrel software and motion controller operated through GCODE represented on (b'), and (c) the printed EAP electrode layer collating with the input object.....	154
Figure 67 The result of using commercial conductive inks (a) silver ink and (b) carbonblack ink to incorporate with the printed EAP composed of terpolymer+DINP based MEK (methyl ethyl ketone) solvent reveals their incompatibility.....	155
Figure 68 The 3D printing setup for printing EAP actuators; (a) the single actuator structure design consists of the EAP layer (terpolymer+DINP) and two electrode layers (terpolymer/CB composite), (b) 3D printing platform demonstrates how the entire actuator is printed layer-by-	

layer on a glass substrate through material extrusion, and (c) the 3D printer model Hyrel™ System 30M.	158
Figure 69 Temperature annealing process for evaporation residual solvent within full-printed EAP.	159
Figure 70 A fast cooling of the printed sample resulted in samples with cracks, making them unsuitable to work under high voltage operation.	160
Figure 71 The central displacement (D_{pp}) of the control surface (S_c) is examined from the preliminary test of full-printed actuators (the EAP layer sandwiched with electrode layers diameter 20mm) constructed with different plasticized electrodes; no DINP added=Electrode pure, 5%DINP added= Electrode-D5, 8%DINP added=Electrode-D8 and Gold electrode for an ideal actuator. All the samples were actuated with a sinusoidal unipolar voltage at a frequency of 50 mHz.	162
Figure 72 Comparison of the maximum displacement at the center of S_c of the full-printed single layer actuator for four electrode dimensions of 16mm, 20mm, 25mm, and 30mm in diameter operated under sinusoidal unipolar electric fields at 50 mHz.	164
Figure 73 The control surface deformation of the full-printed single layer actuator prototype presents the actuated regime $[x,dz]$ cross-sections of (black line) – electrode $\varnothing=20$ mm and (red line) – electrode $\varnothing=30$ mm. Both samples were operated under an applied DC electric field of 30 V/ μm	165
Figure 74 The cross-section image (magnified hundred times) of full-printed multilayer actuator made of three EAP and electrode layers.	165
Figure 75 The full-printed multilayer actuator prototypes present their control surface deformation with $[x,dz]$ cross-sections: (black) 1-layer, (red) 2-layer, and (blue) 3-layer of single layer actuator components. All samples have their electrode diameter of 20 mm and were operated under an applied DC electric field 30 V/ μm	166
Figure 76 Left: The four single-layer actuators set up on the back of control glass surface (S_c) comprises; the printed first-layer electrode pattern (black color), the printed EAP layer (square blue sky color), and the printed top-layer electrode pattern (pink color). Right: The real full 3Dprinted single-layer four actuators and two layers electrodes on a 2mm-thick circular (110mm in diameter) glass sheet.	167
Figure 77 The single layer actuator prototype (electrode diameter 16mm) presents its front glass deformation operated under a DC voltage of 3kV. Black and white illustrations present the S_c deforming when the prototype was operated under an electric field 30 V/ μm ; column (a) the surface color scale with their cross-section lines $[(x,y),dz]$, columns (b) and (c) 3D surface plots of front S_c , and S_c rotating around a horizontal axis, respectively. The various operating conditions are presented via; row (A_n) All actuator=ON, row (B_n) Acts#2,3,4=ON & Act#1=OFF, and row (C_n) Act#1=ON & Acts#2,3,4=OFF. Global wavefront deformation measurements were realized by a Zygo interferometer.	168
Figure 78 The schematic of the full-printed multi-actuator prototype in COMSOL used for simulating the S_c deformation under HV operation. Four full-printed single-layer actuators are implemented on the backside of the glass represented as an S_c in the system.	170
Figure 79 The control surface deformation (S_c) experiments VS models of the full-printed single layer multi-actuator prototype operated at $E_{DC}=30$ V/ μm referred as ON state. Four actuators with an electrode diameter of 16mm, numbered (Act#n) denoting their position on the back of S_c . The grey-scale illustrations present the S_c deforming when (a) Act#1 is ON, (b) Acts#2,3,4 are ON, and (c) Acts#1,2,3,4 are ON.	172
Figure 80 The full-printed single layer multi-actuator prototype presenting its S_c deformation when four actuators were activated in experimental & model analyses; (top images) the S_c deformation investigated in the lab showing its 3D surface plot and $[(x,y),dz]$ cross-section lines,	

and (bottom images) the replication of cross-section lines [(x,y),dz] on the evaluated S_c deformation from COMSOL depicted at different positions on the S_c	173
Figure 81 The center S_c displacement as a function of applied electric field results between experiments in lab and evaluation models of the full-printed single layer actuator with various electrode diameter sizes.....	174
Figure 82 The comparison between experimental observation and modeling analysis presents the S_c center displacement of the full-printed single layer actuator versus its electrode diameter operated under sinusoidal unipolar of $30 \text{ V}/\mu\text{m}$ at 50 mHz	175
Figure 83 The comparison between experimental result and modeling analysis presents the S_c center displacement of the full-printed multilayer actuator versus the number of actuator layers operated at $30 \text{ V}/\mu\text{m}$ at 50 mHz	176
Figure 84 The Laplacian of z-axis displacement $\nabla^2 z(x,y) = c(x,y)$ numerically evaluated through single actuator sample diameter 16 mm operated under applied electric field (E) $30 \text{ V}/\mu\text{m}$: (right) top-view of Laplacian evaluation; and (left) cross-section (x-axis) showing magnitude of curvature.	184
Figure 85 Efforts to make "Live-Mirror" prototype a reality have been our Live-Mirror project team goal. R&Ds for a precise and smooth optical surface controlled by an active and live system via 3D-Printing of force actuators should pave the way for future development of the next-generation telescope mirror dedicated and optimized for high-contrast observations – Exo-Life Finder Telescope.....	186

Lists of Tables

Table 1 EAP material types in electrically field-activated and ionic [2,25].....	45
Table 2 the advantages and the drawbacks of ionic polymer and electrostrictive polymer.....	46
Table 3 The review of EAPs for sensor applications[2,52 - 56].....	50
Table 4 The general properties of Diisononyl phthalate (DINP) and Dioctyl adipate (DOA) plasticizers.....	88
Table 5 Breakdown electric field according to Weibull probability at 63.2% represented scale parameter (λ) and data distribution (k) of terpolymer filled with DINP and DOA respectively.....	93
Table 6 The DC conductivity of modified terpolymers with plasticizer DINP and DOA.....	94
Table 7 The optimized conditions for printing terpolymer composites.....	160
Table 8 Longitudinal strain response (S_{33}) of terpolymer doped with plasticizer DINP and DOA with various percentages as a function of electric fields.....	193
Table 9 Maximum Displacement observed at the center point of the actuator area at the front glass surface as a function of different applied electric fields, actuator sizes, and a number of layers.....	199

Nomenclatures

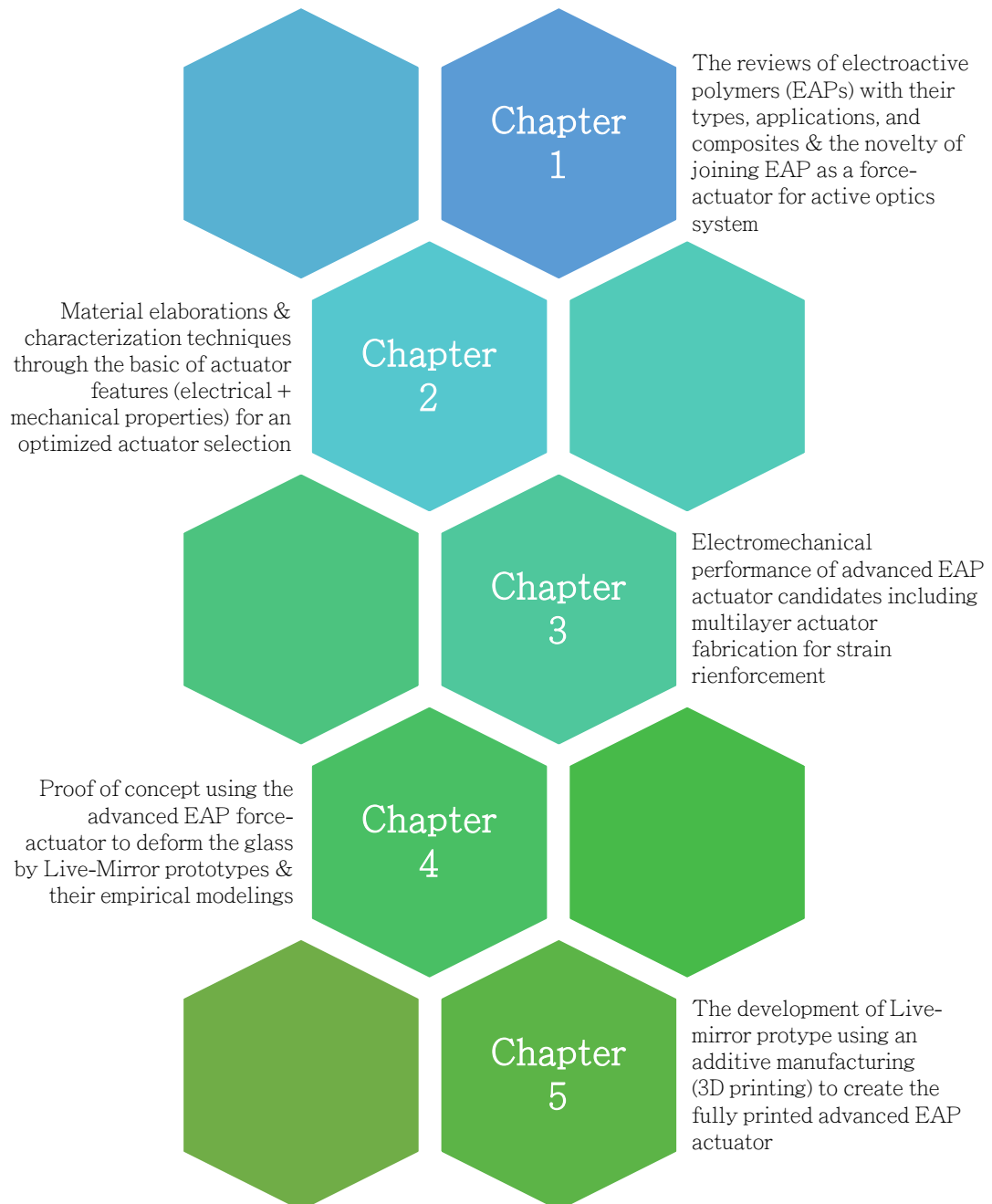
$\%_c$	Composite percentage
$\%_p$	Polymer percentage
$\nabla^2 z(x, y)$	Laplacian of the z-axis displacement
$S_{(E \gg E_0)}$	strain response under high input voltage
$\epsilon'_{(E_0 \ll E)}$	Relative permittivity at low electric field or zero electric field
$\epsilon'_{(E)}$	Relative permittivity under high electric field
ϵ'	Relative permittivity
ϵ_0	Vacuum permittivity
θ_0	Working temperature
χ_0	Dielectric susceptibility
A	Admittance (Siemen: S)
AlN	Aluminum nitride
ArPTU	Aromatic polythiourea
BDS	Broadband dielectric spectroscopy
C	Capacitance (Farad)
CB	Carbon black particle
CBNPs	carbon black nanoparticles
CFE	Chlorofluoroethylene
C_i	Capacitance of the sample layer i-multilayer actuator
CNTs	Carbon nanotubes
CPC	Conductive polymer composite
CTFE	Chlorotrifluoroethylene
D	Displacement
DEAP	Dielectric Electro Active Polymer
DEHP	2-ethylhexyl phthalate
DINP	Diisononyl phthalate
DMF	Dimethylformamide
DNCGS	Deterministic non-contact glass slumping
DOA	Adipic acid di(2-ethylhexyl) ester
D_{pp}	Maximum displacement measured peak-to-peak of sinusoidal generated electromechanical stress
DSC	Differential scanning calorimetry
dz	Displacement variation - Live-mirror prototype
E	Electric field
E_0	Constant applied electric field
EAP	Electro-Active Polymer
E_{BD}	Breakdown electric field
ECPs	Extrinsic conductive polymers
EELT	Extremely Large Telescope
ELF	Exo-life Finder telescope

E_{sat}	Debye/Langevin model parameter — Saturation electric field
EVA	Elastomer ethylene vinyl acetate
EVO	Evoprene 007
F	External applied forces or preloads
F^{block}	Blocking force for longitudinal loads exertion
FOM	Figure of Merit
GNs	Graphene nano sheets
HEEIP	High-energy electron-irradiation
High-k	High permittivity
HMW	High molecular weight
HTO	Hybrid telescope optics
HV	High Voltage
I_{cap}	Capacitive current
ICPs	Intrinsic conductive polymers
I_{loss}	Leakage current
INP	Interpenetrated polymer network
IPMC	Ionic Polymer-Metal Composites
I_{tot}	Total current generated by material
J	Current density
k	Weibull model parameter — shape factor
k_B	Boltzmann constant
m_c	Composite mass
MEK	Methyl Ethyl Ketone
MEMs	Micro-electromechanical systems
M_{ij}	Electrostrictive coefficient
m_p	Polymer mass
m_s	Solvent mass
M_w	Average molecular weight
MWS	Maxwell-Wagner-Sillars or interfacial polarization
n	Number of layers-multilayer actuator
$N(\theta)$	Temperature-dependent dipole density
NR	Natural rubber
P	Polarization of material
ρ	Pseudo-pyroelectric coefficient
$P(E)$	Breakdown probability at given electric field E
PA6	Polyamide 6
PAA	Poly(acrylic acid)
Palamoll® 652	Polymeric plasticizer derived from adipic acid and polyhydric alcohols
PANI	Polyaniline
PDEs	Partial differential equations
PEDOT	Poly(3,4-ethylenedioxythiophene)
PEEU	Poly(arylene ether urea)

PEI	Polyetherimide
PGMEA	Propylene glycol methyl ether acetate
PMMA	Poly(methyl methacrylate)
POM	Polyoxymethylene
PP	Polypropylene
PPy	Polypyrrole
PSF	Polysulfone
PTFE	Polytetrafluoroethylene
PU	Polyurethane
PVDF	Polyvinylidene fluoride
R	Resistance
R^2	Proportion of the variation between observed dependent variable (experiment) and predicted dependent variable (model)
S_{31}	Transversal strain
S_{33}	Longitudinal strain
S_c	Control surface or front mirror surface
S_{ij}	Electrically induced strain
S_M	Maxwell stress
S_r	Reaction surface
STL	Stereolithography CAD software created by 3D Systems
S_{total}	Total longitudinal strain–multilayer actuator
SWNTs	Single–walled carbonnanotubes
t	Time
$\tan\delta$	Loss tangent or Dielectric losses
T_{ij}	Electrically induced stress
TiO_2	Titanium dioxide
T_m	Melting temperature
TMT	Thirty Meter Telescope
TPU	Thermoplastic Polyurethane
TrFE	Trifluoroethylene
U	Electrical energy
UDR	universal dielectric response
V	Voltage
VDF	Vinylidene Fluoride
W_m	Mechanical energy density
WPs	Work packages
wt%	Mass fraction
Y	Young modulus
Z	Impedance
z_0	Unactuated state deformation at 0 kV - Live–mirror prototype
z_{nkV}	Actuated state deformation at n kV - Live–mirror prototype
λ	Weibull model parameter — breakdown probability at 63.2%
σ	Electrical conductivity

σ_{AC}	Frequency-dependent electronic conduction
σ_{DC}	Frequency-independent ionic conduction
ν	Poisson ratio
χ_c	Degree of crystallinity
$c(x,y)$	Curvature of surface deformation
θ	Temperature
μ	Dipole moment

THESIS OUTLINES



LE RESUME DE THESE EN FRANCAIS

Chapitre 1 Introduction

Les polymères électroactifs (EAPs)^[1,2] sont de plus en plus étudiés en raison de la demande croissante en termes de dispositifs d'actionnements et de capteurs auto-alimentés. Pour certaines applications, ces matériaux présentent des propriétés intéressantes telles que la légèreté, la résistance mécanique élevée, la flexibilité, la transparence, la facilité de mise en œuvre sur des films de grande surface, et en particulier la capacité à être moulés et / ou adaptés aux dépôts par fabrication additive (impression en 3D, ink-jet, etc.). Cette nouvelle dimension sensorielle ajoutée aux dimensions spatiales permet de développer des structures 4D dont la facilité de mise en œuvre associée aux propriétés de conversion multiphysique ouvre la voie à une révolution des systèmes électroniques^[3-7].

Récemment, nous avons proposé un nouveau concept de télescope permettant de réaliser des observations à contraste élevé: le télescope Exo-Life Finder (ELF)^[8-10]. Un tel système optique sera limité par le coût et la capacité de fabrication de grands miroirs (1 à 5 m de diamètre) et de grande qualité optique. Le caractère innovant de ce nouveau type de télescope consiste à remplacer les miroirs optiques rigides, lourds et coûteux classiques par des systèmes optoélectroniques dynamiques, « vivants », et peu coûteux composés d'un verre fin (2 à 5 mm d'épaisseur) soutenu activement « sous tension électrique » par de nombreux actionneurs / capteurs de force intégrés et miniaturisés via la fabrication additive et l'impression 3D (Projet Live-Mirror)^[29]. Notre objectif est de présenter le concept de miroir « actif électriquement poli » à l'aide d'EAPs pour l'optique active basse fréquence. Ce travail de thèse est dédié aux développements de matériaux électroactifs aux propriétés de conversion électromécaniques améliorées, leur mise en œuvre par fabrication additive et la démonstration de leur efficacité d'actionnement dans des configurations spécifiques au polissage actif des miroirs pour le projet LiveMirror. Les travaux futurs exploreront comment les capteurs EAP peuvent être intégrés dans des systèmes miroirs (effet inverse). En effet, l'excellente capacité d'actionnement des terpolymères fluorés modifiés ouvre la voie à la génération future de diverses applications. En fin de compte, cette nouvelle R&D interdisciplinaire a

introduit la nouvelle stratégie hybride de surface optique dynamique en direct ^[8,10,11] et fait avancer les nouvelles frontières de la science et de la technologie pour remplacer le verre poli par abrasion qui est coûteux, rigide et lourd. Ce travail de thèse a permis de démontrer la faisabilité du polissage actif permettant de réduire la complexité des télescopes optiques conventionnels ainsi que le coût important lié à la phase de polissage par abrasion des miroirs.

Chapitre 2 Élaborations et caractérisations des matériaux

Ce chapitre est dédié aux protocoles d'élaboration des différents matériaux composites réalisés ainsi qu'aux différentes techniques de caractérisations physico-Chimiques, électriques, mécaniques et couplées utilisées dans cette étude. De par ses propriétés de conversions électromécaniques importantes, le terpolymère fluoré P(VDF-TrFE-CFE) est devenu une base de matériau sélectionnée pour les actionneurs souples à base polymères. De la famille des EAPs diélectrique, ce matériau présente le meilleur compromis déplacement-force en actionnement ouvrant la voie à de nombreuses applications comme par exemple l'optique active. Cependant les champs électriques nécessaires à l'actionnement sont importants et il est crucial de développer et de renforcer la capacité du terpolymère fluoré pour atteindre une excellente performance électromécanique sous faible champ électrique. L'approche proposée est une modification extrinsèque du matériau par ajout de nanoparticules électriquement conductrices (noir de carbone) ou par plastification du polymère fluorée. Les processus d'élaboration des matériaux, y compris les résultats de la caractérisation et les discussions, sont présentés dans ce chapitre. Les caractérisations des propriétés physiques ont été décrites dans ce chapitre à savoir : (1) propriétés électriques ; permittivité diélectrique, polarisation, résistance au claquage diélectrique et conductivité électrique et (2) propriétés mécaniques. Nous avons démontré dans ce chapitre la possibilité de développer un matériau composite à matrice terpolymère fluorée, pour diverses applications électroniques, à savoir capteur capacitif haute permittivité, capteur thermique (pseudo-pyroélectrique), actionneur de force, etc.

Ce chapitre est subdivisé en deux parties ; (1) étude des composites réalisés à partir de charges conductrices et (2) étude des mélanges réalisés par une approche diélectrique toute organique.

Tout d'abord, l'étude de composite à matrice terpolymère chargé en particules électriquement conductrices a été réalisée. Des nanoparticules de noir de carbone (CBNPs) ont été sélectionnées comme charge (OD) à ces composites en raison de leur coût, leur facilité à former un réseau percolant conducteur sous un faible taux de charge et un rapport surface-volume élevé. La dispersion de charges de CBNPs dans la matrice

de polymère électroactif a permis une amélioration significative des performances électroactives de la matrice polymère sous faible champ électrique. Cependant, l'introduction de charges conductrices réduits fortement le champ de claquage diélectrique et limite son utilisation pour des champs électriques nécessaires à l'application envisagée. Pour pallier à ce verrou technologique, une seconde approche a été proposée. Cette approche est basée sur l'utilisation de mélange diélectrique toute organique. Des mélanges terpolymères/plastifiants ont été élaborés. Pour cela deux types de plastifiants à haut poids moléculaire (de la famille des phtalates et des adipates) ont été utilisés : (1) du phtalate de diisononyle (DINP) et (2) de l'adipate de dioctyle (DOA). Ces deux agents plastifiants sont d'une bonne compatibilité, de faibles toxicités aiguës dans les modèles animaux, d'une faible volatilité, résistants à l'eau et peu coûteux^[12-14]. L'ajout d'agents plastifiants dans les terpolymères a permis d'accroître la mobilité moléculaire ainsi qu'une augmentation significative les effets de polarisation interfaciale de Maxwell Wagner Sillars à basse fréquence. Par ailleurs, ces phénomènes conduisent à une diminution du module d'élasticité et à augmentation de la permittivité diélectrique du matériau ce qui va dans le sens d'une augmentation des performances électroactives des terpolymères sous faible champ électrique tout en minimisant la fragilisation diélectrique mis en évidence sur les composites réalisés à partir de charges électriquement conductrices.

Chapitre 3 Performances électromécaniques et conception de systèmes multicouches

Ce chapitre est dédié à la caractérisation des performances électromécaniques des matériaux développés ainsi que de l'optimisation des performances en actionnement. Les terpolymères plastifiés ont été sélectionnés pour leur grande propriété de conversion et leur grande résistance aux claquages diélectriques en comparaison des autres matériaux EAPs. Les performances d'actionnement des terpolymères modifiés ont été démontrées par le biais de mesures de la conversion électromécanique.

Les activités électromécaniques du terpolymère pur et de son composite plastifié ont été caractérisées corrélées à des modèles théoriques. La technique de mesure vise principalement à quantifier la déformation induite sous champ électrique dans la direction du champ électrique appliqué, c'est-à-dire dans l'épaisseur du matériau. Cette déformation longitudinale est notée (S_{33}). Ce test électromécanique permet de déterminer et d'optimiser les contraintes mécaniques et les déformations électrostrictives dans la gamme de fonctionnement de l'actionneur adaptée à l'application.

L'effets du dopage sur les performances d'actionnement des terpolymères purs et modifiés ont été étudiées à travers deux techniques : (1) l'optimisation de la teneur en

plastifiant ajoutée au terpolymère pur, et (2) la fabrication d'actionneur multicouches permettant sous champ constant une augmentation de la déformation apparente.

Il est ainsi démontré que l'utilisation d'un agent plastifiant permet une amélioration très importante des performances électromécaniques de la matrice terpolymère (X600%). Cette augmentation des performances électroactives permet d'allier les grandes propriétés électrostrictives des terpolymères fluorés à des faibles champs électriques d'actionnement. En ce qui concerne la capacité de l'actionneur et la figure au mérite^[15], le poids donné à chaque critère de manière efficace (réponse de déformation, tension d'entrée, charges de remplissage, etc.) dépend du domaine d'application car le but final n'est pas seulement d'atteindre le plus grand comportement électrostrictif (compromis déplacement-force), mais aussi d'avoir une plage de champ électrique raisonnable : défini par l'application et éloigné du champ de rupture diélectrique du matériau. En fin de compte, un tel compromis entre le couplage électromécanique, la résistance au claquage diélectrique, les propriétés mécaniques et l'optimisation de la permittivité diélectrique en fonction du champ électrique dicte le choix du matériau optimisé. Un terpolymère dopé entre 8 à 10% de plastifiant DINP est choisi comme matériaux candidat au développement d'actionneurs de force adapté à notre projet Live-Mirror.

De plus, nous avons observé un comportement « atypique » des formes de courant électrique sous champ électrique pour ces terpolymères plastifiés. Les résultats ont démontré que le terpolymère plastifié présente sous champ électrique élevé de faibles pertes (mis en évidence par la saturation du courant de fuite estimé au-delà de 10V/ μm). Ce phénomène semble responsable des valeurs de résistances aux claquage diélectrique élevés de ces matériaux. Un modèle non-linéaire permettant de décrire les formes de densité de courant/champ électrique a été développé et utilisé afin de déterminer les propriétés électriques de ce matériau dans les gammes (fréquence, champ électrique, température) d'utilisation du projet Live-Mirror. Les données ainsi récoltées servent de propriétés matériaux d'entrée aux modélisations par éléments finis (COMSOL) utiliser pour la conception d'un prototype de Live-Mirror. Ce point est capital car il représente une des plus grandes sources d'erreurs généralement reportées dans la littérature, le développement de modèles à partir de grandeurs mesurées dans des conditions (fréquence, champ électrique, température) différentes des conditions de mesures des réponses électrostrictives. Les saturations, les non linéarités et les effets interfaciaux très présents dans les matériaux polymères (hétérogènes par nature) qui dans le cas des EAP sont souvent utilisés à basse fréquence et au-delà de leur température de transition vitreuse sont des phénomènes pouvant s'avérer majoritaire dans la réponse électrostrictive et nécessitent donc d'être caractérisés dans les mêmes gammes de fonctionnement que la réponse électrostrictive.

La deuxième technique présentée dans ce chapitre consiste à résumer la déformation de l'actionneur en utilisant une conception multicouche. L'utilisation du concept d'actionneur multicouche peut atteindre une permittivité extrêmement élevée tout en conservant de faibles pertes et un déplacement / une charge élevée lorsqu'il est utilisé sous champ électrique.

La conception de systèmes électroactifs multicouches permet d'obtenir une capacité électrique extrêmement élevée tout en conservant de faibles pertes diélectriques et un compromis déplacement / charge élevé pour des tensions d'utilisation modérées. La réponse électrostrictives des actionneurs multicouches développés à partir des terpolymère plastifiés a été caractérisée en fonction du nombre de couches. Les films multicouches ont été modélisés comme une structure de condensateurs connectés en parallèle (connexion électrique pour chaque couche de film unique). Comme attendu par le modèle, la capacité électrique des assemblages augmente linéairement avec le nombre de couches, validant la connectivité électrique des assemblages. La mesure de la déformation induite sous champ électrique des assemblages multicouches a montré une relation linéaire entre la déformation longitudinale et le nombre de couches ($S_{\text{Total}(n=1)} = 0.4\% \rightarrow S_{\text{Total}(n=8)} = 2.7\%$) sous un champ électrique alternatif de $10 \text{ V} / \mu\text{m}$ (Fréquence 50 mHz) et charge externe de 142g. La capacité de l'actionneur multicouche de terpolymère plastifié a permis de démontrer une réponse de déformation substantielle améliorée et stimulée par une faible excitation électrique d'entrée. Cette étude a permis de démontrer la possibilité d'accomplir une correction micronique de la surface du miroir en accord les objectifs de compensation des déformations locales liées aux contraintes en refroidissement des miroirs coulés définis par le projet Live-Mirror.

Chapitre 4 Application Live-Mirror

Les ambitions technologiques et scientifiques de l'approche du projet LiveMirror sont élevées et vont au-delà des technologies conventionnelles de miroirs actifs ou déformables. Nous proposons de développer des techniques qui peuvent considérablement améliorer notre capacité à créer de grandes surfaces optiques précises. Cette technologie de système optique (miroir) à base de métamatériaux légers et à diffraction limitée cible les percées suivantes :

- ✓ Densité de masse surfacique inférieure des miroirs, x7 ;
- ✓ Rugosité de surface et lumière diffusée plus faibles, x10 ;
- ✓ Production plus rapide et moins coûteuse, x15.

L'ambition est de développer des miroirs légers assemblés comme une structure hybride composée de deux couches de verre d'épaisseur quelques millimètres et de deux couches de matériaux électroactifs déposés par fabrication additive. Dans le cas particulier d'un télescope optique pour l'astronomie^[8,10,16], une couche imprimable de 200 microns d'épaisseur de terpolymère plastifié peut avoir une densité d'énergie volumique suffisante pour déformer de plusieurs microns le verre d'une épaisseur de quelques millimètres (2 à 5 mm). L'utilisation de 2 systèmes d'actionnement souples déposés par fabrication additive permettrait de remplacer le polissage abrasif, par un polissage « actif ». Le premier système d'EAP « polissant » essentiellement les non-uniformités à l'échelle cm de la surface réfléchissante liées aux contraintes mécaniques résiduelles générées lors du refroidissement du verre et le second système permettant de compenser les déformations gravitaires en générant une contrainte de cisaillement.

Nous profitons des propriétés de couplage électromécanique exceptionnelles du terpolymère, en particulier lorsqu'il est dopé avec un plastifiant, par ex. Phtalate de diisononyle (DINP). Ce terpolymère dopé crée une réponse en déformation importante ainsi qu'une excellente densité d'énergie mécanique sous des champs électriques relativement faibles. Les EAPs classiques (par exemple, polyuréthane, silicone) nécessitent des tensions d'entrée extrêmement élevées pour atteindre une contrainte mécanique suffisante ou un polymère ferroélectrique (PVDF ou P(VDF-TrFE) nécessite un pré-étirement^[17,18] ou/et une pré-polarisation sous champ électriques élevés qui ne peuvent pas être adaptés dans la technologie d'impression 3D sur de grandes surface (diamètre 50 cm).

Ce chapitre a pour objectif principal de présenter le prototype de miroir et de démontrer le concept de miroir actif « poli » à l'aide d'un actionneur EAPs. Nous avons démontré par une preuve de concept la possibilité de compenser la déformation locale de la surface d'un miroir en utilisant un actionneur en terpolymère plastifié. Deux catégories de prototypes ont été développées pour le projet Live-mirror ; (1) un système EAP multicouche en sandwich permettant de compenser globalement la surface du miroir, et (2) un prototype d'actionneur pré-poli d'actionneur fonctionnant en cisaillement dans le but de corriger localement la surface du miroir. Chaque prototype a été validé préalablement aux mesures expérimentales par une modélisation par éléments finis (Logiciel COMSOL).

Les prototypes que nous avons développé dans ce travail a permis de démontrer l'efficacité et validé le concept Live-Mirror. L'utilisation d'actionneurs à base de polymères électrostrictifs avancés permettent une déformation micronique du miroir : le prototype sandwich permet une déformation d'environ 10 μm , tandis que le prototype d'actionneur en cisaillement permet des déplacements locaux d'environ 1 μm . Ces valeurs sont en accord avec les modélisations préalables du projet LiveMirror

qui ont servies à définir le cahier des charges et valident ainsi la faisabilité de la preuve de concept. Les résultats expérimentaux ont été comparés à des modélisations par éléments finis réalisées à l'aide du logiciel COMSOL. Les résultats expérimentaux et le modèle de simulation sont très bien corrélés. La maîtrise de la modélisation de ces preuves de concepts est un paramètre clef pour la prédiction des comportements de ces actionneurs dans des systèmes complexes.

Chapitre 5 Actionneur EAP imprimé en 3D

Grâce à un projet interdisciplinaire LiveMetaOptics, l'actionneur de force entièrement imprimé est devenu un actionneur EAP avancé qui défie les applications de télescopes optiques vivants et légers. Une fois que nous avons développé et optimisé l'actionneur EAP fabriqué par la technique classique de la méthode de coulée de film mince. Dans ce chapitre, nous présentons le processus de production de film de mise à niveau utilisant la technologie d'impression 3D. Du prototype artisanal au plus avancé dans la fabrication automatisée, l'actionneur unique entièrement imprimé se compose de 3 couches de polymère imprimées : une couche d'EAP modifiée en plastifiant dopé terpolymère DINP pris en sandwich entre deux couches de composite conducteur terpolymère. La couche conductrice a été développée ici en intégrant du terpolymère avec une nanoparticule de noir de carbone pour réaliser une électrode imprimable. En utilisant le même matériau de base-terpolymère dans l'EAP et la couche d'électrode, nous sommes en mesure de compromettre la complexité de la compatibilité chimique et de rendre l'actionneur imprimé permettant de fonctionner sous excitation haute tension. Le prototype entièrement imprimé a été produit dans de nombreuses configurations et a étudié l'activité électromécanique via le mode d'actionnement par cisaillement.

En raison du processus de fabrication et de ses limites, le défi immédiat est la maîtrise de la technologie d'impression 3D qui aura de profondes implications sur le système intelligent d'actionneur. Dans le but d'améliorer la vitesse de construction et d'améliorer la précision de l'approche de fabrication d'actionneurs, nous avons développés une approche permettant l'adaptation du procédé de mise en œuvre des actionneurs EAP développés dans les parties précédentes aux procédés de fabrication additive. Un avantage majeur de la fabrication additive est de pouvoir dimensionner les réseaux d'actionneurs/capteurs de formes variées sans développement de masque de déposition d'électrodes ainsi que d'un contrôle des épaisseurs de dépôt.

Pour démontrer la faisabilité de l'utilisation d'EAP pour l'application d'optique active, la technique de fabrication additive pourrait étendre le processus de fabrication d'EAP conventionnel en développant un EAP imprimable et une électrode compatible. Un

composite terpolymère / CB conducteur électriquement a été développé et choisi pour servir d'électrodes imprimées. Le taux en masse de noir de carbone nécessaire pour atteindre le seuil de percolation électrique de ces composites a été déterminé. La structure de l'actionneur entièrement imprimée se compose d'une couche EAP (terpolymère + 8% en poids DINP) prise en sandwich entre deux couches d'électrodes (haut et bas de terpolymère + 5% en poids CB + 5% en poids DINP). Nous avons finalement réalisé l'actionneur entièrement imprimé validant le prototype imprimé 3D Live-mirror. En outre, la modélisation par éléments finis réalisée à l'aide du logiciel COMSOL Multiphysics® a montré des résultats très cohérents en comparaison des mesures expérimentales. Cette maîtrise de la modélisation nous permet d'envisager le développement d'un algorithme de conception avancée d'actionneurs approchant au mieux l'application réelle du télescope.

Conclusion et travaux futurs

Conclusion

Cette thèse s'inscrit dans le cadre d'un projet international : Live-Mirror est une approche transdisciplinaire entre l'ingénierie des matériaux et l'optique (en astrophysique), en introduisant un concept nouveau basé sur la façon d'exploiter un système d'actionnement EAP avancé et adapté aux procédés de fabrication additive, au contrôle de surface optique. Cette étude prospective sur plusieurs EAPs a permis de définir les propriétés importantes que doivent présenter ces matériaux polymères afin de satisfaire à l'application. Dans l'état actuel de nos connaissances il nous a été possible de définir un candidat matériau qui répond en grande partie à l'exigence de performance de l'actionneur utilisé dans l'application en termes de réponses électromécaniques et d'adaptabilité aux procédés de fabrication additive.

Le terpolymère P (VDF-TrFE-CFE) est devenu la base de matériau sélectionnée pour le système d'actionnement pour cette application d'optique active. L'optimisation des propriétés électrostrictives de terpolymère fluorée ont été améliorées par voie composites ou mélange tout organique. Il a été démontré que l'introduction d'agents plastifiants permet une augmentation significative des propriétés électrostrictives tant du point de vue de la déformation induite sous champs électriques que de la densité d'énergie mécanique générée. Une optimisation du taux de plastifiant a permis de tirer le meilleur compromis de performances dans l'application envisagée. Ces résultats ont démontré que ces actionneurs avancés ont des performances électromécaniques suffisantes pour être utilisées en tant que matériaux actifs du système d'actionneur dans l'application Live-Mirror. Les résultats expérimentaux et le modèle de simulation sont très bien corrélés. La maîtrise de la modélisation de ces preuves de concepts est

un paramètre clef pour la prédiction des comportements de ces actionneurs dans des systèmes complexes. Cette maîtrise de la modélisation nous permet maintenant d'envisager le développement d'un algorithme de conception avancée d'actionneurs approchant au mieux l'application réelle du télescope.

Enfin et surtout, la mise en œuvre des actionneurs EAPs a été adaptée aux techniques de fabrication additive. Cette technique permet un dépôt à la demande de réseaux d'EAPs de formes et surface variées en face opposée aux déformations à compenser sur la surface réfléchissante des miroirs. Pour cela des électrodes composites à matrice terpolymère ont été développées afin de minimiser les problèmes d'interfaces entre les électrodes et le matériau électroactif. Une preuve de concept du processus de fabrication additive d'EAP plus automatique adaptée à une application d'optique active a ainsi été réalisée.

Travaux futurs et perspective

À l'avenir, nous avons l'intention d'étudier les effets du vieillissement physique de l'EAP avancé pour la stabilité à long terme par le biais de caractérisations de propriétés physiques des matériaux (BDS, DSC, XRD, ATG, MEB). La modification chimique optimisée sur terpolymère plastifié sera étudiée en termes d'effet d'humidité dans le processus de préparation des matériaux. Le vieillissement physique des performances électromécaniques de l'actionneur sera caractérisé en quantifiant son impact sur la rigidité diélectrique ainsi que sur les cycles de fonctionnement en temps sur fonctionnement HT. L'effet de l'environnement de température est également important et peut amoindrir la réponse en actionnement, ce qui devrait être réalisé en limitant le fonctionnement en température. Toutefois, une caractérisation des réponses électromécaniques en fonction de la température doit être envisagée.

Du point de vue de la fabrication additive les nombreuses perspectives de cette étude sont :

- Le développement d'un actionneur tout imprimé en 3D multicouche et de forme adaptée géométriquement à la zone à compenser
- L'optimisation de la conductivité du matériau composite utilisé comme électrode afin d'éviter les pertes et les phénomènes d'auto-échauffement. Cette étape de permettra aussi d'augmenter la bande passante de l'actionneur pour des applications dynamiques futures.
- Le problème de migration du plastifiant doit être optimisé en termes de reproductivité de l'échantillon en diminuant la quantité de plastifiant ajoutée à la couche d'électrode.

- Le modèle d'électrode spécifique sera modélisé et fabriqué en fonction d'une valeur par défaut de la surface du miroir et la reproductibilité (épaisseur forme) de production analysée.
- La surface d'adhérence entre l'actionneur entièrement imprimé et le substrat de miroir doit être améliorée. Pour cela 2 options se présentent : L'utilisation d'un primaire d'adhérence à base PVDF avant la phase de déposition par fabrication additive de l'EAP ou l'addition d'un quatrième monomère promoteur d'adhérence sur électrode métallique lors de la synthèse du terpolymère. Cette étape passe inévitablement par la mise en place d'une collaboration avec les sociétés productrices de ce matériau.

Une perspective importante de l'étude est le développement d'une solution fiable permettant de dimensionner l'EAP (épaisseur, géométrie) qui soit adapté à la courbure à compenser. En considérant la courbure locale dérivée du Laplacien du déplacement suivant l'axe z , $\nabla^2 z(x, y) = c(x, y)$, une analyse comparative entre la forme de l'électrode et l'analyse du Laplacien montre que l'amplitude de la courbure locale dépend quasi-linéairement de l'épaisseur et de l'intensité champ électrique appliqué. La surface de l'électrode provoque une déformation influe quant à elle sur la surface de la zone courbée localement mais pas sur l'amplitude de la courbure locale. Ce point est particulièrement intéressant car une analyse de la courbure locale permettrait donc de dimensionner les EAP en forme ET en épaisseur. Les travaux futurs se focaliseront sur l'analyse de la surface du miroir combinée une forme particulière d'actionneurs EAP tout imprimés qui seront conçus à partir de l'analyse de la courbure locale de la surface préalablement défini par mesure interférométrique.

CHAPTER 1

Introduction

CHAPTER 1

I. Introduction

Introduction

Polymers are fascinating flexible materials with broad-utilization in both the research and industrial domains. Thinking of polymers from my parents' point of view, a polymer is a box for containing food or the plastic bag from a supermarket. Literally, there are more types of polymers that we realize. A polymer is just a large molecule consisting of numerous subunits called monomers and we can find polymers all around us in everyday life. For example, the DNA structure in the human body is also a kind of polymer. Many plastic elements of a car, even furniture, are made from polymers. The mechanical properties of polymers can be customized to be as rigid as a metal or as elastic as a rubber depending on their intended use. In addition to the general use of polymers, researchers have been struggling to create multifunctional polymers known as smart polymers which can respond to an external stimulus, such as vibration, temperature change, electricity, chemical reaction, etc. With its special advantages over generic plastic, smart polymers encourage us to discover the underlying scientific principles as well as distribute its utility to the global intelligent platform. Researching such smart material field provides us with an original opportunity - as a Ph.D. thesis requires - to exploit its development-oriented to a novel hybrid meta-material dedicated to the development of actuators and sensors to the high-performance optical mirrors to the ground- and space-based telescope.

Once upon a time in July 2017- for a classical start - I got the opportunity to undertake my Ph.D. in synergy with the Live-Mirror¹ project. This project aims to create interdisciplinary research by integrating the technological advancement of smart polymers (electronics and science material) with optics metrology, control and non-contact surface polishing

¹ The Live-Mirror project is sponsored by the ANR (The French National Research Agency): Project #ANR-18-CE42-0007-01, over 48 months (from 10/218 to 10/2022).

(astronomy and astrophysics instrumentation) to develop Hybrid Dynamic Structures for Optical–Quality Surfaces Shape Control: Live–Mirror. The consortium is a small network of identified eminent interdisciplinary scientists concerned with the impact through R&D excellence and innovation. Dr. Gil Moretto from CRAL/CNRS (Centre de Recherche de Astrophysique de Lyon, Centre National de Recherche Scientifique) is the Project Coordinator and PI, Dr. Jean–Fabien Capsal from the LGEF/INSA (Laboratoire de Génie Electrique et Ferroélectricité at Lyon) is the project CoPI, with Prof. Jeffrey R. Kuhn from the ATRC/UH (Advanced Technology Research Center, Institute for Astronomy, The University of Hawaii, at Maui, Hawaii USA) also the project coPI. The overall project is funded over 4 years based on 188 FTE and a full cost of 1.57M Euros and a requested aid of 420,10K Euros. My implication in the project is to reach the full polymer optimization (materials selections and characterizations) and full 3D printing of actuator procedures R&D. We started with the selection and characterization of the materials to having a preliminary Live–mirror prototype. In this thesis, we describe the methodology to fabricate a thin film actuator based electroactive polymer, presenting its electromechanical features, both experimental and modeled, including the upgraded manufacturing technique with 3D printing technology. Our efforts to create live and light optical mirrors, named *Live–mirrors*, are only three–years–old. The Live–mirror team gave me the hands–on experience to research materials science in order to play an important role on an overwhelming astronomical application.

Electroactive Polymers (EAPs)

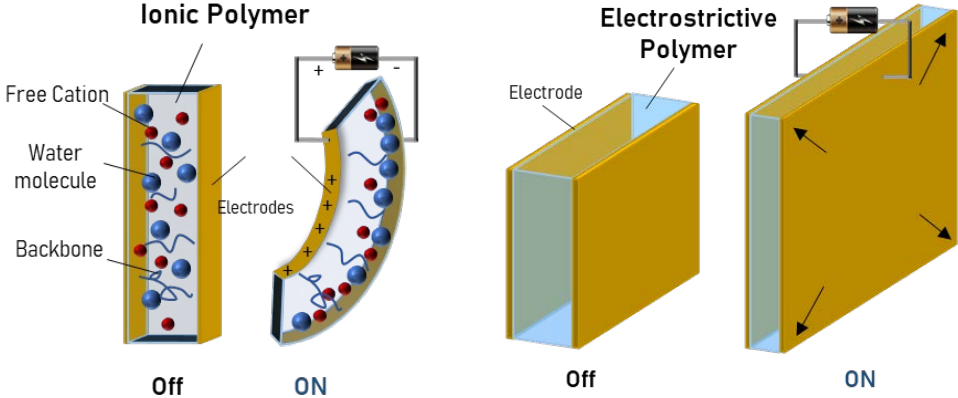
In 1880, Wilhelm Röntgen discovered EAP phenomena on a rubber band which revealed the shape change while applying an electrical voltage^[19]. The discovery of EAPs brought about countless revolutionary studies on electric–strain response activation that have resulted in the development of materials for more than 200 years^[20–24]. Several polymers are considered as field–activated EAP types, such as ferroelectric polymers, dielectric or electrostrictive elastomers, ionic gels, and conductive polymers (see Table 1). Their flexibility and semi–crystalline structure allow a variety of electroactivity development in polymeric materials.

Table 1 EAP material types in electrically field-activated and ionic [2,25].

Types of EAP	Activation Mechanisms	Sample Materials
Ferroelectric polymers	a change in electrical polarization (with their spontaneous electrical polarization that can be reversed) in response to mechanical stress (or vice versa).	<ul style="list-style-type: none"> • PVDF • P(VDF-TrFE) • Electron-radiated P(VDF-TrFE)
Electrostrictive polymers	Electric field arranged dipole moments produced by molecular alignment which are attached to the side chains. The actuated strain is induced by Maxwell stress (Coulomb forces) and electrostrictive force for the actuation mechanism.	<ul style="list-style-type: none"> • Silicone • Polyurethane • P(VDF-HFP) • Terpolymer-P(VDF-TrFE-CFE/CTFE)
Ionic gel	Hydrogen ions are immobilized inside the polymer matrix by an applied voltage	<ul style="list-style-type: none"> • Polyacrylamide (PAM)-based hydrogel^[26] • Ionic Liquid/PU/PEDOT:PSS^[27] • Single-walled carbon nanotubes (SWNTs)/P(VDF-HFP)^[28]
Ionic polymers-metal composites (IPMCs)	Ions migrate to the imposed voltage across the stripe of IPMCs causing the deformation created by non-symmetric free-cations	<ul style="list-style-type: none"> • Nafion® (perfluorosulfonate, made by DuPont) • Flemion® (perfluorocarboxylate, made by Asahi Glass, Japan) Cations: tetra-n-butylammonium, Li+, and Na+ • Poly(styrenesulfonicacid)(PSSA)/PVDF^[29]
Conductive polymers	The overlapping of a conjugated backbone due to the electron delocalization as a result of polymer geometry relaxation or stretching ^[30]	<ul style="list-style-type: none"> • Polypyrrole • Poly(ethylene dioxythiophene) • Polyaniline • A single novel conducting polymer (PF-BTB) doped with porphyrins^[31]
Carbon nanotubes (CNTs)	The interfacial area between the electrolyte and CNTs enhances larger volume change of electrode film by speedy charge injection induced by various fields	<ul style="list-style-type: none"> • Single- and multiwalled carbon nanotubes • MWCNT/PVDF-HFP^[32]
Pseudo pyroelectric polymer^[33]	A polarization variation with the temperature yielded with a bias electric field exhibiting electrothermal coupling	<ul style="list-style-type: none"> • P(VDF-TrFE-CTFE)/Carbon black

Despite several types of EAP require large actuation voltage to generate a high electric field, the advantage is low electrical power consumption, which usually comes from the contribution of leakage current. Particularly, dielectric EAPs (ferroelectric and electrostrictive polymers) require very low power (less than 10 mW) [34,35] to keep the actuator in the given position.

Table 2 the advantages and the drawbacks of ionic polymer and electrostrictive polymer.



A d v a n t a g e s	
<ul style="list-style-type: none"> ⊕ Low voltage requires ⊕ Actuated direction depending on voltage polarity ⊕ Large displacement ⊕ The actuation of some conducting polymers is bistable 	<ul style="list-style-type: none"> ⊕ Maintain shape change under DC voltage ⊕ High mechanical energy density ⊕ Fast response (msec) ⊕ Large actuation force ⊕ Long-serving time under ambient condition
D r a w b a c k s	
<ul style="list-style-type: none"> ⊖ Need to operate using an electrolyte ⊖ Requires particular conditions (protective layer, aqueous system active at > 1.23 V, etc.) ⊖ Slow response (sec) ⊖ Low mechanical energy density ⊖ Low actuation force ⊖ Complex material elaboration (e.g. IMPCs) ⊖ Electrodes made with gold or platinum desire high current operation 	<ul style="list-style-type: none"> ⊖ High voltage (HV) requires ($\sim 100\text{V}/\mu\text{m}$) ⊖ Monopolar actuation (quadratic effect dependence with voltage polarity) ⊖ Low strain response rate ⊖ Limited operation under glass transition temperature

EAPs have been attractive to a great deal of sensor–actuator technology fields called soft actuators, especially for their electromechanical response in piezoelectric, electrostrictive, and ferroelectric materials. Soft actuators perform their capability to convert chemical or physical energy into mechanical energy with dissimilar activation mechanisms. Thus, to clarify the array of performance capabilities of EAP actuators, Table 2 shows the advantages and drawbacks when comparing two essential EAP types; ionic polymers and electrostrictive polymers.

Smart EAP Materials Use for Actuators & Sensors

The increasing demand for actuation devices and self-powered sensors has placed significant attention on EAPs^[1,2] due to their outstanding properties. Among their lightweight, high mechanical strength, flexibility, transparency, easy processing to large-area films, the appeal of EAPs can go beyond the ability to be molded and/or additively manufactured, i.e. 3D printed into various configurations. This technological advancement allows us to execute a very important factor for the revolutionary electronic devices world^[3-7].

Scientific studies have been devoted to enhancing the electromechanical response of EAPs^[36-40] using different methods such as the control of the electromechanical properties by introducing nanoparticles^[41], or irradiating samples^[42]. Such materials seem to be very promising in additive manufacturing whose recent advances become more widespread as it offers exciting opportunities for future development, particularly in high potential applications like astronomy optical communication^[8,43], remote sensing system, smart medical instruments^[44], to structural health monitoring in mechatronics and more recently (the main goal of this thesis) to optical mirrors for astronomy (in the ground and in the space) and optical communication^[8,43], etc. Nowadays, a main issue is an enhancement in electromechanical coupling to achieve large deformations and load exertion: the main limitation to the current EAP actuators used for industrial applications.

1. EAPs as Emerging Actuators

The response of polymers to an external electric field can be divided into two distinct factors: (1) electrical properties (permittivity, dielectric relaxation, conductivity, and electrical breakdown) and (2) mechanical properties (tensile strength or elastic deformation)^[45]. These two parameters ultimately affect the electromechanical conversion efficiency. Optimized EAP materials dedicated performance yielding in a wide range of applications especially electromechanical devices and systems. Such free formability and flexibility make EAPs an emerging key technology for the micro-electromechanical systems (MEMS) devices developments, including our goal here – the smart actuators.

So far EAPs are widely used for several actuator applications (see Figure 1), such as artificial muscles^[46], micro-pumps^[47,48], smart steerable guidelines^[44] and EAP tunable lenses^[49]. As a result of their flexible and excellent electromechanical properties producing high strain and energy density, EAPs are attractive soft-actuator candidates for electronic devices.

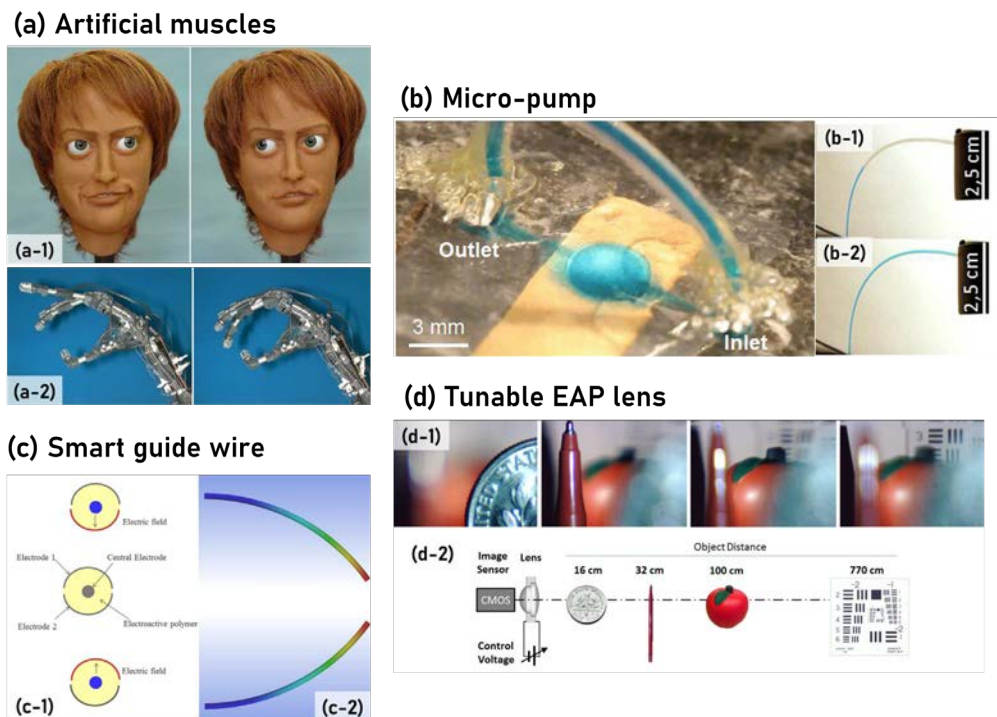


Figure 1 EAP actuator applications (a) Artificial muscles: (a-1) an android head making facial expressions and (a-2) robotic hand made from EAP actuators^[50]; (b) Micro-pump system: (b-1) before and (b-2) after pumping^[48]; (c) Smart guide-wire: (c-1) the structure design purposely providing (c-2) two degree of freedom of deformation^[44]; and (d) Tunable lens: (d-1) images at different focal distances and (d-2) the schematic of measurement setup verifying the tunable lens capability^[49].

2. EAP Sensor Applications

The electromechanical coupling of EAPs has been extensively investigated for actuator applications and is also being investigated for chemical and mechanical charge sensing. Because of their flexibility, wearable electronics, capacitance-like system, high strain, and low electrical power consumption, electronic EAPs have become an influential dielectric elastomer sensor base. Two different types of EAPs using for sensors were mainly divided into ionic and electronic sensing types. The characterizations of relaxation time including stimuli types are categorized in various frequency ranges for dynamic sensing. The two main types of sensor-related materials and applications are summarized as follows^[2];

- Ionic EAP for sensing: where mobile ions and/or molecules within dielectric material are transported between two electrodes.
 - *Free-standing film sensors* based on conducting polymer: the mobility of free-ions creating a voltage difference related to an applied mechanical stress direction.
 - *Bending Trilayer structure*: the produced voltage given by different ion concentration mobilizing within the separate layer, e.g. such as poly(3,4-ethylene dioxythiophene) (PEDOT) used as electrodes of an electro-active interpenetrated polymer network (INP) can produce voltage sinusoidal peak-to-peak approximately 0.2 mV/input 2% applied strain^[51].
- Electronic EAP for sensing: where polarization is induced by electric dipole orientation and/or charge mobility regarding an externally applied field, e.g. voltage, temperature.
 - *Dielectric elastomer sensor*: an applied mechanical stress (stretching, relaxing, or compression) changes the capacitance, e.g. silicone stretch sensor with the sensitivity in a range of 3.98–6.30 pF/mm^[52] (companies like Parker and StretchSense™ have developed sensors based on dielectric elastomers).
 - *Piezoelectric polymers*: In bulk polymers, voided charged polymers, and polymer piezo-composites electric fields are induced by shape deformation or vice versa, e.g. PDMS/PZT

- composite thin film yielded piezoelectricity 25 C/N which possibly to develop for tactile sensors^[53]
- *Pyroelectric infrared detector*: the temperature-dependent parameters; electrical conductivity and pyroelectric coefficient are induced by the incident radiation (IR→heat→voltage), e.g. PANI - DBSA/PVDF blend film provided voltage responsivity 157 V/W at 0.16 Hz^[54].
 - *Pseudo-pyroelectric EAP* for electrothermal coupling sensor^[33]: the novel multifunctional EAP material provides dipole orientation that is influenced by both the electrical field and temperature through thermal agitation. When an electric field is applied to the material, electric dipoles start aligning therefore inducing polarization and charges appearing on the surface (for more explanation, see in chapter 2, subsection 2.1).

Table 3 The review of EAPs for sensor applications^[2,52 - 56].

EAP types	Stimuli types	Sensitivity	Response time
Ionic EAP	Strain or deformation	Up to 10% in strain, ≈ 0.2 mV / 2% strain	0.1–100 Hz
Dielectric elastomer	Strain or deformation	Up to 300% in strain, 0-300 nF	< 50 Hz
Piezoelectric polymers	Compression Temperature	0.7-350 pC/N, 29-54 pm/V, ≈ 8 V/°K	0.001–10 ⁹ Hz
Pyroelectric polymers	Temperature	157-2200 V/W	< 128 Hz

Besides, the review of the relevant EAPs for sensing (see Table 3) could provide the sensory prospects, with their stimuli categories and sensitivity range, for the development of the actuator–sensor hybrid system in Live–mirror perspective. In spite of EAP sensor applications are not include in the scope of this thesis, it will be the main task to my future work in the frame of the Live–Mirror project, as presented next.

EAPs Actuator Improvement & Development Technologies

Different methods to achieve excellent actuation response of EAPs have been investigated in several frames: polymer/composite^[1], blended polymer^[57], and structural design^[58,59] in order to improve intrinsic properties. Xia et al.,^[6] introduced a novel relaxor ferroelectric polymer (hereafter dubbed as terpolymer), leading to the future improvement of EAPs for a broad range of electronic applications. Due to the slightly bulky chlorine atom in terpolymer P(VDF - TrFE - CFE/CTFE) as a combination of ferroelectric–paraelectric phase provides a high dielectric constant (~ 70) and large electromechanical reaction. However, the main drawback of these polymers is their high electric field requirement ($E > 100 \text{ V}/\mu\text{m}$)^[41] to reach sufficient strain.

Hence, the introduction of terpolymer/composites including an effective fabrication processing/assembly has been investigated to enhance the electromechanical conversion^[41,60]. This potential motivated the investigation of an advanced–terpolymer–composite by adding a plasticizer into the terpolymer matrix. The plasticizer molecule leads to increased molecular mobility of the polymer chains, resulting in an increase of the material dielectric permittivity and a decrease of its Young modulus. Note that the charges trapping at the boundaries of the heterogeneous morphology tend to induce large Maxwell–Wagner–Sillars polarization effects. Such an adaptation technique is able to exploit the electromechanical coupling through areas of functional sensor–actuator fabrication technology^[60].

Furthermore, a free–formable attribute of EAPs generates the possibility to develop numerous different designs in large–area of actuator market attractiveness. Considering the manufacturing process of piezoelectric and ferroelectric materials for actuator devices, all intermediate processes require many complex components: e.g. fabrication of PZT by the sol–gel method^[61], spin coating process in PVDF preparation^[18], monolithic polymer construction^[62]. To reduce the complexity of fabrication processes using piezoelectric and ferroelectric materials, terpolymer (or relaxor ferroelectric material) has turned out to be an alternative material for various actuator applications. Apart from intrinsic material modification, there is an opportunity to achieve advance electromechanical response through configuration design, for instant structure multilayer stacking with 15 layers of terpolymer for microlens application^[63,64]. In this thesis, we elaborated the advance

modification of terpolymer properties as well as the newly developed multilayer stack assembly.

1. EAPs Force-Actuator Selections

Large strain response under a low related applied electric field of EAPs is not the only achievement of the actuator applications. The ability to generate force of EAPs have been also paid attention to classify the responding or operating throughout actuator and sensor performance requirements. A summary overview of actuator ability and strain-generated limitation for several EAPs is illustrated through blocked stress versus generated strain in Figure 2.

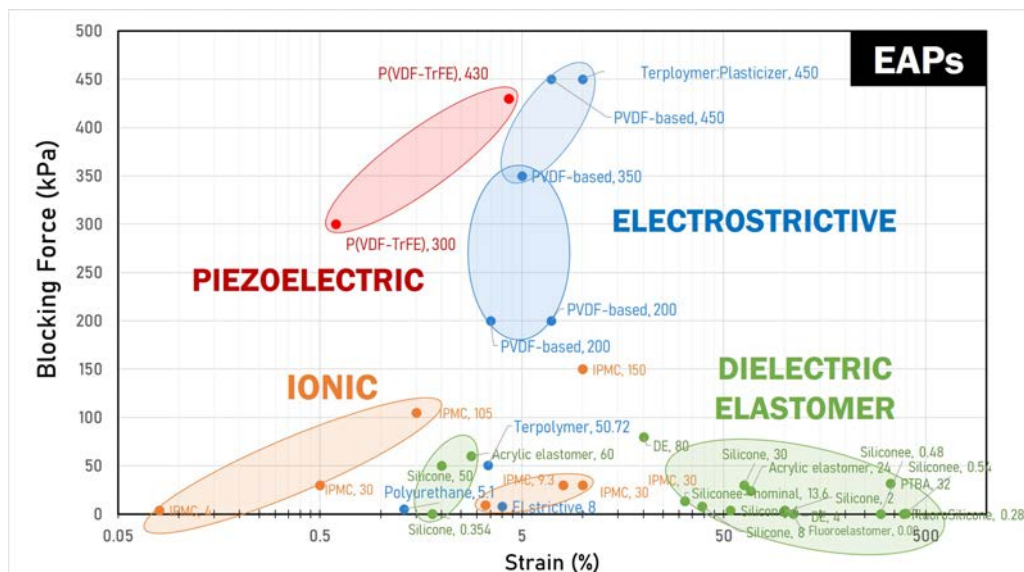


Figure 2 Review of EAPs diagram [25,27,65 - 70] represented blocking stress (kPa) versus maximum strain generated annotating to working limitation range of actuation capability.

It was demonstrated that^[17] the P(VDF-TrFE-CFE) terpolymer exhibited significantly higher permittivity (i.e. dielectric constant) with respect to the conventional EAPs and the PVDF-based copolymer. This makes a terpolymer being one of the most appropriate candidates for various applications in actuator devices where high electromechanical coupling is required. As mentioned above the main drawback of these polymers is their

high electric field requirement ($E > 100 \text{ V}/\mu\text{m}$)^[41] to reach sufficient strain. To overcome this technological barrier a new technique was developed here – the doping of a P(VDF–TrFE–CFE) terpolymer with the DINP plasticizer^[15,34,71,72]. Such a new doping technique radically boosts the strain response as well as the mechanical energy density of the EAPs. This chemical modification leads to large dipolar interfacial effects within the polymer matrix, a contribution of charge trapping between amorphous and crystalline phases, giving the increase of dielectric permittivity and simultaneously the decrease of the Young modulus^[72]. This newly developed approach will permit the uses of exceptional properties of the plasticized terpolymer for an electric field nearly $5\times$ lower plus a 20 -fold increase in strain response as compared to conventional EAPs^[15].

Figure 3 depicts the free longitudinal strain without pre-loading (i.e. the stress $T = 0$) versus the applied electric field of four different EAPs, i.e. 1) *plasticized terpolymer (terpolymer + 10 wt% DINP)*, 2) *pure terpolymer*, 3) *silicone* and 4) *polyurethane (PU)*. Such experimental results corroborate the theoretical model of electrostrictive phenomena where a quadratic relationship between the strain response and the input electric field was obtained.

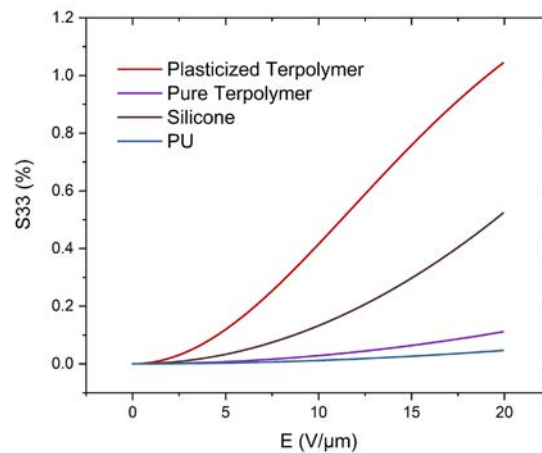


Figure 3 Longitudinal strain (S_{33}) of four different EAPs without external load under different applied electric fields.

Notably, the DINP plasticized terpolymer showed an improvement of longitudinal strain (and deformation) $10\times$ higher with respect to the pure terpolymer under a moderate $E=20 \text{ V}/\mu\text{m}$, and substantially greater than that of silicone and polyurethane under a similar electric field. The DINP plasticizer

incorporated into the terpolymer matrix strongly improved the molecular mobility of the amorphous phase ^[71], leading to increase dielectric permittivity at low frequency (50mHz).

As aforementioned that the ability to generate force of EAPs should be taken into account for obtaining the electromechanical strength limitation from optimized materials. The force–actuator ability can be observed through the value of blocking stress or blocking force. The blocking force is the maximum load that an EAP sample will no further generate electromechanical activity or strain = 0 ^[73]. Figure 4 shows the blocking force of the four EAPs (logarithmic scale) versus the applied electric fields confirming the excellent ability of the plasticized terpolymer to sustain under high load up to 300 N at $E = 20 \text{ V}/\mu\text{m}$. Bear in mind that the goal blocking force required for active optics controlling based terpolymer doped with the plasticizer (Live–Mirror) is about 1N for a spatial pitch of one actuator every 5cm radius.

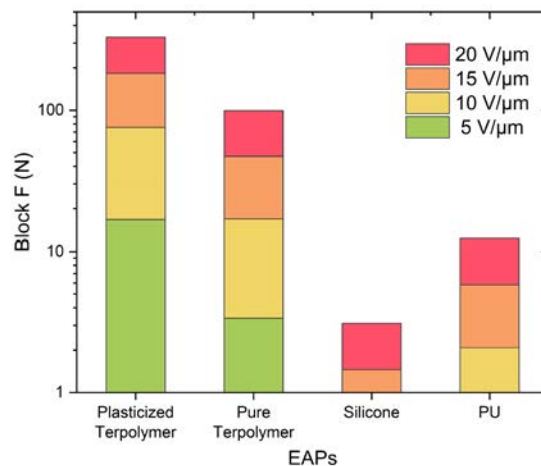


Figure 4 Blocking force (Block F) of different EAPs at a different level of electric fields.

The results above confirm that multilayer plasticized terpolymer actuators deliver optimum actuation performance under low applied electric field and significant external load conditions. Such a large strain is compliant with the development of force actuators for the Live–Mirror project (as discussed in the next section) with the goal specification of seeking deformations of few microns under $E = 10$ to $20 \text{ V}/\mu\text{m}$ and an external load of 1N.

2. EAPs Composite Modification Approaches

The possibility to develop material properties, i.e. electrical and mechanical property can be achieved by composing a variety of composite fillers along the direction of their reinforcement properties. For decades materials science has dealt with electronic devices and pursued improving energy-storage density and dielectric permittivity in EAPs. Among various techniques^[74-76] used to modify not only intrinsic polymer structure but also extrinsic topology has been studied and developed for having better electromechanical coupling. Research and developments^[70,77] had been improved elemental EAPs conformation. For instance, the following studies were conducted on enhancing the dielectric constant of materials intrinsically for good piezoelectric and pyroelectric responses by:

- (1) Copolymerizing process of P(VDF-TrFE) or P(VDF-HFP) is automatically formed ferroelectric beta-phase without mechanical orientation^[78,79];
- (2) Unidirectional and/or biaxial mechanical stretching processes are used for alignment polymer topography chains^[80,81];
- (3) Electric poling process is used for inducing an orientation of polymer chains^[82] and internal doped microfiber alignment^[83];
- (4) Cross-linked polymers provide high-k and low loss for dielectric elastomers, i.e. cross-linked divinylbenzene (DVB)^[84], cross-linking sites in nonpolar polydimethylsiloxane (PDMS)^[85];
- (5) High-energy electron-irradiation (HEEIP) treatment on P(VDF-TrFE)^[6,42] exhibits large electrostriction and high energy density.

Most early studies as well as current work have focused on the extrinsic EAPs electromechanical property enhancement implementations. Several extrinsic material development techniques were reported in the literature to address their widespread used for high-k EAPs and conductive polymer composites:

- (1) Polymers blending, i.e. a high dielectric constant polymer ($k=7.5$) created from two dipolar polymers poly(arylene ether urea) (PEEU, $k=4.7$) and an aromatic polythiourea (ArPTU, $k=4.4$)^[86];

- (2) Purification polymer solution is done by filtering out unwanted contaminants for improving ionic conductivity and dielectric loss of EAPs^[87];
- (3) Electro-thermal annealing can reduce leakage current and achieve considerable actuation strain of terpolymer^[35,88];
- (4) Doping high-permittivity particles, i.e. TiO_2 , ZrO_2 , BaTiO_3 , $\text{CaCu}_3\text{Ti}_4\text{O}_{12}$, $\text{Pb}(\text{Zr,Ti})\text{O}_3$ and/or conductive particles, i.e. nano-/micro-particles of CB, Ag, Cu for achieving high- k EAPs composite^[89] or conductive polymer composite.

2.1 Carbon Nanomaterial-Polymer Composites

Carbon nanomaterials – as a functional conductive filler – have been highly attractive for polymer matrix nanocomposites for high permittivity (high- k) material composites and large-scale energy storage technologies. Due to their simply uniform dispersion, high- k dielectric nanocomposites, and great flexibility polymer composites with low filler loading, such new carbon nanomaterial became an outstanding conducting functional filler contributed to the development and evolution of EAPs for sensors and electronic devices.

We can divide carbon nanomaterial composites into 4 different types of dimensionality^[90-92] as illustrated in Figure 5: 3D of graphite nanoparticles and nanodiamonds used as a potential material in medical and biological electronic applications^[93]; 2D of graphene nanosheets (GNs); 1D of carbon nanotubes (CNTs); and 0D of fullerenes or carbon black nanoparticles (CBNPs or CB).

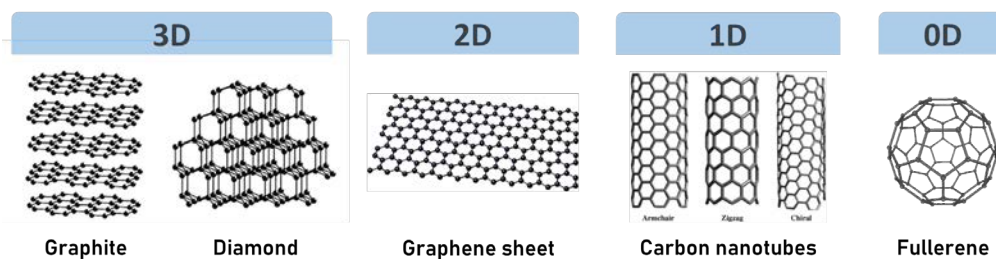


Figure 5 Carbon nanomaterials structures differentiated dimensionally: 3D of graphite nanoparticles and nanodiamonds used as a potential material in medical and biological electronic applications; 2D of graphene nanosheets (GNs); 1D of carbon nanotubes (CNTs); and 0D of fullerenes or carbon black nanoparticles (CBNPs or CB).

Considering an electrically conductive EAPs composite approach^[91], ceramic and/or metal nanoparticles require very high-volume fractions to reach the percolation threshold, i.e. 16vol% of Ag added to PVDF. Besides the fact that carbon nanofillers added to PVDF^[91] can reach the percolation region with less than 2% by volume, e.g. 0.31vol% of GNs, 1.61vol% of CNTs, and 0.13vol% of CBNPs added to PP/PMMA blend^[94].

Interestingly, the ability to form electrical networks of polymer composites also depends on the morphology interaction of polymer host. Zhang et al., (2019)^[95] reported the conductive polymer/CB composites based on simultaneous dispersion in four different dielectric polymers blends. For example, POM/1%TPU needs 6wt% of CB, and POM/1%PA6 needs 7wt% of CB, whereas pure POM requires 12wt% of CB to reach the percolation threshold. Because of CBNTs or CB can make its polymer composites achieving high electrical conductivity at low filler contents, ease processing, and very low cost (~6€gram, 100 times cheaper than CNTs)², so carbon black nanoparticles become a good nanofiller candidate for improving an electrical conductivity in the terpolymer/CB composite in this work.

2.2 Plasticizer for EAPs Electromechanical Reinforcement

The novel technique of doping a polymer with a specific and optimized plasticizer has enhanced the flexibility and pliability of a large range of EAPs increasing its range of usability from the automotive industry to medical tools. Such an optimized plasticized polymer challenges a crucial rule to customized EAPs - for example soft actuators.

Back to terpolymers P(VDF-TrFE-CFE/CTFE), it has been introduced to the plasticizer or dispersant blending into terpolymers to improve their electromechanical coupling^[34,71], i.e. the actuation strain and the blocking force. Capsal et al., (2014)^[71] reported the chemical modification using plasticizer blending into a terpolymer matrix could achieve an excellent mechanical energy density with around 5.5 times higher with respect to the conventional terpolymer. The results confirm that terpolymer filled with plasticizer improves molecular mobility and interfacial polarization effects (Maxwell Wagner Sillars) at low frequency; decreasing the Young modulus and increasing the dielectric permittivity of the modified terpolymer.

² Information from SigmaAldrich

Schiava et al., (2017)^[34] had compared the DINP plasticizer with Palamoll 652 and DEHP (2-ethylhexyl phthalate) doped into terpolymer P(VDF-TrFE-CTFE). The electromechanical performance of the modified terpolymer was presented through the transversal strain (S_{31}) investigated from the cantilever beam deflection. The results showed that the modified terpolymer with 15%DINP presented the highest $S_{31} \approx 0.5\%$ whereas the sample doped 15%DEHP and 15%Palamoll gave their $S_{31} \approx 0.4\%$ and 0.2% , respectively at $E=10V/\mu m$. It was concluded in this study that DINP is a remarkable plasticizer agent showing biocompatibility characteristics and well improving the electromechanical response of its terpolymer composite.

Similar studies, Ni et al., (2020)^[96] introduced plasticizer, dioctyl phthalate (DOP), to enhance the electromechanical performance of the modified natural rubber, TiO_2/NR . Using a double-roll open mill to mix DOP into TiO_2/NR in a unit of parts per hundreds of rubber (phr), the dielectric constant at 100Hz increases from 3.1 in pure TiO_2/NR to 4.0 in DOP 50 phr to TiO_2/NR . Furthermore, the actuated strain (transversal direction) of the sample doped DOP 50 phr presents approximately 5 times higher than the pure counterpart operated under alternative electric field $40V/\mu m$, 33Hz.

2.3 Terpolymer Composites for Electronic Applications Perspectives

Focusing on the terpolymer composite presented in Figure 6, several advantages considering the electrical conductivity regime can serve with various electronic applications. In this work, we investigate two types of terpolymer composite; (1) a terpolymer filled with carbon black composite, and (2) a plasticized terpolymer which will be discussed in the next chapter.

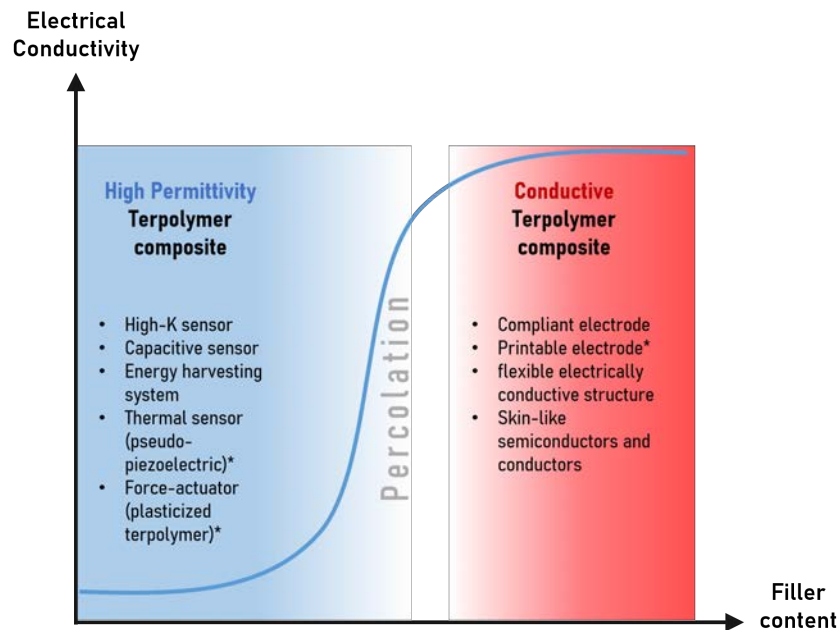


Figure 6 The tradeoff between high permittivity and conductivity of a terpolymer composite permits its development and optimization into various electronic applications (sensors & actuators)^[2,5,33,97,98]. This thesis will concentrate on the terpolymer composite actuators and conductivity issues.

3. Multilayer Actuator Approach

The optimization and improvement of a dedicated EAPs by increasing dielectric permittivity, reducing losses, as well as improving dielectric breakdown strength have been carried on in material properties development. Alternatively, a mitigation approach towards dedicated and improved EAPs can be the multilayer-actuator-assembly^[99]. Several investigations have been realized in the multilayer topologies for actuator applications to achieve a low driven voltage, low dissipation factor, low leakage current, high dielectric breakdown strength, high mechanical response, and high energy density^[100-103]. Multilayer topologically-structured actuator demonstrates a number of advantages over conventional materials and other actuator systems. Such advantages place the multilayer piezoelectric actuator developments as a crucial technology to several applications: bi-stable MEMS switches^[59], ultrasonic drills, and stacked ultrasonic transducers^[104,105], and piezoelectric stack actuator for fuel injector^[106]. Also, note that nowadays the EAPs

multilayer is a key technology on the development of smart materials for sensor-actuator applications. Such a high activation field ($\sim 100\text{V}/\mu\text{m}$) is still required to produce large strain for the EAP actuator^[25] as well as long term stability (thermal stability, humidity system, and breakdown probability), costs and toxicity.

The structure of multilayer actuators^[102] is typically designed by connecting EAPs electrically in parallel as a stack of n -layers. The particular interest of multilayer stack-topologically-structured development is its low cost, simple component fabrication (one-dimensional assembly), and low voltage supplies needed^[102]. The technique, layer-by-layer (LbL) assembly of polyethylenimine (PEI)/poly(acrylic acid) (PEI-PAA), and polyurethane (PU)/poly(acrylic acid) (PU-PAA) has been used for a vapor-driven multilayer polymer actuator^[107]. A film capacitor fabricated through layer-by-layer of PVDF/P(VDF-TrFE-CTFE)/PVDF composites was able to reach a dielectric constant of 18.61 for a sandwich-structure^[108]. Also, DEAP-based multilayer stack-actuators have been developed for a novel automated actuator manufacturing process to maximize the force or absolute deformation^[101] as shown in Figure 7 which illustrates the multilayer actuator applications and designs: piezoelectric bi-stable membranes and MEMS, and the DEAP automated multilayers.

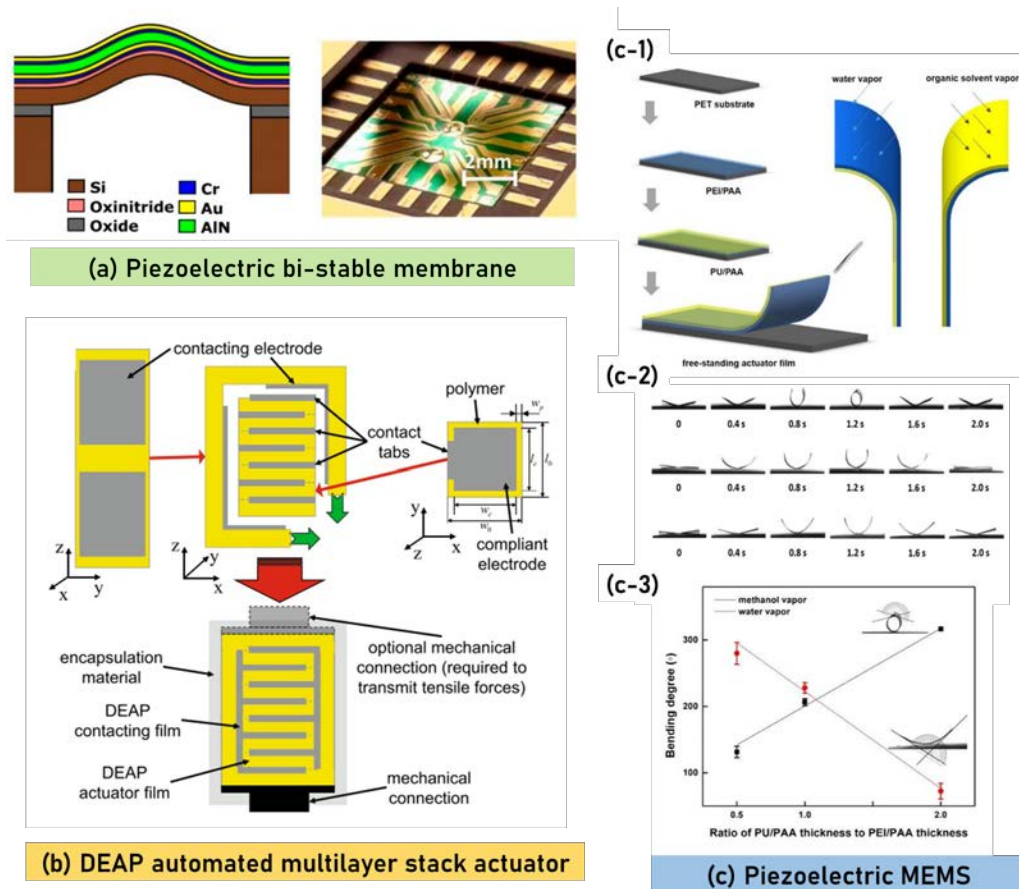


Figure 7 Multilayer actuator applications and designs; (a) bi-stable design using silicone membrane with aluminum nitride (AlN) piezoelectric layer, (b) multilayer stack-actuator schematic made from dielectric electroactive polymers (DEAP), and (c) Piezoelectric microelectromechanical systems (MEMS): (c-1) free-standing (PEI/PAA)/(PU/PAA) multilayer actuator membranes, (c-2) actuation cycles with regular pulses 40Vpp and (c-3) bending curvature versus PU/PAA: PEI/PAA thickness ratio in water and methanol.

EAPs Actuators and Sensors to Control Precise Optical Surfaces - Live-Mirror Project

Optical communication and remote sensing, including astronomy, are currently limited by the cost and manufacturability of their high-quality large optics. Innovations that decrease the cost or allow larger mirrors may greatly improve high-bandwidth communication, civil space surveillance technologies, wireless optical communication systems (UV and free-space systems), hyper-aperture multi-mirror structures, geo-engineering (space-mirror) and astronomical systems^[109,110].

Recently, we have proposed a new concept of a dedicated telescope to achieve high-contrast observations: The Exo-Life Finder (ELF) Telescope^[8-10]. Such an optical system will be limited by the cost and manufacturability of large mirrors. The mitigation here is to replace classical rigid, heavy and expensive optical mirrors with “live” and inexpensive light dynamic optoelectronic systems consisting of a thin optical glass sheet actively “live” supported by many degree-of-freedom force actuators /sensors integrated and miniaturized via additive manufacturing and 3D printing (Live-Mirror Project)^[29].

Such optical surface, supported and sensed via the EAP^[8,16] force actuators-sensors, is developed in this work in order to achieve active mirror surface shape control. EAP force active-actuators, integrated into the mirror structure allows correcting the mirror shape with a continuous actuator force distribution. This novel approach will extend conventional active mirror technologies to larger smooth optical surfaces without abrasive polishing. This means that it will be possible to create precisely-shaped low scattered-light mirrors - suitable for astronomical applications - faster and at lower production costs. Our long-term vision for the new technology is to decrease the mass density (and cost) of mirrors by an order of magnitude.

Figure 8 models how EAPs work, as elastic electromechanical deforming spring. This “electrical polishing” can correct surface shape errors that would be conventionally removed by abrasive grinding. To achieve high optical mirror quality surfaces with thickness of a few mms, the EAP glass deformation must have a dynamic range of a few microns corresponding to actuator forces of about 1N (overall high-level specifications to Live-Mirror). The technique we propose could potentially be achieved using only additive manufacturing via 3D-Printing technology, as presented in chapter 5.

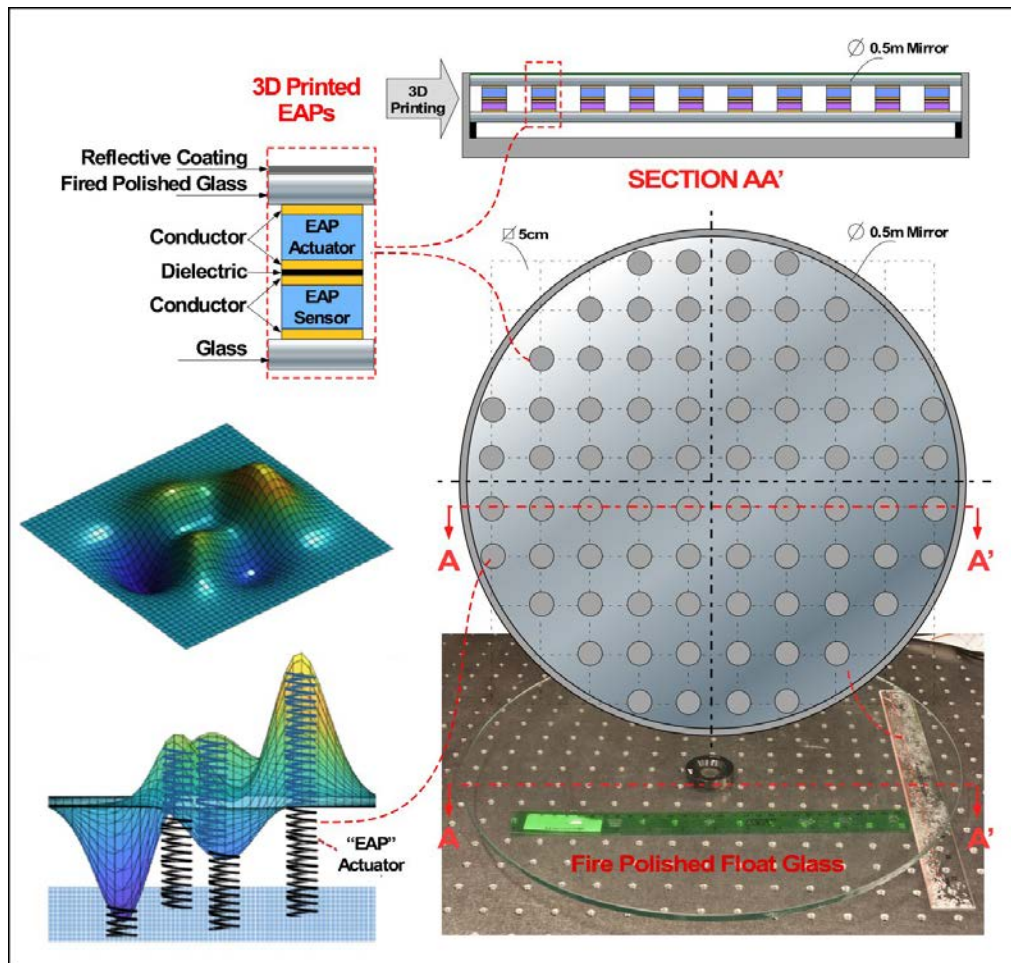


Figure 8 (Left–Bottom): A simulated warpable glass surface and the surface force correction mechanism: the surface roughness is controlled by the electromechanical activity generated in each “EAP–spring” actuator. (Right): A design for the hybrid structure Live–Mirror a sandwich of warpable surfaces separated by a lattice of variable force EAP actuators in series with force EAP sensors. The upper surface (fired polished glass) is called the control surface and the lower surface (glass) is the reaction surface. The static force of each force EAP sensor is controllable and determined by independent metrology of the top surface shape. This particular sensor–actuator geometry assumes preliminarily only vertical (gravity) external force components with assumed lateral material stiffness of the actuators. Section AA’ – The 1/2 meter Live–Mirror prototype using the additive manufacturing via 3D Printing technology is in development to fulfill the miniaturized requirements: each individual sensor–actuator system must fit into a circle of less than 5 cm diameter (pitch).

We aim to present the Live–Mirror concept using EAP as a force–sensor actuator to accomplish an active optics device for the ELF telescope. We evaluate different polymers from EAP–based actuator basic properties in

order to test their electromechanical performance suit for Live-mirror prototypes. Future work will explore how EAP sensors can be integrated into mirror systems. Indeed, the excellent actuation ability of the modified terpolymer opens the track for future generations for various actuator applications. In the end, such novel interdisciplinary R&D introduced the novelty hybrid dynamic live-optical surface strategy^[8,10,11] and forwards the advancement to the next frontiers of science and technology to replace stiff and heavy abrasive glass allowing to reduce complexity cost scaling of conventional optical telescopes.

Summary

In chapter 1, we have built up interdisciplinary research between materials science engineering (smart material optimization) and astrophysics (deformed optical surfaces for active mirrors) technology. By introducing the novel concept on how to exploit EAPs applied as active actuators, we presented the possibility to control and deform precise optical surfaces with an open range of applications. Moreover, the number of actuator and sensor applications including the development of technologies were reviewed within this chapter for acquiring the material best suited to achieve the requirements of a given application. We believe that the feasibility of using advanced EAP which has an excellent performance in mechanical actuation potentially will dedicate the next generation mirrors.

CHAPTER 2

Material Elaborations and Characterizations

CHAPTER 2

II. Material Elaborations and Characterizations

Material Elaborations

In general, polymer thin films are obtained by the solution casting method which is the oldest technology being developed over a hundred years for polymer thin film manufacturing^[111]. We summarize in this chapter the thin film preparation that we have developed in this thesis. All materials and tools used in this work are described in the following subsections.

1. Materials and Tools

Materials

- Terpolymer commercial powder from Piezotech S.A.S (Arkema)
 - P(VDF-TrFE-CTFE) (61.7/27.4/11.4): terpolymer/CB composite for high permittivity EAP
 - P(VDF-TrFE-CTFE) (65-69/21-27/8-9): terpolymer/CB composite for conductive EAP composite
 - P(VDF-TrFE-CFE) (65-69/21.5-27.5/7.5-9.5): terpolymer/plasticizer composite for EAP actuator
- Butanone or methyl ethyl ketone (MEK) purchased from VWR
- Carbon black (CB) nanoparticles (Vulcan XC72R) with diameter ~30 nm from the Cabot Corporation
- Plasticizer agents from Sigma Aldrich
 - Diisononyl phthalate (DINP)
 - Adipic acid di(2-ethylhexyl) ester (DOA)

Tools

- Doctor Blade™, a trademark of Elcometer;

- Mechanical Comparator (FLORENZA THYEZ, France) in 0.001 μm order;
- Cressington Sputter Coater (208 HR);
- Ultrasonic processor UP400S (400 watts, 24kHz) from Hielscher;
- Hot-Press;
- Hyrel 3D printer model System 30M;
- Wave generator (Agilent 33220A);
- Trek high-voltage amplifier 20/20C;
- Force sensor LC102-TC-10N Doerler Mesures.
- 3M™ anisotropic Z-axis electrical conductivity adhesive tape
- Capacitive sensor- Fogale nanotech, sensitivity 0.1mm/1V

2. Thin Film Preparation

The uniform film thickness is a crucial process obtained from the stable polymer solution, i.e. well-soluble polymer in the used solvent and homogeneous dispersion of the material composite preparation. Because of the terpolymer we use constitutes in a class of fluorinated polymer which is a highly non-reactive thermoplastic fluoropolymer. The fluoropolymers are soluble in aprotic polar solvents^[112]. In the case of solution-based processing, typical solvents used to dissolve the fluoropolymer are as follows; Dimethylformamide (DMF), N-Methyl-2-pyrrolidone (NMP), triethyl phosphate (TEP), Dimethylacetamide (DMAc or DMA), and Methyl ethyl ketone (MEK). Considering the health hazard, MEK is less toxic than other members of this class, i.e. exposure would irritate with only minor residual injury, which will reduce the risk with safety solvent exposure especially in 3D printing polymer manufacturing. Hence, the terpolymer thin film preparation developed in this work is obtained by terpolymer/MEK solution-based.

Figure 9 illustrates the flowchart explaining the thin film preparation methods, required conditions, and techniques to fabricate an optimized terpolymer film as well as its composite of plasticizer agent and carbon black (CB) nanoparticles. From the flowchart illustration, we can divide the preparation process into two main groups; (i) pure terpolymer, and (ii) terpolymer composites which are detailed as follows. Note that all the solvent mixtures are prepared in terms of weight ratios (w/w).

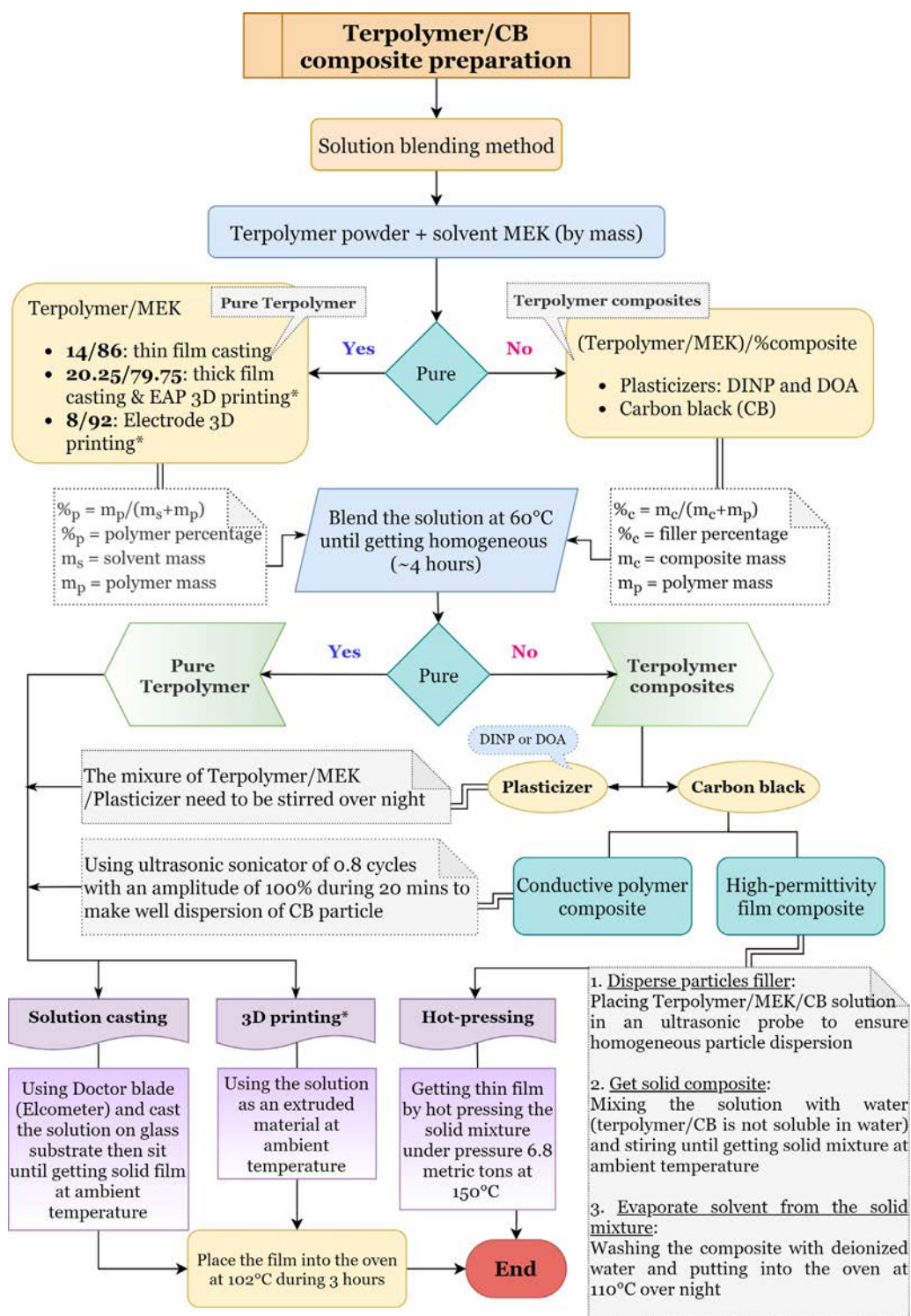


Figure 9 The flowchart for the thin film preparation methods, required conditions, and techniques to fabricate an optimized EAP Terpolymer and its composites.

2.1 Pure Terpolymer Preparation

Terpolymer, P(VDF-TrFE-CFE/CTFE), the powder is dissolved in MEK solvent. The polymer concentration is prepared dependent on the final product requirement (Figure 9), e.g. thin film thickness $\leq 100 \mu\text{m}$, terpolymer solution-based for 3D printing, etc. The solvent mixture was stirred at 60°C with a magnetic stirrer in a tightly closed glass bottle until getting a homogeneous solution ($\sim 2-4$ hours). Then, the mixed terpolymer/MEK solution is ready to proceed as a pure terpolymer film using the casting method and 3D printing technique.

- (1) **Film casting method:** the mixture solution is poured directly on the glass substrate and then spread out with Doctor Blade along with a desire thickness pre-calibration. This casted polymer layer will be pre-drying in room temperature around 2-4 hours then it will be removed and placed in the oven at 102°C within 3 hours to be fully evaporated a residual solvent within the polymer matrix. An additional technique to avoid an unremovable film sticking on the glass is to precoat the glass substrate with a very thin layer of the mixing 8wt% egg lecithin in MEK. The egg lecithin has a lubricant property that used to reduce friction between surfaces in mutual contact.
- (2) **3D printing thin-film fabrication:** Similar preparation processes to the casting method, we use the material extrusion technique to eject the mixture solution into a required shape. The sample will then be pre-dried and evaporated solvent in the oven. More details of 3D polymer manufacturing will be described in chapter 5.

Besides the pure terpolymer film preparation, the pure mixture solvent is also used to continue the proceedings of terpolymer composite preparation.

2.2 Terpolymer Composite Preparation

The continuation of pure terpolymer/MEK mixture is to process terpolymer composites. In this work, we introduce two filler composites mixing to pure terpolymer; (1) plasticizers-DINP & DOA, and (2) CB nanoparticles. The blending material processes are described as follows:

- (1) **Plasticized terpolymer:** the mixture pure terpolymer/MEK solution is directly added plasticizer agents, DINP or DOA, and continued stirring

overnight (~12–15 hours). This composite mixture will be kept at 4° C for thin–film casting and/or 3D printing film fabrication.

- (2) **Terpolymer/CB composite:** The pure terpolymer mixture is used again as a solution–based, then CB particle will be carefully added into the solution. Because CB particles have a high surface tension energy which leads to agglomeration and phase separation from the polymer matrix^[89]. Indeed, the terpolymer/CB mixture solution requires an ultrasonic probe to get well particle dispersion within the polymer matrix. There are two different purposes of terpolymer/CB composite investigation;

- i. *High- k terpolymer composite:* (CB ≤ 4wt%) The terpolymer/CB solution will be freezing the dispersion of CB particle in the solution by immediately changing from a liquid to a solid mixture to avoid the agglomeration issue. This solid mixture can be obtained by mixing the composite solution directly into deionized water then will be evaporated the MEK solvent in the oven. The thin–film composite is prepared by hot–pressing machine pressing through the solid mixture.
- ii. *Electrically conductive terpolymer composite:* (CB ≥ 4wt%) After mixing CB nanoparticles using an ultrasonic probe, the composite mixture will be ready for thin–film casting and/or 3D printing film fabrication.

3. Material Characterization Techniques

Terpolymer thin film test samples were prepared their electrodes by a gold sputtering technique. The designed electrode has a circular shape to acquire homogenous repartition of an external load that was applied in an experimental test bench. Samples were sputtered with 25nm gold electrodes on both sides using a Cressington Sputter Coater (208 HR). For the electrical properties characterizations, broadband dielectric spectroscopy, and breakdown electric field strength, all the samples were prepared with gold electrodes diameter 8mm both sides (top and bottom) as shown in Figure 10a. Subsequently, the mechanical and electromechanical characterizations have different specimen configurations as described below.

Considering the actuator performances by electromechanical features, the procedures of performing EAP actuator potential followed the suggestions of:

1. The Broadband Dielectric Spectroscopy (BDS) was presented with dielectric permittivity; permittivity real part (ϵ') and loss tangent ($\tan\delta$) in relation to various frequencies, and electrical conductivity (σ) for conductive terpolymer composite. The measurement was handled throughout sweep frequencies from 50 mHz to 1 MHz under a low applied electric field of $1V_{AC}$ at ambient temperature;
2. The mechanical property expressed as the Young modulus (Y) was measured under dynamic stretching at a frequency of 0.1 Hz. Tensile specimen size of $1\text{ cm} \times 4\text{ cm}$ was fixed between a metal holder and a force sensor;
3. The dielectric breakdown probability of plasticized terpolymer films was examined using a DC ramp waveform at a rate of 500 V/s. The breakdown measurement setup consists of a wave generator and a high-voltage amplifier;
4. The electromechanical characterization was set up with the above (item 3) high-voltage amplifier and the waveform generator. The longitudinal strain (S_{33}) of samples with gold electrode coating diameter 20 mm (Figure 10b) was measured using a non-contact capacitive sensor with a 10nm precision. The experimental bench will be described in detail in CHAPTER 3.

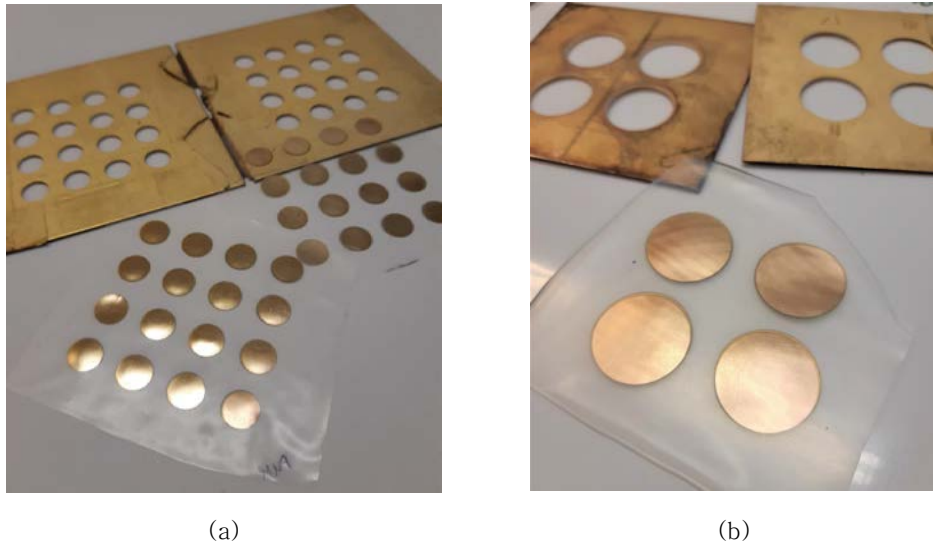


Figure 10 Samples preparation with gold electrode sputtering both sides (top&bottom) (a) for the electrical characterizations with gold electrodes with a diameter of 8mm and (b) for the electromechanical characterization with gold electrodes with a diameter of 20mm.

Material Characterization: Results & Discussions

1. Electrostrictive Material Models

The application of EAP as an actuator had been limited due to its failure to provide sufficiently large deformation and/or stronger force. Promising developments incorporating a plasticizer into an EAP matrix improves radically its strain response and mechanical energy density^[15,34]. Such a chemical modification leads to large dipolar interfacial effects within the polymer matrix – a contribution of charge trapping between amorphous and crystalline phases – resulting in the increase of dielectric permittivity and simultaneously in the decrease of the Young modulus.

In the case of a dielectric polymer, the electrostrictive strain can be generated under the electric field attributed to dipolar orientation within the

material (Maxwell forces). Such electrostriction contributes to the quadratic coupling of strain and polarization. The strain is proportional to a square of electric field or polarization which can be observed in all materials with crystalline symmetry [36]. Besides, it is known that induced strain by an external electric field mainly originates from electrostrictive strain (S_E), which depends on the interaction of dipole moments within dielectric materials and strain generated by Maxwell stress (S_M) result from the interaction of free charges between the electrode and/or Coulomb interaction^[41]. Therefore, the overall strain is thus given by

$$S = S_E + S_M = ME^2 \quad (1)$$

where M is the global electrostrictive coefficient and E is an external electric field. In the longitudinal direction, the compressive strain S_{33} under a given electric field can be expressed as:

$$S_{33} = M_{33}E_3^2 + s^E T_3 \quad (2)$$

$$M_{33} \propto \frac{\varepsilon' \varepsilon_0}{Y} \quad (3)$$

where s^E is compliance of material (the inverse of the Young modulus) and T_3 is the stress generated by applying the electric field. Regarding Eqs. (1)–(3), the strain can be improved by simultaneously increasing permittivity and reducing Young modulus. It is possible to apply a high electric field but this parameter is however limited by dielectric breakdown strength and dipolar saturation of material. As reported on [15], the figure of merit (FOM) of the strain can be defined by:

$$FOM_{\text{strain}} = \frac{\varepsilon' \varepsilon_0}{Y} \quad (4)$$

In the longitudinal case when $S_{33} = 0$ yields to stress T_3 :

$$T_3 = YM_{33}E^2 \quad (5)$$

Combining Eqs. (3)–(5), results that it is possible to induce the FOM of the blocking force for a given electric field:

$$FOM_{\text{force}} = \varepsilon' \varepsilon_0 \quad (6)$$

The above Eqs. (4) and (6) demonstrate that the mechanical strain and the blocking force under low electric field can be simultaneously enhanced by increasing the polymer dielectric permittivity. Considering a better electromechanical coupling, especially in low-frequency actuator applications, a decrease of the Young modulus should be involved but it must be limited in order not to change the elasticity or the compliance of the materials drastically.

2. Terpolymer Filled Carbon Black Composite

In this research, we carried out the development of material composites utilizing carbon black nanoparticles as composite fillers (0D). Thanks to its cost-effective, easy to form the conducting network under a low loading, high conductivity, and high surface-area-to-volume ratio, carbon black nanoparticles (CBNPs) have been widely introduced to electroactive polymer matrices to improve the electroactivity performance of the hosting polymer.

2.1 High Permittivity Terpolymer/Carbon Black Composite

In the field of small energy conversion under heat surroundings, using polymers with high electroactive response has been of significant interest in the development of stimuli-responsive systems for performance materials. Particularly, relaxor ferroelectric polymers known as terpolymer have remarkable sensory smart structures and high electrostrictive strain^[72,78]. Thanks to their conformability, small thickness allowing better heat exchange, flexibility, low density, and high dielectric breakdown strength offer several key components for actuators and sensors development.

Terpolymer P(VDF-TrFE-CTFE) has been investigated^[33] for thermal energy conversion through the analysis of its dielectric response and the effect of temperature on its electric polarization. The purpose of this task is to develop and study new composites based on such materials to enhance their high permittivity terpolymer/CB composite. More specifically focusing on the effect of temperature on the dielectric response – in order to achieve a larger electrothermal response – the terpolymer was filled with carbon black nanoparticles in varied concentrations fabricated by the solution blending method as aforementioned in Material Elaborations section, page 67. This novel composite has shown potential in the development of thermal energy harvesting and micro-energy storage systems.

a. Dielectric Permittivity

The electrical characterization was presented in Figure 11 with dielectric broadband spectroscopy of dielectric permittivity real part (ϵ') and loss tangent ($\tan \delta$) in relation to various frequencies. Figure 11a shows the

relation between real dielectric permittivity and frequency of terpolymer film and composite films at room temperature. Note here that the dielectric constant of the samples increased along with the increase of CB contents. The film with 4 % of CB by mass gave the highest dielectric constant (over 250), however, its loss tangent (Figure 11b) was significantly higher than any other samples. Such results can be explained by interfacial polarization from conductive particles in the polymer matrix, with a small amount of energy being stored in the high dielectric filler phase affecting the increase of the net electric field in the polymer matrix. In any case of doping conductive nanoparticle in polymer, it produces defect density and breakdown path through aggregated fillers resulting in high dielectric loss and low dielectric strength^[98].

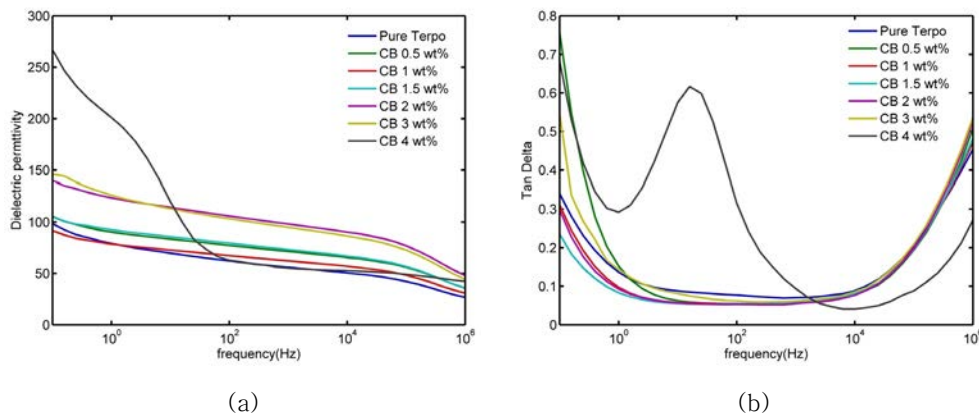


Figure 11 Experimental measurements of the dielectric permittivity (a) and the dielectric loss (b) of a terpolymer and its composites under applied bias voltage 1 Vpp. Measurement was handled throughout sweep frequencies Solartron 1260 impedance – analyzer from 0.1 Hz to 1 MHz under a low applied electric field of 1VAC at ambient temperature.

b. Electrothermal Coupling Concept (*Pseudo-pyroelectric*)

The conceptual and theoretical background between thermal and electrical domains for the considered materials (i.e., dielectric electrostrictive polymers) is described in this section. The model is based on the mean dipole orientation that is influenced by both the electrical field and temperature through thermal agitation. When an electric field is applied to the material, electric dipoles start aligning, therefore inducing polarization and charges appearing on the surface (Figure 12 (b)). Increasing the temperature introduces some disarrangement in the dipole alignment as demonstrated in

(Figure 12 (c)). The immediate disorderliness of electric dipoles leads to decreased polarization and surface charges for the same applied electric field. These phenomena showing the temperature–dependence of the polarization and surface charges allow using the material as a pseudo–pyroelectric element.

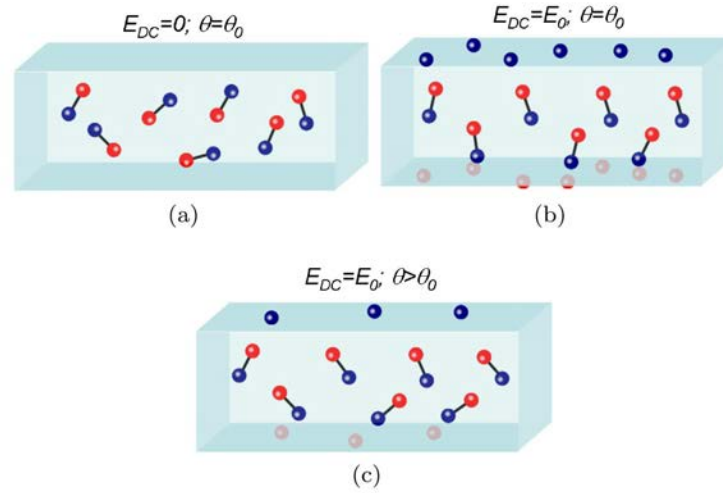


Figure 12 The pseudo–pyroelectric working principles: (a) dielectric material with randomly dipole arrangement (zero mean polarization) when no applying electric field; (b) a polarization appears as an electric field is applied; (c) when the temperature increases, the thermal agitation of dipoles leads to a decrease of the mean polarization, as the required energy to overcome the thermal agitation increases^[33].

The increase in temperature will play a role in the dipole alignment which leads to a decrease of both the surface charge density and the polarization. It is well known^[33,72] that according to the Boltzmann statistics and the Debye/Langevin formalism, the polarization within the material matrix – assuming that the material has one dominant phase– is expressed by;

$$P = N(\theta)\mu \left[\coth\left(\frac{\mu E}{k_B \theta}\right) - \frac{k_B \theta}{\mu E} \right] \quad (7)$$

where P is the polarization of the material, θ is the temperature, $N(\theta)$ is the temperature–dependent dipole density, μ is the dipole moment, k_B is Boltzmann’ s constant, and E is an applied electric field. Considering that the material does not experience any phase transition in the temperature working range. The variation of polarization with respect to temperature under a constant applied electric field (E_0) can be expressed as the pseudo–pyroelectric coefficient (p) as follow;

$$p = \left. \frac{\partial P}{\partial \theta} \right|_{E_0} \approx -\frac{N\mu^2}{3k_B\theta^2} E_0 = -\frac{\chi_0\theta_0}{\theta^2} E_0 \quad (8)$$

which at low electric field operation, the pseudo-pyroelectric coefficient can be simplified using dielectric susceptibility (χ_0) and working temperature (θ_0).

c. Terpolymer CB Composites Polarization and Temperature Effects

Polarization measurements of terpolymer thin films in various percentages of CB filler (Figure 13) reveal that: (i) polarization of terpolymer and its composites indicates P–E loop which has remnant polarization nearly zero represented as the relaxor ferroelectric behavior^[98,113] and (ii) terpolymer with a higher percentage of CB provided the greater polarization. As mentioned above, a high CB fraction in terpolymer leads to low dielectric strength. It is denoted that the sample can become conductive or broken during the measurement process.

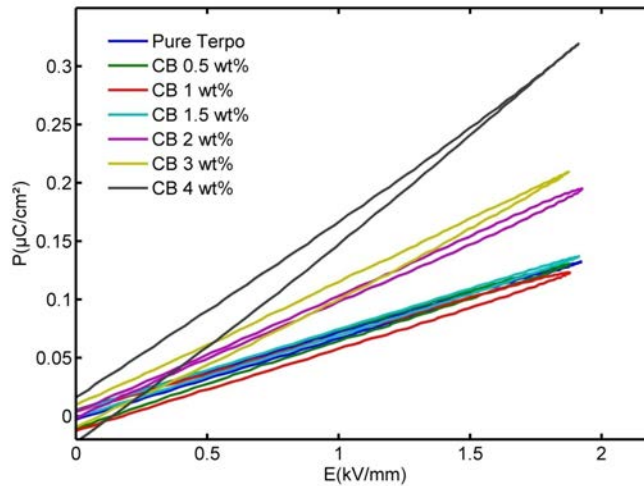


Figure 13 Polarization measurements polarization of terpolymer thin films in various percentages of CB filler under $E_{max} = 2 \text{ kV/mm}$ at room temperature.

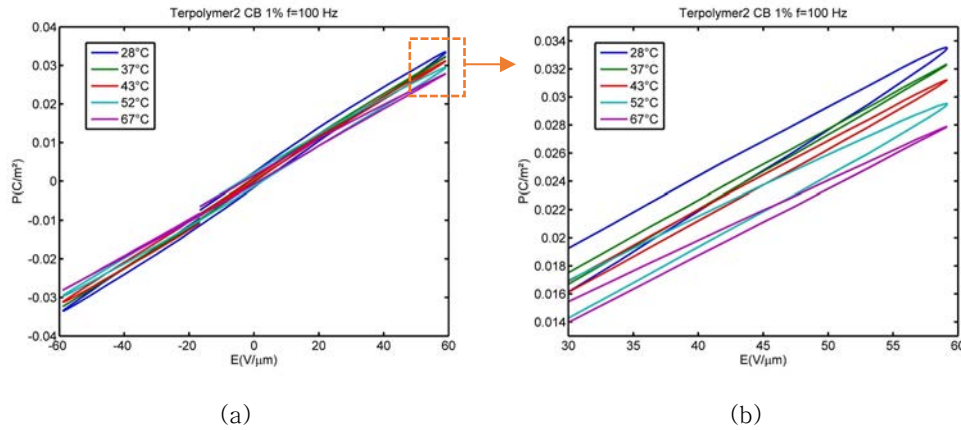


Figure 14 Polarization of terpolymer doped 2wt% carbon black as a function of an applied electric field for five different temperatures: (a) the hysteresis loop under bias voltage is applied and (b) the zoom into the part of maximum polarization represented the diminution of polarization while temperature increase. The polarization versus with temperature was measured by the following set up: (i) the sample was soaked in a silicone oil bath and high voltage was applied by an amplifier driven by waveform generator; (ii) the temperature of the sample was controlled via test chamber device; (iii) following voltage application and warming up, the generated current was measured by a low noise current preamplifier connected to an oscilloscope.

Because of its good trade-off between dielectric strength and dielectric response, the polarization of terpolymer with 2 wt% CB was measured for five different temperatures under a maximal applied electric field of 60 $\text{V}/\mu\text{m}$ (Figure 14). These results confirm the dependence of the polarization with temperature, the latter showing lower values as the temperature is increasing. Such a dependence temperature versus polarization can be attributed to both permanent dipole moments and ion displacement ability to rearrange under the electric field at high temperature.

The evaluation of the pseudo-pyroelectric coefficient regarding Eqs. (7) and (8) correlating to experimental polarization measurement ($\chi_0 = 63\epsilon_0$ and $\theta_0 = 301\text{K}$) can reach up to $-80 \mu\text{C}/\text{m}^2\text{K}$ under bias applied electric field 60 $\text{V}/\mu\text{m}$. Hence, because of this change in the polarization at the constant electric field for varying temperature, applying a bias voltage to the sample would allow electrothermal conversion and thus energy harvesting potentials.

Ultimately, this study of the relationship between polarization and electrical field for varying temperatures would yield a low-cost yet efficient way for converting energy from the thermal domain into electricity. However, to use terpolymer/CB composite as actuator applications, it probably will not be the most appropriate choice because of the limitation of applied voltages due

to its low dielectric breakdown strength. Hence, terpolymers/CB composite with high permittivity will be an attractive alternative for serving as a thermal sensor or thermal energy harvesting applications under high effective electrothermal conversion. On the other hand, this polymer composite is available for use as the conductive polymer composite which will be discussed in the following section.

2.2 Conductive Terpolymer/Carbon Black Composite

Electrically conductive polymers and composites have been widely developed and studied in favor of growing usage in flexible electronic devices. With their electrical conductivity in the range of semiconductor materials (see Figure 15), conductive polymers field has overcome the conventional polymer properties and highly compliant comparing to metals. Two main types of conductive polymers ^[30] are:

- (1) Intrinsic conductive polymers (ICPs) – known as conjugated polymers and synthetic metals, e.g., polyaniline (PANI), polypyrrole (PPy), poly(3,4-ethylenedioxythiophene) (PEDOT) and;
- (2) Extrinsic conductive polymers (ECPs) - conductive polymer composites achieved by blending conductive fillers into a polymer matrix, e.g., carbon black (CB), carbon nanotubes (CNTs), metal powders (ITO, AZO) and ICPs.

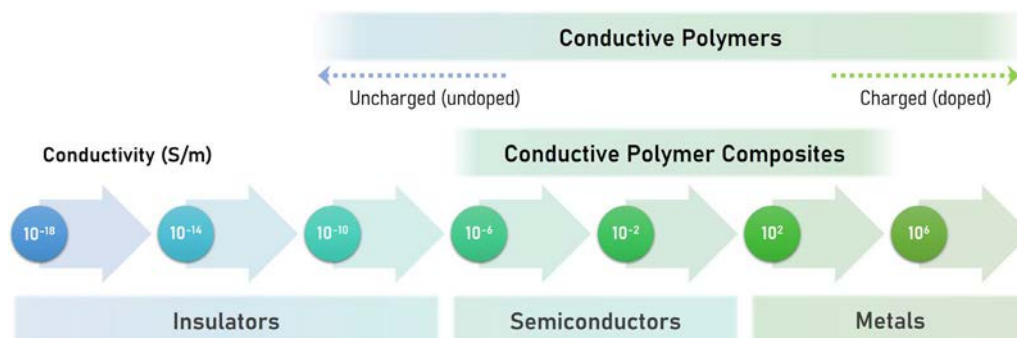


Figure 15 The comparison of conductivity range between conductive polymers composites with insulators, semiconductors, and metals (reproduced from ^[30]). Note that its conductivity is in the range of semiconductor materials.

Despite the fact that ICPs or ECPs have lower conductivities than metallic materials, there are many advantages using ICPs or ECPs as conductive materials. Thanks to their flexibility, low cost, non-fragility, light-weight, and biocompatibility lead many researchers to carry forward the development of their electrical conductivities for flexible actuator and sensor applications. There have been numerous studies to investigate ICPs or ECPs for compliant electronic devices, such as:

- A stretchable scaffold made from an intrinsically synthesizing PEDOT:PSS was described to develop soft and skin-like semiconductors and conductors ^[76];
- Evoprene™ compounds have been used for polymer host filled with carbon black powder to be a smart flexible sensor ^[75];
- An elastomer ethylene vinyl acetate EVA doped with graphite and CNC-assisted was manipulated as a three-dimensional flexible electrically conductive structure for soft robotics applications ^[114].

In order to demonstrate the printability of such newly developed materials numerous parameters must be considered: compatibility between conductive inks and substrate or cooperative materials; wettability (substrate-polymer); surface bonding (polymer-polymer) and curing temperature. Those will play a crucial rule to optimize a full-printed actuator design – a driver goal concerning Live-Mirror development – including printed electrodes and printed EAP layers. Considering here that conductive polymer composite was selected to be our printed electrode, and using the same polymer host (based terpolymer) between an electrode and EAP actuator layer. Such a procedure reduces the complexity of ink preparation and avoids some material incompatibility issues.

Considering the performance of carbon black particle filler in terms of cost-effectivity; ease to form the conducting network under low loading; high conductivity and high surface-area-to-volume ratio; in this work, the fluorinated terpolymer P(VDF-TrFE-CTFE) (TP3) filled with carbon black powder (Vulcan XC72R) was used as a printable conductive polymer composite.

The characterization of terpolymer with CB fillers from 0% to 9% by mass, is hereafter presented:

a. Young Modulus

Measurements in the lab, confirm that the effect of using conductive particle fillers introduced to the polymer matrix leads to an increase in the elastic modulus of the material composite. Figure 16 exhibits an elastic modulus of terpolymer/CB composite, which significantly increase the proportion to the filler contents. Considering rigid filler and interphase between filler and matrix, these attributes lead to promote higher tensile strength of constituent material [115].

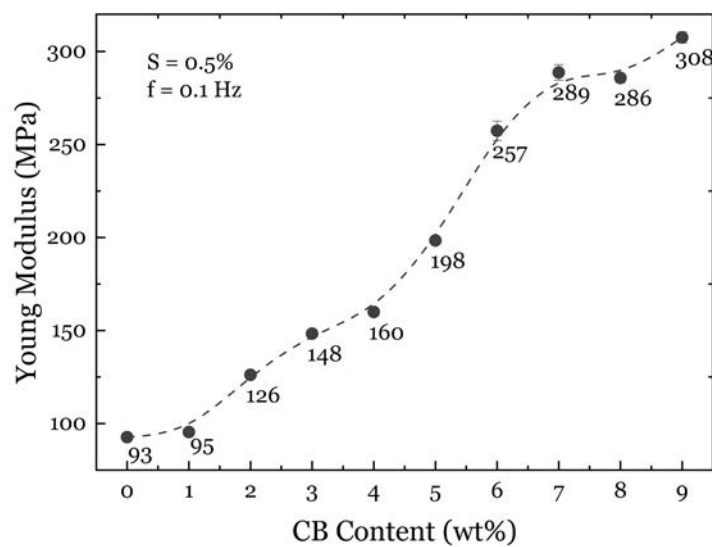


Figure 16 The Carbon Filler percentages on the mechanical property of the material (Young modulus) for the terpolymer (TP3) composite. The terpolymer/CB composited thin films ($1\text{ cm} \times 4\text{ cm}$) were prepared by solution casting method (Figure 7). The measurements were handled by fixing the tensile specimen between a metal holder and a force sensor LC102-TC-10N. The samples are stretched transversely with 0.5% of strain under frequency 0.1 Hz at room temperature.

b. Electrical conductivity

In dielectric materials, the process of electronic conduction is usually represented by a linear variation of admittance value (A), measured in Siemen (symbol S) defined as the reciprocal of impedance Z ($A=1/Z$) as a function of frequency. The electrical conductivities (conductivity: σ (S/m)) of conductive Terpolymer/CB composite with different weight fraction of CB particles is presented in Figure 17.

Frequency-dependent electrical conductivity observed in dielectric materials usually represents a linear slope close to 1. In the case of conductive materials, the electrical conductivity is independent of frequency. The electrical conductivity can be influenced by ohmic conduction (caused by the movement of mobile electrons in the conduction band and holes in the valence band: frequency-independent) and ionic conductivity (interfacial polarization or Maxwell - Wagner - Sillars polarization: at low frequency). Note, the linear relation of σ versus frequency on pure terpolymer and terpolymer filled with carbon black 1wt%. In higher CB contents (from 2 to 9 % by mass), the conductivity behaves independently with frequency until 10^4 Hz approximately. The following results (Figure 17) confirm that:

- *Pure and 1 % of CB*: the conductivity increases with frequency showing the typical dielectric material manifested by the universal dielectric response (UDR)^[116];
- *2 to 3 % of CB filler*: the composite becomes a conductive polymer composite with $\sigma \sim 10^{-4} - 10^{-1}$ S/m presenting heterogeneous mixtures of insulator-conductor behavior;
- *4 to 9% of CB filler*: the composite reaches percolation threshold demonstrating the frequency-independent nature of material composites and electrically conductive network within the polymer matrix.

According to the percolation model analysis for polymer composites, the sigmoidal-Boltzmann equation is well known to predict evidence of transition of an insulator to a conductor for conductive polymer-composite^[117]. Figure 18 confirms that the S-shaped is exhibited through the percolation threshold for all the composite systems, also the percolation model displayed a well-fitting curve to the experimental result. For example (Figure 18) at 5 wt% of CB filler, Terpolymer/CB ink reached the conductive region, which presented the conductivity of 0.57 ± 0.02 S/m. Above the percolation region (over 5% CB filler), the conductivity of Terpolymer/CB ink slightly dropped which can be assumed from CB particles generating a cluster of particle agglomeration. However, the percolation threshold depends on many factors, e.g., size, shape, dispersion, structure, volume, and conductivity of doped particles^[118]. This analysis found evidence for possibly using terpolymer/5wt% of CB filler as the printable electrode by reasons of great homogeneously dispersing in polymer host, sufficiently high electrical conductivity with a low percentage of doping filler.

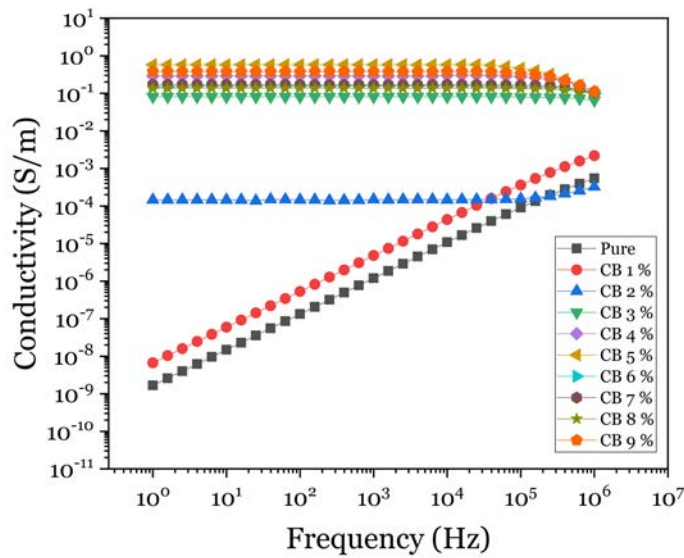


Figure 17 The electrical conductivity versus frequency for the terpolymer (TP3) filled with different carbon black contents. The terpolymer/MEK/CB solution was prepared by the solution blending method and CB particles got well-dispersed with an ultrasonic probe.

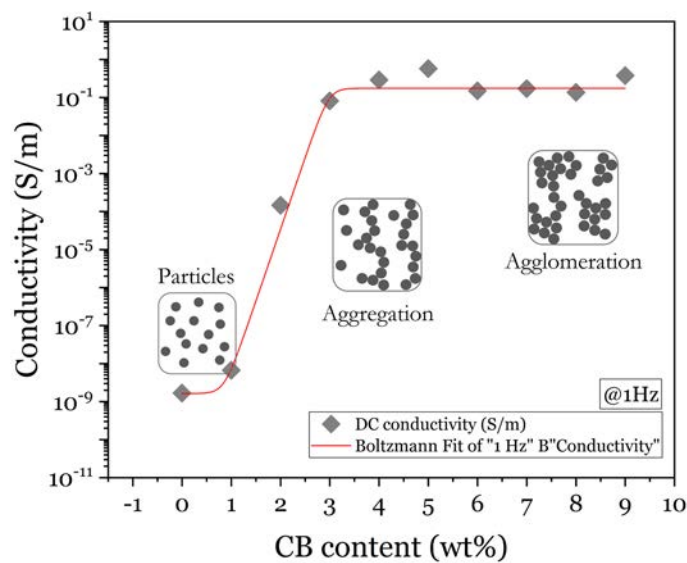


Figure 18 The electrical conductivity as a function of carbon black particle loading presented a site of percolation threshold for terpolymer (TP3) filled with carbon black particles.

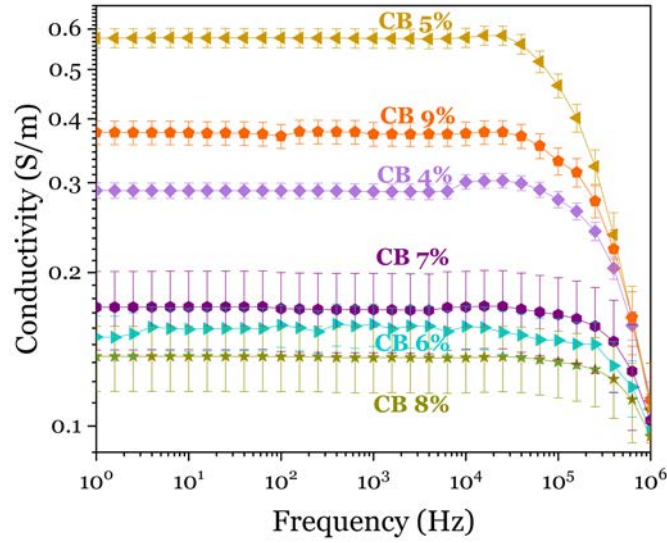


Figure 19 The electrical conductivity in the percolation region as a function of the electric field of terpolymer (TP3) filled with different carbon black loading from 4 to 9% by mass.

We observed the conductivity behavior of high CB fraction above the percolation regime (see Figure 19). The conductivity values lapse over a frequency of 10^4 Hz. The conductive terpolymer CB composite has heterogeneous phases of the polymer matrix and conductive particle. Thus, we can assume our terpolymer composite as a capacitive-like material modeled as RC parallel circuit^[119,120] (Figure 20). We determined admittance value: A based terpolymer doped CB above percolation region (doping $CB \geq 4\text{wt}\%$). As confirmed in Figure 20a, when the frequency of input voltage reaches to the high region (over 10^4 Hz), the admittance magnitude has a significant reduction corresponding to Eqs (12). Terpolymer doped with high CB concentration (4%–9% by mass), have their resistance and capacitance approximately between 2–10 ohms and 360 nF respectively with the film thickness of $64 \mu\text{m}$.

$$\frac{1}{z_{\text{total}}} = \frac{1}{z_{\text{R}}} + \frac{1}{z_{\text{C}}} \quad ; z_{\text{R}} = \text{Resistance and } z_{\text{C}} = \text{Reactance} \quad (9)$$

$$Z = \frac{R}{1 + j(2\pi f)RC} \quad (10)$$

$$|Z| = \frac{R}{\sqrt{1 - (2\pi fRC)^2}} \quad (11)$$

$$|A| = \frac{\sqrt{1 - (2\pi fRC)^2}}{R} \quad ; A = 1/Z \quad (12)$$

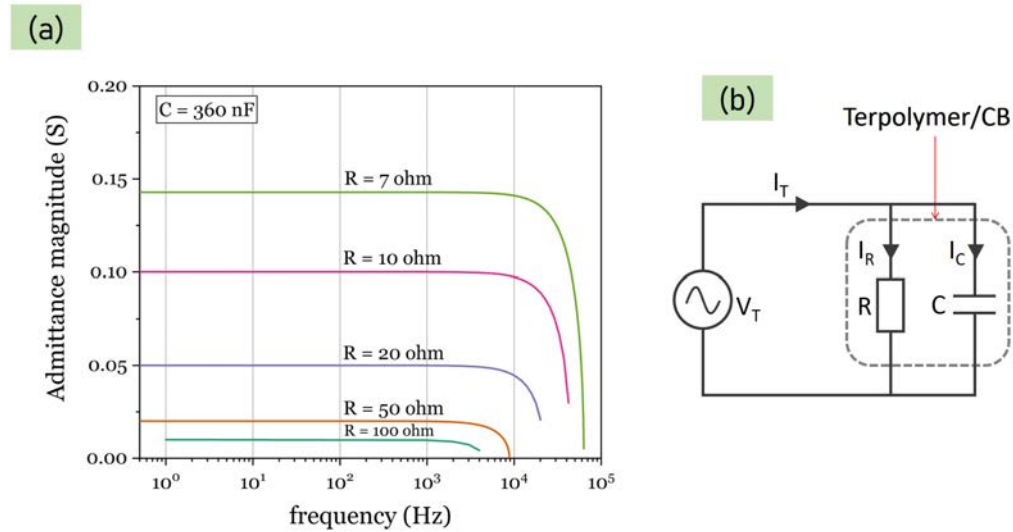


Figure 20 (a) The calculated admittance based on the RC parallel circuit as a function of frequency by the use of real capacitance and the real resistance value of terpolymer/CB composite and (b) parallel RC circuit reflected on terpolymer/CB composite.

Considering the admittance model according to Eq. (12), the cutting frequency under AC voltage is predominantly influenced by material resistance. Compare the cutting frequency given by experimental measurement (Figure 19) with respect to empirical modeling using Eq. (12) of the conductive sample above the percolation region (over 4 wt% of CB added). Both results showed an averagely cutting frequency of around 73 kHz presented in Figure 21. The unstable measured data of cutting frequency (Figure 19) conceivably affect by the agglomeration of CB particle which provides an inconsistent resistance value to the material composite.

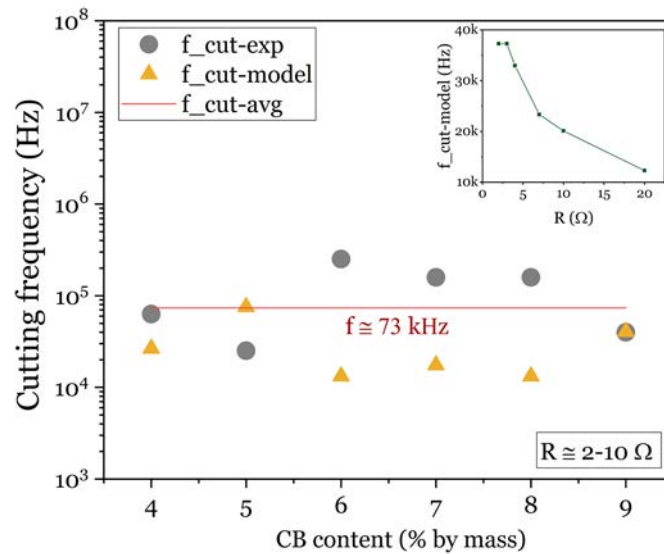


Figure 21 Cutting frequency under bias applied voltage of Terpolymer/CB above percolation region (over 4% by mass) carried out by experimental measurement; $f_{\text{cut-exp}}$, and evaluation model; $f_{\text{cut-model}}$. The small right-top graph presenting evaluated cutting frequency affected by an increase in material resistance.

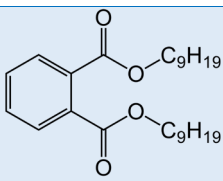
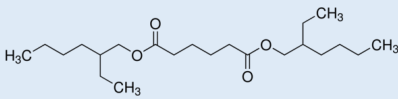
In this work, we focus on operating the polymer actuator at a low-frequency range (lower than 50 mHz), which will serve Live-Mirror application focusing on an active optic controlling system (no high bandwidth requirement). This means that the effect of the AC filter at a very high-frequency range could be neglected.

3. Plasticized Terpolymer for Soft Actuators Optimization

How to dope and to control a customized polymer? - The basic formulation of plasticizer substances attempts to decrease the attraction between the polymer chains improving its elasticity. Amongst several categories of plasticizers, the phthalates and adipate type comes out as the more compliant for the soft actuator applications. The phthalates and adipate are characterized by low volatility, water-resistant, inexpensive, and low acute toxicities^[12-14]. Their manufacturability relies on reacting phthalic anhydride with alcohols, which range from the methanol & ethanol (C_1/C_2) to the tridecyl alcohol (C_{13}), either as a straight chain and/or branching. In the end, two types

of plasticizers: (1) *Diisononyl phthalate (DINP)* and (2) *Dioctyl adipate (DOA)* were used to investigate an optimized plasticized terpolymer for force-actuator. Both plasticizers are more effective at stabilization and durability comparing with other low phthalates plasticizers^[13] as shown in Table 4.

Table 4 The general properties³ of *Diisononyl phthalate (DINP)* and *Dioctyl adipate (DOA)* plasticizers.

Plasticizer	DINP	DOA
Molecular structure		
Chemical formula	C ₂₆ H ₄₂ O ₄	C ₂₂ H ₄₂ O ₄
Plasticizer type	Phthalates	Adipates
Molar mass	418.61 g/mol	370.574 g/mol
Density	0.972 g/mL at 25 °C	0.925 g/mL at 20 °C
Boiling point	244 to 252 °C	175 °C/2 mmHg(lit.)
Melting point	-43 °C	-70 °C
Appearance	transparency, oily viscous liquid	transparency, oily liquid

In this work, the plasticizer molecules DINP and DOA were selected to dope the P(VDF-TrFE-CFE) terpolymer in order to achieve high mechanical deformation and high driven force operated through an externally applied electric field, as requested by an optimized soft actuator. The material composite electrical and mechanical characterizations are described below.

3.1 DINP and DOA Improving Terpolymer Electrical Properties

The electrical characterization was presented with dielectric broadband spectroscopy of dielectric permittivity real part (ϵ') and loss tangent ($\tan \delta$) in relation to various frequencies. The dielectric constant of the terpolymer significantly enhanced as a function of the plasticizer contents (DINP and

³ Information from SigmaAldrich

DOA). In such a way making the use of the high molecular weight and a liquid plasticizer agent can serve as the secondary phrase inside the polymer matrix. This means that there are an increase of the free volume and the distance between polymer chains consequently improving the charge mobility for the modified with respect to the pure terpolymer^[12].

The dielectric relaxation of plasticized terpolymer Figure 22, where $\text{Tan}\delta$ behavior confirms that the ionic conduction of polymer appears at low-frequency range, and its dissipation factors contain dipolar relaxation losses, ionic conductivity and interfacial phenomena^[34]. In particular, a terpolymer with higher plasticizer contents, both DINP and DOA, presents a shift of interfacial relaxation regime, e.g. the loss $\text{Tan}\delta$ versus frequency (Figure 22), toward higher frequency. Note the fact that plasticizer incorporates to the amorphous phase of the polymer matrix, the agent remains independently without attaching to the primary polymer chain^[12].

Both ionic conductivity and interfacial polarization of polymer composite doped with high plasticizer content may take less time to be completed its polarization^[12,34,71,121] as providing the shift of relaxation peak to a higher frequency (Figure 22). This prominent peak attribute superior charge mobility generated by larger amorphous domain in the terpolymer doped high plasticizer content. Also, the dielectric loss increased as a function of the plasticizer fraction, indicating that the loss of energy mostly depends on the defect sector (large free volume) and free charge attribution.

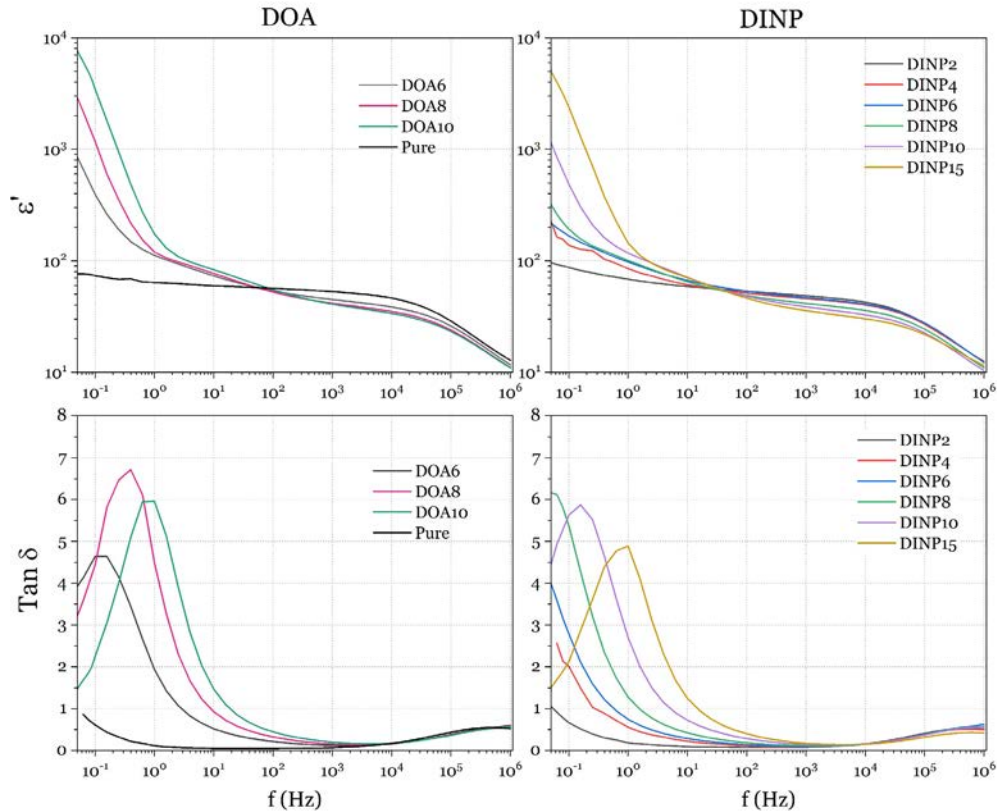


Figure 22 The dielectric broadband spectroscopy as a function of the frequency of terpolymer filled with plasticizer agents DOA and DINP. The measurement was handled throughout sweep frequencies Solartron 1260 impedance-analyzer from 50 mHz to 1 MHz under a low applied electric field of 1VAC at ambient temperature.

3.2 DINP and DOA Improving Terpolymer Mechanical Properties

The mechanical property defined as the Young modulus (Y) was measured under dynamic stretching at 0.1 Hz. Tensile specimen size of 1 cm \times 4 cm was fixed between a metal holder and a force sensor (Doerler Mesures LC102-TC-10N). The mechanical characterization of the samples through the measurements of Y (Figure 23) related to the electrostriction performance was presented in Eqs. (2) and (3). Note that Y decreases with increasing plasticizer fraction, particularly terpolymer filled with DOA content yielding lower Y with respect to terpolymer doped DINP (see Figure 23a). Based on the main characteristics of the plasticizer (in Table 4), plasticizers in the adipate group (DOA) have higher gelation and fusion temperature with respect to those in

the phthalate group (DINP); $T_m^{DOA} = -70^\circ \text{C} < T_m^{DINP} = -43^\circ \text{C}$, which can provide superior flexibility at low temperature^[12]. Note that the sample were at room temperature.

The plasticizer agent was usually used for reducing tensile strength and improving the flexibility of the polymer. Notably, with diisononyl phthalate (DINP), the short-chain of phthalate including polarizable benzene nucleus tends to provide great flexibility and faster fusion to polymer matrix with respect to other current industrial plasticizers^[12] while does not overthrow mechanical property of polymer host. In the end adding DINP agent leads to reduced Young modulus (see Figure 23b) and thus enhanced electromechanical coupling of EAP, but plasticizer filler quantity should be limited in order to neither create polymer failure nor deteriorate dielectric breakdown strength.

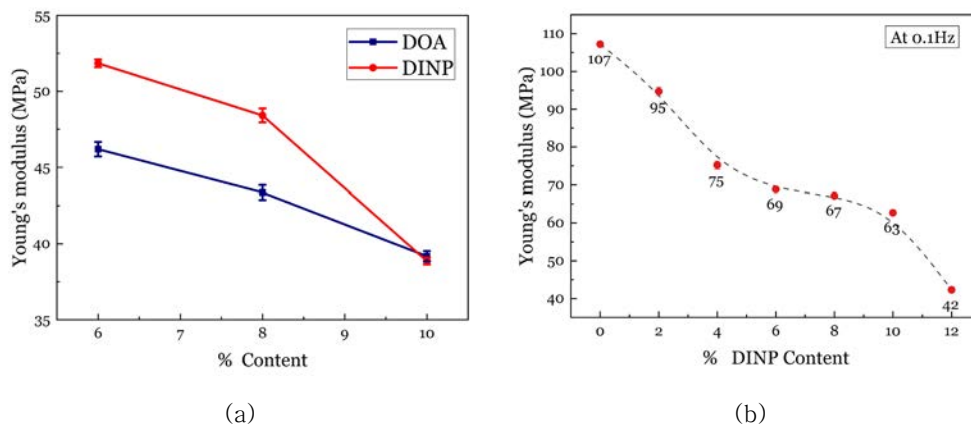


Figure 23 Young modulus of terpolymer doped plasticizer agents in a mass fraction which shows (a) the comparison of Young modulus of terpolymer filled DINP and DOA and (b) Young modulus versus added DINP contents.

3.3 Dielectric Strength (Breakdown Electric Field)

The electrical breakdown probability of plasticized films was examined using a DC ramp waveform at a rate of 500 V/s. The breakdown measurement setup consists of a wave generator (Agilent 33220A) and a high-voltage amplifier (Trek 20/20C).

Regarding the limitations of EAP actuator ability, an exceeded current flow through a dielectric medium can cause dielectric breakdown during the voltage operation. The DC breakdown strength probability of plasticized terpolymer is analyzed via the Weibull probability $P(E)$:

$$P(E) = 1 - \exp[-(E/\lambda)]^k \quad (13)$$

where E is the breakdown electric field of each sample, λ is a scale parameter portrayed as the breakdown voltage at 63.2% of breakdown probability, and k is data distribution or standard deviation of the experiment. Figure 24 shows the breakdown probability of modified terpolymer with various amounts of DINP and DOA plasticizer. The dots represent the experimental measurement of the breakdown probability whereas the solid lines show the fitted models based on Eq. (13). Excellent coherence between experimental and theoretical results has been achieved, allowing us to determine two pertinent parameters accurately, i.e. the data distribution (k), and the scale parameter (λ) corresponding to the breakdown voltage at 63.2% represented in Table 5.

The result revealed that terpolymer filled with the maximum plasticizer weight fraction, both DINP and DOA, gave the lowest electrical breakdown strength. Additionally, it was demonstrated that terpolymer doped with DOA featured lower breakdown field (E_{BD}) compared to terpolymer doped with DINP at the same filler content; $E_{BD}^{DOA} < E_{BD}^{DINP}$. A similar conclusion was reached by overly reducing tensile strength in modified terpolymer can cause a decrease in E_{BD} . The decrease in E_{BD} also depends on sample operating conditions (temperature, voltage input, material host compatibility, etc.).

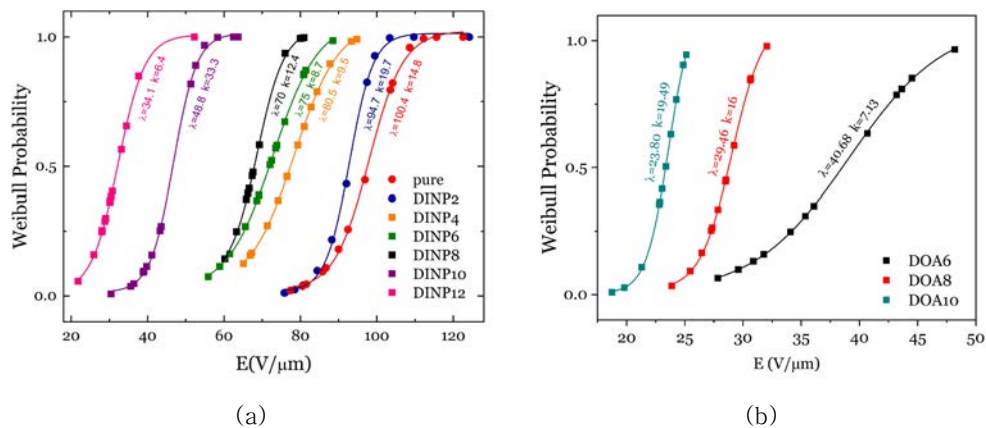


Figure 24 The breakdown probability versus electric field of (a) terpolymer/DINP and (b) terpolymer/DOA measured with an applied DC ramp.

Table 5 Breakdown electric field according to Weibull probability at 63.2% represented scale parameter (λ) and data distribution (k) of terpolymer filled with DINP and DOA respectively.

Filler (%)	Weibull Probability			
	DINP		DOA	
	λ (V/ μm)	k	λ (V/ μm)	k
Pure	100.40	14.80		
2	94.70	19.70		
4	80.50	9.50		
6	75.00	8.70	40.68	7.13
8	70.00	12.40	29.46	16.00
10	48.80	33.30	23.80	19.49
12	34.10	6.40		

As a consequence of some defections in modified terpolymer (free volume), increasing the plasticizer content can limit the operating voltage, which will minimize the strain production. Confirming one of the goals for the Live–Mirror actuators system, the new optimized material is more adaptable for low electrical input applications.

3.4 Electrical Conductivity

The electrical conductivity of modified terpolymers follows a classical dielectric material conductivity curve throughout various frequencies displayed in Figure 25. Both plasticizer fillers (DINP and DOA) provided DC plateau, σ_{DC} , (frequency-independent ionic conduction), and enhancement of AC conductivity, σ_{AC} , (frequency-dependent electronic conduction) in the high-frequency range. In general, at low frequency, the contribution of material losses (leakage current) is due mostly to electrode polarization or interfacial polarization (Maxwell–Wagner–Sillars) and charge migration. At high-frequency ranges, dipole relaxation is taking place while occurring dielectric losses in resonance regimes (atomic polarization and electronic polarization^[114,120,122]). Practically, dielectric material reacting to a given frequency could be explained simply with R–C parallel circuit whose impedance depends on angular frequency^[122].

According to the electrical conductivity mechanism of dielectric materials^[116], the DC conductivity (plateau region at low frequency) of plasticized terpolymers increases with increasing filler content (see in Table 6). This effect caused by the impurities within terpolymer host that the higher plasticizer content allowing more elevated charges and ions mobility in ionic conduction. It is also worth noting that terpolymer filled with DOA having its conductivity similar with respect to the same amount of DINP filler. Even if the electrical conductivity of plasticized terpolymer is low comparing to conductive materials, the DC conductivity serves the attribution of leakage current (material' s loss) that abate the dielectric breakdown strength of plasticized terpolymer.

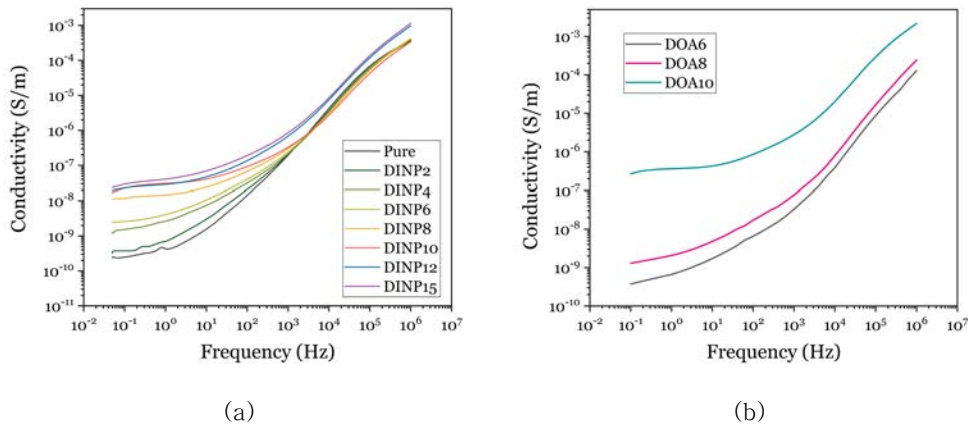


Figure 25 The electrical conductivity (DC and AC) frequency dependence for modified terpolymers (a) doped DINP and (b) doped DOA.

Table 6 The DC conductivity of modified terpolymers with plasticizer DINP and DOA.

Plasticizer	DC Conductivity, σ_{DC} (S/m)							
Filler (%)	Pure	2	4	6	8	10	12	15
DINP	2.48E-10	3.74E-10	1.53E-9	2.62E-9	1.16E-8	2.24E-8	2.30E-8	2.94E-8
DOA		3.73E-10		1.29E-9		2.65E-7		

Summary

Terpolymer became the selected material base for force-actuator in an active optics application. The thin film terpolymer and its composite were prepared using the solution blending method. The electrical & mechanical characterizations of the modified terpolymer were investigated. Based on force-actuator achievement features, the characterization of dielectric permittivity, polarization, Young modulus, dielectric breakdown strength, and electrical conductivity were described in this chapter. This chemical modification aims to achieve (1) high- k and conductive polymer composite using terpolymer doped CB particles and (2) advanced EAP actuator using plasticized terpolymer.

CHAPTER 3

Electromechanical Performance and Multilayer Design

CHAPTER 3

III. Electromechanical Performance and Multilayer Design

Actuator is a type of transducer device being categorized by a mechanical output responding to the external voltage stimuli. In order to demonstrate the actuator performance, the ability to convert between an electrical signal into a mechanical movement of the modified EAP is presented in this chapter. We investigate the electromechanical activity of pure terpolymer and its plasticized composite both experimentally and theoretically. The measurement technique is mainly aimed to observe the deformation of the actuator sample in thickness direction called longitudinal strain (S_{33}). This electromechanical test can enlarge the actuator optimization and operation constraints suited for the actuator application approach.

Electromechanical Characterization Technique

The setup for the characterization of the electromechanical actuator consists of the high-voltage amplifier, the waveform generator, the non-contact capacitive sensor, and the sample holder presented in Figure 26. This experimental test bench was designed to investigate the longitudinal strain (S_{33}) generated by the EAP electromechanical conversion. Under an exciting input voltage, the material deforms itself due to the electrostrictive effect attributed to the Maxwell stress and electrostriction force as mentioned in chapter 2, section Electrostrictive Material Models. This material deformation leads to the motion of the pole standing on the actuator sample and creates a variation of the capacitance of the air-gap between the pole tip and the capacitive sensor head. Such a variation was converted into a voltage which was used to measure the displacement of sample deformation. The sensitivity of the capacitive sensor is 0.1 mm/V. In this experiment, we observed the

longitudinal strain calculated by dividing the displacement to the initial film thickness.

Such soft actuators, the non-uniform flexure motion of a sample is a major cause of error in the strain measurements. Consequently, the film samples were placed on horizontal brass disks of 20 mm diameter to avoid measuring a parasitic flexure motion (see Figure 26). The error from the undesired flexure motion can be reduced by applying a slight preload to an active area of the sample. By having the slight preload integrating to the electromechanical characterization test bench, we can make sure that the sample has full contact and lying parallel to the sample holder.

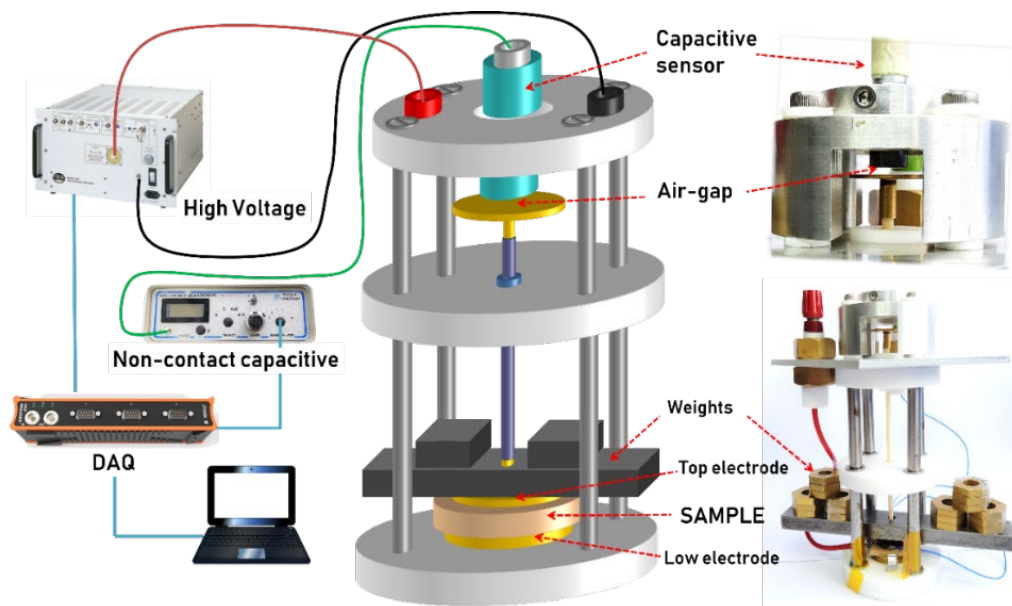


Figure 26 The setup of the displacement measurement using a capacitive displacement sensor to measure the electromechanical activity of the electrostrictive polymer. The sample holder consisting of the moving structure including the rod and the two discs having the initial weigh of 5 grams was created to measure the longitudinal strain of EAP actuators. An external load can be inserted into this sample holder structure to simulate the weight of a piece of glass in live-mirror applications. All the data were monitored and recorded via DEWE Soft (SIRUS STG), followed by a post-treatment with OriginLab®.

Intending to create an electric contact, a second brass disk positioned on the top of the film enabled to easily apply an electric field. The whole moving structure including the pole and the two discs depicted in Figure 26 having the

initial weight of 5g, which was considered to be suitably small stress (~ 0.15 N/cm²) that did not affect the movement of the material. To simulate the preloads that represents the weight of a deformable mirror, several metal pieces were successively put on the film as shown in Figure 26. Analysis in the actuation behavior of the developed material was carried out by evaluating the strain behavior as functions of applied electric fields and external loads. Indeed, actuator performance is not only evaluated by its maximum displacement in free charge but also by its blocking force under very low or zero displacement. Thereby, force measurement was investigated in this study to define the maximum force generated by the developed EAP actuator under a given electric field.

Electromechanical Performance

1. Electrostrictive Phenomena

As reported in literatures^[34,35,121,123], a pure terpolymer and a plasticized terpolymer confirm the electrostrictive behavior. Furthermore, with respect to classical ferroelectric polymers, this class of EAPs offers the technological advantage of no poling steps (or polarization process) required before their use.

Figure 27 highlighted the non-linear relation (with hysteresis) between an applied electric field and the resulting strain on the modified terpolymer sample. The mechanical strain response shows a quadric dependence with the applied electric field and its direction is not dependent on the polarity of the voltage excitation. Note that the terpolymer doped plasticizer DINP performed the relaxor electrostrictive effect with significant-high longitudinal strain driven, i.e. $S_{33} \sim 0.2$ % under $E=10$ V/ μ m. The current evolution versus the electric field enables to confirm the capacitive behavior of the polymer relating to typical hysteresis losses of EAPs^[34,35].

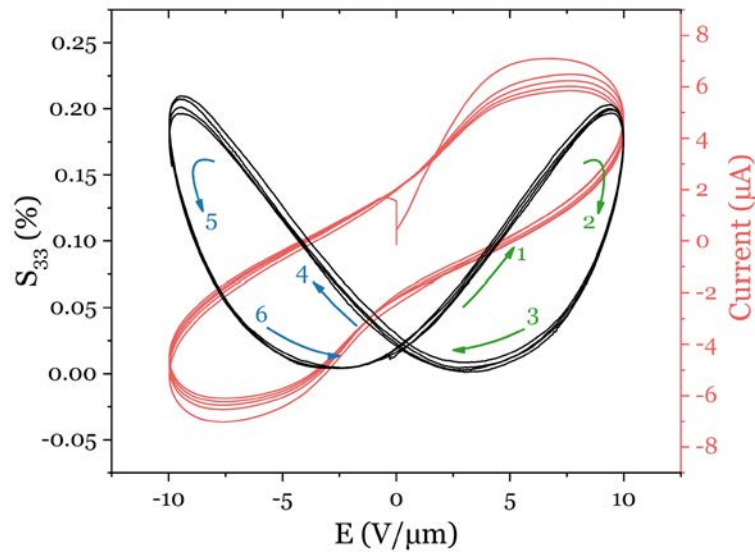


Figure 27 The longitudinal strain (S_{33}) and generated current of terpolymer doped with 10% DINP under sinusoidal excitation field of $10 \text{ V}/\mu\text{m}$.

The generated strain under applying the electric field (Figure 27) is occurred by the contribution of Maxwell stress and electrostrictive strain from the dipole moment alignment of the EAP material. Such a transitory strain response is driven by a bias AC voltage (sinusoidal 50 mHz) started from a positive voltage region (green arrows, stage 1–3) and reversed back to a negative voltage region (blue arrows, stage 4–6). This hysteresis strain–versus–electric–field response displays the electromechanical losses generated by the sample during actuation, which depends on the electric field variation and mechanical property of the electrostrictive materials^[124].

2. Strain Measurement under Applied Electric Fields

One of the key features reflecting actuator performance is the electromechanical coupling that can be characterized by the conversion between the strain (S_{33}) and the applied electric field (E_3). Figure 28a and Figure 28b present the displacement (D) of the pure terpolymer and the plasticized terpolymer which was deformed and compressed under applied electric fields. Note that the deformation rates of modified polymer exhibited

prominently superior with respect to the pure counterpart ($D_{\text{pure}} \sim 0.6 \mu\text{m}$ and $D_{\text{plasticized}} \sim 2.0 \mu\text{m}$, at $E=30\text{V}/\mu\text{m}$).

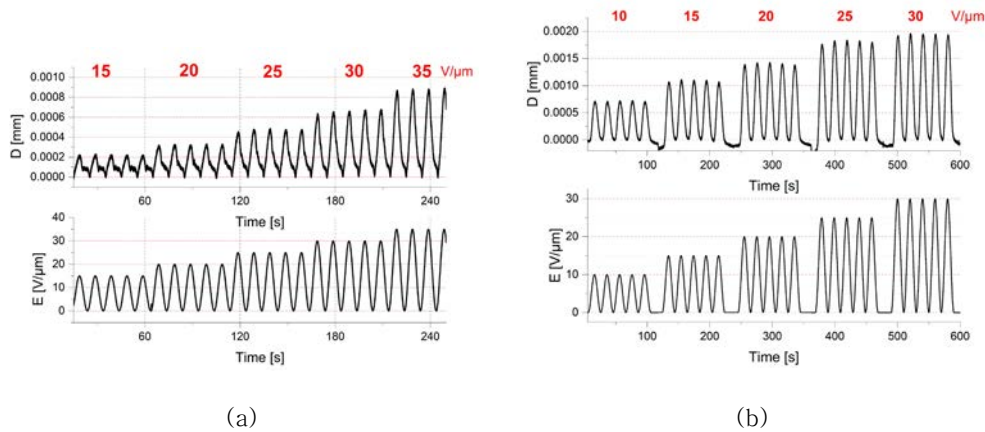


Figure 28 The longitudinal displacement of (a) pure terpolymer film of a thickness $222 \mu\text{m}$ and (b) terpolymer doped 8wt%DINP film of a thickness $176 \mu\text{m}$ operated under preload 76g as a function of applied electric fields sinusoidal 50mHz unipolar.

By comparing the different amounts of DINP adding to the pure terpolymer from 2% to 12% by mass, the result of activated strain is presented in Figure 29. The performance of electromechanical coupling is improved by increasing the amount of plasticizer, i.e. S_{33} of the composite 12wt% DINP yielded the strain actuation approximately 10 times higher with respect to pure terpolymer. Because increasing the plasticizer content lowers the breakdown voltage (see in Figure 24a, chapter 2, page 92), the fraction of plasticizer added to terpolymer should be optimized.

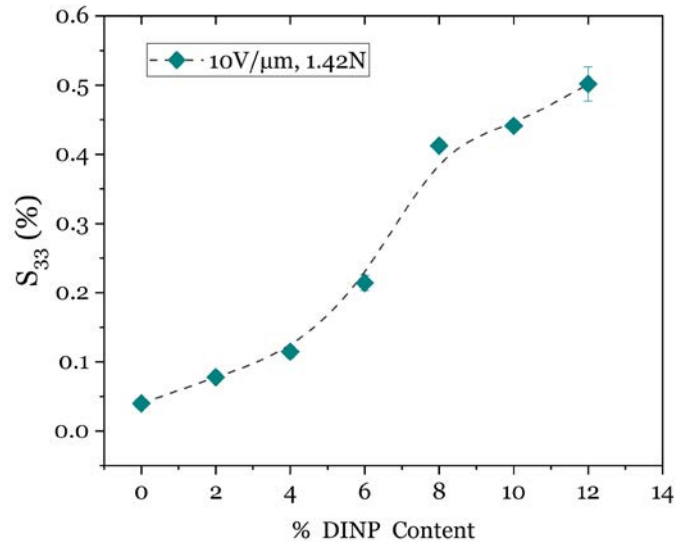


Figure 29 The longitudinal strain response in according with various percentages of DINP added to pure terpolymer operated under $E = 10 \text{ V}/\mu\text{m}$. The experimental error is very smaller to be observed in the graph scale.

According to the electromechanical performance as presented with the figure of merit of the EAP material in Eqs. (3)–(6) in chapter 2, depends on the dielectric permittivity, the Young modulus, and an electric field excitation. Indeed, the apparent limitation of actuator performance can refer to an electrical breakdown field of materials that will limit the electromechanical conversion rate. Moreover, the ability to generate force can be limited by material dielectric permittivity and actuator operation system, i.e. the EAP actuator material will be operated under an external preload.

Note that the final purpose here is not only to achieve the greatest strain actuation but also to have a reasonable electric field operating range, providing in such a way a better range to the material choices for suitable actuator applications. Figure 30 shows the achievable strain as a function of the intensity of the electric field and the slope of each curve refers to the electrostriction coefficient (M_{33}). As observed from material characterizations, the sample with extra plasticizer added (**Plasticized++**) or above 10% of DINP has a larger M_{33} value. However, its electric field rupture of **Plasticized++** is relatively low which possibly limits electromechanical conversion output. On the other hand, with low plasticizer content or below 6% of DINP including pure terpolymer (**Pure**) have significantly lower actuation ability related to an applied electric field. That makes pure materials and low plasticizer contents

required high input voltage to drive sufficient strain. In the end, such a trade-off between the strain actuation and the dielectric breakdown strength dictates the optimized EAP - terpolymer filled with 8 to 10% of plasticizer (**Plasticized+**) - to be used as force actuators for our Live-Mirror development.

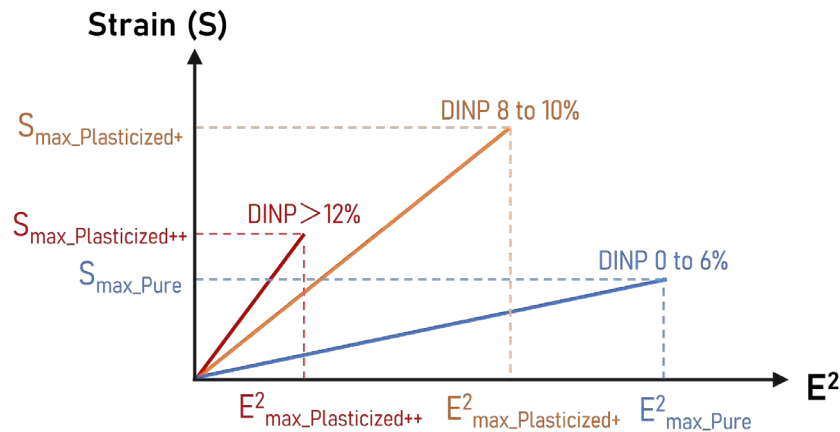


Figure 30 The achievable strain versus maximum electric field squares (electric breakdown field) represents the electromechanical performance depending on plasticizer loads (Pure = DINP0-6%, Plasticized+ = DINP8-10%, and Plasticized++ = DINP >12%).

According to the optimized plasticized terpolymer, we determined the strain response results of terpolymer doped with 8wt% DINP operated through different experimental conditions as demonstrated in Figure 31. All the experimental measurements were operated with unipolar 50 mHz sinusoidal electric fields. The strain response was characterized by a hysteresis versus applied electric fields. In particular, the electromechanical hysteresis curve in Figure 31b reflects the electromechanical losses generated by the sample during actuation^[34,72]. This hysteretic behavior attests to a phase shift between the mechanical response and the applied electric field.

Regarding the limitations of actuator performance, Figure 31c and d illustrate some experimental results of S_{33} of modified terpolymer actuated under different applied external loads. Significant loads from 0.76N to 2.74N were exerted on the sample under different electric field values. The results show that S_{33} slightly decreases when an extra force is applied to the actuator samples, as shown in Figure 31c. Considering the ability to generate a strain of terpolymer doped 2 to 12 wt% DINP under the same amount of preloads and

electric field excitation (Figure 31d), the higher plasticizer content remains higher strain actuation under an extra force application.

Note that it is difficult to investigate the blocking force experimentally because these plasticized terpolymers including other electrostrictive materials have extremely high blocking stress as reported in literature reviews [25,27,43,65 - 70]. However, the blocking force we achieved from the plasticized terpolymer is far from the preload condition in the Live-Mirror application requirement (1N). The blocking stress limitation of our optimized modified EAP can be neglected.

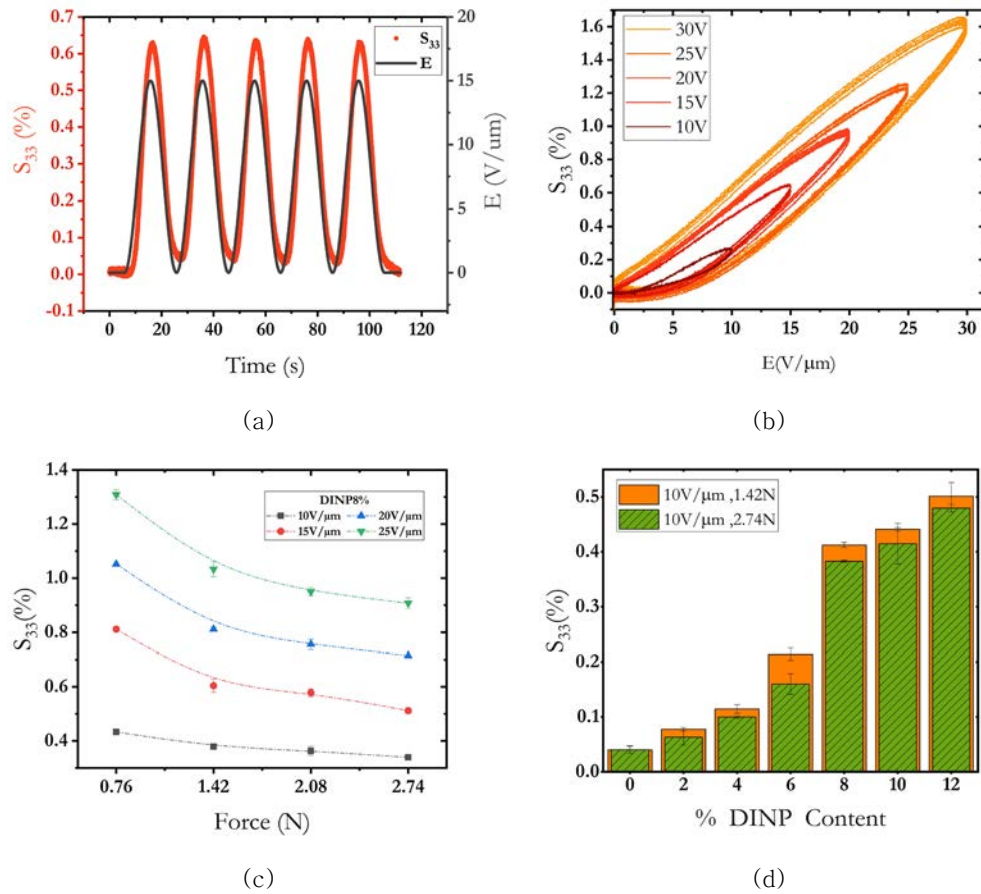


Figure 31 The longitudinal strain response (S_{33}) of the modified terpolymers operated under sinusoidal 50 mHz applied electric fields: (a) the temporal evolution of S_{33} of terpolymer+8wt%DINP activated at $E=15 \text{ V}/\mu\text{m}$ & preload 1.42 N; S_{33} of terpolymer+8wt%DINP versus (b) input electric fields and (c) externally applied forces; and (d) S_{33} of terpolymer doped 2 to 12wt% DINP under two different preloads activated at $E=10 \text{ V}/\mu\text{m}$.

3. Current Behavior of Plasticized Terpolymer under High Applied Voltage

The current generated from the modified terpolymer under high voltage (HV) presents an unconventional behavior (Figure 32) when compared to those of pure terpolymer and other electroactive polymers^[34,35]. This phenomenon might be explained by the impact of the modification of the terpolymer matrix due to the plasticizer filler. The plasticizer molecules tend to mix with the amorphous phase of the material host, which leads to a decrease in the regular chain density of the material. Since the plasticizer agent is used to increase the elasticity of the polymer, the mobility of polymer chains, including free charges and ions, are increased in the same way.

Figure 32 shows that by increasing plasticizer contents, the generated current of the modified terpolymer started a reversal direction (dropping down) with a certain applied electric field. Theoretically, the leakage current of dielectric material should increase proportionally to an increase of the input voltage according to Ohm's law. Alternatively, the generated current of plasticized terpolymer carries on a gradual decrease until the maximum input voltage. This phenomenon can be explained by the polarization behavior of the plasticized terpolymer as described below.

As shown in Figure 32 the higher DINP filler amount can reach the reversal point of current at a lower applied electric field. The uncommon compartment can be described by the polarization activities of the modified material. At lower voltage input, the electrical dipole moments including free ions are simpler to be orientated or rearranged following the direction of the external electric field due to the great mobility of polymer chains and free ions of the plasticized terpolymer. It is assumed that the polarization of plasticized terpolymer reached saturation when an input voltage goes over the reversal point. The polarization saturation is observed by the gradual drop of current after the reversal point.

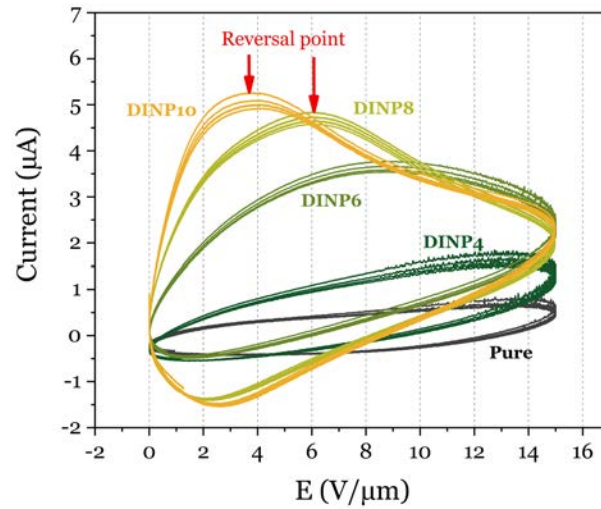


Figure 32 The current behavior under high electric field applying ($15 \text{ V}/\mu\text{m}$ sinusoidal unipolar 50 mHz) constituted of different plasticizer DINP loads from 0 to 10 % by mass.

A similar pattern of results was obtained in Figure 33 presenting the generated current of terpolymer doped 10wt% DINP operated under different high input electric fields. At the same amount of plasticizer content, increasing an input field excitation provides an indifferent reversal point of generated current. According to the ohmic loss ($I=V/R$) in a dielectric material, the result of generated current seems to have higher losses at the lower HV input as can be seen from the estimated loss represented with the dashed line in Figure 33. While at higher HV input, the measured current provides relatively saturation in losses. As aforementioned, the plasticized terpolymer is more attainable to reach the polarization saturation activities with respect to the pure terpolymer. Thus, the plasticized terpolymer contributes to lower loss (low ionic conduction) throughout the HV operation range as presented in Figure 34. The saturation in polarization provides evidence to enlarge the dielectric breakdown field of the sample under HV operation, even if loss tangents ($\text{Tan}\delta$) measured at low voltage (from BDS) are high. The different of loss contribution^[35] under the different intensity of voltage operation can be explained as follows:

- (1) **At low voltage:** the sample maintains spontaneous ions distribution causing ionic conduction & electronic conduction referred as a material's losses;
- (2) **At high voltage:** the distribution of the ions is reinforced to have a significant hetero-charges separation which leads to having a local

electric field against an electron motion resulting in a decrease of electronic conduction.

This phenomenon is apparently caused by the greater chain mobility of plasticized terpolymer related to pure terpolymer - incidentally, plasticized terpolymer remains mysterious circumstances and it is still challenging to study the nature of plasticizer filler effect.

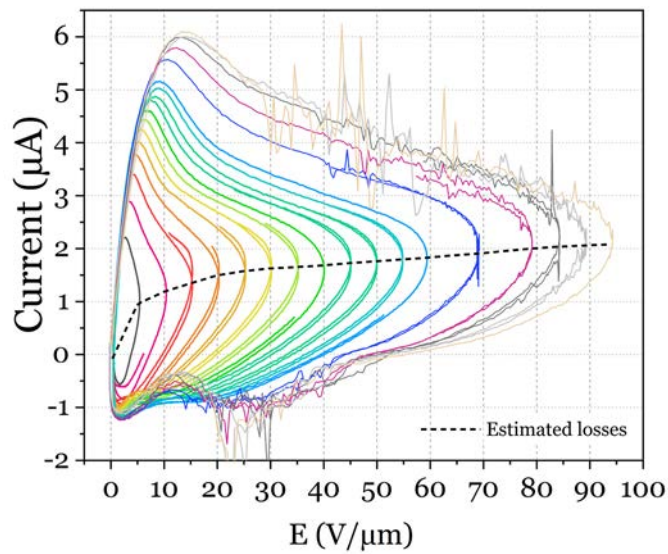


Figure 33 The generated current of terpolymer filled with 10%DINP as a function of applied electric fields (sinusoidal unipolar 100 mHz) with its loss' s estimated guideline. The spikes came from an electric arc in the experimental measurement.

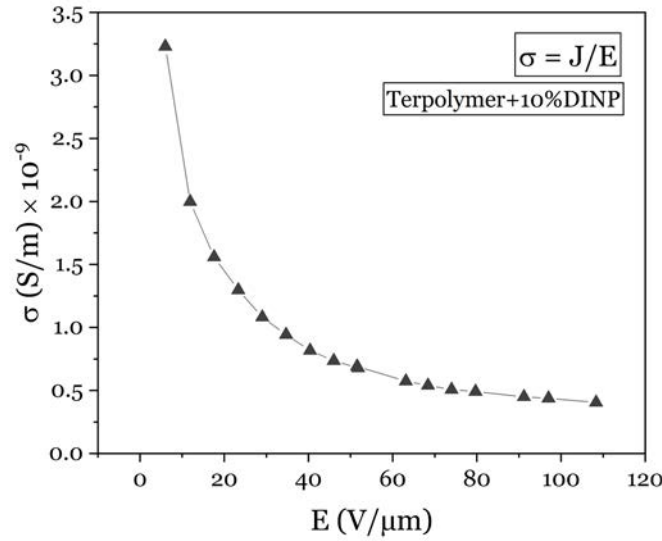


Figure 34 The evaluated electrical conductivity (estimated losses) of terpolymer doped 10wt% DINP as a function of applied electric fields.

4. Empirical Modeling with Debye-Langevin Formula for HV Operation

The plasticized terpolymer here developed produces an unconventional current under HV operation, such a behavior calls to consider a non-linear dependence of the dielectric permittivity. In order to have an accurate electrostrictive material model, the dielectric permittivity of the modified terpolymer was determined under HV operation and also because it is a semi-crystalline polymer, an inherent microscopic parameter of this dielectric material can be induced polarity in the crystalline phase, allowing to create huge dipole moments in amorphous regime mainly caused by interfacial phenomena, i.e. Maxwell-Wagner-Sillars (MWS) polarization. Note that Capsal et al., (2012)^[72] reported the possibility to use the Debye/Langevin formalism predicting an actuation ability of electrostrictive effect in dielectric materials. Thus, the relative permittivity under a high electric field $\epsilon'_{(E)}$ is:

$$\epsilon'_{(E)} = 3(\epsilon'_{(E_0 \ll E)} - 1) \left[(E_{SAT}/E)^2 - \left(1/\sinh^2 \left(\frac{E}{E_{SAT}} \right) \right) \right] \quad (14)$$

where $\epsilon'_{(E_0 \ll E)}$ is the dielectric constant at a very low electric field, E is the local applied electric field, and E_{SAT} is the saturation electric field or an electric field required to reach the non-linear zone whereas $E \ll E_{SAT}$. In such a way, the estimated losses under high input voltage (Figure 33 and Figure 34) could enable to evaluate the capacitive current as a function of applied electric field being as follows:

$$I_{tot} = I_{cap} + I_{loss} \quad (15)$$

where I_{tot} is the total current generated by sample, I_{cap} is capacitive current and I_{loss} is leakage current obtained by an estimated loss under HV operation.

The reliability of the estimated current using Eqs. (14) and (15) is correlated with the experimental current measurement (Figure 35). The measured current is a capacitive current given by the subtraction of leakage current (estimated loss or conduction current) from the total measured current^[35]. The dielectric permittivity under HV operation of plasticized terpolymers evaluated through Eqs. (14) and (15) is presented in Figure 36.

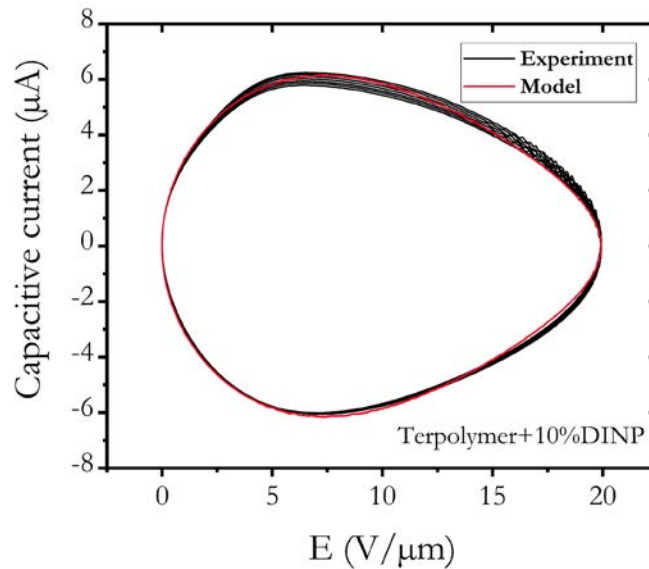


Figure 35 The evaluated electrical behavior represented with the capacitive currents of a plasticized 10%DINP terpolymer under applied electric field $E=20V/\mu m$ between estimated model and experimental measurement.

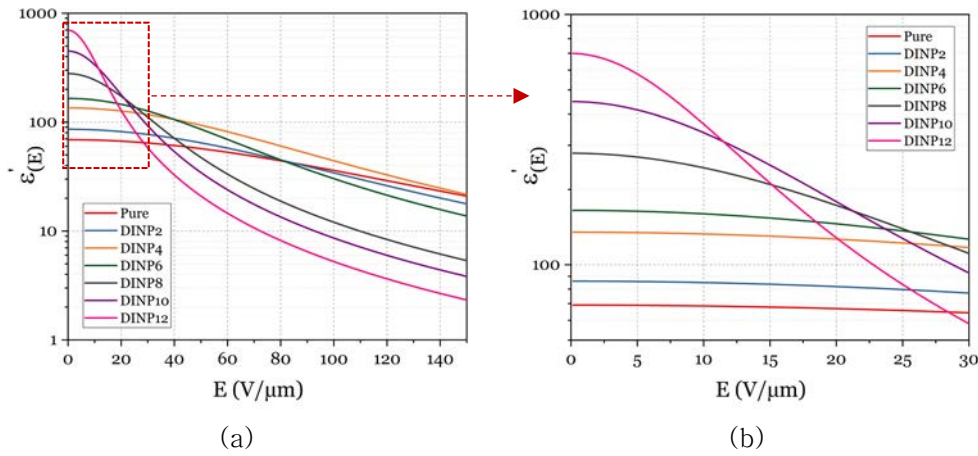


Figure 36 The relative dielectric permittivity of terpolymer filled DINP from 2–12 % by mass measured and calculated from the Debye/Langevin evaluation model.

The results in Figure 36 show that the dielectric constant of the terpolymer and its composites behave non-linearly under HV operation. These non-linear permittivity results are directly in line with the previous discussion on current behavior. We believe that the higher DINP doping content in terpolymer is able to reach the saturation in polarization under a lower HV. As shown in Figure 36, the permittivity tends to decrease when increasing an applied electric field. This result can be explained by the mobility of dipole moments that they are no longer tilted and/or oriented over the saturation electric field. In this circumstance, the material polarization became saturated related to the decrease of dielectric susceptibility.

According to the empirical modeling; an estimated permittivity from Eq. (14) allows us to evaluate the electromechanical response of plasticized terpolymer under HV operation. Instead of employing the relative permittivity (ϵ') under low voltage characterization, the following strain response ($S_{(E \gg E_0)}$) under HV input can be inferred from the relative permittivity ($\epsilon'_{(E)}$):

$$S_{(E \gg E_0)} = \frac{\epsilon_0 \epsilon'_{(E)}}{Y} E^2 \quad (16)$$

Eqs. (14) and (16) could devote the evaluation of electromechanical properties under HV input especially in the case of plasticized terpolymer. Figure 37 presents the estimated longitudinal strain, calculated through Eq (14) and (16), under maximum input electric field of 20 V/μm.

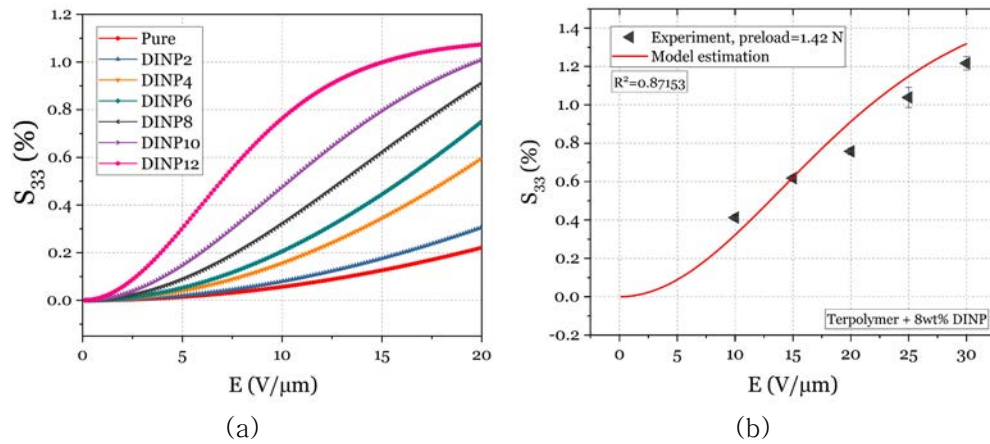


Figure 37 The estimated strain of (a) plasticized terpolymers under applied electric field up to $20 V/\mu m$ and (b) the comparison of strain response of terpolymer filled 8wt% DINP between experimental measurement and strain model estimation as a function of an applied electric field.

The result in Figure 37a reveals electromechanical strain that agrees with the expectations based on the theoretical electrostrictive material properties. The S_{33} evaluation model shows reasonable success fitting the experimental result ($R^2 = 0.872$) in Figure 37b. There is a small difference between experiment and model value because the experimental results were measured under preloading of 1.42 N while the evaluation modeling was considered as freely electromechanical strain. It is interesting to note that the samples with DINP fillers content above 8 wt% can reach the strain saturation at a lower voltage which will limit actuator performance in terms of electric field excitation. Thus, the figure of merit under different operating conditions should be taken into consideration.

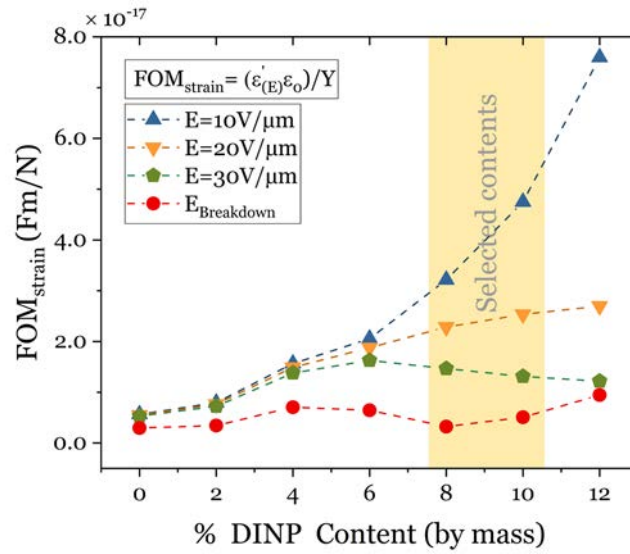


Figure 38 The figure of merit strain generated consideration (FOM_{strain}) of terpolymer filled with various DINP contents (by mass) under activated fields of 10, 20, 30 $\text{V}/\mu\text{m}$, and nearly breakdown field ($E_{\text{breakdown}}$).

Considering the figure of merit of free strain generated (no preloads) by employing Eq. (4) from Chapter 2, it seems that the higher DINP content would provide greater FOM_{strain} (by increasing the relative permittivity and decreasing the Young modulus of the material host). Nevertheless, the non-linear permittivity of plasticized terpolymer under HV operation does seriously impact its electromechanical performance. Figure 38 presents the figure of merit of the ability to generate strain under different levels of high input electric fields. Under low related applied electric field ($E=10 \text{ V}/\mu\text{m}$), terpolymer filled with 12 wt% DINP gave the highest FOM_{strain} with respect to other lower DINP filler contents. Meanwhile, its FOM_{strain} value dropped drastically after the input voltage is increased up to 20 $\text{V}/\mu\text{m}$, and so on. In order to remain actuator ability under high applied electric field, the optimized DINP content has been selected between 8–10 % by mass.

Another limitation on actuation ability is the dielectric breakdown probability which would limit the actuator operation range. We considered the relation between strain generated under $E=10 \text{ V}/\mu\text{m}$ and breakdown electric field (E_{BD}) shown in Figure 39. Even if terpolymer doped 12wt% DINP produced significantly larger strain comparing to the others, the limited electric field operation range is related extremely low. The results of FOM_{strain} presented in Figure 38 shows the agreement with the strain response in Figure

39 that the selected plasticized terpolymer modification (8–10 wt% of DINP filler) can be a good actuator candidate in this work.

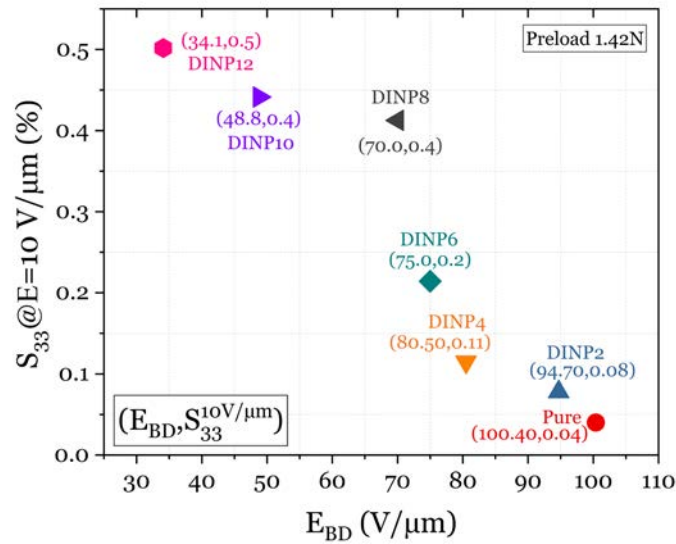


Figure 39 The strain generated under activated field $10V/\mu m$ of terpolymer added DINP 0 to 12wt% by reference to their breakdown field (E_{BD}).

This empirical modeling enables the prediction of advanced EAP actuator electromechanical performance, which explains how plasticized terpolymer actuator dynamics will be. On this basis, we can take advantage of this advanced electromechanical model to design the Live–Mirror prototypes and model the force–actuator controlling system in future development.

Multilayered Actuator

1. EAPs Multilayer Initiative

The technique to achieve extremely high permittivity while keeping low losses and high displacement/load are developed here – the multilayer design. Considering the fundamental concepts of electricity, we can bypass the chemical material modification and work on the circuit of the electronic component. An EAP actuator can be considered as a capacitor. If the EAP films or capacitors are connected in parallel, a common voltage is supplied across them, and total capacitance is equal to the sum of all the individual capacitances. The simplest design to connect EAP films in parallel is to building a multilayer stack layer-by-layer of films – a multilayer EAP.

To investigate the multilayer actuator, the pure terpolymer and plasticized terpolymer films were structured as a multilayer stack by depositing up to n layers where n is the number of layers. These multilayer stacks were modeled as a structure of capacitors in parallel mode with their capacitance increasing directly proportional to n . The main goal here is to investigate a multilayer actuator performance to achieve extremely high permittivity while keeping low losses and the same voltage input. The preliminary consideration is that the permittivity is linearly increased in terms of the number of layers. Based on the electrical connection of every single film, the multilayer film was modeled as a structure of parallel capacitors and its resulting capacitance C is:

$$C = \sum_{i=1}^n C_i \Rightarrow C = nC_0 \quad (17)$$

where C_i is the capacitance of the layer i , n is the number of layers, and assuming the capacitance of the n layer is the same C_0 .

2. Multilayer Strain Boosting

2.1 Multilayer Stack Fabrication

The multilayer structure actuator presented in Figure 40 was made by superposing several single layers of the terpolymer films together. A conductive adhesive and aluminum foil sheets were inserted between each layer for ensuring the electrical connection of the whole sample, which can be modeled as several capacitors in parallel. The total thickness of the final structure with 10 deposited EAP layers is 3 mm. The extra thickness includes the thickness of conductive adhesive interlayers and aluminum foil sheets within the structure.

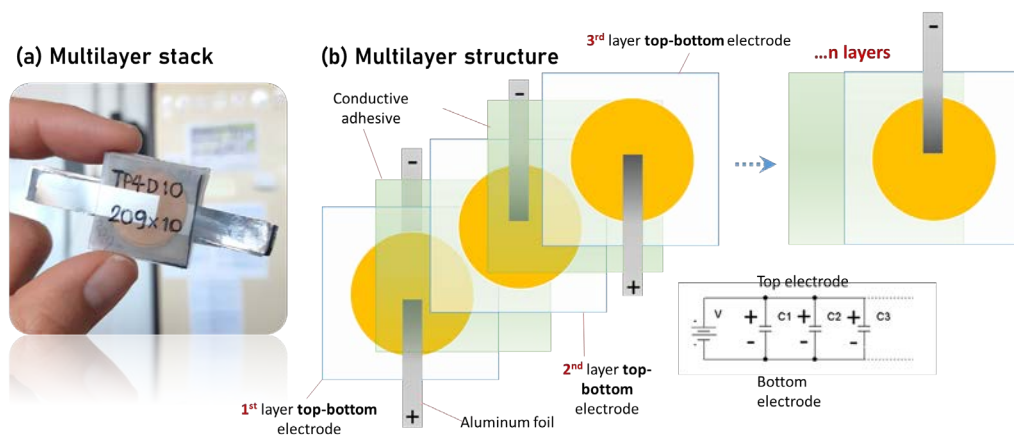


Figure 40 The multilayer actuator design: (a) the stack of 10 layers-terpolymer+10%DINP 209 μm of each layer thick; and (b) the multilayer topology consists of the EAP layers coated gold electrode, electrically conductive adhesive interlayers, and aluminum foil sheets for HV connection. The multilayer structure was designed imitating several capacitors connected in parallel.

2.2 Electromechanical Performance of Multilayer Stack

For the multilayer sample deformation test, the displacement measurement is given by an EAP multilayer stack generally shows higher measurement precision than the single-EAP-layer sample. Thanks to its superior thickness and less flexibility, we are able to reduce a parasitic-motion effect in the multilayer stack design. The measurement was examined using the electromechanical test bench presented in Figure 26.

a. Total Strain VS Number of Layers

Figure 41 presents the total longitudinal strain (S_{total}) of the pure and the plasticized (10% DINP) terpolymers multilayer for $n=1$ to 6 layers. The total strain was evaluated considering that $S_{total} \Rightarrow n S_{measured}$. The result in Figure 41 shows that the multilayer actuators, both pure and plasticized stacks, provide significantly large strain response with respect to the single-layer actuators. In particular, the 6-layer stack of plasticized terpolymer generated 10 times of strain actuation higher than the single-layer plasticized terpolymer under the same field excitation at $10 \text{ V}/\mu\text{m}$. This preliminary result of a multilayer stack delivers the EAP potential carrying through the extraordinary electromechanical conversion operated under a low related electric field.

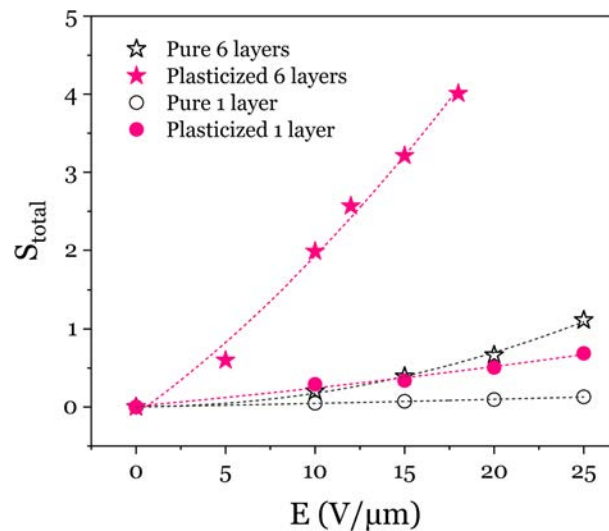


Figure 41 The total longitudinal strain (S_{total}) of the pure and the modified 10% DINP terpolymers for single layer and 6-layer stack as a function of electric fields.

The strain achieved with plasticized terpolymer films versus the number of layers is shown in Figure 42. The samples were driven through an alternating unipolar electric field of $10 \text{ V}/\mu\text{m}$ 50 mHz. The capability of the multilayer actuator working under preload exertions (142g or 458g) was determined in Figure 42 as well. The result shows the linear relationship between the S_{total} versus the number of layers ($S_{\text{Total}(n=1)} = 0.4\% \rightarrow S_{\text{Total}(n=8)} = 2.7\%$), which attests a good agreement with the model of Eq. (17).

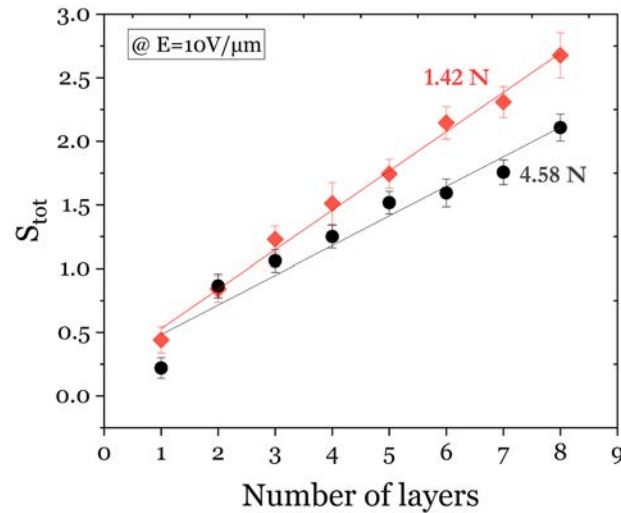


Figure 42 The total longitudinal strain (S_{Total}) versus the number of layers ($n=1$ to 8) for plasticized (10%DINP) terpolymers operated at $10 \text{ V}/\mu\text{m}$ under applied external loads of 1.42 N and 4.58 N .

b. Total Strain VS Applied Forces

The experimental measurement was operated under an alternating unipolar electric field of $10 \text{ V}/\mu\text{m}$ 50 mHz as a function of external load (from 2N to 15N) directly applied to the actuator stack. Different weights simulating external preloads from 250g to 1500g were directly applied to the active area of the multilayer samples. The total strain response of stacks with $n=1, \dots, 8$ layers of plasticized terpolymer was measured under those preloads at field activation of $10 \text{ V}/\mu\text{m}$ is presented in Figure 43. Experimental results demonstrated that the S_{total} of all samples gradually decreases as the applied forces increase. The highest S_{total} was recorded for the plasticized-8-layers stack. It is interesting to note that even as the applied force reaches 15 N, the S_{total} is still different from zero, reflecting excellent actuation performance of the plasticized multilayer terpolymer under a high-load condition. Indeed, the exerted force to doped terpolymer is still far from the presented blocking force

in Figure 4, page 54. The multilayer actuator capability of plasticized terpolymer undoubtedly shows substantially improved strain response stimulated by low input voltage excitation. Ideally, these experimental results should be replicated in the development of a force-actuator system to accomplish the goal of Live-Mirror involving strain/displacement surface correction in a few microns.

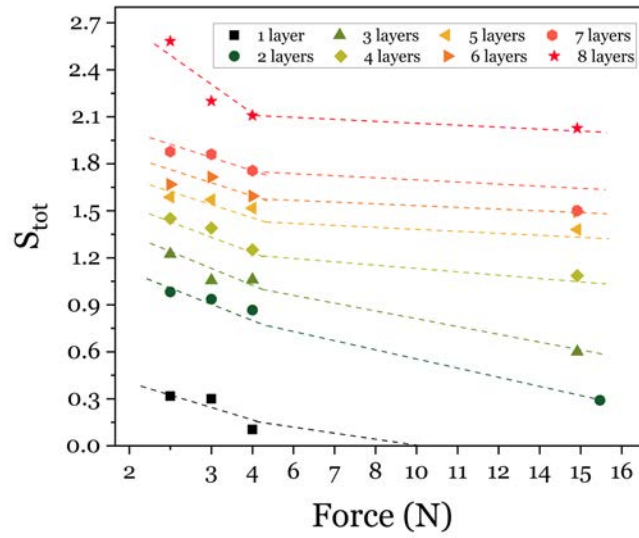


Figure 43 The total strain (S_{total}) generated by multilayer plasticized terpolymer under different external applied forces (F) operated at electric field $10 \text{ V}/\mu\text{m}$.

Summary

The actuation performance of modified terpolymer was demonstrated through its electromechanical conversion potential. We observed an unconventional current behavior of plasticized terpolymer under high voltage operation. The results demonstrated that plasticized terpolymers apparently contribute lower loss (observed through the saturation of the estimated leakage current). This effect could enlarge to increase the electric breakdown field of the sample. Furthermore, the empirical modeling for the modified terpolymer strain prediction was described in this chapter. Overall, the optimized plasticized terpolymer and the multilayer actuator could attain a large strain response under a lower HV operation. The results proved that these advanced actuators have sufficient electromechanical performance to complete the force-actuator system in the Live-Mirror application.

CHAPTER 4

Live-Mirror Application

CHAPTER 4

IV. Live-Mirror Application

Live-Mirror Project

Recently the worldwide astronomical community is making an effort to create the World' s largest telescope (Figure 44) named the Exo-life Finder (ELF) to discover life on extrasolar planets^[8]. Our interdisciplinary approach "Live-Mirror Project" aims to create the next generation of large mirrors using EAP actuators and sensors without classical abrasive polishing of glass. The novelty is to replace classical rigid and heavy optical mirrors with live and light dynamic optoelectronic systems. These consist of a thin optical glass sheet actively (live) supported by many-degree-of freedom force-actuators/sensors integrated and miniaturized via additive manufacturing and 3D printing. Such a novel development is distributed amongst three key new technology components:

1. A deterministic, non-contact, glass slumping (DNCGS) technique that generates optically accurate aspheric shapes from commercial (window glass) fire-polished "float" glass with an extremely smooth optical surface which is never abrasively polished;
2. Active shape control with many-degree-of-freedom force actuators which will be achieved by the development and optimization of advanced EAP systems for the proof of concept. The design and optimized additive EAP manufacturing should be developed here in order to obtain the various actuator shapes suited for mirror surface defaults;
3. Hybrid structures and optical model which require a fast and efficient optical calibration model for a controlled surface image and its image surface calibration algorithms.

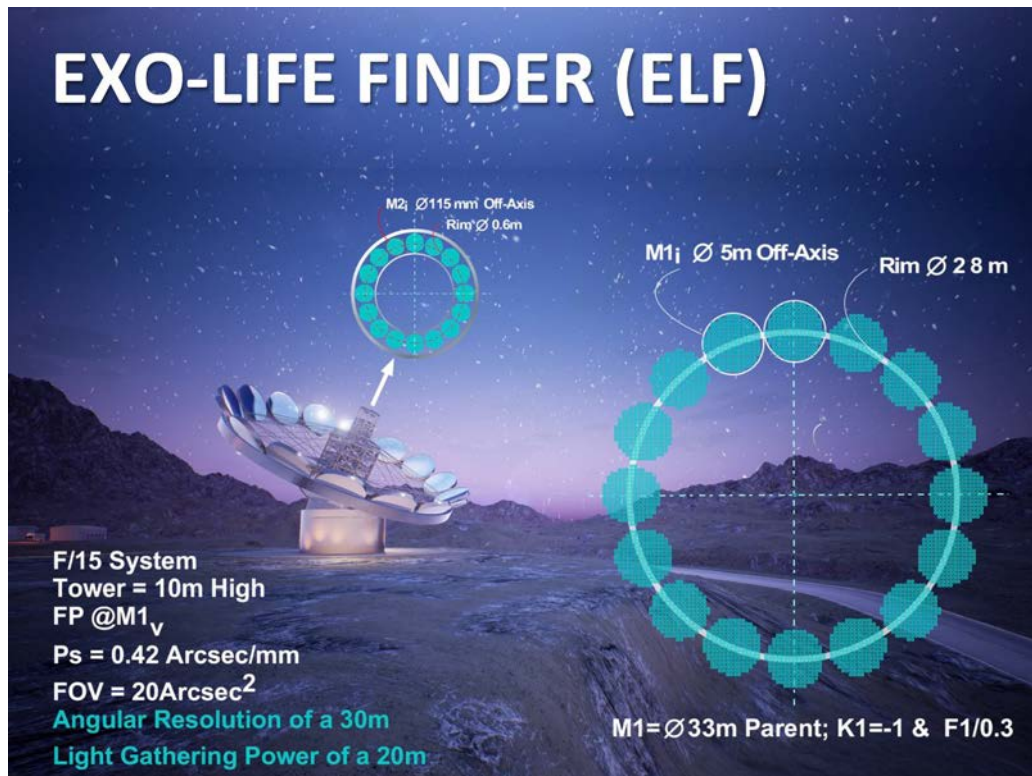


Figure 44 The ELF design configuration consists of 16 parabolic apertures (M_{1i}) with diameter 5m—each, a secondary mirror (M_2) with a diameter of 115 mm, and sub-apertures mechanically arranged on a 28m in diameter rim^[8].

The development, optimization, and manufacturing of advanced additive EAP systems - key technology #2 - for the Live-Mirror project is the main part and has been accomplished in this thesis. We expect to fabricate these light-weight mirrors as a hybrid material composed of two layers of mm-scale thick glass with interspersed layers of EAP material with a final very light mechanical truss. In the particular case of an optical telescope for astronomy^[8,10,16] printable 200 micron-scale thick layers of plasticized terpolymer can have areal energy density sufficient to bend mm-scale thick glass by several microns. These mirrors would not be abrasively polished, the first EAP layer essentially 'polishes' the reflecting surface of the commercial, fire-polished glass to micron scales using shear stress (acting from the backside).

Large telescopes presently planned or under construction are massively segmented telescopes like the European Extremely Large Telescope (EELT)^[16] or the Thirty Meter Telescope (TMT)^[125] which use

“Keck-era”^[126] optics. Their mirror sub-apertures create a dynamically rigid primary optical surface from 100’ s of 1m-scale, few-cm thick mirrors. Thus, Live-Mirror is designed to build the next generation of extremely large telescopes, decreasing the mirror mass density significantly and thus lower the cost greatly since this payload mass sets the cost scale for the entire optomechanical structure.

In the future, we want to use hybrid and multilayer doped terpolymers to make smart remote sensing systems. This pushes development towards optimized and miniaturized EAP actuator-sensors. For instance, with 3D-printed terpolymers with flexible electrodes on the back of a mirror, many-actuator degree-of-freedom optical elements will be possible for more advanced in automated manufacturing in various shapes suited for local surface correction. The ultimate goal is to demonstrate a novel hybrid “smart” meta-material with superior stiffness-to-density ratio mechanical properties for general optical applications.

Live-Mirror EAPs Conceptual Design

Classical EAPs such as Polyurethane, Silicone-based require extremely high input voltages to reach sufficient mechanical strain. In particular ferroelectric based polymers (PVDF or P(VDF-TrFE) require electrical pre-poling and pre-stretching^[17,18] for film elaboration to align polymer chain and dipole moments, which would be more complex through 3D printing technology. In our goal case, the Live-Mirror active optics application requires a high-efficiency force-actuator to deform the mirror surface and the integration of 3D printing technology within manufacturing processes. Thus, terpolymers will serve those requirements because they exhibit a large electromechanical strain and so not requiring the poling and pre-stretching. Also, terpolymers P(VDF-TrFE-CFE/CTFE) present a crucial very high electrostrictive strain, and thanks to their high dielectric constants featuring superior dielectric permittivity when compared to other conventional EAPs. These relaxor fluorinated polymers exhibit high dipole density presenting high electrostrictive contribution to electromechanical coupling. Note that terpolymers present dielectric constant values in the range $\epsilon'_{\text{terpolymer}} = 50-70$, which are between 10-20 times higher than conventional EAPs $\epsilon'_{VHB} = 4.7$, and

$\epsilon'_{silicone} = 3-4$. Such a valued property makes terpolymers the most adequate candidates for electrically driven soft actuators.

Developing an actuator-optimized terpolymer, we have demonstrated outstanding electromechanical performance, particularly when doped with plasticizer, e.g. Diisononyl phthalate (DINP). This doped terpolymer features a large strain response as well as excellent mechanical energy density under relatively low electric fields. Using the high permittivity doped terpolymer and the concept of stacking multilayers we generated high displacements and large forces.

The electromechanical performance of EAPs can be limited when they work against an external load in an actuator device system. Indeed, studies have shown^[15,43] that the figure merit of the blocking force strongly depends on the dielectric permittivity of the material. Investigation on the blocking force, reveals that plasticized terpolymer exhibits the largest blocking force as illustrated in Figure 4 – chapter 1, page 54. When subject to a field $20 \text{ V}/\mu\text{m}$, the plasticized terpolymer yielded a blocking force of approximately 200 N whereas pure terpolymer, polyurethane, and silicone reached only blocking forces of 100N, 12N, and 3N, respectively. This result allows us to confirm the high potential of the proposed material for the Live-mirror application. This technology can significantly advance our ability to create large and precise optical surfaces. This light-weight diffraction-limited metamaterial-based optical system (mirror) for ground- and space-based astronomy and communications telescopes.

1. EAP Actuator-Sensor Hybrid System

Recently, our research collaboration introduced a novel hybrid dynamic live-optical surface technique^[8,10,11] in the Live-Mirror project. We have investigated the feasibility of an advanced EAP using plasticized terpolymer and its multilayer structure yielding a remarkable electromechanical strain. By integrating force-actuator elements to the back of the mirror (Figure 45), the strain given by the actuated EAP can produce an active and live mirror. The level of mirror wavefront deformation depends on the ability of force-actuator to generate electromechanical strain. Figure 45b illustrates the conceptual design for a hybrid dynamic structure which consists of:

- (1) optic elements comprise the front mirror (control surface), and supported glass (reaction surface);
- (2) active systems constituted of the multilayer EAP actuator for global surface deformation, the shear EAP actuators for local curvature correction (here dubbed *electronic-polishing*), and surface force sensor;
- (3) inactive sections involve a soft elastomer layer used for filtering local forces transferring between multilayer and shear EAP actuators, and mechanical supporting system.

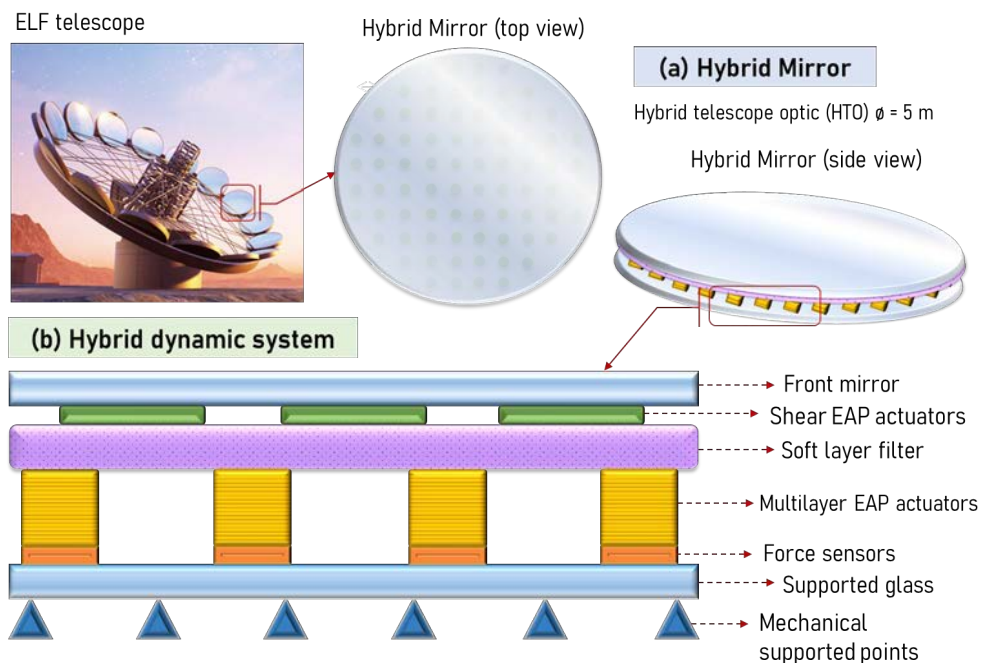


Figure 45 The Live-Mirror conceptual design for a hybrid dynamic structure: (a) the hybrid telescope optic (HTO) diameter 5m represented hybrid mirrors, top view & side view, separated by a lattice of variable force EAP actuators; and (b) the hybrid dynamic structure represented a sandwich of warpable glasses (in a blue sky) with the advanced EAP actuators and the operating system support for each component.

Such hybrid structures (Figure 45b) and its optical model will require a fast and efficient optical calibration model for a controlled surface image and its image surface calibration algorithms. Force actuator and sensor system work in combination with an optical metrology and solver control algorithm, integrated into a highly-parallel information network system allowing dynamic maintenance of a desired large-scale single mirror shape.

Optical calibration and modelization algorithms are outside scopes of this thesis, but they drive here the Live-Mirror actuators low-level specifications: (i) multilayer EAP actuators should correct global surface requiring deformations of several microns; (ii) shear EAP actuator should deal with local surface correction in small-scale order of $\leq 1\mu\text{m}$ i.e. surface polishing.

Live-Mirror Prototypes Proof-of-Concept

1. Displacement Measurement Techniques

1.1 Interferometric Dynamic Calibrator

The set-up for the displacement measurement over the Live-Mirror prototype is operated through an interferometric dynamic calibrator (Figure 46). This technique is used to validate the dynamic activity by measuring the deformation of the surface of the front glass, the control surface (S_c). To receive the positional signal back to the laser head, a small mirror was placed on S_c at the measured position. The sample was subject to a sinusoid voltage of 50 mHz. The built-in receiver system will record the positional motion in real-time and indicate it through a software interface as can be seen in Figure 46-Right. To map the S_c deformation on a 3D image with XYZ coordination, we considered the motion signal as the Z deformation and the XY coordinate plane as the S_c dimension. The small mirror was swept through S_c both horizontally (X-axis) and vertically (Y-axis) intending to measure the S_c deformation with centimeter resolution in each case.

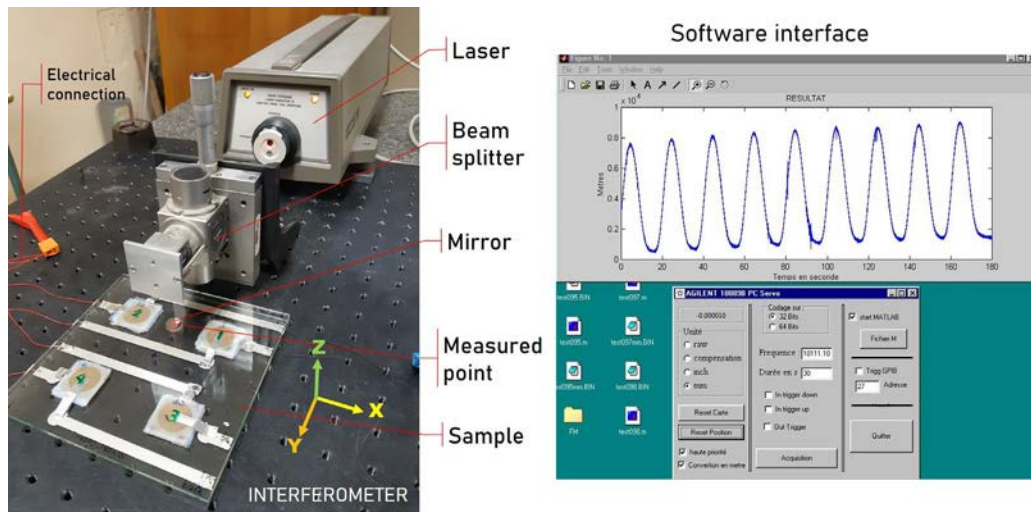


Figure 46 The interferometer dynamic calibrator setup with the Live-mirror prototype for measuring the deformation of the dynamic control surface (S_c) deformation under subject to an alternating sinusoidal input voltage. A high-resolution interferometer laser (AGILENT 5519A HeNe Laser System) is used to measure the displacement generated by an actuator which was driven by an alternating voltage input.

1.2 Zygo Interferometer Wavefront Analysis

In order to observe the full profile of S_c deformation from the Live-mirror prototype, the measurement was carried out using a Fizeau laser (633 nm) interferometer (Zygo verifire™), Figure 47. This technique can measure the transmitted wavefront of optical systems and assemblies. Note that this displacement measurement technique is unadaptable to the dynamic actuator operation. This means that the Live-mirror prototype is operated under DC voltage via Zygo interferometer measurement in order to provide the static deformation of the optic element by being to retain its activated shape.

The glass surface profile reveals many interference fringes with an intensity map (Figure 47–software interface) providing the information about the difference in optical path length. The surface profile of the sample can be obtained by the static fringe interpretation analysis using a Fourier transform to the intensity distribution and switches to the spatial frequency domain through the Zygo software interface. From the phase calculation-based fringe projection, we can obtain the three-dimensional surface plotting represented in (Figure 47–software interface).

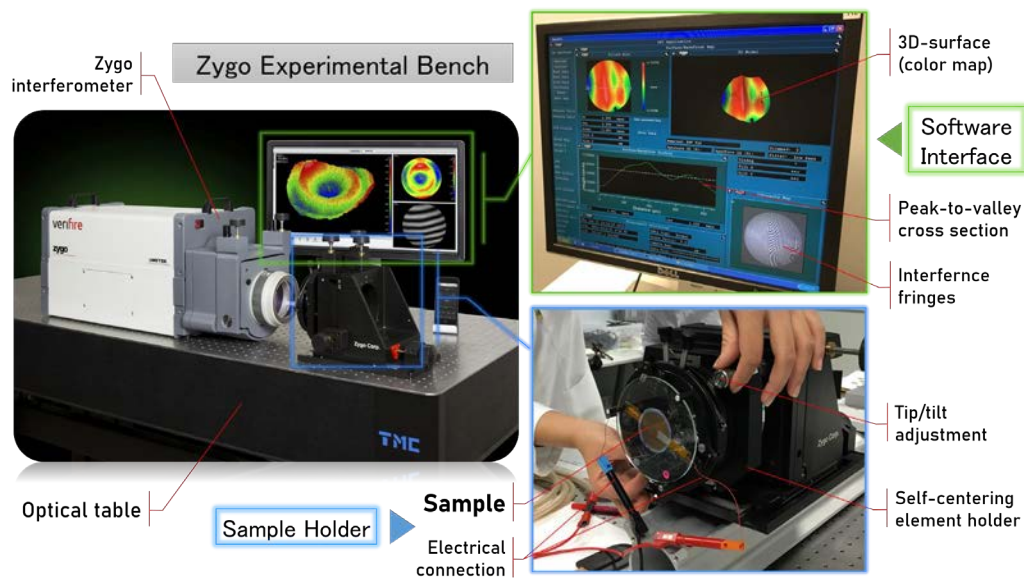


Figure 47 The Zygo interferometer experimental bench used for measuring the surface profile of the optical element. The prototype sample was held with the optic element holder that can be aligned in two axes of tilt. The sample was aligned to the front of the interferometer mainframe and connected to an external voltage amplifier.

2. Experimental Results

2.1 Single Stack Sandwich Prototype

In order to validate the proof of concept using the EAP actuator for controlling glass surface deformation, the plasticized terpolymer multilayer stack (with $n=8$ -layer stack, active area 20 mm-diameter) was integrated between two flat glasses hereafter called the “*sandwich prototype*.” The schematics and experimental tests are discussed in the following subsection.

a. Prototype Schematic

The first sandwich prototype consists of two 15cm square and 3mm thick flat glass sheets set in parallel with four inactive spacers at and the multilayer single stack at the center of the two glasses (Figure 48).

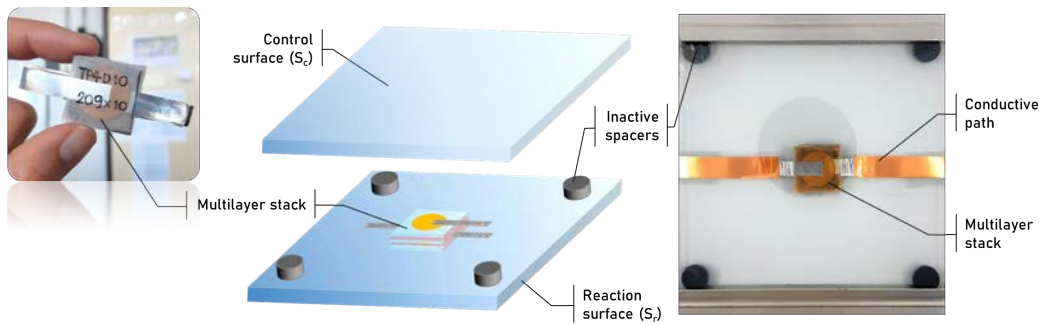


Figure 48 The sandwich prototype schematic of the EAP multilayer actuator: a single stack of 8-layer-terpolymer doped 10wt%DINP with electrodes with a diameter of 20 mm, as discussed at Chapter 3, section Multilayer Stack Fabrication.

b. Dynamic Deformation Preliminary Test

The results for the quasi-static displacement versus position of the glass under input electric fields of $10\text{V}/\mu\text{m}$ and $20\text{V}/\mu\text{m}$ are presented in Figure 49. The measurement of the glass surface deformation has been obtained via interferometric dynamic calibrator. The glass surface deformation attained the maximum value at the central position (actuated area) and gradually decreased when the measured position is farther from the actuated area.

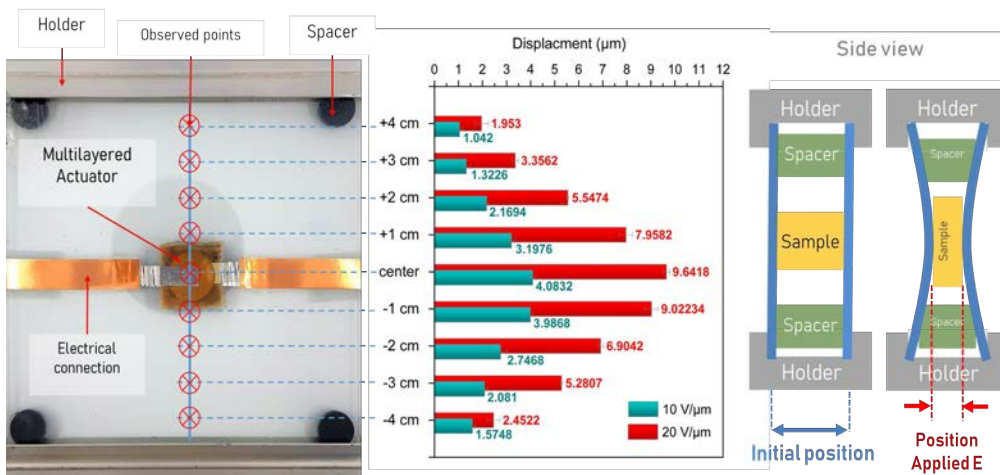


Figure 49 The proof of concept of the sandwich prototype—single multilayer 8-layer stack of plasticized terpolymer 10wt%DINP provides different deformation levels of two warpable glasses being pulled by the driven actuator at $E=10$ and $20\text{ V}/\mu\text{m}$.

One could ask why the slightly asymmetric behavior of the displacement plots. It is due to the fact that the holder clamp forces on the glass surface were not perfectly identical. In the end, the proposed device can achieve a deformation of 10 μm with a sufficient driven force. Deformation value fulfills the requirement of actuation performance in shaping Live-Mirror goal displacement in vertical direction correction by a few microns.

c. The Control Surface Profile of Sandwich Prototype – Single Stack

A longitudinal multilayer force-actuator stack of plasticized terpolymer (10wt%DINP) on glass has been validated: sandwiched between two commercial flat circular glass plates (110 mm in diameter and 3mm thick) referred to as the control mirror surface (S_c) and a reaction surface (S_r). These two glasses were set in parallel with three cylindrical inactive spacers ($\varnothing=0.7$ mm, the thickness of 2 mm), as presented in Figure 50a. The spacers are slightly thinner than the actuators so that the stack experiences a “preload” compression force of a few N/cm^2 .

The S_c fringe profile intensity of the circular sandwich prototype without actuation ($E_0 = 0 \text{ V}/\mu\text{m}$) (Figure 50b). The 3D surface plot of the S_c at field 0 and 20 $\text{V}/\mu\text{m}$ (Figure 50c). The result shows that the bump at the initial state of S_c was pulled down by the work of the multilayer actuator stack operated through an external applied electric field. Considering the difference between the two levels of deformation (with and without electric field), 2D cross-section lines (X-axis) were examined as shown in Figure 50d. The difference of the displacement (dz) in Figure 50d was obtained by subtracting the shape at a zero-electric field. In Figure 50d, the 2D cross-section lines are represented with the negative sign of dz that signifies a contraction of the glass sandwich in the z -direction. It was found that the magnitude of dz increases with an increase of input voltage excitation where maximum value is presented at the location of the center of the actuator. Also, the glass deformation amplitude, dz increases faster than linearly with field strength (c.f. Figure 3, page 53) as expected for the electrostrictive effect. We note that the actuator sample also expands in the transversal direction as the longitudinal actuator shrinks where the actuator stack is glued to the glass. This shear force is ignored here but will be considered and modeled in shear actuator assessments.

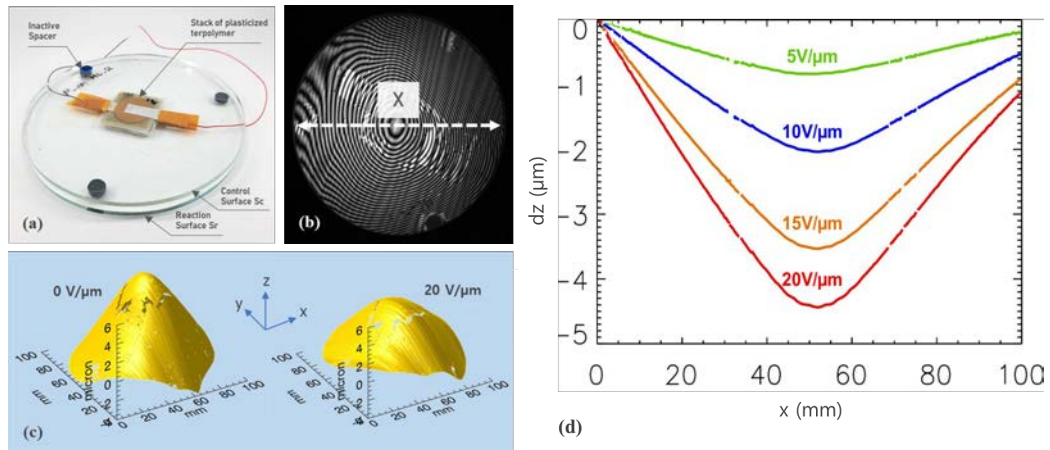


Figure 50 (a) An 8-layer stack of plasticized terpolymer 10wt%DINP sandwiched between two flat circular glass plates: reaction surface (S_r) and control surface (S_c). (b) The interferometric intensity fringes ($E = 0 \text{ V}/\mu\text{m}$) from the front glass control surface (S_c). (c) The 3D-surface for the S_c at $E = 0$ and $20 \text{ V}/\mu\text{m}$ is derived from interferometric fringes (b). (d) The change of the S_c along with a horizontal cut through the glass bump under different applied electric fields. All measurements were done with a Fizeau laser (633 nm) interferometer (Zygo® verifire™).

Our proof-of-concept actuator multilayer stack creates a controllable contraction in the z -direction when it is sandwiched between glass surfaces. The overall glass separation deformation, accounting for both surfaces, is about 10 microns for conventional high voltage drivers. Since EAP actuators are relatively inexpensive and can, in principle, be created on glass using typical additive manufacturing methods, we believe this technique is promising for the development of precise and fully 3D printed large active optical mirror surfaces.

2.2 Four-Actuator Stacks Sandwich Prototype

As a validation for an EAP multilayer stack actuator, here we advanced the sandwich prototype from a single actuator to a multi-actuator allowing the possibility of applying the input voltages independently or simultaneously.

a. Prototype schematic

This multi-actuator Live-mirror prototype was structured with four identical 8-layer plasticized (10% DINP) actuators sandwiched between two

flat 3mm thick ($14\text{cm} \times 16\text{cm}$) pieces of glass - control S_c and reaction S_r surfaces. Each actuator was located apart (pitch) from its neighbors by 8 cm, and separately connected through silver adhesive electrical paths. The schematic of the four-actuator stacks sandwich prototype is illustrated in Figure 51.

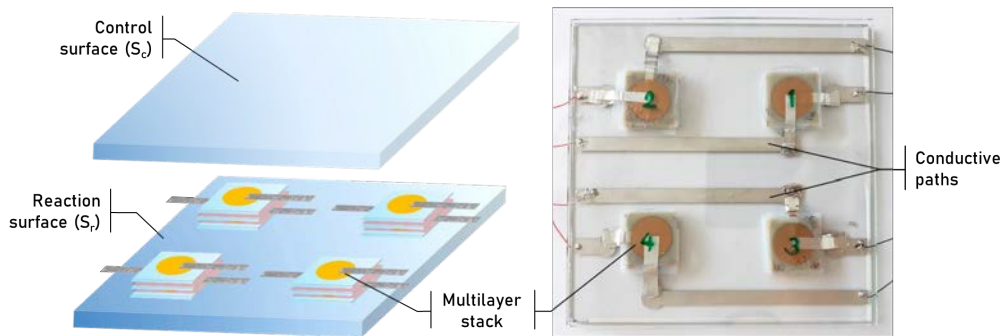


Figure 51 Four-actuator stacks sandwich prototype with four 10-layer stacks of terpolymer doped 10wt% DINP with their electrode diameter size of 2cm implemented between two square ($14 \times 16\text{cm}$) window glasses 3 mm thick.

b. Optical Control Surface Deformation: Experimental VS Simulation

The optical control surface (S_c) deformation of the four-actuator sandwich prototype was evaluated through a laser-interferometric dynamic calibrator. Figure 52 presents the results obtained in the lab (left column Figure 52a,c,&e) and the evaluation models using COMSOL Multiphysics® simulations (right column Figure 52b,d,&f). The S_c deformation was examined under two different conditions regarding the levels of input electric field and the actuated actuator position, (I) actuators #1 and #2 are subject to $E_{12}=10 \text{ V}/\mu\text{m}$, and actuators #3 and #4 are subject to $E_{34}=13 \text{ V}/\mu\text{m}$; (II) actuators #1 is subject to $E_1=10 \text{ V}/\mu\text{m}$ and actuators #2, #3 & #4 are turned off ($E_{234}=0 \text{ V}/\mu\text{m}$). The surface deformation in the lab was mapped sweeping through S_c of the prototype with a resolution of 1 cm. As expected, a similar deformation pattern S_c was confirmed by COMSOL simulations.

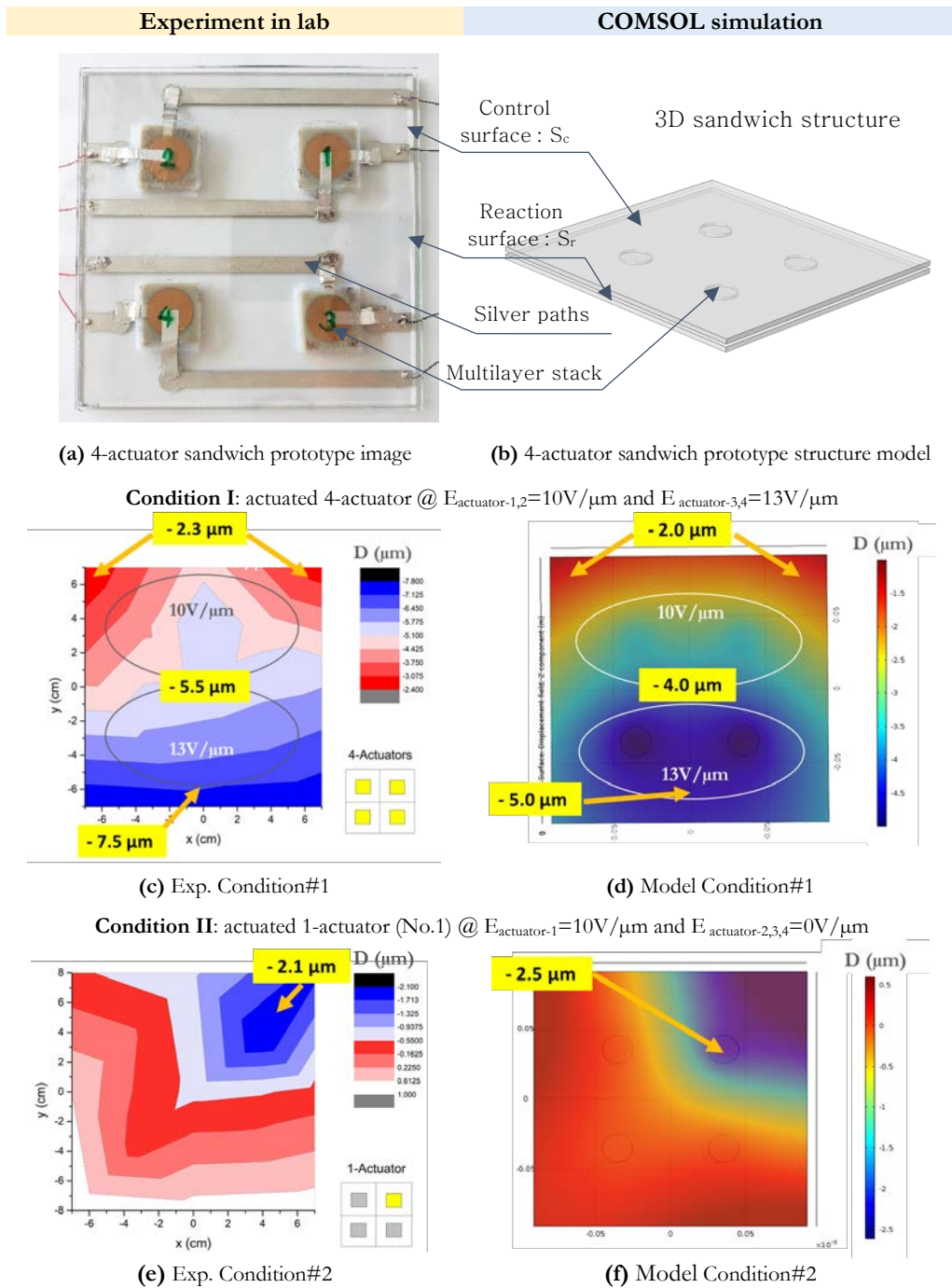


Figure 52 (a) A glass sandwich with a four-stack of actuators in a square distribution and (b) as modeled via COMSOL™. The strain mapping results for the control surface (S_c) laser-interferometrically measured are: (c) four actuators “on” under $E_{12}=10\text{V}/\mu\text{m}$ for actuators #1 and #2 and $E_{34}=13\text{V}/\mu\text{m}$ for actuators #3 and #4; (e) $E_1=10\text{V}/\mu\text{m}$ for actuator #1 “on” and $E_{234}=0\text{V}/\mu\text{m}$ actuators #2, 3 and 4 “off”. (d) and (f) show the modelization and simulation results respectively for the (c) and (e) configurations.

The lab results are in accordance with the results for the optical control surface (S_c) evaluation as presented in Figure 52. They demonstrate that the S_c deformation increases as a function of the applied voltage, leading to higher deformation in the area around actuators #3 and #4 under the test condition (I) represented in Figure 52b and e. In test condition (II), actuator #1 was controlled individually (Figure 52c) and the similar S_c deformation pattern is confirmed by simulation (Figure 52f). Such a procedure provides a + degree of freedom to local control the optical surface. When the experimental result ($D=2.1\mu\text{m}$) in Figure 52c is compared with the simulated result ($D=2.5\mu\text{m}$) in Figure 52f, the slight difference is likely due to the fact that the multilayer stack actuator contains a soft conductive adhesive interlayer which was neglected in the model simulations.

Referring to the unconventional behavior of plasticized terpolymer current and saturation polarization issue in chapter 3, we involved the Debye/Langevin formalism in the modeling part to analyze the electromechanical coupling of the plasticized terpolymer operated under high electric field ($E \geq 10 \text{ V}/\mu\text{m}$). By estimating the absolute permittivity under high voltage which corresponds to the non-linear behavior of Eqs. (14) and (16) it is possible to evaluate the strain response under high input electric field ($S_{(E \gg E_0)}$).

Subsequently, such architecture and the confirmed results by simulations significantly enhance the active surface spatial resolution, i.e. a precise and a local mirror control. The EAP multilayer stack force-actuator is intended to act (shaping) the mirror wavefront via longitudinal strain following possible local changes in the glass global optical surface (one of Live-Mirror high-level specifications).

c. The Control Surface Profile of the Sandwich Prototype- Four Stacks

The four-actuator sandwich prototype layout is based on four actuators stacks sandwiched between two circular glasses (110mm in diameter and 3mm thick). Each actuator is composed of 10-layer of terpolymer+8%DINP with their electrodes (10 mm in diameter) and individually connected to their electronic paths (Figure 53).

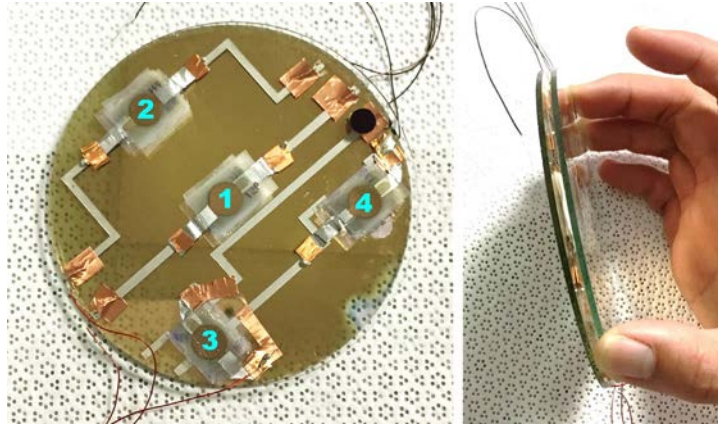


Figure 53 The four actuators sandwich prototype: 10-layer of terpolymer+8%DINP with their electrodes (10 mm in diameter) and individually connected to their electronic paths.

The results show how the four actuators (Figure 54a) deform the control surface (S_c) under different levels of voltage inputs (2.0 to 4.5kV) examined on cross-section line (blue-dash) passing through S_c optical aperture and with actuator #1 actuated (Figure 54b). Note here that the measurements describe the actuated state deformation at n kV (Z_{nkV}) being subtracted from the inactivated state (z_0) representing the variation in S_c deformation (dz). View to simplification two voltage inputs of 2kV (red line) and 3kV (pink line) was applied to a variety of actuator positions presenting dz of the cross-section (blue dash) line (Figure 54c).

The results of both sandwich prototypes (single actuator and multi-actuator) have an issue on border effects: from cross-section plots in Figure 54c, the sample border was lifted over z_0 (light orange dash line) when the prototype was operated under driven electric fields. This issue is due to the holding points set up on the border of glass sandwich prototypes. Holding setups will be addressed in the further sections for precise measurement technique.

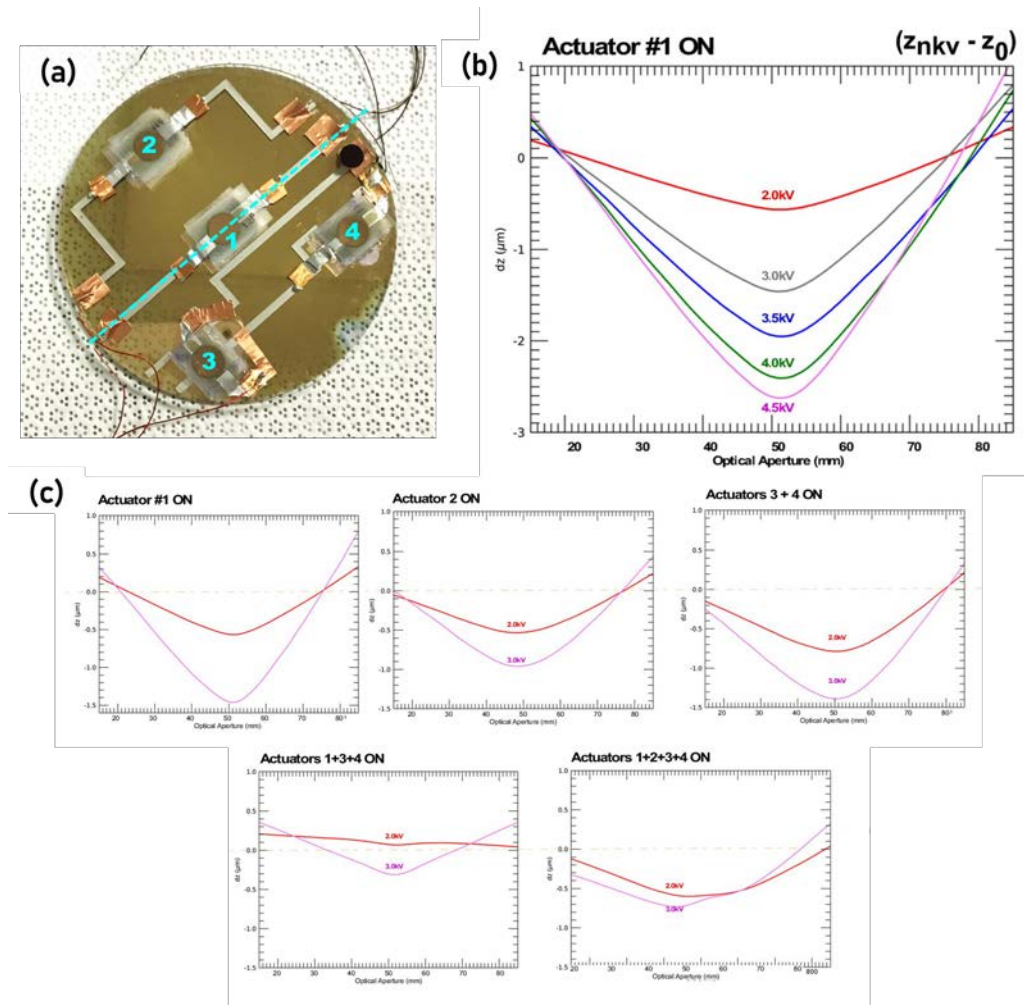


Figure 54 The S_c deformation of four-actuator stacks sandwich prototype: (a) the top view prototype presents the actuator positions and the examined cross-section line passing through S_c optical aperture; (b) the S_c deformation, dz of cross-section line when the actuator no.1 was actuated; (c) two voltage inputs of 2kV (red line) and 3kV (pink line) were applied to a variety of actuator positions presenting dz of the cross-section line.

2.3 Shear Actuator Proof of Concept

We demonstrate here the shear effect generated by terpolymer actuators that shape the glass surface via transversal shearing force. Such transversal shearing force is intended to correct local and small-scale glass surface-induced defects – hereafter dubbed as *electronic-polishing*. The deforming/acting optimally on the optical surface with the shear stress

actuation generated by the transversal strain of the EAP actuator is by now called the shear prototype.

a. Shear Prototype Design

A proof of concept design for a shear actuator is presented in Figure 55: a terpolymer filled with 8wt% DINP thin film and coated with gold (40mm in diameter) on both sides (top-bottom) of the electrode was silicone adhesive glued on a single circular glass sheet (110mm in diameter and 3mm thick) control surface (S_c). The same setup was also used to access analysis on shear transferring effect on multilayer structures fabricated layer-by-layer as the EAP multilayer stack illustrated in Figure 40, page 117.

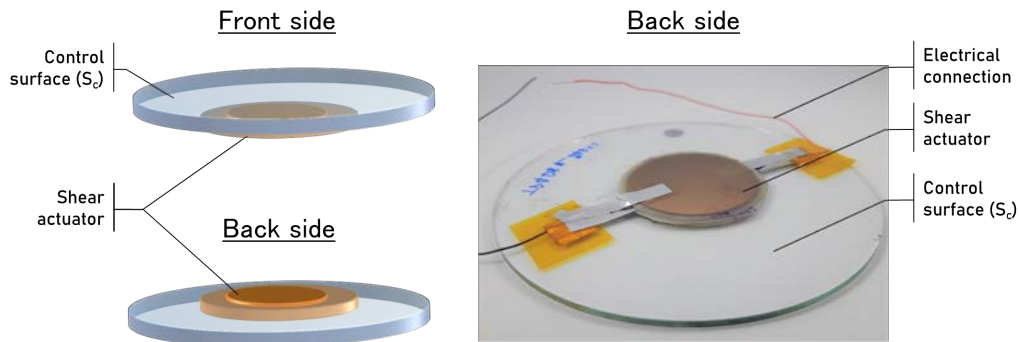


Figure 55 The EAP shear prototype design: a terpolymer filled with 8wt% DINP thin film and coated with gold (40mm in diameter) on both sides (top-bottom) of the electrode was silicone adhesive glued on a single circular glass sheet (110mm in diameter and 3mm thick) control surface (S_c).

b. Shear Actuator for Glass Deformation

How the actuator transfers a shear force to the glass? – View to simplification a schematic shear actuator for a single layer is illustrated in Figure 56. The production of a transversal strain (S_{31}) depends on the applied electric field (E) to the terpolymer actuator: when $E \neq 0$ the glass surface is bent down when under the expansion and transfer of transversal strain from the terpolymer actuator single layer (Figure 56b), or/and from the terpolymer actuator composed of a multilayers structure (Seg1 + Seg2 + Seg3) (Figure 56c). The shear stress performance can be described by the ability to transfer force-generated through actuator layer thickness. In the particular case where the equal division of actuator layer into 3 segments (Seg1 + Seg2 + Seg3),

the generated stress total stress (s) is produced from $s_1 + s_2 + s_3$ where $s_1 < s_2 < s_3$. Seeking to accomplish the maximum deformation of the glass surface produced by the shear actuator, one would optimize the global actuator thickness/number of layers (Seg1 + Seg2 + Seg3) in the multilayer structure.

The maximum displacement (D_{pp}) of the control glass surface (S_c) increases as a function of an applied electric field (E) and EAP number of layers (Figure 57) and present a saturation behavior for No. Layers between 4 to 5, i.e. the total thickness of deposited layers reached ~ 1 mm. However, the stronger electric field can drive the EAP actuator to create higher transversal strain (S_{31}) as well as reinforce the ability to transfer shear force from the top EAP layer in the multilayer structure. Thus, the S_c deformation of the shear actuator configuration can be limited by an intensity of applied electric field and the EAP thickness or number of layers in the multilayer structure.

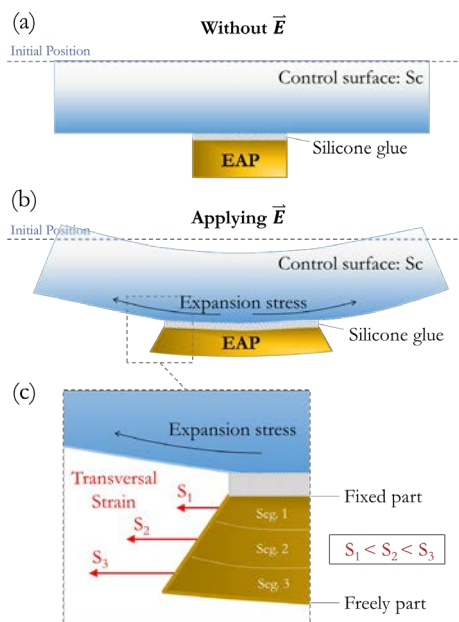


Figure 56 The 2D illustration of shear actuator prototype: (a) without applying an electric field, (b) under an applied electric field, the glass surface is bent down by the expansion stress from the EAP layer, and (c) the divided segments of the EAP layer showing the ability to transfer their transversal strain.

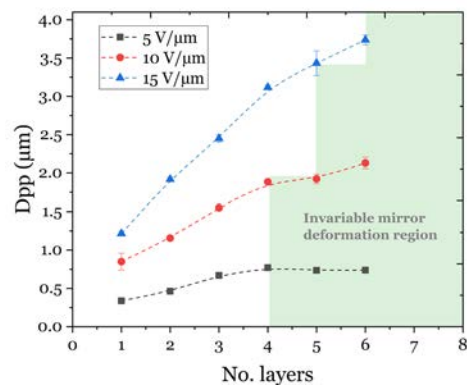


Figure 57 The maximum displacement at the center of S_c of the shear prototype versus the number of EAP layers in the multilayer structure operated under three different levels of applied electric fields. Each layer of the EAP is made from terpolymer+10wt%DINP 225 μ m-thick. The invariable deformation region presents the mirror deformation being settled after reaching a certain total thickness of the actuator.

c. Multilayer Shear Actuator Prototype

To investigate the shear transversal strain force on a glass surface (S_c), a multilayer EAP proof-of-concept was developed as showed in Figure 58a: a single 2mm thick glass surface S_c with an integrated 8%DINP terpolymer 4cm in diameter circular actuator. The control surface deformation (S_c) was assessed using the Zygo laser-interferometer. Once again, we analyze the cross-section lines at (X,0) and (0,Y) through S_c (Figure 58a) to observe the deformation level in different working conditions (different applying electric field). As showed in Figure 58b and c, the S_c is significantly bent downwards when induced by a transversal strain from the EAP actuator operated under external electric fields from 0 to 18V/ μm . As expected, a multilayer setup improves consequently the control optical surface displacement D , i.e. 3 \times for a 5-layers compared with a single layer shear actuator.

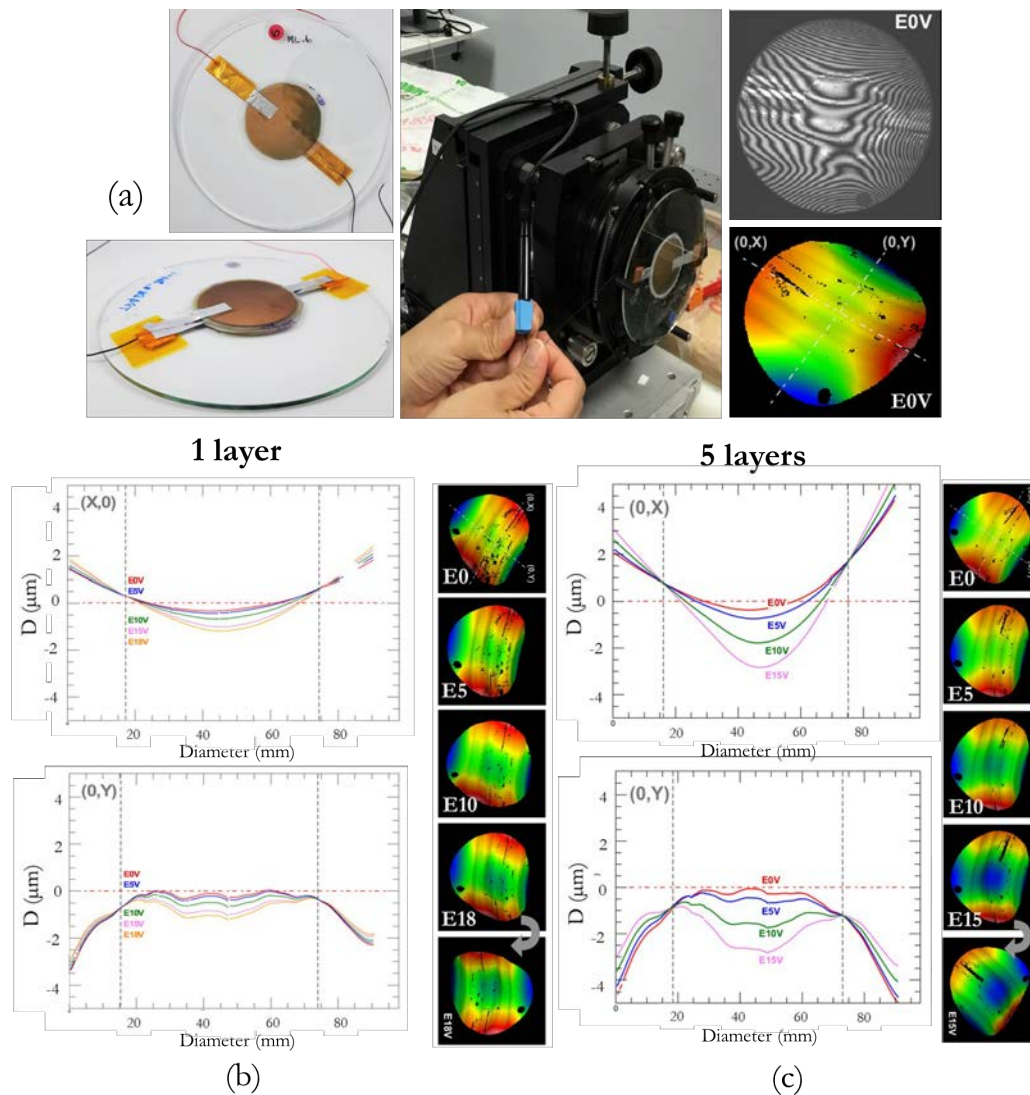


Figure 58 (a) A multilayer EAP shear actuator proof-of-concept: a single 2mm thick glass optical surface S_c with an integrated 8%DINP terpolymer 4cm-diameter circular actuator. (b) and (c) show 3D intensity plots on the $(0,X)$ and $(0,Y)$ orthogonal sections for the control optical surface deformation D_z respectively produced by the one-layer and the 5-layer under an electric field E from 0 to $18\text{V}/\mu\text{m}$ applied in a thickness direction.

d. Adhesive Interlayer Shear Effect of Multilayer Shear Actuator

We have demonstrated that the S_c deformation of the shear actuator configuration can be limited by the input voltage and the EAP thickness or its number of layers. Another possibility that can lessen the actuation performance by the shear actuator multilayer configuration is the optimization of the Young modulus (Y) of adhesive interlayer: if too soft (low Y) might cause mechanical absorbing energy between actuator layers; if too rigid (high Y) might cause a blocking actuator deformation.

For the sake of simulations (via COMSOL Multiphysics), a simplified shear actuator multilayer configuration model is presented in Figure 59a. Under the electric field of $10\text{V}/\mu\text{m}$, the shear actuator stack is squeezed and transfers its shear stress to deform the glass surface as shown in Figure 59b. This model result also confirms the visual explanation in Figure 56 showing how the multilayer shear actuator works.

As simulated in Figure 60, the increase in the Young modulus of the adhesive interlayer (Y_{Adhesive}) (0.5 to 50 MPa) integrated into the six layers shear actuator model impacts the shear force transferring between actuator layer and the glass substrate. Figure 60 reveals the stress distribution, i.e. stress concentration, of the multilayer shear model constructed with five different Y_{Adhesive} values operated under a constant electric field.

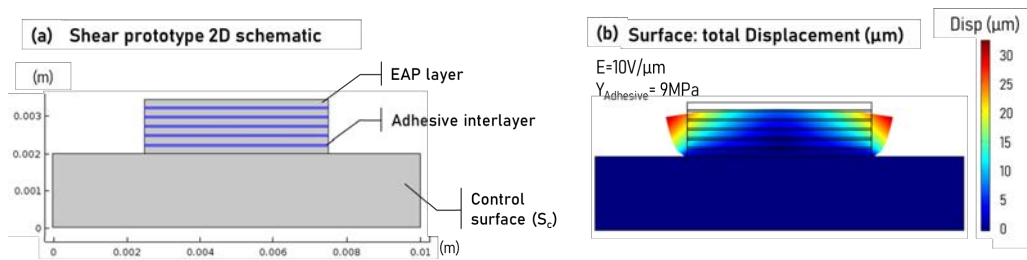


Figure 59 The simplified shear prototype 2D model analysis: (a) shear actuator multilayer geometry: a six-layers $200\ \mu\text{m}$ thick each, a 5mm in diameter of the gold electrode, five adhesive interlayers $50\ \mu\text{m}$ thick, applied on a glass substrate 2mm thick and 10mm diameter in diameter; (b) total displacement generated by 6-EAP-layer under for an applied electric field excitation $10\ \text{V}/\mu\text{m}$.

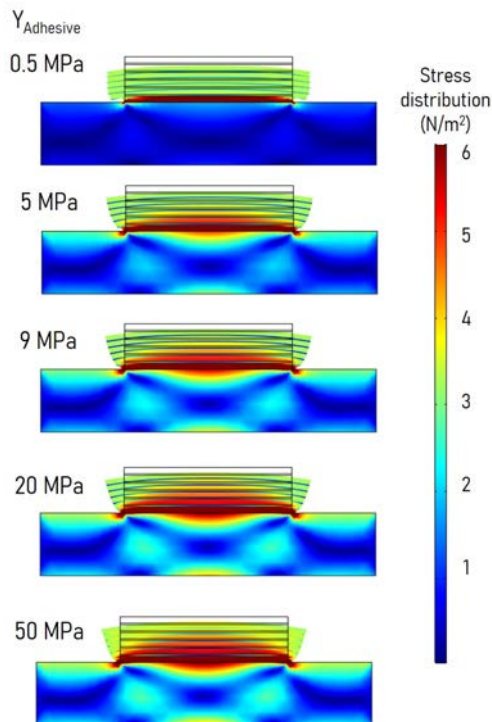


Figure 60 Stress distribution (von Mises stress) analysis of multilayer shear prototype assembled with different Young modulus adhesive interlayer for studying shear stress transferring effect. The sample was analyzed under $E=10V/\mu\text{m}$ with six EAP layers.

As expected, the Young modulus of the adhesive interlayer gain improves the ability of stress transferring generated by the EAP shear actuator as demonstrated when analyzing the stress distribution (Figure 60). exhibits evidence for this shear effect. Considering the normalized achieved displacement at the center of S_c (the ratio of achieved central displacement to the maximum central displacement) presented in Figure 61, the optimized Y_{Adhesive} should be higher than 20 MPa in order to reach the maximum ability of EAP stress transferring. As demonstrated in Figure 62, the simulated normalized central displacement results validate the experimental S_c measurement $Y_{\text{Adhesive}} \approx 9 \pm 1$ MPa, which shows the same trend reaching maximum deformation when the EAP total thickness being approximately 1mm ($\approx 4-5$ EAP layers).

However, when improving Y_{Adhesive} to very high values will limit the deformability/expansion stress of shear actuators. In such a way, the $Y_{\text{Adhesive}} \approx 20-50$ MPa is the better choice being an optimized adhesive layer for the multilayer shear actuators prototype.

As expected, the Young modulus of the adhesive interlayer gain improves the ability of stress transferring generated by the EAP shear actuator as demonstrated when analyzing the stress distribution (Figure 60). exhibits evidence for this shear effect. Considering the normalized achieved displacement at the center of S_c (the ratio of achieved central displacement to the maximum central displacement) presented in Figure 61, the optimized Y_{Adhesive} should be higher than 20 MPa in order to reach the maximum ability of EAP stress transferring. As demonstrated in Figure 62, the simulated normalized central displacement results validate the experimental S_c measurement $Y_{\text{Adhesive}} \approx 9 \pm 1$ MPa, which shows the same trend reaching maximum deformation when the EAP total thickness being approximately 1mm ($\approx 4-5$ EAP layers).

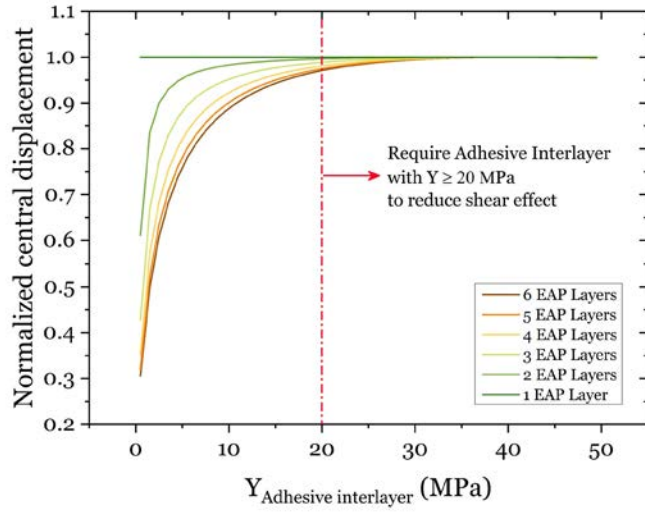


Figure 61 The normalized S_c center displacement of shear actuator multilayer topology of 1 to 6 EAP layers under $E=10V/\mu\text{m}$ as a function of the different Young modulus of the adhesive interlayer.

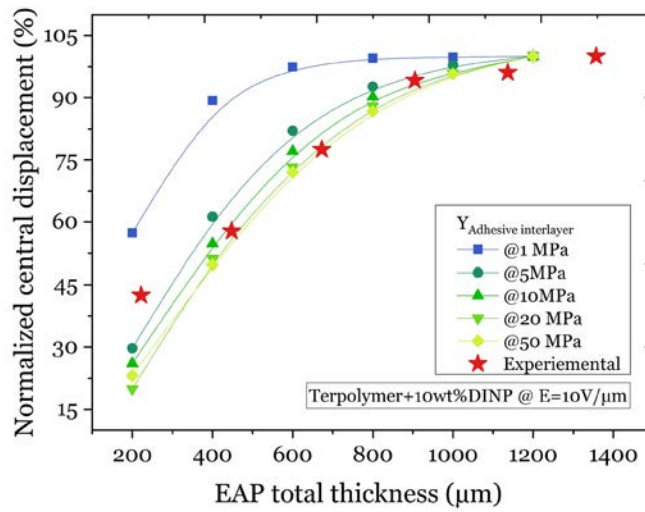


Figure 62 The normalized S_c center displacement from the experimental test in lab and S_c data simulation as a function of EAP total thickness driven by $E=10V/\mu\text{m}$.

In the end, the ability of the shear actuator to transfer shear stress to the mirror substrate/control optical surface (S_c) depends on; (1) the active area (electrode) of the EAP actuator, (2) the EAP total thickness, i.e. the number of EAP layers, (3) the level of the driven electric field, and (4) the

Young modulus of the adhesive interlayers constructed within the multilayer topology.

The experimental result of the shear-actuator prototype confirms the feasibility of using force-actuators acting/deforming the glass through its shear mode via its transversal strain. The shear actuator enlightens the possibility to deform an optical surface locally corresponding to its shape and size which will validate the 3D printing technology for the EAP actuator application, i.e. to 3D printed specific actuator shape suited for local and specific surface defects and operating via shear-mode.

Summary

In chapter 4, the description of the Live-Mirror project including research objectives and perspectives were presented. The main scope of this chapter is to introduce the proof of concept prototypes to validate and to improve the level of readiness of active mirror making use of the novel technology of EAP actuators. We demonstrated the possibility to overcome mirror surface deformation employing the plasticized terpolymer actuator through to categories for the proof of concept: (1) *sandwich prototype* in a favor of global surface adjustment, and (2) *shear actuator prototype* with the aim of local surface correction. Our experimental results demonstrated and validated surface deformations of several microns under reasonable load conditions. Such a level of deformation is fully compliant to control large optical telescope mirrors surfaces - a major and crucial goal for the Live-Mirror project.

CHAPTER 5

3D-Printed EAP Actuator

CHAPTER 5

V. 3D-Printed EAP actuator

Through an interdisciplinary Live-Mirror project, the full-printed force-actuator has been developed as an advanced EAP actuator to challenge live, light, and large optical telescope applications. In precedents chapters we have presented the method-classical technique; the thin-film casting, to fabricate the optimized EAP actuator and its multilayer structure. In this chapter, we present the novel EAP production process using here developed 3D printing technology. From handcrafted proof of concept to more advanced automated manufacturing, the fully printed multi-EAP-actuator prototype is presented in Figure 63. The single full-printed actuator consists of three printed polymer layers of a modified EAP terpolymer doped plasticizer DINP sandwiched between two layers of conductive terpolymer composite. The conductive layer has been developed here integrating terpolymer with carbon black nanoparticles for achieving a printable electrode. By using the same base material-terpolymer in the EAP and the electrode layer, we are able to address the complexity of chemical compatibility and make the printed actuator enabling it to be operated under high voltage excitation. The full-printed prototype was produced in many configurations and the electromechanical activity through shear actuation mode was investigated.

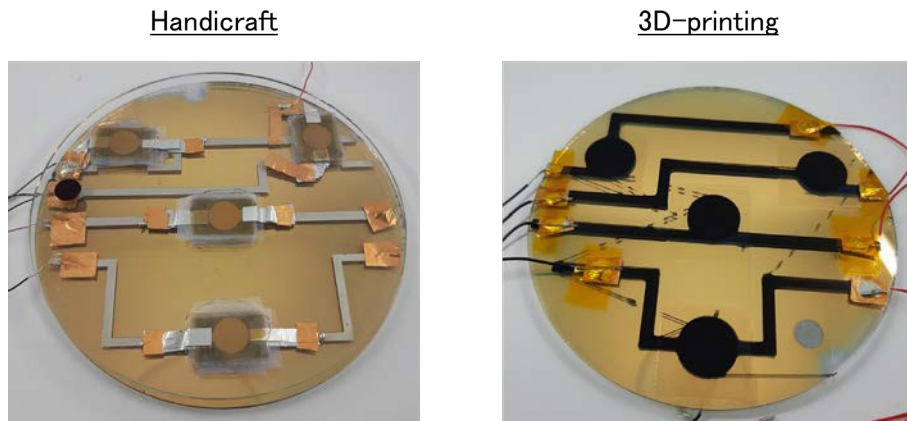


Figure 63 The evolution of Live-Mirror proof of concept presents: (left) the film casting handcrafted four actuators configuration, and (right) the same setup configuration 3D-printed.

The 3D-printed actuator was printed on the flat window glass that represented an active telescope mirror. From a conventional EAP actuator to a full-printed actuation device, we are able to show the possibility to create a free-form actuator. Importantly, 3D-printing technology is a promising step that opens the door to a large-area of electromechanical devices and actuator applications.

Dielectric Elastomer Printing

The 3D printing technology ultimately provides several advantages to diverse materials processing, such as rapid prototyping, and prints an object from a computer-aided design (CAD). In the field of additive manufacturing, 3D printer industries have developed printer adequacies serving the demand for customized products. To overcome the time-consuming process, a complex structure fabrication, and unique shape products, it is necessary to exploit the advantages brought by developments in 3D printing technological advancement. In particular, flexible printed materials have been attractive for large-area electronic devices, e.g., wearable electronics of 3D printed: tactile sensors^[127]; cellulose nanocrystal scaffolds for specific cell integration^[128]; photo-detectors^[129]; and soft dielectric elastomer actuators^[130]. The common technique used to build a structure of any desired shape of dielectric elastomer

printing is material extrusion ^[131]. This 3D printing process allows kinds of materials to be extruded to build up a platform along a predetermined path. The main and critical issue for this printing technique is to deal with the use of a fluid or solution-based material which requires the control of a variety of parameters that characterize the material/solvent: solvent evaporation rate, viscosity, flow regulation, mould temperature, chemical compatibility for multi-material structure, etc., in order to achieve an efficient and reproducible printing process.

Recently, we reported the possibility of using an EAP based modified terpolymer as a force-actuator system in a “Live-Mirror” prototype^[43,132]. Because of our intention to develop the actuator manufacturing process, the immediate challenge to the 3D printing technology results in a major implication on the smart force-actuator system. We aim to assemble a unique actuator shape and to integrate actuators precisely into certain mirror positions (pitch). To accomplish the force-actuator additive manufacturing approach, we apply the material extrusion technique to the 3D printing process.

3D-Printing Technique Interfaces

In order to use the material extrusion technique, we make use of a Hyrel 3D System 30M^[133] printer which runs a proprietary RepetierTM software and firmware. Such a printer system allows creating printing paths through regulated GCODE files (a computer numerical control programming language) following the various designs of 3D shapes, i.e. a 3D printer STL files (format native to the stereolithography (STL) CAD software created by 3D Systems). The software and processes are illustrated in Figure 64 to Figure 66. We obtained a consistent material deposition for the printed EAP plasticized terpolymer film with a thickness between 90–100 μm and the printed electrode layer, the conductive terpolymer composite, with a thickness between 15–20 μm . The main printing procedures are described as follows;

1) Create a 3D object: OpenSCAD

OpenSCAD documents are human-readable scripts which are mostly used to design 3D printed parts and exported into STL format. The example script for creating a printed electrode layer is illustrated in Figure 64.

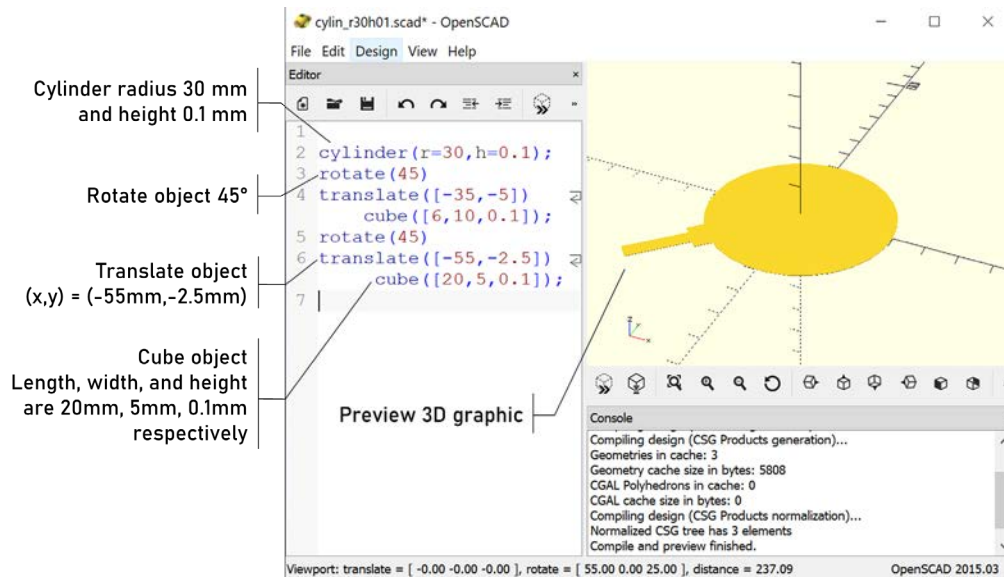


Figure 64 The OpenSCAD software interface used for creating 3D objects and rendering into the STL file.

2) Input & build printing paths of 3D object: Repetrel & Slic3r

After the STL file is created, this 3D object will be placed on the simulated printing bed in the Repetrel program. To accomplish the printing paths, Slic3r (a Repetrel's plug-in software) is used to generate G-code from 3D CAD files (STL or OBJ). The printing paths are generated depending on the input parameters (first layer thickness, printing pattern, line density, etc.) within Slic3r software. All of the printing parameters are presented in the following section. Here we proposed additional lines in G-code added manually in order to avoid the unwanted drop from printing processes on the glass substrate as illustrated in Figure 65. These starting and ending codes are usually added manually before the printing job begins.

```

;---
; heading codes to be added

G0 Z3 ; quick move (G0) & lift up the printer head 3mm from printer bed

G1 X120 Y120 F7800 ; normal move (G1) with speed 7800mm/min (F7800) to the
starting position (X=120mm, Y=120mm) on printer bed

G1 Z0.1 F7800 ; normal move & set the printer head 0.1mm apart from printer bed

G1 X120 Y120 F7800 ; normal move to the starting position of printing pattern

G1 X120.25 Y120 E0.0067 F1200 ; normal move to from X=120 to X=120.25 with
material extrusion 0.0067 mm3 calculated automatically by Slic3r

...

; ending codes to be added

G1 X150 Y150 F7800 ; normal move to the end position of printing path

G0 Z3 ; quick move & lift up the printer head before move back to origin

G92 E0 ; set position (move back to origin position) without extrude material

;---

```

Figure 65 The Gcode example used for consistent material deposition additionally with the code to avoid the residual drop from the printing process.

3) Printed EAP layer

After finishing the printing job, the wet film layer on the glass substrate (Figure 66c) is required to be slowly dried at room temperature, in such a way the sample will be ready to print the next layer on the top of the dried precedent layer. The duration of solvent evaporation depends on the solvent content and thickness of the sample presented in the following section.

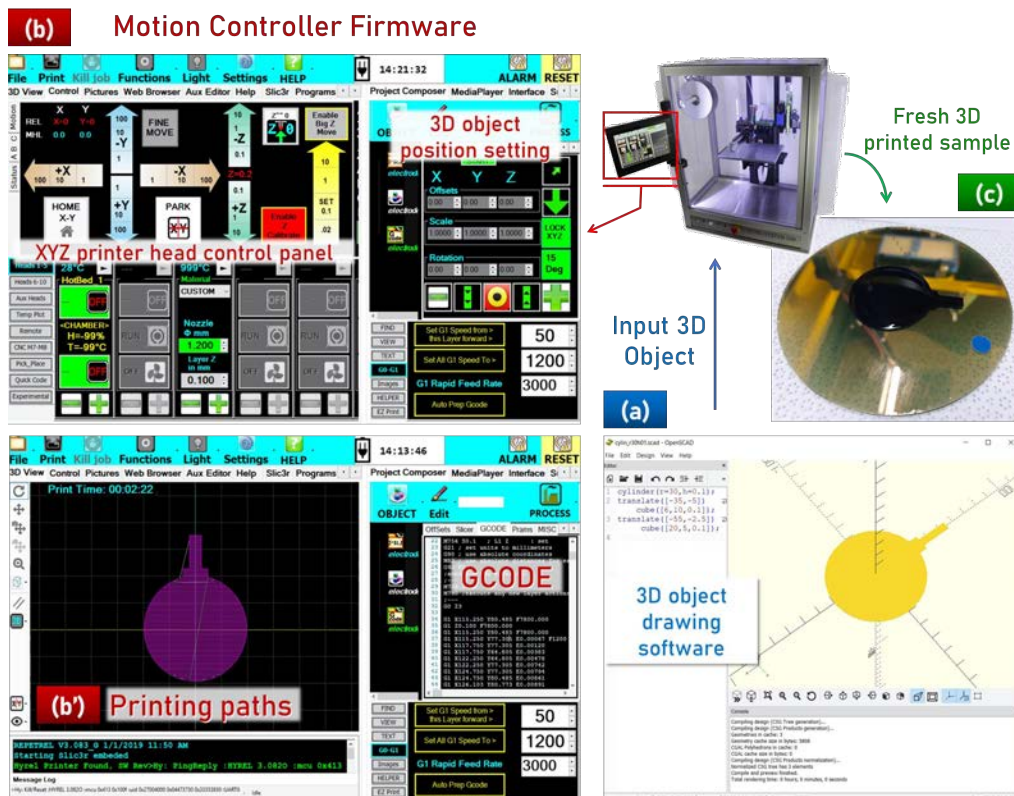


Figure 66 The software interfaces used to assemble the full-printed EAP; (a) OpenSCAD freeware for creating 3D object-based script modeler, (b) Repetier software and motion controller operated through GCODE represented on (b'), and (c) the printed EAP electrode layer collating with the input object.

Printable Electrode Investigation

1. General Electrically Conductive Ink Composite

There are several types of high conductive printable inks, such as nanoparticle colloid suspensions, organometallic inks, conductive polymers, carbon nanotubes, graphene oxides, and reactive inks^[134]. These conductive inks reveal their high potential when implemented for flexible and stretchable electronic devices. Most of the metallic based conductive ink requires sintering to reach a good conductive range and bulk content. Generally, sintering procedures of some conductive inks, e.g. silver ink, operate at temperatures of 150° C and above. However, the stretchable electronic applications need to be

fabricated at low temperatures to prevent sample damage and/or degrade incorporated materials. Dearden et al.,^[135] reported the possibility to reduce sintering temperatures of organometallic inks below 150° C.

We examined two conductive inks, commercial silver (Ag) ink and carbon black (CB) ink, as a layer to the printable electrode. The test was carried out by printing the conductive inks on the glass as the 1st layer. After the conductive layer solidified by the sintering process (both Au and CB inks being annealed under 130° C), the plasticized terpolymer layer was printed over the 1st layer. As shown in Figure 67, both conductive inks are incompatible with the EAP layer, which was damaged when incorporating those inks. Note that the solvent used for the preparation of the electrode ink belongs to the class of dipolar aprotic solvents, e.g. N-Methylpyrrolidone, dimethylformamide, and dimethyl sulfoxide, which is the same class of MEK (methyl ethyl ketone) solvent used to dissolve wide-ranges of polymers^[14]. Such an interaction between MEK class solvent and conductive layers explains and guides us to the right choice of conductive inks to doped terpolymer actuators design.

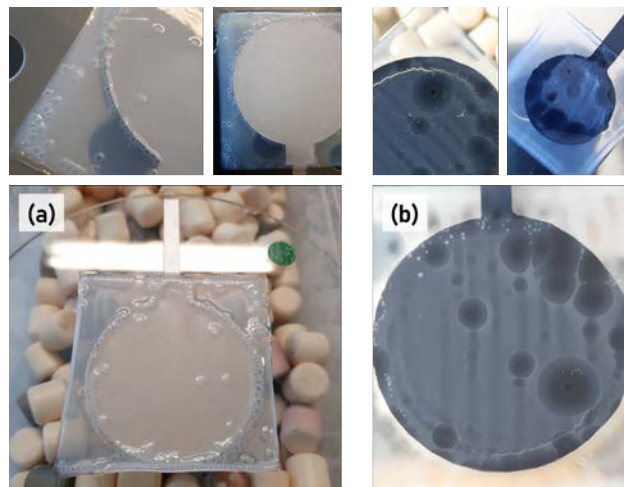


Figure 67 The result of using commercial conductive inks (a) silver ink and (b) carbonblack ink to incorporate with the printed EAP composed of terpolymer+DINP based MEK (methyl ethyl ketone) solvent reveals their incompatibility.

Other possibilities are to have the printable electrodes made of intrinsically conductive polymers (ICP) and/or conductive polymer composites (CPC). Even though ICP or CPC have lower conductivities than metallic ink, the advantages of their compliance, low cost, non-brittleness, light-weight,

and biocompatibility have led many researchers to develop and improve their electrical conductivities for flexible actuator and sensor applications. Numerous studies of ICP or CPC for electronic applications have led to the following results;

- (1) A stretchable scaffold made from an intrinsically synthesizing variant of PEDOT:PSS was described to develop soft and skin-like semiconductors and conductors ^[76];
- (2) Evoprene 007 (EVO) was used for a polymer host doped with carbon black powder to be a smart flexible sensor ^[75];
- (3) Elastomer ethylene vinyl acetate EVA doped with graphite and CNC-assisted was developed as a three-dimensional flexible electrically conductive structure for soft robotics applications ^[114].

Hence, ICP and/or CPC could intimate the printability to avoid an incompatible solvent interaction between the electrode and EAP layers. Particularly, CPC materials, the high-temperature production process is unnecessary for material fabrication. In the end, in order to demonstrate the printability of materials, numerous parameters must be considered, e.g., compatibility between conductive inks and substrate or cooperative materials, wettability (substrate-polymer), surface bonding (polymer-polymer), curing temperature, etc. Considering those all parameters, we improve the CPCs derived from the same terpolymer base doped with CB nanoparticles to be the optimized printable electrode to the doped terpolymers based actuators developed here.

2. Conductive Terpolymer Carbon Black Composite

Terpolymer/CB composite is the more compliant to be the printable electrode for the full-printed EAP actuator. The fluorinated terpolymer P(VDF-TrFE-CTFE) filled with carbon black powder (Vulcan XC72R) was prepared using the solution blending method to produce an electrically conductive ink for this work. The material preparation process, the mechanical and electrical characterizations of terpolymer/MEK/CB were described in chapter2, section Conductive Terpolymer/Carbon Black Composite, page 80.

The electrical characterization of the terpolymer/CB ink reveals that the ink reaches a conductive region with a conductivity of 0.57 ± 0.02 S/m. The percolation threshold at which the composite becomes a conductive

material was found in the terpolymer doped CB over 5wt%. Even if the terpolymer/CB ink has quite low electrical conductivity in comparison to other metallic materials, its ability to propagate electrical signals over the actuator system is sufficient when being operated under high voltage excitation.

Full-Printed EAP Actuator Performance

1. Actuator Design

Based on our terpolymer actuator design prepared by the film casting method, we propose here a similar configuration but different preparation to be compliant with 3D material extrusion technique. In this case the EAP solution is prepared in a liquid form ready for printing by dissolving it in MEK or Butanone solvent at a fraction of 20.25 wt%. The preparation process was described in more detail in Chapter 2, section Material Elaborations, page 67. The achievement test for the fully printed EAP actuator is to launch its activation mechanism and measure the performance of the new actuator. In shear mode actuation, i.e. when the mechanical transverse expansion of the EAP actuator creates shear stress which can shape the glass surface, this shear stress potential depends on the shape and size of the active area, i.e. the electrode area of the actuator.

The simple actuator design intends to minimize the complexity associated with both experiment and model simulation. We formulate a circular shape for the electrode layer and print it in several diameter sizes of 16, 20, 25, and 30 mm. The full-printed actuator structure consists of the EAP layer sandwiched between two layers of electrode (top and bottom) presented in Figure 68a. The EAP layer is designed to have larger area than its electrode in order to avoid an electrical arc between top and bottom electrodes under high voltage operation.

Using the material extrusion technique to print a polymer layer, the 3D printing setup is illustrated in Figure 68b. The modular head SDS extruder cold flow is implemented in the 3D printer model Hyrel™ System 30M (Figure 68c) for extruding the EAP solution through a syringe. After commanding any shape and printing paths to the built-in software, the EAP liquid solution will be ejected through the syringe attached in the printing head directly on a glass

substrate placed on a printing platform (Figure 68b). The printing head can move in both x- and y-directions, and the printing platform can move in the z-direction synchronized with the command codes. Note that the full-printed EAP prototype is effectuated as a 3D printed shear prototype.

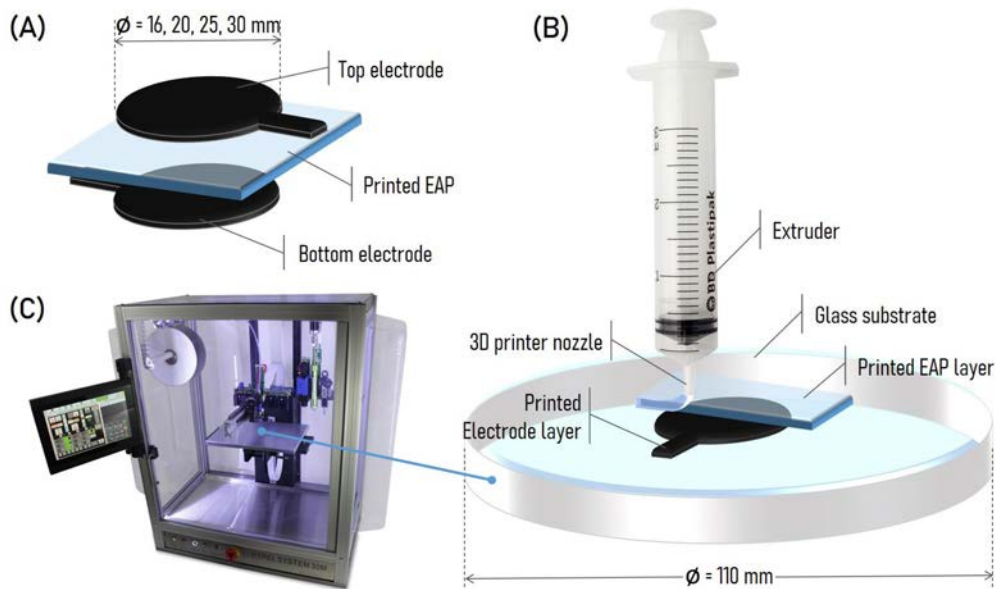


Figure 68 The 3D printing setup for printing EAP actuators; (a) the single actuator structure design consists of the EAP layer (terpolymer+DINP) and two electrode layers (terpolymer/CB composite), (b) 3D printing platform demonstrates how the entire actuator is printed layer-by-layer on a glass substrate through material extrusion, and (c) the 3D printer model Hyrel™ System 30M.

2. Full-Printed Prototype

2.1 Practical Difficulties of The Full-Printed Actuator

There are several challenges to introducing additive manufacturing technology to soft actuator fabrication: actuator thickness control, solution flow rate, an evaporation process, plasticizer filler migration, etc. In addition, the material compatibility concern over two different printed materials of the electrode and the EAP possibly comes from a disjointed thermal expansion rate and/or surface tension driven effect of different materials. These issues have been addressed as follows:

a. EAP and Electrode Printed Layer

We show the optimized functional conditions for a full-printed actuator in Table 7 on printing polymer composite. The solvent needs to be completely evaporated from the full-printed actuator (electrode-EAP-electrode) with the temperature proceeding as shown in Figure 69. The reason that the full-printed sample requires a long cooling down duration is because of the different thermal expansion rates between the electrode and the EAP layers. This effect harms the full-printed EAP by creating several cracks on the sample as shown in Figure 70.

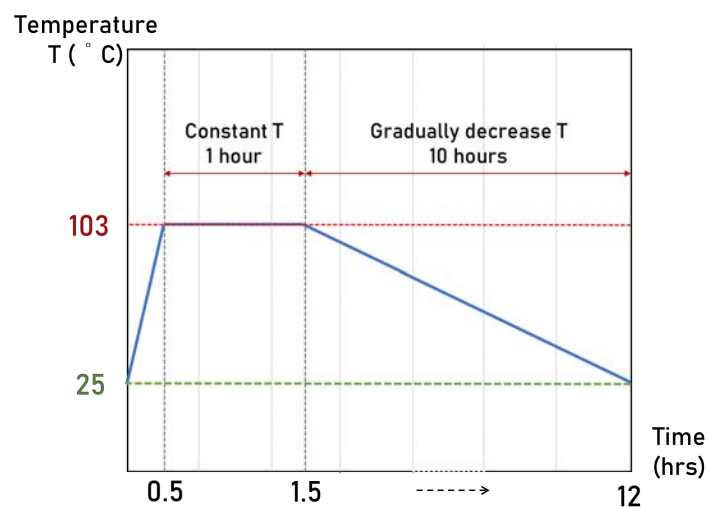


Figure 69 Temperature annealing process for evaporation residual solvent within full-printed EAP.

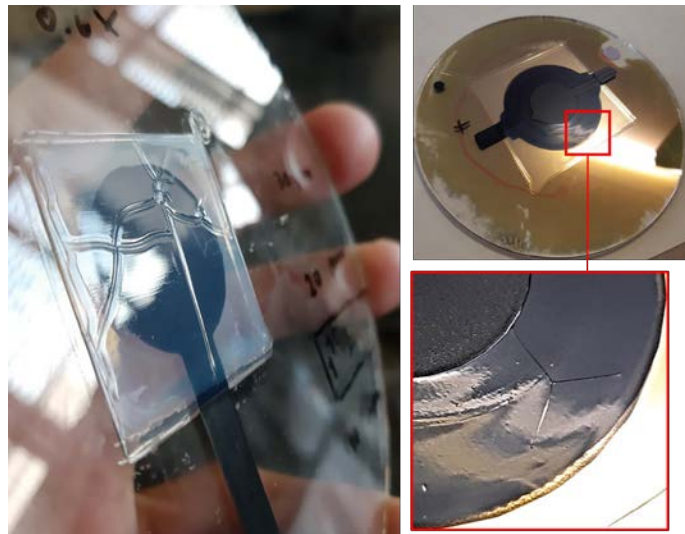


Figure 70 A fast cooling of the printed sample resulted in samples with cracks, making them unsuitable to work under high voltage operation.

Table 7 The optimized conditions for printing terpolymer composites.

Functional conditions	EAP	Electrode
Terpolymer	P(VDF-TrFE-CFE)	P(VDF-TrFE-CTFE)
Solution concentration in MEK	20.25 %	9 %
DINP filler	8 %	5 %
Carbon black filler	–	5 %
A blunt metal nozzle diameter	1.6mm (14 gauge)	0.838mm (18 gauge)
Glass syringe	30 ml	30 ml
Rate flow	800 mm/min	1200 mm/min
First layer Z distance	0.3 mm	0.1 mm
Duration of solvent evaporation at ambient temperature (for depositing another layer on top)	1–1.5 hour	20–30 minutes
Film thickness	90–100 μm	15–20 μm

b. Plasticizer Migration & Leaching

Throughout the preliminary full-printed actuator test (Figure 71), we observed the result of unexpected lower glass deformation than it used to be. The actuator efficiency test was examined on the control surface (S_c) at the central displacement (D_{pp}), which displayed significantly smaller deformation than the standard actuator coated with gold electrodes on both sides of the shear prototype as presented in Figure 71.

In view of the fact that the EAP layer and the electrode layer are both based on terpolymer, the issue of plasticizer migration between both layers should be taken into account and tested for their compatibility. Considering the attributes of the plasticizer^[12] in the polymer host, plasticizers regularly incorporate in the amorphous phase of the polymer matrix, and the crystalline phase within the polymer host is unaffected. Additionally, plasticizer molecules do not attach to polymer chains, i.e. the plasticizer molecules are only blended into the amorphous regime and create larger volume for the polymer host. This action appears to be a case of plasticizer leaching and migration issues.

The first full-printed actuator consists of the EAP layer (terpolymer+8%DINP) sandwiched between two layers of the printed electrode (terpolymer+5%CB). It could be possible that DINP molecules within the EAP layer (8%DINP) may relocate to electrode layers (no DINP) and equalize DINP content among the whole actuator. Thus, we attempted to figure out how to prevent the plasticizer migration problem by blending an optimized amount of DINP into the electrode solution. Figure 71 shows D_{pp} of S_c in microns when preliminary full-printed actuator prototypes were driven under high voltage operation. By introducing DINP 5wt% and 8wt% to the electrode layer (terpolymer+5%CB), their D_{pp} results exhibit (Figure 71) clearly that the prototype composed of the plasticized electrode attains larger S_c center deformation with higher DINP added. The ideal case to achieve the greatest glass deformation is represented by the shear sample prepared with gold electrodes referring to an excellent conductive electrode and no plasticizer leaching issue.

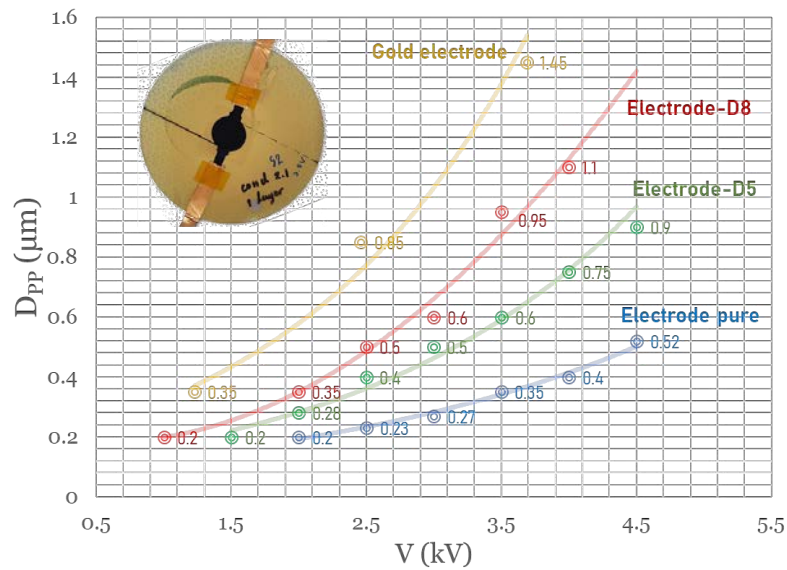


Figure 71 The central displacement (D_{pp}) of the control surface (S_c) is examined from the preliminary test of full-printed actuators (the EAP layer sandwiched with electrode layers diameter 20mm) constructed with different plasticized electrodes; no DINP added=Electrode pure, 5%DINP added= Electrode-D5, 8%DINP added=Electrode-D8 and Gold electrode for an ideal actuator. All the samples were actuated with a sinusoidal unipolar voltage at a frequency of 50 mHz.

Note here that the modified electrode doped with higher plasticizer content performs a better electromechanical activity for the full-printed actuator as presented in Figure 71: $D_{pp}^{\text{Electrode-D8}} > D_{pp}^{\text{Electrode-D5}} > D_{pp}^{\text{Electrode pure}}$. However, practically speaking, the reproducibility of the full-printed actuator constructed from the plasticized electrode with 8% DINP is inconsistent. It is possibly due to the overmuch plasticizer content causing an intolerable large free volume and high ionic conduction. In the case for the 80% of the prepared samples integrated with the plasticized electrode 8wt% DINP broke down during the preparation process and HV operation (4/5 samples). For these reasons, the optimized plasticized electrode - terpolymer + 5%CB + 5%DINP was selected for the forthcoming full-printed Live-Mirror proof-of-concept prototype.

2.2 Full-Printed Single Actuator Prototype

In order to achieve enough glass substrate (mirror) deformation by the transversal strain of the printed actuator, electric fields of 10 to 40 V/ μm were applied directly through the samples. Four different sizes (16, 20, 25, and 30 mm) of electrode diameter and multilayer actuator configuration were fabricated as full-printed single actuator prototypes. The electromechanical activity is investigated by measuring the central displacement (D_{pp}) via the interferometer dynamic calibrator, and the control surface (S_c) deformation profile via the Zygo interferometer. The surface variation between zero voltage and applying a non-zero voltage demonstrated displacements changing in the micron range (0.05–2.00 μm) depending on electrode size and construction system, i.e. single layer and/or multilayer actuator. Note that the printed EAP layer is made from terpolymer+5%DINP, and the printed electrode layer is made from terpolymer+5%CB+5%DINP.

a. Single Layer Actuator

The single-layer actuator samples (configuration as presented in Figure 68a: electrode–EAP–electrode) were assembled on a 2mm-thick flat glass substrate. With the purpose of investigating the shear effect, we fabricated the single layer prototype with four different circular electrode sizes of 16, 20, 25, and 30 mm. According to the shear actuator configuration explained in chapter 4, Shear Actuator for Glass Deformation, page 139, the shear force transferred to the glass depends on the actuator active area and the number of layers. The measured shear prototype–single layer (Figure 72) relates to what we have said that the larger active area (electrode size) could provide glass substrate (mirror) greater deformation.

All samples were subject to different applied electric fields from 10 to 40 V/ μm . As shown in Figure 72, the maximum displacement at the center of S_c increases with the size of the electrodes deposited on the actuator. The maximum D_{pp} magnitude is found at $E=40$ V/ μm for the full-printed single layer actuator with an electrode diameter of 30mm. Figure 72 shows that D_{pp} increases by a factor of about 1.4 for each 5mm increment of the electrode diameter.

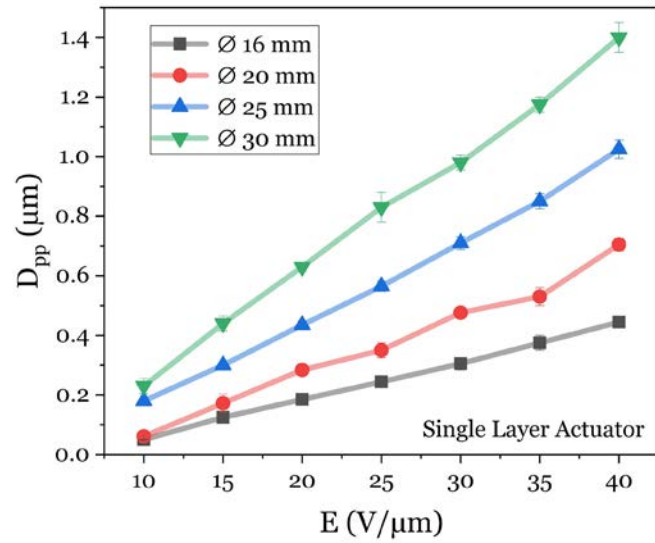


Figure 72 Comparison of the maximum displacement at the center of S_c of the full-printed single layer actuator for four electrode dimensions of 16mm, 20mm, 25mm, and 30mm in diameter operated under sinusoidal unipolar electric fields at 50 mHz.

Figure 73 presents the cross-section $[x, dz]$ lines of the S_c deformation profile analyzed from the subtraction of active stage (under electric field E operation) from initial stage (no electric field E applied) obtained by measuring (Zygo interferometer) the wavefront amplitude variation due to the S_c deformation. Full-printed actuators with the electrode of 20mm and 30mm in diameter are presented in Figure 73 aiming to showcase the shear effect. We show the S_c deformation with $(x, 0)$ cross-section obtained with electrode samples 20mm and 30mm in diameter. Predictably, the full-printed 30mm-diameter sample could modify the glass shape determined by the S_c deformation by a significantly greater magnitude than the 20mm-diameter sample could.

It should be noted that the Zygo interferometer used in this work has an aperture of 100mm in diameter whereas the sample prototype has a diameter of 110 mm. This leads to D_{pp} results measured by the interferometric dynamic calibrator and by the Zygo interferometer to have slightly different maximum displacement values. The D_{pp} result obtained from the interferometric dynamic calibrator is referred to the whole prototype system which is involved overall glass border lifting implication. Thus, if we neglect the border issue, i.e. 10mm from the glass edge, the D_{pp} results from both measurement techniques are reasonably similar.

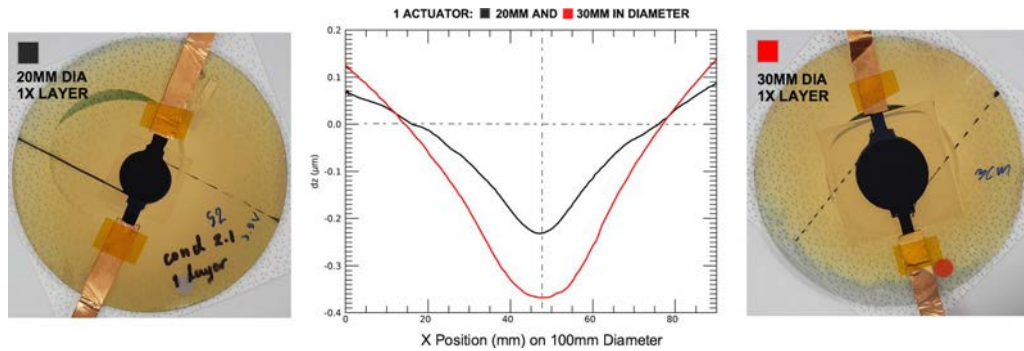


Figure 73 The control surface deformation of the full-printed single layer actuator prototype presents the actuated regime $[x,dz]$ cross-sections of (black line) – electrode $\varnothing=20$ mm and (red line) – electrode $\varnothing=30$ mm. Both samples were operated under an applied DC electric field of 30 V/ μm .

b. Multilayer Actuator

Another challenge in additive manufacturing is to fabricate multilayer-actuators. Previously (chapters 3 and 4), we reported the ability of the actuator multilayer topology to induce large actuation strain. According to the EAP multilayer stack fabrication, the full-printed multilayer actuator was structured using the multilayer design, i.e. full-printed actuator layer-by-layer toward strain boosting times number of layers. The structure of electrode/EAP/electrode is mentioned as a single layer actuator. Thus, the design of full-printed multilayer actuator is structured by depositing n -layer of the single-layer actuator (Figure 73) as a stack design. Figure 74 presents the cross-section image of the full-printed multilayer actuator made of three EAP and electrode layers.

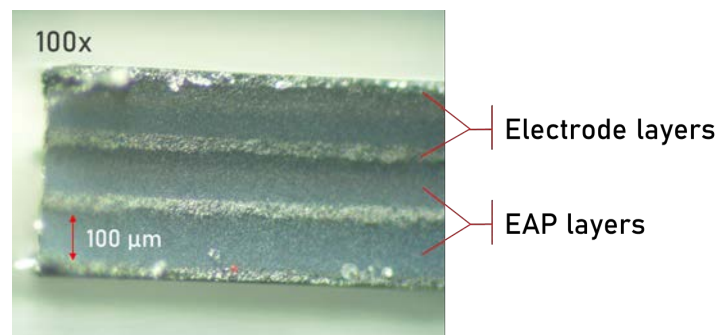


Figure 74 The cross-section image (magnified hundred times) of full-printed multilayer actuator made of three EAP and electrode layers.

A full-3D printed multilayers actuator of 20mm in diameter and for 1X, 2X, 3X layers are presented in Figure 75. Results for the displacement (dz) confirm the increase of glass deformation magnitude by developing shear force reinforcement through a multilayer actuator structure.

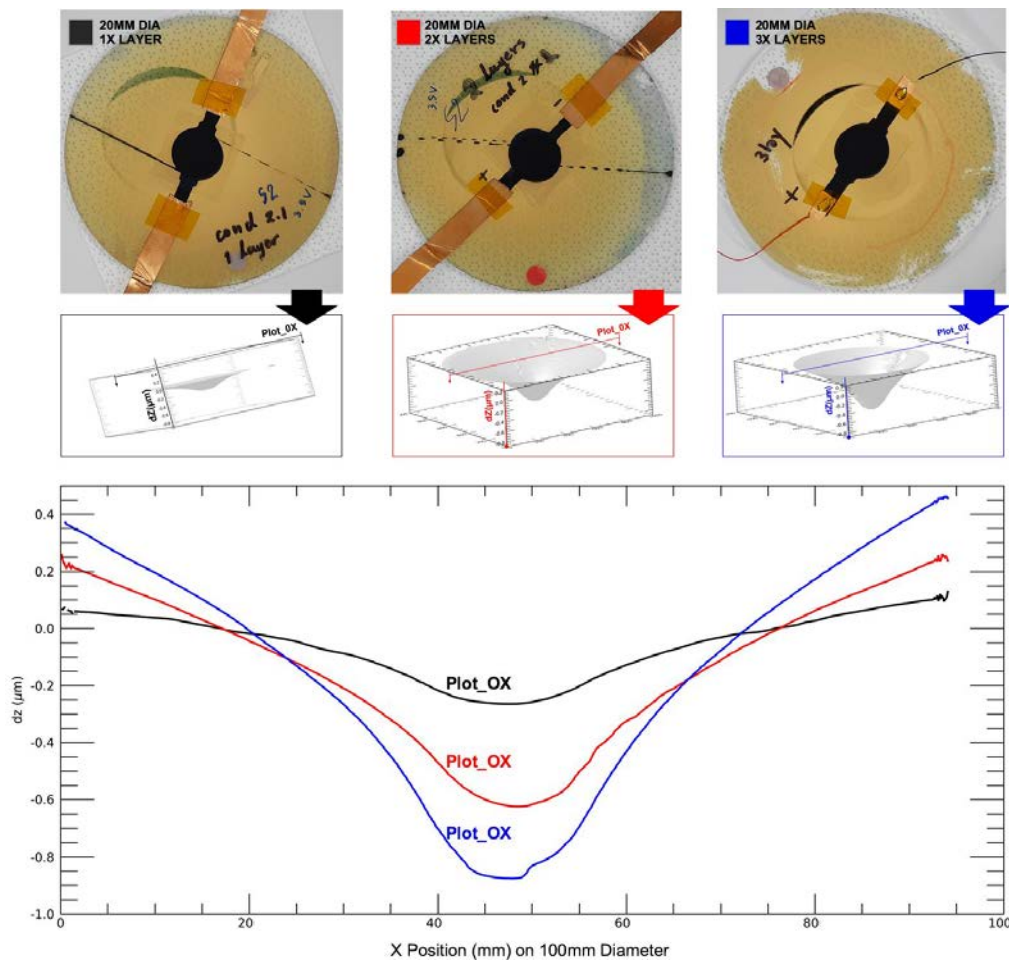


Figure 75 The full-printed multilayer actuator prototypes present their control surface deformation with $[x,dz]$ cross-sections: (black) 1-layer, (red) 2-layer, and (blue) 3-layer of single layer actuator components. All samples have their electrode diameter of 20 mm and were operated under an applied DC electric field $30 \text{ V}/\mu\text{m}$.

Based on the measurements (Figure 73 and Figure 75) and considering different input electric fields, electrode size, and multilayer actuator structure,

an improvement for the deformation attained by the actuator as aimed. However, the multilayer structure working in shear-mode has a limitation by its number of layers that the top deposited actuator layer unable to fully transfer its force-generated to shape the glass, i.e. mechanical energy-absorbing between soft actuator layer, and/or weak driven electric field. This constraint implies that the force generated from the actuator could reach the saturation regime. Strain saturation can originate from non-transferable shear force from top layer, and/or actuator interlayer clamping. More details on strain saturation will be presented in the following section of COMSOL Glass Deformation Modeling.

2.3 Multi Single Layer Actuator

The purpose of the multi-actuator investigation is to investigate the interaction between each actuator (single or multi layered) across the surface of a glass sheet (S_c). The actuators operation modes could be operated one-by-one or all at once with an independent electrical circuit printed on the S_c . The goal here is to examine on each actuator the shear-mode operation. Our first multi-actuator set up is composed of four full-3D printed, single-layer actuators on a 2mm-thick circular (110mm in diameter) glass sheet (S_c) as shown in Figure 76.

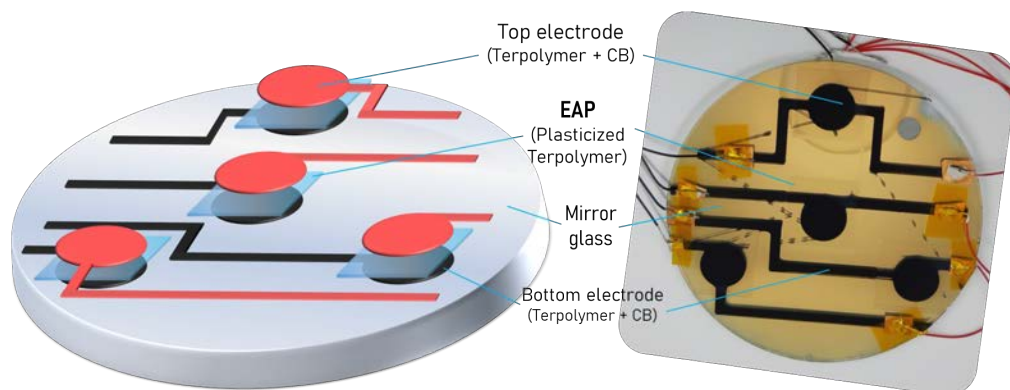
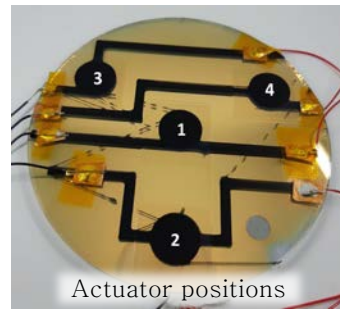


Figure 76 Left: The four single-layer actuators set up on the back of control glass surface (S_c) comprises; the printed first-layer electrode pattern (black color), the printed EAP layer (square blue sky color), and the printed top-layer electrode pattern (pink color). Right: The real full 3Dprinted single-layer four actuators and two layers electrodes on a 2mm-thick circular (110mm in diameter) glass sheet.



Operating conditions
 ON = applying $30\text{V}/\mu\text{m}$
 OFF = no E applied
 Act#1 = actuator number 1

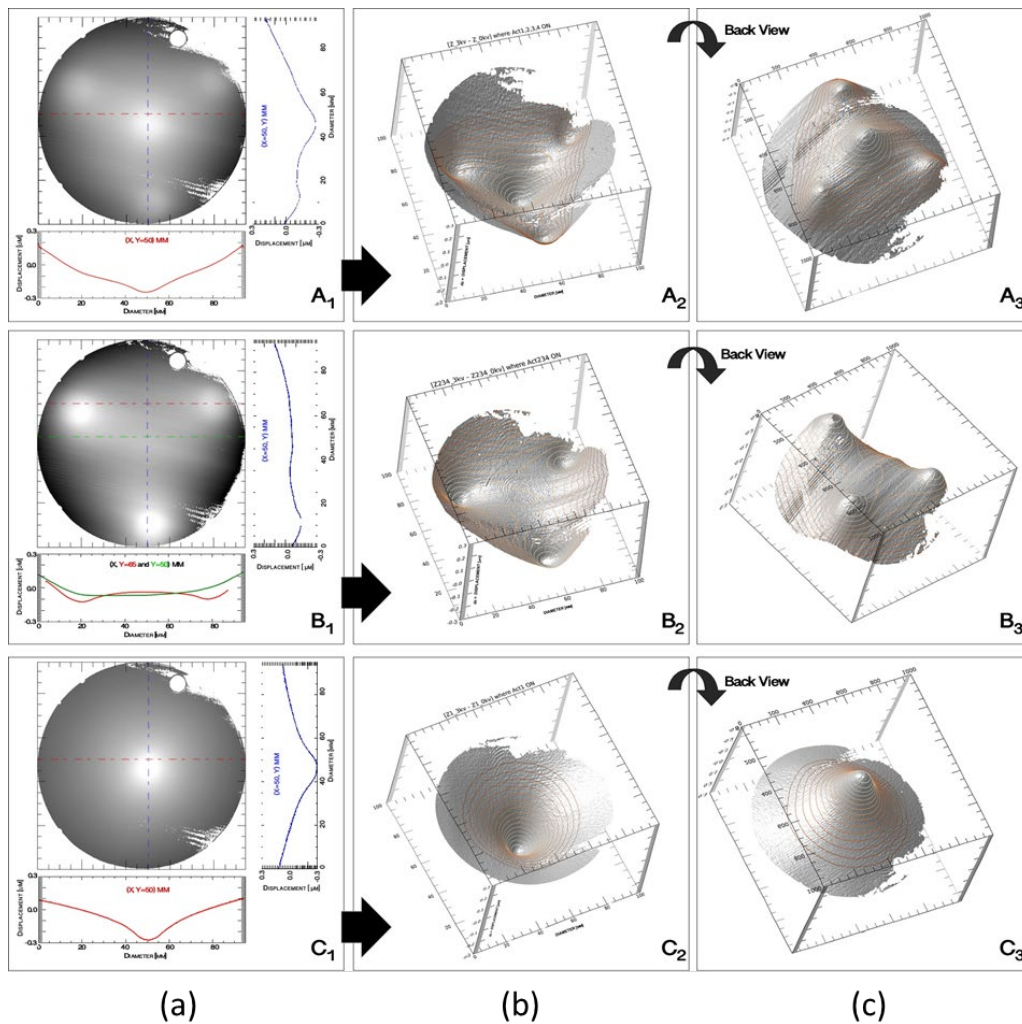


Figure 77 The single layer actuator prototype (electrode diameter 16mm) presents its front glass deformation operated under a DC voltage of 3kV . Black and white illustrations present the S_c deforming when the prototype was operated under an electric field $30\text{V}/\mu\text{m}$; column (a) the surface color scale with their cross-section lines $[(x,y),dz]$, columns (b) and (c) 3D surface plots of front S_c , and S_c rotating around a horizontal axis, respectively. The various operating conditions are presented via; row (A_n) All actuator=ON, row (B_n) Acts#2,3,4=ON & Act#1=OFF, and row (C_n) Act#1=ON & Acts#2,3,4=OFF. Global wavefront deformation measurements were realized by a Zygo interferometer.

The local deformation of S_c due each single-layer actuator (1,2,3,4) under an electric field (E) of $30 \text{ V}/\mu\text{m}$ is presented in Figure 77. The 3D surface deformation is represented using black and white gradient maps to show the S_c surface-depth including the S_c cross-section $[(x,y),dz]$ to compare the deformation scale obtained for each operation mode (Figure 77a): row A, the multi-actuator being operated all at once (Acts#s 1, 2, 3, 4); row B, the three actuators (Acts#s 2, 3, 4) being actuated, and row C, a single-actuator (Act# 1) being operated.

Note here that each mode front & back view of the S_c 3D surface deformation plots were analyzed minding the surface wavefront subtraction ($S_c^{z@E30} - S_c^{z@E0}$) yielding the straightforward result of operated actuator positions as presented in Figure 77b and c. Each operating condition starting from three activated actuators (Acts#2, 3, 4) in Figure 77, row B₁, the cross-section $[x,dz]$ **red line** shows two little valleys, i.e. superative locally deformation affected by Acts#3&4, and the cross-section $[x,dz]$ **green line** shows the cumulative surface deformation affected by 3 actuators. Noticeable that the **green line** cross-section has no little valley because the line is considered through the area where there is no actuator being integrated.

On to the condition of all actuators being actuated in Figure 77, row A₁, the cross-section $[y,dz]$ **blue line** indicates two evident little valleys coming from Acts#1&2. It is noticeable that, in the condition of all at once actuation, the deformation at the center (Act#1) provided superlative S_c deformation with respect to the Act#1 was actuated alone presented in Figure 77, row C₁. These results can be explained by the cumulative deformation of S_c which is possibly induced over actuator neighbors being operated at the same time.

The multi-actuator prototype paves the way for a more detailed investigation of both relative and absolute deformation of the control mirror. Ultimately, the variation of the surface deformation for a future version of the live-mirror prototype will be described with the numerical model for cumulative surface deformation.

Among the overall results, we could observe that the shear actuator seems to deform the glass locally corresponding to its shape. Such results will drive the next development of the electrode design and the algorithm to calculate the mirror surface profile activated through various actuator shapes and structures.

COMSOL Glass Deformation Modeling

1. Material and Simulation Parameters

We have discussed in chapter 3 the estimated dielectric permittivity under HV operation using the Debye/Langevin formalism, which enables the possibility to predict the actuation ability of the advanced plasticized terpolymer actuator. In this section, we integrate the investigated permittivity model into the S_c deformation modeling with the COMSOL Multiphysics® software. Such a modelization allows conventional physics-based user interfaces and coupled systems of partial differential equations (PDEs) making it possible to analyze, solve, and model our system^[136]. In order to model the Live-Mirror prototype performance precisely, all of the properties of the material and precise structure design, e.g. the dielectric permittivity at HV operation, film & glass thicknesses, actuator positions, etc. are required. Figure 78 illustrates the prototype assembly used for the finite-element analysis in COMSOL. Input parameters and prototype design are described as follows;

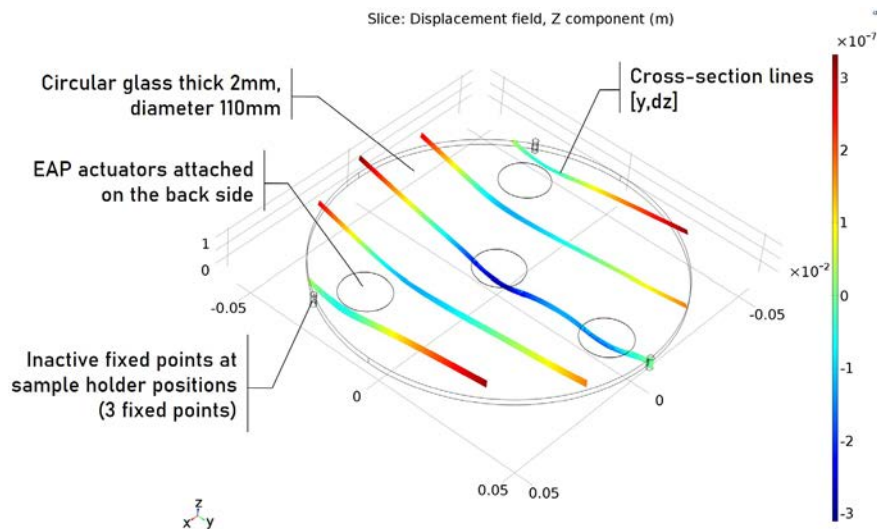


Figure 78 The schematic of the full-printed multi-actuator prototype in COMSOL used for simulating the S_c deformation under HV operation. Four full-printed single-layer actuators are implemented on the backside of the glass represented as an S_c in the system.

- **EAP actuators** were represented with circular shape ($\varnothing=16\text{mm}$) according to their electrode shape and having a thickness of $100\ \mu\text{m}$ each. All the actuators were attached to the back of the mirror. One actuator was placed at the center with the other three equally spaced along a circle of 145mm in radius. The relative permittivity and Young modulus were the corresponding ones to terpolymer doped $8\text{wt}\%$ DINP. Note that the dielectric permittivity and electromechanical conversion were calculated numerically as a function of applied voltage through Eq. (14) and (16), page 110–112.
- **Glass substrate** denoted S_c in the prototype system has a thickness of 2mm and a size of 110mm in diameter. The Young modulus of glass is $47.7\ \text{GPa}$. The whole system was fixed with 3 fixation points according to the sample holder in the experimental test bench (see Zygo setup, page 129).

2. Control Surface (S_c) Simulation

Modeling results from COMSOL analysis present a good agreement between model simulations and experimental measurements obtained from the full-printed, single-layer, multi-actuator prototype as presented in Figure 79. Analysis of S_c deformation combined with Debye/Langevin formalism confirm these results. The evaluation model was examined under three operating conditions at $E=30\text{V}/\mu\text{m}$; Act#1=ON, Acts#2,3,4=ON, and Acts#1,2,3,4=ON matching the experiment in the lab. The result in Figure 79 shows the precise dz scale deformation 97% fitting by R-square with the result in the lab.

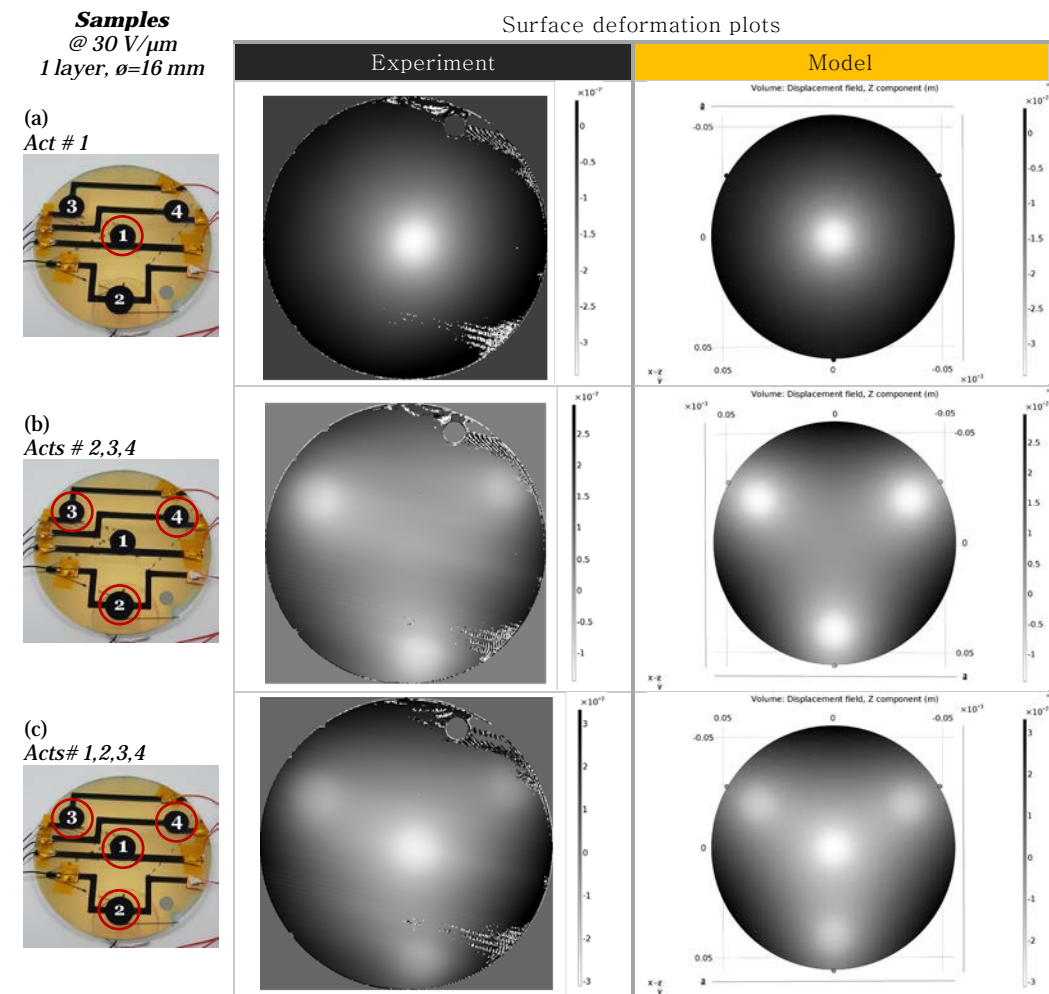


Figure 79 The control surface deformation (S_c) experiments VS models of the full-printed single layer multi-actuator prototype operated at $E_{DC}=30$ V/ μ m referred as ON state. Four actuators with an electrode diameter of 16mm, numbered (Act#n) denoting their position on the back of S_c . The grey-scale illustrations present the S_c deforming when (a) Act#1 is ON, (b) Acts#2,3,4 are ON, and (c) Acts#1,2,3,4 are ON.

Considering the cumulative surface deformation, the simulated 4-actuator model is highlighted with five curves of x and y cross-sections versus the S_c deforming variation (dz) when all actuators are being operated under an applied electric field of 30 V/ μ m (Figure 80). The simulation shows the related deformation magnitude, as well as demonstrate harmonized cross-section curvatures via 4-activated actuators prototype. The COMSOL simulations of these experiments have succeeded in modeling the glass surface deformation. The appeal of these empirical models unravels the complex system simulation involving the electromechanical behavior of terpolymer/plasticizer composite working as a force-actuator.

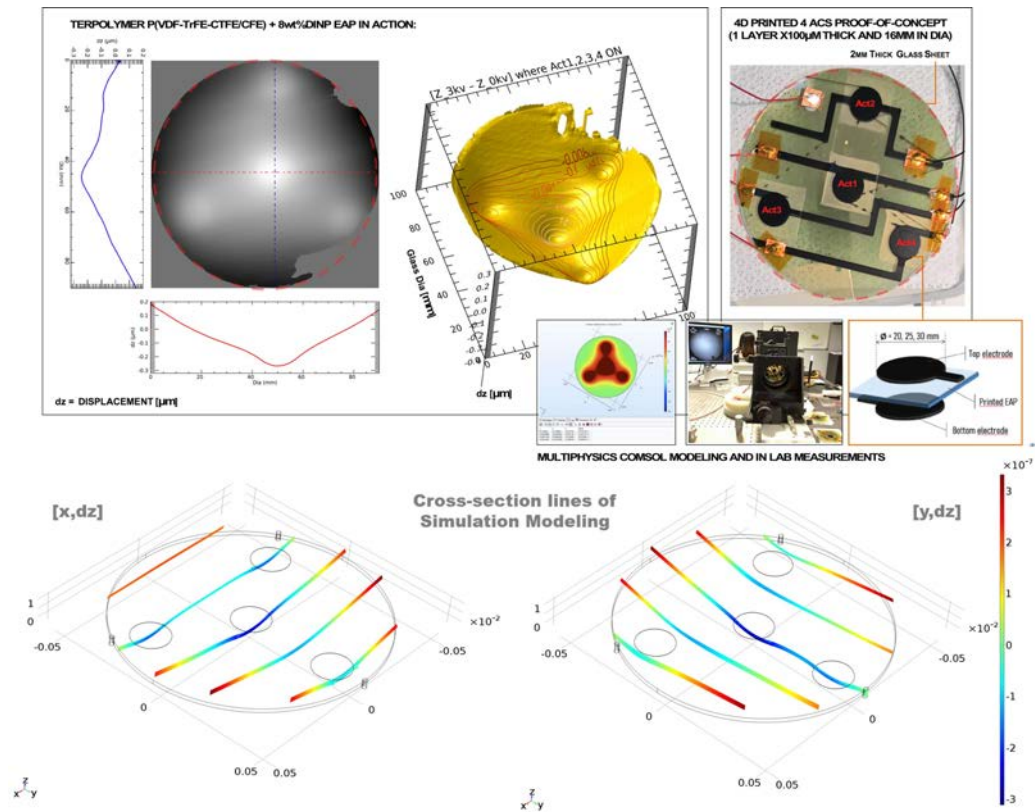


Figure 80 The full-printed single layer multi-actuator prototype presenting its S_c deformation when four actuators were activated in experimental & model analyses; (top images) the S_c deformation investigated in the lab showing its 3D surface plot and $[(x,y),dz]$ cross-section lines, and (bottom images) the replication of cross-section lines $[(x,y),dz]$ on the evaluated S_c deformation from COMSOL depicted at different positions on the S_c .

3. Maximum Displacement (D_{pp}) In Lab VS Model

To realize and simulate the influence of electrode sizes as well as the multilayer structure, we reproduced all full-printed Live-Mirror prototypes using COMSOL simulations. Note here that the maximum deformation (D_{pp}) of S_c the experimental results obtained from full-printed actuators set up (Figure 80). The variation of electrode sizes and multilayer actuator, have measurement uncertainties of $\pm 0.025 \mu\text{m}$.

The maximum surface deformations the central S_c displacement presented in Figure 81 and Figure 82 show an increase of D_{pp} when increasing an applied electric field, an electrode size, and a number of EAP layers in both experiments and models. In the case of varying electrode sizes, the evaluation model shows the results similar to the experimental variable around 94–99% –calculated R–square among data groups.

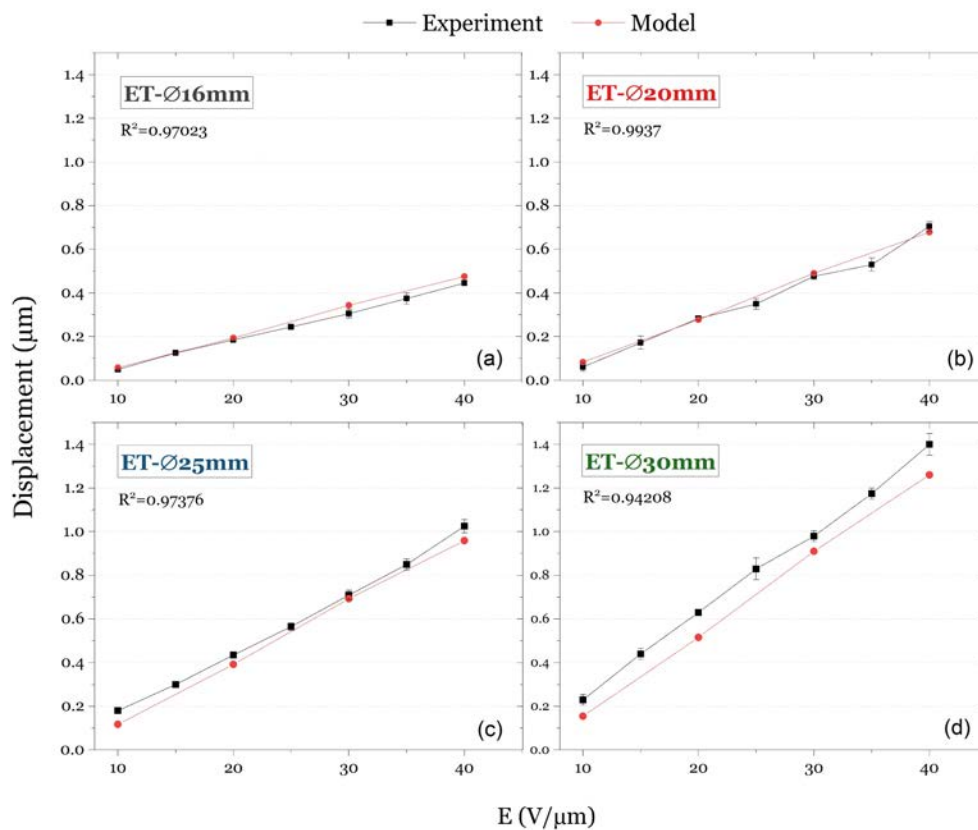


Figure 81 The center S_c displacement as a function of applied electric field results between experiments in lab and evaluation models of the full–printed single layer actuator with various electrode diameter sizes.

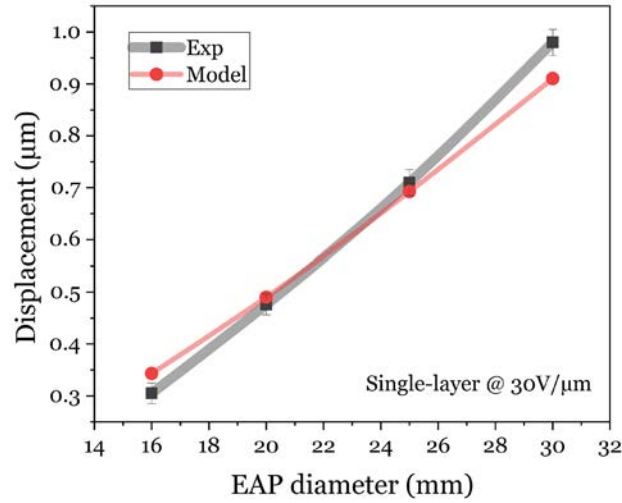


Figure 82 The comparison between experimental observation and modeling analysis presents the S_c center displacement of the full-printed single layer actuator versus its electrode diameter operated under sinusoidal unipolar of $30 \text{ V}/\mu\text{m}$ at 50 mHz .

There are some differences between measurements and model results, i.e. in Figure 81d: the experimental D_{pp} has a slightly higher value than that of the model, are possibly coming from the Ohmic heating occurring in the actual prototypes, due to low conductivity of the electrode layer (higher resistivity comparing to an ideal conductive whereas this was neglected in the model calculation).

Considering Joule's first law that the power dissipated by an electrical conductor is given by the product of its resistance and the square of the current:

$$P = I^2 R \quad (18)$$

where P is the loss of power consumption, I is the generated current, and R is the resistance of the material. Thus, the resistive heat can indeed modify the glass deformation, especially, a large electrode area involving a larger amount of leakage current (heat loss) than a small electrode area according to Eq. (18). This self-heating issue can influence the glass displacement in the actual prototype having a slightly higher value than in the model (see Figure 81d).

The Ohmic heat also depends on the frequency of voltage operation. Considering our printed electrode as a capacitor (low resistance), the capacitance can be written by:

$$C = Q/V \quad (19)$$

where Q is the charge accumulated on the electrodes, and V is an input voltage. The capacitive current is defined by:

$$I = dQ/dt = C \frac{dV}{dt} \quad (20)$$

Combining Eqs. (18)–(20), the power consumption can be written as:

$$P = C^2 R \left(\frac{dV}{dt} \right)^2 \quad (21)$$

Therefore, the self-heating depends on two main reasons; loss in the material and operating frequency. The unwanted heat generated from the sample can be minimized by improving the conductivity of the printed electrode. However, Live-mirror systems are expected to be operated at very low frequency (~ 50 mHz) or DC voltage for an active optics application. This means that the issue of heat loss at high frequency can be neglected.

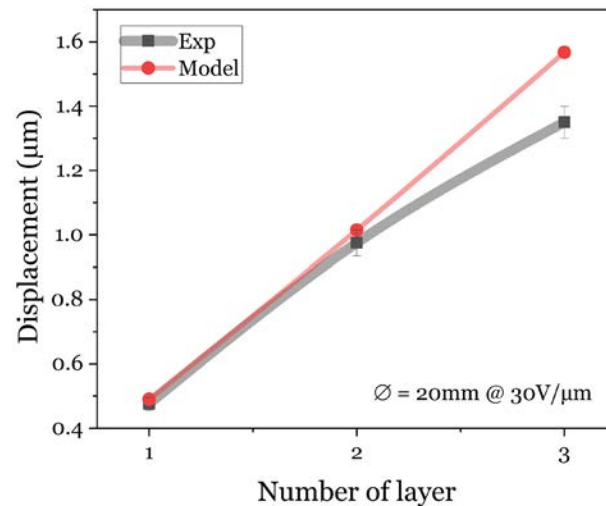


Figure 83 The comparison between experimental result and modeling analysis presents the S_c center displacement of the full-printed multilayer actuator versus the number of actuator layers operated at $30 \text{ V}/\mu\text{m}$ at 50 mHz .

Figure 83 presents the comparison of multilayer actuation displacements via their S_c center displacement from the experiment and the simulation. Even if we have well demonstrated the possibility to estimate the electro-mechanism of the actuator operating in shear-mode, the result of the full-printed multilayer actuator in the 3-layer-actuator case shows a slight divergence with the calculation. The disagreement of displacement values

between measurements and models in the multilayer actuator must be addressed in future developments.

We reported in chapter 4 (subsection: Shear Actuator Pro, page 138) that the EAP actuator working in shear-mode can allow the generated strain transfer onto the glass at some EAP thickness. The main attribution parameters disrupting actuation efficiency in the real-scale experiment might come from the interlayer shear stress within the multilayer structure ^[137] especially for the 3D-printing multilayer topology. This inter-stress in the multilayer structure impedes the effort to reinforce transferable transversal strain by increasing the number of layers. In order to improve model predictions, the interlayer stress algorithm of the multilayer structure will be considered in future model development.

Summary

To demonstrate the feasibility of employing advanced EAPs for an active-live optics application, the additive manufacturing technique is possibly integrated into the EAP actuators fabrication. By developing a printable advanced EAP with a compatible electrode, we finally achieved the full-printed actuator that qualifies as a Live-Mirror 3D printed prototype. The full-printed actuator prototype demonstrated great electromechanical response transfer to the glass substrate by deforming a single glass plate in the micron range depending on electrode size and a number of actuators. The result of the 3D printed actuator is hoping for a breakthrough in the new growth of a powerful force-actuator considering the soft actuator field. Furthermore, the empirical modeling operated by COMSOL Multiphysics® showed remarkable results agreeing well with the experimental measurements which should allow us to develop the algorithm to develop the advanced actuator design approaching to a real active-live mirror application - Live-Mirror project.

CONCLUSION

CONCLUSION

VI. Overall Research

We have launched an interdisciplinary program combining material science engineering and astronomical optics to develop and optimize an advanced and novel EAP actuator, i.e. a plasticized terpolymer to control actively & lively the shape of an optical surfaces dedicated to telescope mirrors. Starting from a perceptive study of several EAPs in order to select the optimal polymer-based actuator, we have developed a novel and an optimized EAPs, e.g. terpolymer doped with a plasticizer compliant with the high-level requirements of force-actuator performance. Several technological developments were improved in this thesis in order to advance “the-material” best suited to achieve the requirements for force-actuators-terpolymers-based to optical mirror surfaces applications.

Terpolymer- P(VDF-TrFE-CFE) has become the selected material base for the force-actuator used in an active optics application. As presented in Chapter 2 of this thesis, such a novel material was elaborated employing material modification techniques to achieve an excellent electromechanical performance: terpolymer composite adding carbon black nanoparticles and plasticizer agents. In the end the novel material characteristics are compliant with the requirements by force-actuator: (1) electrical properties: dielectric permittivity, polarization, dielectric breakdown strength, and electrical conductivity, and (2) mechanical property: Young modulus.

The actuation performance of pure and plasticized terpolymers was demonstrated and compared through their electromechanical conversion. By optimizing the plasticizer added amount and assembling its multilayer structure, this advanced EAP actuator could able to attain large strain response under low related applied electric fields. Furthermore, we observed the unexpected current behavior of the plasticized terpolymer under high voltage (HV) operation. The results demonstrated that plasticized terpolymers apparently contribute lower loss (observed through the saturation of the estimated leakage current) throughout HV operation even if loss tangents ($\tan \delta$) measured at

the low electric field (from BDS) are high. This effect can be predicted by using the Debye/Langevin formula to evaluate the dielectric permittivity of the advanced EAP operated under HV. The model of the electromechanical behavior of the advanced EAP is suited to the experimental measurements and provides the vision for Live-Mirror prototype design.

In Chapter 4, we demonstrated the possibility to overcome mirror surface deformation employing plasticized terpolymer actuator as a proof of concept through; (1) *a sandwich prototype* for global surface adjustment using the multilayer design, and (2) *a shear prototype* with the aim of achieving local surface correction using a shear mode actuator.

Next the additive manufacturing technique, i.e. 3D printing, is utilized to demonstrate the feasibility to scale-up a conventional EAP fabrication process to a more automatic soft actuator fabrication suited for an active optics application. By developing the printable advanced EAP and its compatible electrode, we finally achieved the full-printed actuator qualifying as a Live-Mirror 3D printed prototype. Furthermore, the modeling through the COMSOL Multiphysics®, showed an admirable result in excellent agreement with the experimental measurements. We intend to develop the algorithm to control the advanced actuator design for application to a real telescope in future work.

VII. Future Work

Material Perspectives

A frequently asked question on the real usability of the advanced EAP is— “*will the actuator performance change as a function of working conditions and/or with time?*” It is possible that a high temperature and humidity environment can impact the physical aging of the materials. Thus, the implications of the physical aging of our advanced EAP actuator will be considered when assessing its long-term stability in future work. The optimized chemical modification on plasticized terpolymer will be studied in-depth in terms of the humidity effect in the material preparation process. The physical aging of the electromechanical performance of the actuator will be studied by monitoring its dielectric strength as well as through working cycles in time under HV operation. The environment temperature effect is also important and can devastate the performance of the actuator, we hope to determine the limitations on operating temperature.

The development of 3D printed actuator, e.g. material manufacturing process, actuator design, etc. requires the following work:

- The terpolymer/CB composite used for the printable electrode will be developed to increase its electrical conductivity to avoid resistive self-heating under voltage operation. One possible idea to increase the electrical conductivity is to use carbon fiber or flake as particle composite;
- The plasticizer migration issue needs to be optimized in order to improve sample reproducibility by decreasing the amount of plasticizer added to an electrode layer;
- A more specific electrode pattern will be modeled and fabricated matching mirror surface defects;
- The adhesion between the full-printed actuator and the mirror substrate needs to be improved by including a surface adhesion PVDF-based spray into the fabrication process.

The 3D printing technology can allow an assessment of extensive actuator assembly, but it still needs to be developed the fabrication process, e.g. homogeneous solvent evaporative-control, stress distribution on actuator

interlayer, operation temperature, etc. The full-printed EAP actuator fabrication process control is imperative to be developed associated with the optimized mechanism.

Live-Mirror Prototype Development

Numerical Model Development-Local Curvature Analysis

Considering the mirror shape change related to actuator diameter size, we can clearly see the actuator shaping the glass locally and providing local curvature correction corresponding to its electrode size. Each actuator contributes to local curvature to the mirror surface. The curvature can affect the surface displacement far from the actuator, but the glass surface curvature is affected only where the EAP has influence. We characterize this curvature, $c(x,y)$, using the Laplacian of the z -axis displacement $\nabla^2 z(x,y) = c(x,y)$. This is evaluated numerically from the measured surface profile of the glass with the EAP actuator layer applied.

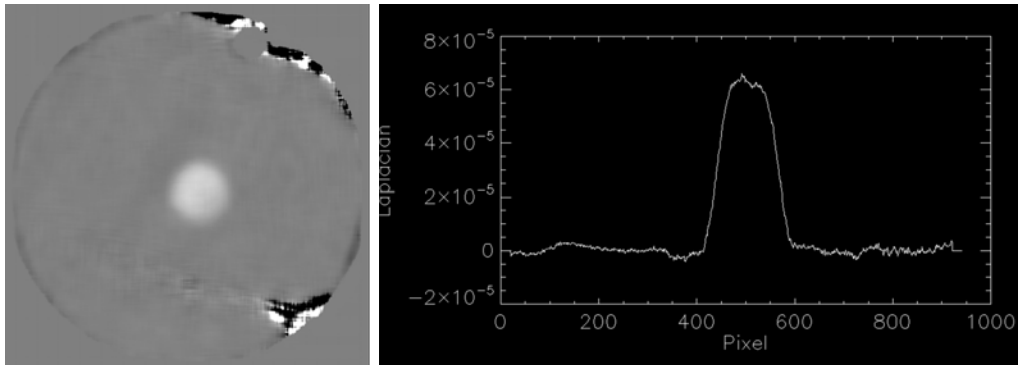


Figure 84 The Laplacian of z -axis displacement $\nabla^2 z(x,y) = c(x,y)$ numerically evaluated through single actuator sample diameter 16 mm operated under applied electric field (E) $30 \text{ V}/\mu\text{m}$: (right) top-view of Laplacian evaluation; and (left) cross-section (x -axis) showing magnitude of curvature.

Figure 84 shows the numerically computed Laplacian of the glass surface difference between $V=0$ and 3kV actuator voltages. In these arbitrary

units, we see that the 3kV actuator can provide a larger curvature than our raw glass sample surface distortion. The local curvature correction – “*curvature polishing*” – technique begins by measuring the glass curvature (characterized by the Laplacian) followed by the application of an EAP layer with sufficient displacement range to remove this curvature.

The association between the electrode shape and the Laplacian of the glass surface height is displayed in Figure 84 showing that the magnitude of the local curvature depends on the EAP thickness as well as the intensity of an applied electric field. The effect from the electrode shape causes an attached area deformation not the magnitude of local curvature. This means that the Laplacian analysis can reduce the actuator parameter design into one factor, which is the actuator thickness (and/or the number of layers). Such an effect provides an idea of a new design 3D–printed EAP, i.e. the unique electrode shape will be realized following the defect of the mirror surface. Several EAP unique shapes can work specifically to correct mirror surface default by an identical applied voltage.

The details of our algorithm for applying the electrode and approximating the local glass curvature with EAP electrode geometry will be presented in our next publication (end of 2020). Bear in mind that a large optical mirror has several unique surface defects that require specific actuator shapes and sizes in order to correct the local curvature and accomplish the desired mirror global shape by electrically polishing.

In the long term, we aim to scale–up the Live–Mirror prototype in order to address real–scale telescope mirror production. This research for a precise and smooth optical surface controlled by an active and live system via 3D–Printing of force actuators should pave the way for the future development of the next–generation telescope mirror dedicated and optimized for high–contrast observations, Exo–Life Finder Telescope^[8,10,11] (Figure 85). The world of polymers continues to grow and offers many designs, cost, and performance advantages to choose from. We hope this innovation may breakthrough conventional research and development in smart polymer fields as well as multi–interdisciplinary scientific advancement.



Figure 85 Efforts to make “Live-Mirror” prototype a reality have been our Live-Mirror project team goal. R&Ds for a precise and smooth optical surface controlled by an active and live system via 3D-Printing of force actuators should pave the way for future development of the next-generation telescope mirror dedicated and optimized for high-contrast observations – Exo-Life Finder Telescope.

BIBLIOGRAPHY

- [1] T. P. D. Rajan, J. M. Gladis, *Bio-based Plast. Appl.* 2017.
- [2] T. Wang, M. Farajollahi, Y. S. Choi, I.-T. Lin, J. E. Marshall, N. M. Thompson, S. Kar-Narayan, J. D. W. Madden, S. K. Smoukov, *Interface Focus* 2016, *6*, 20160026.
- [3] F. Bauer, *IEEE Trans. Dielectr. Electr. Insul.* 2010, *17*, 1106.
- [4] L. Yang, X. Li, E. Allahyarov, P. L. Taylor, Q. M. Zhang, L. Zhu, *Polymer (Guildf)*. 2013, *54*, 1709.
- [5] Z. Wang, Z. Zhang, T. M. Chung, *Macromolecules* 2006, *39*, 4268.
- [6] F. Xia, Z. Cheng, H. Xu, H. Li, Q. Zhang, G. J. Kavarnos, R. Y. Ting, G. Abdul-Sedat, K. D. Belfield, *Adv. Mater.* 2002, *14*, 1574.
- [7] F. Bauer, E. Fousson, Q. Zhang, *IEEE Trans. Dielectr. Electr. Insul.* 2006, *13*, 1149.
- [8] G. Moretto, J. R. Kuhn, J.-F. Capsal, D. Audigier, K. Thetraphi, M. Langlois, M. Tallon, M. Gedig, S. V. Berdyugina, D. Halliday, *Proc. SPIE – Int. Soc. Opt. Eng.* 2018, *10700*, DOI: 10.1117/12.2312599.
- [9] G. Moretto, J. R. Kuhn, S. Berdyugina, M. Langlois, M. Tallon, E. Thiébaud, D. Halliday, *Proc. SPIE – Int. Soc. Opt. Eng.* 2016, *9906*.
- [10] J. R. Kuhn, S. V Berdyugina, M. Gedig, M. Langlois, G. Moretto, K. Thetraphi, *Soc. Photo-Optical Instrum. Eng. Conf. Ser.* 2018, *10700*.
- [11] G. Moretto, J. Kuhn, J.-F. Capsal, D. Audigier, K. Thetraphi, M. Langlois, M. Gedig, S. V. Berdyugina, D. Halliday, *Int. Soc. Opt. Photonics* 2019, *10926*, 66.
- [12] M. Rahman, C. S. Brazel, *Prog. Polym. Sci.* 2004, *29*, 1223.
- [13] B. Nielsen, D. Andersen, E. Giovalle, M. Bjergstrøm, P. Larsen, *Copenhagen, Denmark Danish Environ. Prot. Agency* 2014.
- [14] S. S. Chadwick, *Ref. Serv. Rev.* 1988.
- [15] N. Della Schiava, K. Thetraphi, M. Q. Le, P. Lermusiaux, A. Millon, J.-F. Capsal, P.-J. Cottinet, *Polymers (Basel)*. 2018, *10*, 1.
- [16] J. R. Kuhn, G. Moretto, R. Racine, F. Roddier, R. Coulter, *Publ. Astron. Soc. Pacific* 2001, 1486.
- [17] Prateek, V. K. Thakur, R. K. Gupta, *Chem. Rev.* 2016, *116*, 4260.
- [18] L. Ruan, D. Zhang, J. Tong, J. Kang, Y. Chang, L. Zhou, G. Qin, X. Zhang, *Ferroelectr. Their Appl.* 2018, DOI: 10.5772/intechopen.77167.
- [19] W. C. Roentgen, *Ann. Phys. Chem* 1880, *11*, 771.
- [20] I. Krakovský, T. Romijn, A. Posthuma De Boer, *J. Appl. Phys.* 1999, *85*, 628.
- [21] S. Zhang, B. Neese, K. Ren, B. Chu, Q. M. Zhang, *J. Appl. Phys.* 2006, *100*, DOI: 10.1063/1.2335778.

- [22] Y. M. Shkel, D. J. Klingenberg, *J. Appl. Phys.* 1996, *80*, 4566.
- [23] Y. Liu, C. Lu, S. Twigg, J.-H. Lin, G. Hatipoglu, S. Liu, N. Winograd, Q. M. Zhang, in *Electroact. Polym. Actuators Devices 2011*, 2011, p. 797620.
- [24] C. Ning, Z. Zhou, G. Tan, Y. Zhu, C. Mao, *Prog. Polym. Sci.* 2018, *81*, 144.
- [25] Y. Bar-Cohen, Q. Zhang, *MRS Bull.* 2008, *33*, 173.
- [26] H. Wang, Z. Wang, J. Yang, C. Xu, Q. Zhang, Z. Peng, *Macromol. Rapid Commun.* 2018, *39*, 1800246.
- [27] K. Asaka, O. Hidenori, *Soft Actuators: Materials, Modeling, Applications, and Future Perspectives*, Springer Nature, 2019.
- [28] K. Mukai, K. Asaka, K. Kiyohara, T. Sugino, I. Takeuchi, T. Fukushima, T. Aida, *Electrochim. Acta* 2008, *53*, 5555.
- [29] S. Mehraeen, S. Sadeghi, C. Fevzi, S. A. Gürsel, *Sensors Actuators A Phys.* 2018, *279*, 157.
- [30] G. Ana M, J. Ivona, V. Koncar, C. Cochrane, F. M. Kelly, D. Soulat, X. Legrand, *J. Ind. Text.* 2018, *48*, 612.
- [31] C. H. A. Esteves, B. A. Iglesias, T. Ogawa, K. Araki, J. Gruber, *ACS omega* 2018, *3*, 6476.
- [32] H. Kato, A. Shimizu, T. Sato, M. Kushida, in *J. Phys. Conf. Ser.*, 2017, p. 012005.
- [33] M. Lallart, K. Thetraphi, J.-F. Capsal, *Phys. Lett. A* 2018, *382*, 449.
- [34] N. Della Schiava, M. Q. Le, J. Galineau, F. Domingues Dos Santos, P.-J. Cottinet, J.-F. Capsal, *J. Polym. Sci. Part B Polym. Phys.* 2017, *55*, 355.
- [35] F. Pedroli, A. Marrani, M. Q. Le, O. Sanseau, P.-J. Cottinet, J.-F. Capsal, *RSC Adv.* 2019, *9*, 12823.
- [36] F. Li, L. Jin, Z. Xu, S. Zhang, *Appl. Phys. Rev.* 2014, *1*, DOI: 10.1063/1.4861260.
- [37] C. Ribeiro, C. M. Costa, D. M. Correia, J. Nunes-Pereira, J. Oliveira, P. Martins, R. Gonçalves, V. F. Cardoso, S. Lanceros-Méndez, *Nat. Protoc.* 2018, *13*, 681.
- [38] K. B. Subramani, R. J. Spontak, T. K. Ghosh, *Compos. Sci. Technol.* 2018, *154*, 187.
- [39] S. Rat, M. Piedrahita-Bello, L. Salmon, G. Molnár, P. Demont, A. Bousseksou, *Adv. Mater.* 2018, *30*, 1.
- [40] K. Tagashira, K. Z. Takahashi, J. I. Fukuda, T. Aoyagi, *Materials (Basel)*. 2018, *11*, DOI: 10.3390/ma11010083.
- [41] X. Yin, J.-F. Capsal, D. Guyomar, *Appl. Phys. Lett.* 2014, *104*, 2012.
- [42] Z. Cheng, V. Bharti, T. Mai, T. Xu, Q. M. Zhang, S. Member, T. Ramotowski, K. A. Wright, R. Ting, 2003, *47*, 1296.
- [43] K. Thetraphi, M. Q. Le, A. Houachtia, P. Cottinet, L. Petit, D. Audigier, J. Kuhn, G. Moretto, J. Capsal, *Adv. Opt. Mater.* 2019, *1900210*, 1900210.
- [44] F. Ganet, M. Q. Le, J.-F. Capsal, P. Lermusiaux, L. Petit, A. Millon, P.-J. Cottinet, *Sci. Rep.* 2015, *5*, 1.

- [45] Y. Bar-cohen, S. Leary, *Smart Struct. Mater. Mater.* 2000, 3987, 12.
- [46] T. Mirfakhrai, J. D. W. Madden, R. H. Baughman, *Mater. Today* 2007, 10, 30.
- [47] S. Rudykh, K. Bhattacharya, G. Debotton, *Int. J. Non. Linear. Mech.* 2012, 47, 206.
- [48] M. Q. Le, J.-F. Capsal, J. Galineau, F. Ganet, X. Yin, M. D. Yang, J. F. Chateaux, L. Renaud, C. Malhaire, P.-J. Cottinet, R. Liang, *Sci. Rep.* 2015, 5, 1.
- [49] S. Shian, R. M. Diebold, D. R. Clarke, *Opt. Express* 2013, 21, 8669.
- [50] Y. Bar-cohen, in *IV Conf. Panam. END Buenos Aires, 2007*, pp. 2 - 9.
- [51] N. Festin, P. Pirim, C. Chevrot, *Sensors Actuators B Chem.* 2014, 193, 82.
- [52] Stretchsense, Stretch Sensors for Measuring Human Body Motion, <https://stretchsense.com/sensors/>, accessed: Nov., 2019.
- [53] I. Babu, G. De With, *Compos. Sci. Technol.* 2014, 91, 91.
- [54] S. Ebrahim, A. M. Elshaer, M. Soliman, M. B. Tayl, *Sensors Actuators A. Phys.* 2016, 238, 389.
- [55] S. B. Lang, S. Muensit, *Appl. Phys. A Mater. Sci. Process.* 2006, 134, 125.
- [56] K. K. Sappati, S. Bhadra, *Sensors* 2018, 18, 3605.
- [57] M. Shahinpoor, *Electrochim. Acta* 2003, 48, 2343.
- [58] Y. Wang, Y. Hou, Y. Deng, *Compos. Sci. Technol.* 2017, 145, 71.
- [59] M. Dorfmeister, B. Kössl, M. Schneider, U. Schmid, in *Multidiscip. Digit. Publ. Inst. Proc.*, 2019, p. 912.
- [60] J.-F. Capsal, J. Galineau, M. Q. Le, F. Domingues Dos Santos, P.-J. Cottinet, *J. Polym. Sci. Part B Polym. Phys.* 2015, 53, 1368.
- [61] B. H. Chen, L. Wu, M.-C. Chure, Y.-C. Chen, in *Proc. 2010 Symp. Piezoelectricity, Acoust. Waves Device Appl.*, 2010, pp. 310 - 314.
- [62] G. Miron, B. Bédard, J.-S. Plante, *Actuators* 2018, 7, 40.
- [63] S. T. Choi, J. O. Kwon, F. Bauer, *Sensors Actuators A Phys.* 2013, 203, 282.
- [64] S. T. Choi, J. O. Kwon, W. Kim, F. Bauer, in *2011-14th Int. Symp. Electrets*, IEEE, 2011, pp. 61 - 62.
- [65] S. Ahmed, *Electroactive Polymer-Based Materials for Responsive Origami-Inspired Structures*, Pennsylvania State University, 2017.
- [66] X. Yin, *Modification of Electrostrictive Polymers and Their Electromechanical Applications*, INSA DE LYON, 2015.
- [67] P. Cottinet, *Actionnement et Récupération d' énergie à l' aide de Polymères Electro-Actifs*, INSA de Lyon, 2010.
- [68] J.-F. Capsal, *Elaboration Et Analyse Des Proprietes Physiques De Nanocomposites Hybrides Ferroelectriques*, L' université de Toulouse, 2008.
- [69] M. Bashir, P. Rajendran, *J. Intell. Mater. Syst. Struct.* 2018, 29, 3681.
- [70] X. Lu, A. Schirokauer, J. Scheinbeim, 2000, 47.

- [71] J.-F. Capsal, J. Galineau, M. Lallart, P.-J. Cottinet, D. Guyomar, *Sensors Actuators, A Phys.* 2014, *207*, 25.
- [72] J.-F. Capsal, M. Lallart, J. Galineau, P.-J. Cottinet, G. Sebald, D. Guyomar, *J. Phys. D. Appl. Phys.* 2012, *45*, 205401.
- [73] Forces and Stiffness, <https://www.piceramic.com/en/piezo-technology/properties-piezo-actuators/forces-stiffnesses/>, accessed: Dec., 2018.
- [74] H. Liu, Q. Li, S. Zhang, R. Yin, X. Liu, Y. He, K. Dai, C. Shan, J. Guo, C. Liu, *J. Mater. Chem. C* 2018, *6*, 12121.
- [75] C. Cochrane, V. Koncar, M. Lewandowski, C. Dufour, *Sensors* 2007, *7*, 473.
- [76] L. V Kayser, M. D. Russell, D. Rodriguez, S. N. Abuhamdieh, C. Dhong, S. Khan, A. N. Stein, J. Ram, D. J. Lipomi, *Chem. Mater.* 2018, *30*, 4459.
- [77] Y. Tajitsu, A. Hirooka, A. Yamagishi, M. Date, *Jpn. J. Appl. Phys.* 1997, *36*, 6114.
- [78] F. Bauer, E. Fousson, Q. M. Zhang, L. M. Lee, *IEEE Trans. Dielectr. Electr. Insul.* 2004, *11*, 293.
- [79] A. J. Lovinger, *Science (80-.)*. 1983, *220*, 1115.
- [80] R. Al-Itry, K. Lamnawar, A. Maazouz, N. Billon, C. Combeaud, *Eur. Polym. J.* 2015, *68*, 288.
- [81] Y. You, X. Huang, Z. Pu, K. Jia, X. Liu, *J. Polym. Res.* 2015, *22*, 211.
- [82] M. V Kakade, S. Givens, K. Gardner, K. H. Lee, D. B. Chase, J. F. Rabolt, *J. Am. Chem. Soc.* 2007, *129*, 2777.
- [83] S. Zhang, X. Liu, S. F. Barreto-ortiz, Y. Yu, B. P. Ginn, N. A. Desantis, D. L. Hutton, W. L. Grayson, F. Cui, B. A. Korgel, S. Gerecht, H. Mao, *Biomaterials* 2014, *35*, 3243.
- [84] Y. Su, Y. Ren, G. Chen, Q. Li, *Polymer (Guildf)*. 2016, *100*, 179.
- [85] Y. Rao, A. Chortos, R. Pfattner, F. Lissel, Y. Chiu, V. Feig, J. Xu, T. Kurosawa, X. Gu, C. Wang, M. He, J. W. Chung, Z. Bao, *J. Am. Chem. Soc.* 2016, *138*, 6020.
- [86] Y. Thakur, B. Zhang, R. Dong, W. Lu, C. Iacob, J. Runt, J. Bernholc, *Nano Energy* 2017, *32*, 73.
- [87] F. Pedroli, A. Marrani, M. Q. Le, C. Froidefond, P.-J. Cottinet, J.-F. Capsal, *J. Polym. Sci. Part B Polym. Phys.* 2018, *56*, 1164.
- [88] Q. Liu, X. Yin, C. Richard, J.-F. Capsal, *J. Polym. Sci. Part B Polym. Phys.* 2016, *54*, 1645.
- [89] Z.-M. Dang, J.-K. Yuan, S.-H. Yao, R.-J. Liao, *Adv. Mater.* 2013, *25*, 6334.
- [90] C. Gao, G. Chen, *Compos. Sci. Technol.* 2016, *124*, 52.
- [91] Z. Dang, M. Zheng, J. Zha, *Mater. views* 2016, 1688.
- [92] O. Kanoun, A. Benchirouf, A. Bouhamed, *Nanotechnol. Opt. Sensors, One Cent.* 2014.
- [93] V. N. Mochalin, O. Shenderova, D. Ho, Y. Gogotsi, *Nat. Nanotechnol.* 2011, *1*.

- [94] M. Sumita, K. Sakata, S. Asai, K. Miyasaka, H. Nakagawa, *Polym. Bull.* 1991, *271*, 265.
- [95] Q. Zhang, J. Wang, B. Zhang, B. Guo, J. Yu, Z. Guo, *Compos. Sci. Technol.* 2019, *179*, 106.
- [96] Y. Ni, D. Yang, Q. Wei, L. Yu, J. Ai, L. Zhang, *Compos. Sci. Technol.* 2020, *195*, 108202.
- [97] M. Mokni, F. Pedroli, G. D. Ambrogio, M.-Q. Le, P.-J. Cottinet, J.-F. Capsal, *Polymers (Basel)*. 2020, *12*, 349.
- [98] B. Chu, X. Zhou, K. Ren, B. Neese, M. Lin, Q. Wang, F. Bauer, Q. Zhang, *Science (80-.)*. 2006, *313*, 334.
- [99] E. Baer, L. Zhu, *Macromolecules* 2017, *50*, 2239.
- [100] Z. Zhou, M. Mackey, J. Carr, L. Zhu, L. Flandin, E. Baer, *J. Polym. Sci. PART B Polym. Phys.* 2012, 993.
- [101] J. Maas, D. Tepel, T. Hoffstadt, *Meccanica* 2015, *50*, 2839.
- [102] J. Pritchard, C. R. Bowen, F. Lowrie, *Br. Ceram. Trans.* 2001, *100*, 265.
- [103] Y. Wang, J. Chen, Y. Li, Y. Niu, Q. Wang, H. Wang, *J. Mater. Chem. A* 2019, 2965.
- [104] D. J. Powell, G. Hayward, S. Member, R. Y. Ting, *IEEE Trans. Ultrason. Ferroelectr. Freq. Control* 1998, *45*, 667.
- [105] S. Sherrit, C. M. Jones, J. B. Aldrich, C. Blodget, X. Bao, M. Badescu, Y. Bar-cohen, in *Behav. Mech. Multifunct. Compos. Mater. 2008*, 2008.
- [106] M. Senousy, F. Li, D. Mumford, M. Gadala, R. Rajapakse, *J. Intell. Mater. Syst. Struct.* 2009, *20*, 387.
- [107] Y. Song, S. Qin, J. Gerringer, J. Grunlan, *Soft Matter* 2019, *15*, 2311.
- [108] L. Wang, H. Luo, X. Zhou, X. Yuan, K. Zhou, D. Zhang, *Compos. Part A* 2019, *117*, 369.
- [109] H. Henniger, O. Wilfert, *Radioengineering* 2010, *19*, 203.
- [110] European Southern Observatory, The European Extremely Large Telescope, <https://www.eso.org/public/teles-instr/elt/>.
- [111] U. Siemann, in *Scatt. Methods Prop. Polym. Mater.*, Springer, 2005, pp. 1 - 14.
- [112] Z. Cui, E. Drioli, Y. Moo, *Prog. Polym. Sci.* 2014, *39*, 164.
- [113] L. Zhu, Q. Wang, *Macromolecules* 2012, *45*, 2937.
- [114] N. Kumar, P. K. Jain, P. Tandon, P. M. Pandey, *J. Brazilian Soc. Mech. Sci. Eng.* 2018, *40*, 175.
- [115] C. Basaran, E. Gunel, *Int. J. Mater. Struct. Integr.* 2013, *7*, 100.
- [116] A. K. Jonscher, *Nature* 1977, *267*, 673.
- [117] O. Folorunso, Y. Hamam, R. Sadiku, S. S. Ray, A. G. Joseph, *Polymers (Basel)*. 2019, *11*, 1250.
- [118] M. Rahaman, A. Aldalbahi, P. Govindasami, N. Khanam, S. Bhandari, P. Feng, T. Altalhi, *Polymers (Basel)*. 2017, *10*, 527.

- [119] F. Kremer, S. Andreas, *Broadband Dielectric Measurement Techniques*, Springer Science & Business Media, 2002.
- [120] A. Kahouli, *Tech. I' ingénieur Matériaux isolants en électrotechnique* 2016, TIB255DUO.
- [121] L. Zhu, *J. Phys. Chem. Lett.* 2014, 5, 3677.
- [122] J. Mijovic, B. D. Fitz, *Appl. Dielectr. Relax. Spectrosc.* 1998, 1.
- [123] G. S. Buckley, C. M. Roland, R. Casalini, A. Petchsuk, T. C. Chung, *Chem. Mater.* 2002, 14, 2590.
- [124] R. Farhan, A. Eddiai, M. Meddad, M. H. Mazroui, D. Guyomar, *Smart Mater. Struct.* 2019, 28, 035024.
- [125] TMT International Observatory, Thirty Meter Telescope Astronomy' s Next-Generation Observatory, <https://www.tmt.org/>, accessed: Mar., 2019.
- [126] W. M. Keck Observatory, Keck I And Keck II Telescopes, <http://www.keckobservatory.org>, accessed: Mar., 2019.
- [127] S. Z. Guo, K. Qiu, F. Meng, S. H. Park, M. C. McAlpine, *Adv. Mater.* 2017, 29, 1.
- [128] V. C. F. Li, C. K. Dunn, Z. Zhang, Y. Deng, H. J. Qi, *Sci. Rep.* 2017, 7, 1.
- [129] S. H. Park, R. Su, J. Jeong, S. Z. Guo, K. Qiu, D. Joung, F. Meng, M. C. McAlpine, *Adv. Mater.* 2018, 30, 1.
- [130] G. Haghiashtiani, E. Habtour, S. H. Park, F. Gardea, M. C. McAlpine, *Extrem. Mech. Lett.* 2018, 21, 1.
- [131] Additive manufacturing, <https://www.ge.com/additive/additive-manufacturing>, accessed: May, 2019.
- [132] K. Thetraphi, S. Chaipo, W. Kanlayakan, P.-J. Cottinet, M. Q. Le, L. Petit, D. Audigier, J. Kuhn, G. Moretto, J.-F. Capsal, *Adv. Eng. Mater.* 2020, 22, 1901540.
- [133] Hyrel 3D, Hyrel 3D SYSTEM 30M, <http://www.hyrel3d.com/portfolio/system-30m/>, accessed: Feb., 2020.
- [134] G. Cummins, M. P. Desmulliez, *Circuit world* 2012, DOI: 10.1108/03056121211280413.
- [135] A. L. Dearden, P. J. Smith, D. Shin, N. Reis, B. Derby, P. O. Brien, *Macromol. Rapid Commun.* 2005, 26, 315.
- [136] COMSOL, <https://www.comsol.com/>, accessed: Mar., 2020.
- [137] S. Faulhaber, C. Mercer, M.-W. Moon, J. Hutchinson, A. Evans, *J. Mech. Phys. Solids* 2006, 54, 1004.

APPENDIX

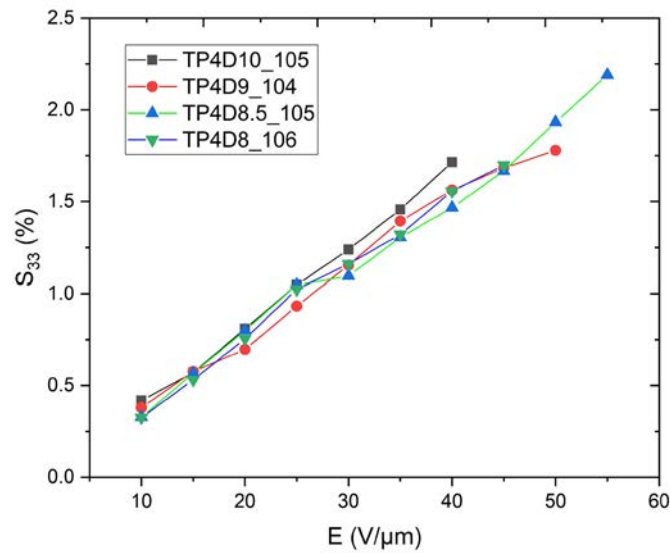
Strain vs Plasticizer contents variation

CHAPTER 3, Strain Measurement under Applied Electric Fields, page 102

Table 8 Longitudinal strain response (S_{33}) of terpolymer doped with plasticizer DINP and DOA with various percentages as a function of electric fields.

F pre-load = 1.42 N, Sinusoid Unipolar 50 mHz
 Sample thickness = 180-200 μm
 Active area = 12.567 cm^2 (circular electrode $\phi=2\text{ cm}$)

Terpolymer P(VDF-TrFE-CFE)	S_{33} (%)				
	10 V/ μm	15 V/ μm	20 V/ μm	25 V/ μm	30 V/ μm
Pure	0.0362	0.1710	0.2460	0.2767	
Δ pure	0.0010	0.0060	0.0030	0.0066	
DINP2	0.0778	0.1135	0.1821	0.2783	
Δ DINP2	0.0033	0.0028	0.0047	0.0028	
DINP4	0.1147	0.1968			
Δ DINP4	0.0078	0.0075			
DINP6	0.2142	0.3238	0.1051		
Δ DINP6	0.0111	0.0017	0.0014		
DINP8	0.4125	0.6182	0.7579	1.0387	1.2168
Δ DINP8	0.0047	0.0039	0.0165	0.0523	0.0356
DINP10	0.2905	0.3386	0.5050	0.6878	0.8711
Δ DINP10	0.0042	0.0042	0.0035	0.0138	0.0046
DINP12	0.4914	0.7692	1.0942		
Δ DINP12	0.0162	0.0053	0.0017		
DINP15	0.4203				
Δ DINP15	0.0104				
DOA6	0.1406	0.1674			
Δ DOA6	0.0091	0.0050			
DOA8	0.4343	0.5458			
Δ DOA8	0.0291	0.0154			
DOA10	0.2963				
Δ DOA10	0.0607				

Plasticizer small different contents effect*CHAPTER 3, Strain Measurement under Applied Electric Fields, page 102*

Plasticizer DINP slightly variation contents (from 8 to 10 wt%) affecting the longitudinal strain response as a function of applied electric fields

Notes:

TP4D(n)_nnn

TP4 = terpolymer P(VDF-TrFE-CFE)

D(n); n=8, 8.5, 9, 10 = DINP filler content percentage by mass

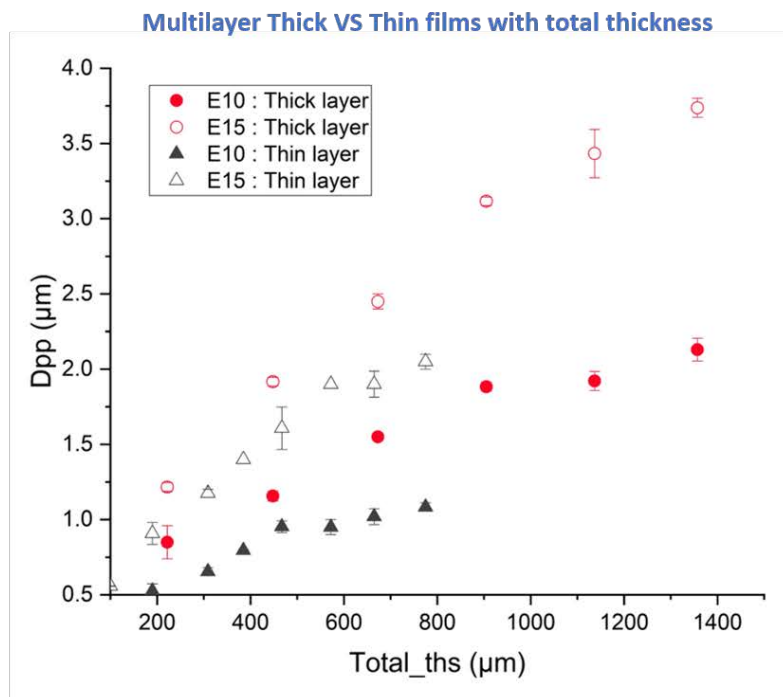
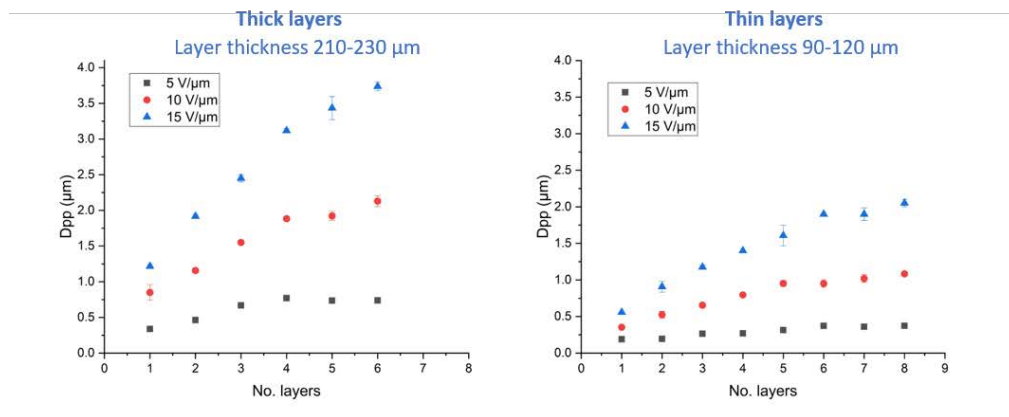
_nnn = thickness in micron scale

Layer thickness effect

CHAPTER 4, Shear Actuator for Glass Deformation, page 139

Shear Test
 TP4D10_Multilayer Thick VS Thin films
 Glass \varnothing 11 cm, 3mm-thickness

Center Displacements of S_c



*total thickness = summation of each thickness layer

The S_c central displacement results from Zygo interferometer and interferometric dynamic calibrator

CHAPTER 4, Live-Mirror Prototypes, Experimental Results, page 130

One could ask why the S_c central displacement carried out by interferometric dynamic calibrator, has a slightly higher value than the central S_c displacement observed from the wavefront surface profile measured via the Zygo interferometer. Considering the differences between the two measurements set up are as follows:

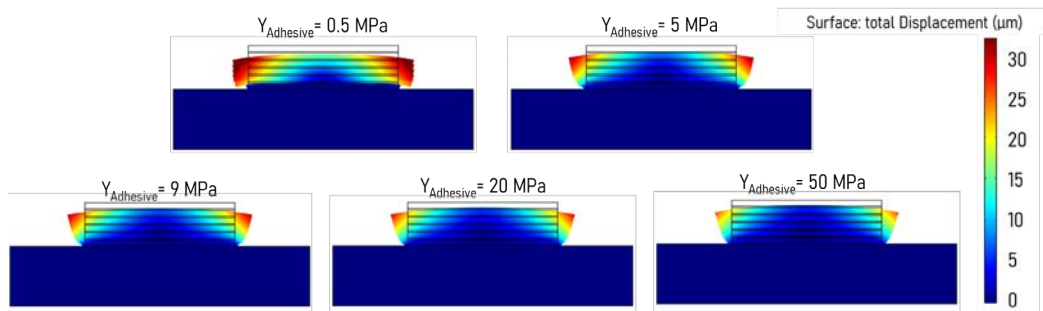
- (i) The Zygo test bench has a laser detector aperture size of 100mm in diameter which means the maximum displacement of S_c obtained from this technique is referenced by the distance from center to the edge of the collimated laser beam, i.e. likely the control surface (S_c) is reduced the S_c size from 110mm to 100mm in diameter. Thus, the cumulative deformation of the partial area 10mm from the edge of S_c is eliminated somewhat over the measurement analysis. Moreover, the sample holder used in the Zygo test bench has 3-holder points (see Figure 47 or Figure 58a). Such holder three points constraint the S_c displacement when the actuator is on.
- (ii) The interferometric dynamic calibrator is used to measure the one-point displacement on the S_c . This means that the maximum glass-deformation, at the central S_c , is referenced by the distance from center to the edge of the entire prototype-110mm in diameter and the observed displacement is involved in the entire S_c cumulative deformation. Additionally, the prototype is placed freely on the optical table (see Figure 46), i.e. without any sample holder gripping. Thus, under non-constraint operation, the S_c displacement measured via interferometric dynamic calibrator certainly gives slightly higher value compared to the one obtained from the Zygo.

However, we intend to demonstrate the actuator performance in several prototype designs, e.g. sandwich multilayer prototypes and shear prototypes. The investigation is to compare the electromechanical ability among their various prototype structures. It is complicated to compare experimental results obtained from different measurement techniques because the operational constraints are unrelated. This issue brings about the border effect consideration and operational constraints that require to be developed in future work.

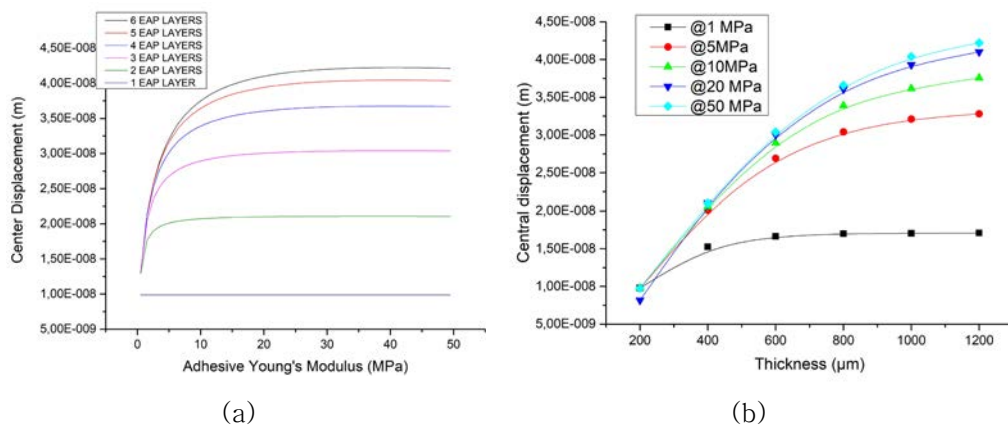
Shear effect of multilayer topology evaluation model–Shear prototype

CHAPTER 4, Adhesive Interlayer Shear Effect of Multilayer Shear Actuator, page 143

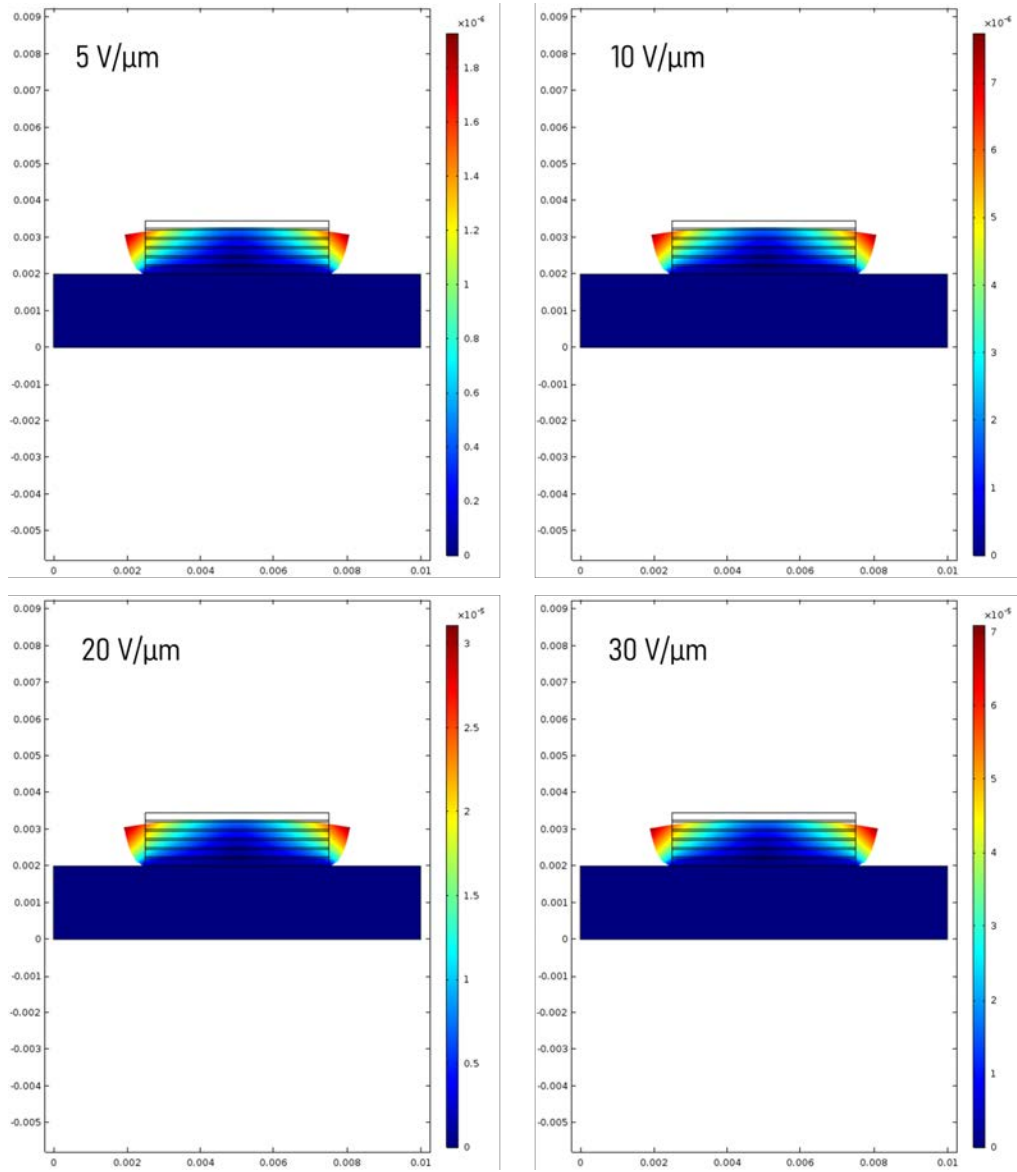
1. The total displacement of 6-layer-EAP varying $Y_{Adhesive}$ under $E=10V/\mu m$



2. S_c center displacement as a function of (a) adhesive's Young modulus value and (b) EAP total thickness



3. The total displacement of 6-layer-EAP with $Y_{\text{Adhesive}} = 9 \text{ MPa}$ activated through $E=5-30\text{V}/\mu\text{m}$



The S_c central displacement of full-printed prototypes measured by interferometric dynamic calibrator

CHAPTER 5, Full-Printed Single Actuator Prototype, page 163

Table 9 Maximum Displacement observed at the center point of the actuator area at the front glass surface as a function of different applied electric fields, actuator sizes, and a number of layers.

E (V/ μ m)	Maximum Displacement (μ m)											
	1 layer								2 layers		3 layers	
	ϕ 16 mm		ϕ 20 mm		ϕ 25 mm		ϕ 30 mm		ϕ 20 mm			
	Exp.	Model	Exp.	Model	Exp.	Model	Exp.	Model	Exp.	Model	Exp.	Model
10	0.050	0.058	0.061	0.083	0.180	0.118	0.230	0.155	0.230	0.173	0.278	0.267
15	0.125		0.173		0.300		0.440		0.390		0.525	
20	0.185	0.194	0.284	0.278	0.435	0.392	0.630	0.515	0.555	0.575	0.777	0.888
25	0.244		0.350		0.565		0.830		0.745		1.010	
30	0.305	0.343	0.476	0.490	0.710	0.693	0.980	0.910	0.975	1.015	1.350	1.568
35	0.375		0.530		0.850		1.175		1.193		1.564	
40	0.445	0.475	0.705	0.678	1.025	0.959	1.400	1.260	1.493	1.405	1.838	2.170

PUBLICATIONS

Peer-reviewed publications:

1. Lallart, M., Thetpraphi, K. and Capsal, J.F., 2018. Analysis of temperature effect in dielectric response of electrostrictive polymers for pseudo-pyroelectric operations. *Physics Letters A*, 382(7), pp.449–454.
2. Della Schiava, N., Thetpraphi, K., Le, M.Q., Lermusiaux, P., Millon, A., Capsal, J.F. and Cottinet, P.J., 2018. Enhanced figures of merit for a high-performing actuator in electrostrictive materials. *Polymers*, 10(3), p.263.
3. Thetpraphi, K., Le, M.Q., Houachtia, A., Cottinet, P.J., Petit, L., Audigier, D., Kuhn, J., Moretto, G. and Capsal, J.F., 2019. Surface Correction Control Based on Plasticized Multilayer P (VDF-TrFE-CFE) Actuator—Live Mirror. *Advanced Optical Materials*, 7(13), p.1900210.
4. Saha, S., Bhowmick, A.K., Kumar, A., Patra, K., Cottinet, P.J. and Thetpraphi, K., 2020. Polyvinylidene Fluoride/Hydrogenated Nitrile Rubber based Flexible Electroactive Polymer Blend and its Nanocomposites with Improved Actuated Strain: Characterization and Analysis of Electrostrictive Behaviour. *Industrial & Engineering Chemistry Research*.
5. Thetpraphi, K., Chaipo, S., Kanlayakan, W., Cottinet, P.J., Le, M.Q., Petit, L., Audigier, D., Kuhn, J., Moretto, G. and Capsal, J.F., 2020. Advanced Plasticized Electroactive Polymers Actuators for Active Optical Applications: Live Mirror. *Advanced Engineering Materials*, 22(5), p.1901540.
6. Della Schiava, N., Pedroli, F., Thetpraphi, K., Flocchini, A., Le, M.Q., Lermusiaux, P., Capsal, J.F. and Cottinet, P.J., 2020. Effect of beta-based sterilization on P (VDF-TrFE-CFE) terpolymer for medical applications. *Scientific Reports*, 10(1), pp.1–12.
7. Last paper of 3D printed EAP - waiting for the submission

Conferences publications:

8. Moretto, G., Kuhn, J.R., Langlois, M., Tallon, M., Gedig, M., Norton, A., Capsal, J.F., Audigier, D., Thetpraphi, K., Berdyugina, S.V. and Halliday, D., 2018, June. The ExoLife Finder (ELF) Telescope: new adaptive optics and hybrid dynamic live-optical surfaces strategies. In Adaptive Optics: Analysis, Methods & Systems (pp. OTh2F-4). Optical Society of America.
9. Kuhn, J.R., Berdyugina, S.V., Capsal, J.F., Gedig, M., Langlois, M., Moretto, G. and Thetpraphi, K., 2018, July. The Exo-Life Finder Telescope (ELF): design and beam synthesis concepts. In Ground-based and Airborne Telescopes VII (Vol. 10700, p. 1070015). International Society for Optics and Photonics.
10. Moretto, G., Kuhn, J.R., Capsal, J.F., Audigier, D., Thetpraphi, K., Langlois, M., Gedig, M., Berdyugina, S.V. and Halliday, D., 2019, April. Hybrid dynamic structures for optical-quality surfaces shape control: Live-Mirror. In Quantum Sensing and Nano Electronics and Photonics XVI (Vol. 10926, p. 109261X). International Society for Optics and Photonics.
11. Thetpraphi, K., Moretto, G., Kuhn, J.R., Cottinet, P.J., Le, M.Q., Audigier, D., Petit, L. and Capsal, J.F., 2019, March. Live-Mirror shape correction technology operated through modified electroactive polymer actuators. In Electroactive Polymer Actuators and Devices (EAPAD) XXI (Vol. 10966, p. 109662U). International Society for Optics and Photonics.
12. Thetpraphi, K., Moretto, G., Kuhn, J.R., Cottinet, P.J., Le, M.Q., Audigier, D., Petit, L. and Capsal, J.F., 2020, April. Advanced 3D-printed EAP actuator applied to high precision large optical-quality surface fabrication: first results. In Electroactive Polymer Actuators and Devices (EAPAD) XXII (Vol. 11375, p. 113751X). International Society for Optics and Photonics.

CONFERENCES

2017

- Les Journées Nationales sur la Récupération et le Stockage d'Energie (JNRSE): [Poster presentation](#)
- The 16th International Symposium on Electrets (ISE16), Leuven, Belgium: [Participated](#)

2018

- International conference on Electromechanically active polymer (EAP) transducers & artificial muscles (EuroEAP 2018), Lyon, France: [Pitch talk & Poster presentation](#)
- Global congress and expo on materials science and engineering (GCEMSE2018), Rome, Italy: [Oral presentation](#)
- The association of Thai professional in European Region conference (ATPER2018), Oslo, Norway: [Pitch talk](#)
- The 44th congress on science and technology of Thailand (STT44), Bangkok, Thailand: [Oral presentation](#)

2019

- SPIE Smart Structures + Nondestructive Evaluation, Denver, United States: [Poster presentation](#)
- SDM 2e Colloque Français sur la Spectroscopie Diélectrique appliquée aux Matériaux, Lyon, France : [Oral presentation](#)
- International Symposium on Applications of Ferroelectrics (ISAF2019), Lausanne, Switzerland: [Oral presentation](#)
- Seminar strategy for research collaboration, Department of Physics, Prince of Songkla University, Thailand: [Live-Mirror project divulgation](#)

2020

- Anaheim SPIE [Oral presentation \(Pre-recording & Video conference\)](#)





FOLIO ADMINISTRATIF

THESE DE L'UNIVERSITE DE LYON OPEREE AU SEIN DE L'INSA LYON

NOM : THETPRAPHI

DATE de SOUTENANCE : 15 JUILLET 2020

Prénoms : Kritsadi

TITRE : Development of Electroactive Polymer Actuators for Next Generation Mirror: Live-Mirror

NATURE : Doctorat

Numéro d'ordre : 2020LYSEI058

Ecole doctorale : E.E.A.

Spécialité : Electronique - Génie électrique

RESUME : We have developed new and interdisciplinary technology for creating extremely lightweight, diffraction-limited, meta-material-based optical systems with exceptional optical quality and spectacularly lower cost and production time: Live-Mirror. The novelty is to replace classical rigid and heavy optical mirrors with “live” and light dynamic optoelectronic systems consisting of a thin optical glass sheet actively supported by multiple force-actuators/sensors integrated and miniaturized via additive manufacturing and 3D printing. Our breakthrough Live-Mirror features and active shape control with many-degrees-of-freedom force actuators achieved by developing an additive 3D-printing-based technology to apply an optimized electroactive polymer (EAP) system to a sandwich of thin glass surfaces, thus creating a novel hybrid meta-material with superior stiffness-to-density ratio properties. This thesis describes the development of soft actuators based on modified/doped EAPs, here dubbed terpolymer P(VDF-TrFE-CFE). We will show that this new and Live-Mirror customized terpolymer matrix features an outstanding electromechanical coupling property, particularly when doped with a plasticizer, e.g. diisononyl phthalate (DINP). Here we demonstrate that by optimizing the structured multilayer design, the electromechanical coupling of the modified terpolymer can be enhanced, yielding high dielectric permittivity, low Young modulus, and exceptional dielectric strength. This leads to a large strain response as well as high mechanical energy density under relatively low electric fields according to the electrostriction phenomenon – the main goal of the high-level specifications of Live-Mirror. In addition to a customized terpolymer matrix, the concept of stacked multilayers is demonstrated as a simple and effective technique to boost actuation abilities. Several 3D-printed, proof-of-concept (in the lab) experimental results, which are in good agreement with numerical models, validate the actuator performance with a large electromechanical response. This technology shows feasibility for active optical surface shape control and demonstrates the Live-Mirror optical shape control and correction with only a few degrees-of-freedom. Such a novel and advanced actuator application via additive manufacturing technology are compliant for ground- and space-based astronomy and communications telescopes as well as many modern electronic devices.

MOTS-CLÉS : Electroactive polymers (EAPs), Plasticized terpolymer, Force-actuator, Actuators and sensors, Development actuator performance, Multilayer actuator, Deformable mirrors, Active optics application, Live-Mirror, 3D-printing Actuator, Additive manufacturing, 4D printing Astronomy and optical communication applications.

Laboratoire (s) de recherche : Laboratoire de Génie Electrique et Ferroélectricité (LGEF) INSA Lyon

Directeur de thèse: Prof. Lionel PETIT, and Dr. Jean-Fabien CAPSAL

Président de jury : Prof. Jean-Yves CAVAILLE

Composition du jury : CAVAILLE, Jean-Yves
DANTRAS, Eric
PUTSON, Chatchai
COLIN, Annie
LANGLOIS, Maud
USON, Juan
PETIT, Lionel
CAPSAL, Jean-Fabien

